NAM

Depletion-induced fault slip and seismic rupture

2D Geomechanical models for the Groningen field, The Netherlands

Shell Global Solutions International B.V., Rijswijk

Peter A. J. van den Bogert

Date December 2018

Editors Jan van Elk & Dirk Doornhof

General Introduction

Several geomechanical studies investigating the induced seismicity in the Groningen field have been initiated. This includes development of geomechanics-based seismological models (Ref. 1 to 4) and geomechanical studies to fundamentally better understand the destabilization of the faults as a result of reservoir depletion and the dynamics of the fault rupture process (Ref. 5 to 6).

The current report describes the progress of the studies into the earthquake initiation and development since 2015 (Ref. 5 and 6), which has the objective to develop an understanding of:

- the potential conditions under which fault slip and seismic rupture occurs.
- the impact of reservoir depletion, reservoir offset and reservoir thickness on the occurrence of fault instability and the magnitude of the simulated seismic rupture.
- the mechanical response imposed by assuming a linear fault slip-weakening relationship. This includes the sensitivity of the various fault modelling parameters on the simulated seismic rupture.

Furthermore, it is the aim

- to develop hypotheses that may explain the spatial differences between the observed and predicted activity rate using alternative models for the Groningen field (Ref. 7).

The current status of this research is further presented in reference 8.

References

1. NAM, Shell and Imperial College, Jan van Elk, Dirk Doornhof, Stephen Bourne, Steve Oates, Julian Bommer, Clemens Visser, Rob van Eijs and Peter van den Bogert, Technical Addendum to the Winningsplan Groningen 2013 - Subsidence, Induced Earthquakes and Seismic Hazard Analysis in the Groningen Field and Supplementary information to the "Technical Addendum of the Winningsplan Groningen 2013, Dec 2013
2. Sanz, P.F., Lele, S.P., Searles, K.H., Hsu, S.-Y., Garzon, L., Burdette, J.A., Kline, W.E., Dale, B. A., and Hector, P.D. (2015), Geomechanical Analysis to Evaluate Production-Induced Fault Reactivation at Groningen Gas Field. SPE-174942-MS, SPE Annual Technical Conference and Exhibition, Houston, Texas, USA, 28-30 September 2015.
3. ExxonMobil Upstream Research Company, Suvrat Lele, JorgeGarzon, Sheng-Yuan Hsu, Nora DeDontney, Kevin Searles and Pable Sanz-Reherman, Groningen 2015 Geomechanical Analysis, Mar 2016
4. Baker RDS, Romain Guises, Jean-Michel Embry and Colleen Barton, Dynamic Geomechanical Modelling to Assess and Minimize the Risk for Fault Slip during Reservoir Depletion of the Groningen Field - Part 1: 1D Geomechanical Model and Part 2: 3D Geomechanical Model, June 2015
5. Buijze, L., Orlic, B., Wassing, B.B.T. (2015), Modelling fault rupture in a depleting gas field. Report TNO project report 2015 R10844, November 2015.,
6. Van den Bogert, P.A.J. (2015), Impact of various modelling options on the onset of fault slip and fault slip response using 2 -dimensional Finite-Element Modelling. Report SR.15.11455, Shell Global Solutions International B.V.
7. Bourne, S. J., and Oates, S. J. (2017). Extreme threshold failures within a heterogeneous elastic thin sheet and the spatial-temporal development of induced seismicity within the Groningen gas field. J. Geophysical Research: Solid Earth, 122.
8. Buijze, L., van den Bogert, P. A. J., Wassing, B. B. T., & Orlic, B. (2019). Nucleation and arrest of dynamic rupture induced by reservoir depletion. Journal of Geophysical Research: Solid Earth, 124. https://doi.org/10.1029/ 2018JB016941

NAM

Title	**Depletion-induced fault slip and seismic rupture 2D Geomechanical models for the Groningen field, The Netherlands**		**Date**	December 2018
			Initiator	NAM
Autor(s)	**Peter A. J. van den Bogert**	**Editors**	Jan van Elk and Dirk Doornhof	
Organisation	Shell Global Solutions International B.V., Rijswijk	**Organisation**	NAM	
Place in the Study and Data Acquisition Plan	Study Theme: Geomechanical Modelling of Fault Ruptures Comment: Several geomechanical studies investigating the induced seismicity in the Groningen field have been initiated. This includes development of geomechanics-based seismological models (Ref. 1 to 4) and geomechanical studies to fundamentally better understand the destabilization of the faults as a result of reservoir depletion and the dynamics of the fault rupture process (Ref. 5 to 6). The current report describes the progress of the studies into the earthquake initiation and development since 2015 (Ref. 5 and 6), which has the objective to develop an understanding of: ▪ the potential conditions under which fault slip and seismic rupture occurs. ▪ the impact of reservoir depletion, reservoir offset and reservoir thickness on the occurrence of fault instability and the magnitude of the simulated seismic rupture. ▪ the mechanical response imposed by assuming a linear fault slip-weakening relationship. This includes the sensitivity of the various fault modelling parameters on the simulated seismic rupture. Furthermore, it is the aim ▪ to develop hypotheses that may explain the spatial differences between the observed and predicted activity rate using alternative models for the Groningen field (Ref. 7). The current status of this research is further presented in reference 8.			
Directliy linked research	(1) Seismological modelling (2) Experiments for friction during ruptures (3) Geophysical observations			
Used data				
Associated organisation	NAM			
Assurance	Internal			

Depletion-induced fault slip and seismic rupture

2D geomechanical models for the Groningen field, The Netherlands

Shell Global Solutions International B.V., Rijswijk

SR.18.01927

December 2018

Depletion-induced fault slip and seismic rupture

2D geomechanical models for the Groningen field, The Netherlands

P.A.J. van den Bogert (GSNL-PTD/E/Q)

Executive summary

This study is part of NAM's Study and Data Acquisition plan, which addresses the production induced-seismicity in the Groningen gas field (NAM, 2016b), and extends the work of Van den Bogert (2015) and Buijze (2015) with the objective to develop an understanding of

- the potential conditions under which fault slip and seismic rupture occurs, with the ambition to develop a fault-based seismological model for the Groningen field.
- the impact of reservoir depletion, reservoir offset and reservoir thickness on the occurrence of fault instability and the magnitude of the simulated seismic rupture.
- the mechanical response imposed by assuming a linear fault slip-weakening relationship. This includes the sensitivity of the various fault modelling parameters on the simulated seismic rupture.

Furthermore, it is the aim

- to develop hypotheses that may explain the spatial differences between the observed and predicted activity rate using alternative models for the Groningen field (Bourne and Oates, 2017).

In-house technology and expertise has been developed to simulate the nucleation and arresting of seismic events in the subsurface. The dynamic rupture modelling capability developed as part of this study enables simulation of seismic events along existing natural faults in 2D, including their wave forms and source-time function, with moment magnitude in the range that is observed in the Groningen field. More than 250 dynamic rupture simulations have been conducted to systematically explore the influence of reservoir offset, reservoir thickness and the parameters of the linear slip-weakening relationship on the occurrence of fault instability and seismic rupture.

For seismic events to occur, the shear stress along a fault plane should have reached the shear strength *and* the fault shear strength should reduce with increasing slip displacement (slip-weakening). Fault slip is a-seismic as long as incremental reservoir depletion is required to increase the slip displacement and propagate the slip patch. A seismic event occurs (with seismic slip) if no incremental reservoir depletion is required anymore. A seismic event nucleates if the size of an a-seismic slip patch exceeds a critical length L_c when using a linear fault slip-weakening relationship. The critical length adheres to the analytical expression derived by Uenishi and Rice (2003) and is dependent on the slope of the descending branch in the linear slip-weakening relationship. Another root cause of fault instability and seismic rupture is the merging of two (stable) a-seismic slip patches. The occurrence and location of two slip patches is influenced by the reservoir offset. So, both fault friction parameters and reservoir offset strongly influences the depletion level at which seismic events occur.

Three distinctly different rupture mechanisms have been found: one associated with instability of a single slip patch, one associated with merging of two slip patches, and the third associated with merging of the two slip patches after one of the slip patches has become instable. The source-time function is distinctly different for each rupture mechanism, and may provide an opportunity to associate observed seismic events with any of the three rupture mechanisms.

All three rupture mechanisms can generate seismic events with a moment magnitude M_w between 0.5 and 4 in the Groningen field, albeit that seismic rupture of a single slip patch tends to yield a smaller moment magnitude. Also, all three rupture mechanisms can occur on any reservoir thickness and offset by selecting appropriate fault strength

parameters. Recognition of the rupture mechanism of observed seismic events in the Groningen field would substantially constrain the fault friction parameters for locations with known reservoir thickness, reservoir offset and fault orientation. This may facilitate a better understanding of the actual stability condition of the Groningen faults and to characterise potential future seismicity.

The following recommendations are made based on the insight and quantified relationships developed in this study:

- Develop a fault-based seismological model using the fault location and moment magnitude of historical seismic events in the Groningen field. If possible, use the analytical solution provided by Nowacki (1986) to represent the findings of this study and to develop a probabilistic approach similar to Dempsey and Suckale (2017) to forecast seismic events in the Groningen field.
- Investigate if the three different rupture mechanisms can be identified from recorded wave forms of actual seismic events in the Groningen field. This would provide the opportunity to assess the mechanical condition of faults after seismic events and develop hypotheses of future seismicity.
- Investigate if the slope $W\mu$ in the linear slip-weakening relationship can be constrained from recorded seismic wave forms. This would provide an independent source for calibrating one of the fault friction parameters and also increases the reliability of the values estimated for the other friction parameter. This work can be done as part of the investigations mentioned under the previous point.
- Extend the dynamic rupture simulation capability to 3D to facilitate potential recognition of the rupture mechanisms from observed seismic events and to support research into the relationship between the character of seismic sources and recorded wave forms.

Contents

1. Introduction

1.1. Business context

The Groningen field in The Netherlands is the largest onshore gas field in Western Europe with an initial recoverable volume of about 2800 billion m^3 (NAM, 2018). About 75% of the original volume has been produced since 1963, while supplying international customers and virtually all households in The Netherlands. Gas production has reduced reservoir pressure from about 350 bar (35 MPa) at the Gas-Water contact initially to less than 100 bar (10 MPa) at some parts of the field today. Compaction and subsidence has always been a main concern for the NAM, the regulator and other stakeholders (e.g. Geertsma, 1973; Pruiksma, 2015; NAM, 2016a). The first earthquake was felt in 1986 (van Eck et al., 2004) in a period when the field was used as swing producer to accommodate fluctuating gas demand, and yearly production was about halve of the peak production of more than 80 billion m^3 (bcm) per year in the mid 1970-ies (NAM, 2016a). Between 2000 and 2010, the production increased again from about 21 bcm to around 50 bcm per year and caused a marked increase in seismicity in the field (Dost et al., 2012), leading to the Huizinge M_w=3.6 earthquake on 16 August 2012. Besides the increasing damage to houses, this earthquake caused unrest under the Groningen population and concerns if the estimated maximum magnitude of 3.9 (van Eck et al., 2004) would be exceeded.

The Huizinge earthquake led to the start of an extensive study program at the end of 2012 to better understand the relationship between gas production and the occurrence of seismic events in the Groningen field, their magnitude, frequency, duration, peak ground velocity and acceleration, and damage to buildings. This plan was updated and extended for the Groningen Winningsplan 2016 (NAM, 2016b) and included among others a densification of the monitoring network and a wide range of studies into the root cause of seismicity, the transmission of seismic waves to the ground surface and damage to buildings. Bourne and Oates (Bourne et al., 2014, 2015, 2017) developed a seismological model that describes the probability distribution of possible future earthquake locations and their magnitude based on reservoir compaction. The results culminated in a Probabilistic Seismic Hazard Assessment (PSHA) for alternative production scenario of the Groningen field (van Elk et al., 2017). The Geomechanical studies are part of the Study and Data Acquisition plan for the Groningen field since 2013, with the aim to gain a better understanding of the geomechanical conditions under which seismic events occur. This report documents the latest results and insights from these geomechanical studies.

1.2. Technical problem description

Earthquakes are characterised by the acceleration and subsequent deceleration of rock mass (e.g Dost et al., 2012). This is direct evidence of temporarily loss of equilibrium of forces (Newton's laws) and motivates the evaluation of the stress condition in the subsurface. The Groningen earthquakes are classified as "induced seismicity" (van Eck et al., 2004), which implies that seismicity is caused for a large part by stress changes in the subsurface induced by human activity. Other human activity related sources of seismicity are for instance water dams and injection of water in subsurface formations (Klose, 2012). This in contrast to so-called "triggered seismicity" in which human-activity-induced stress changes are relatively small, and critical stress conditions are developed predominantly by natural causes, such as tectonic plate

movements. The induced-seismicity in the Groningen field therefore calls for an evaluation of the depletion-induced stress changes in the subsurface.

Earlier work by Segall et al. (1989, 1994) and Grasso (1992) have shown that reservoir depletion by oil and gas production causes stress changes in the reservoir as well as in the overburden. Geological faults are generally regarded as planes of weakness in the subsurface that are vulnerable to re-activation if the shear stress condition reaches a critical level. An evaluation of more than 100 producing gas fields in The Netherlands (Van Eijs et al., 2006) has revealed that fault density (fault length per km^2) and reservoir depletion pressure are parameters that discriminate gas fields with and without seismic events. Van Eijs et al. (2006) have shown that a reduction of reservoir pressure of 100 bar (10 MPa) or more is required to induce earthquakes in Dutch gas fields. The required reservoir depletion implies that the subsurface is not under a critical stress condition initially, and that seismicity is induced by gas production. This is the reason why previous studies by Roest and Kuilmans (1994), Glab and Van Eijs (2001), Mulders (2003) and Cappa and Rutqvist (2012) have focused on the development of critical shear stress conditions along fault planes in the reservoir and overburden and the use of stress-based failure criteria to forecast fault slip. Also, in the Groningen field seismic events are located with increasing confidence on known faults, due to improved monitoring and interpretation techniques (Willacy et al., 2018). In this study, therefore, attention is given to the loss of equilibrium by evaluating the impact of reservoir depletion on the stress distribution along fault planes that have been formed during the geological history of the field (Visser, 2012).

Forecasting future seismicity using deterministic geomechanical models is not possible, because of the uncertainty of known and unknown physical processes as well as their variability across the Groningen field. This is also the reason why stochastic approaches as followed by Bourne and Oates (Bourne et al., 2014, 2015, 2017) are more appropriate and useful to forecast seismicity. Nevertheless, understanding of the underlying physics that lead to seismicity is needed to improve the stochastic assessments. However, the complexity of the problem and the lack of field data makes it hard to formulate and test alternative modelling hypotheses. The complexity of induced seismicity covers the four categories that all geomechanical models have in common:

1. Geometry:
   In principle, the stress changes in the subsurface induced by reservoir depletion are influenced by geometrical aspects on different scales. Reservoir shape and reservoir dimensions disturb the subsurface stress condition on the 1 – 10 km scale, while reservoir offset and fault intersections are influential on a scale proportional to the reservoir thickness (10 – 100 m). Formation property contrasts also act on this scale, while small scale inhomogeneities, also referred to as asperities, can have a sphere of influence in the order of 1 m. The scale of interest in this study is 10 – 100 m, because earthquakes with a moment magnitude M_w between 0.5 and 2.5 have a rupture area in this order of magnitude (as demonstrated in this study; e.g. Madariaga and Olsen, 2012). Therefore, geometrical features that are larger than about 10 m, such as reservoir thickness and reservoir offset which have a demonstrated influence on the stress distribution along fault plane, are considered. The element size in numerical models need to be substantially smaller than 10 m in order to capture stress concentrations caused by these geometrical features (Buijze et al., 2015). However, evaluation of geometrical features in the

range between 10 m and 10 km in a single 3D finite-element model is technically challenging and very costly, and does not allow evaluation of a large number of options in a reasonable timeframe. A two-dimensional modelling approach is an acceptable compromise and has been followed by various studies in the past (Roest and Kuilmans, 1994; Cappa and Rutqvist, 2012; Orlic and Wassing, 2012). The influence of reservoir depletion on field scale is limited to uniaxial deformation and stress conditions, while priority is given to geometrical features that are relevant to simulate fault slip and seismicity, such as reservoir thickness and offset (van den Bogert, 2015). It also facilitates conducting sensitivity studies into these parameters. This is relevant because the accuracy of these geometrical parameters, which are derived from seismic interpretation, is also in the order 10 – 100 m.

2. Constitutive behaviour:
   The largest uncertainty is probably caused by non-linear and time-dependent behaviour of the subsurface due to reservoir depletion (Templeton and Rice, 2008; Sanz et al., 2015; Pijnenburg et al., 2018). The presence of salt in the Groningen overburden may cause time-dependency of induced stress changes on a production time scale. Fault slip behaviour is largely unknown, although recent results (Spiers at al., 2017) provide the first Groningen specific results. An important aspect is the loss of frictional strength after the onset of fault slip, which is an essential requirement to explain the occurrence of earthquakes (e.g. Scholz, 1998). Thermal aspects and (un)drained behaviour of the fault zone and adjacent formations may play a role during fast seismic deformations (Zbinden et. al., 2017).
3. Initial stress and reservoir depletion:
   The initial stress condition in the Groningen field is rather poorly constrained (Van Eijs, 2015). Vertical stress is relatively well known from integrated density log data, but is influenced by the variable thickness of the Zechstein salt formation in the overburden. Reliable minimum horizontal stress data and its orientation is very limited considering the size of the field, and available data suggests differences across the field. Similarly, field data on the orientation of the maximum horizontal stress is limited. On the other hand, experimental and field data consistently suggest a maximum to horizontal total stress ratio between 1.05 and 1.10.
4. Equilibrium condition:
   As mentioned before, seismic events are characterised by mass acceleration and subsequent deceleration. This implies that the dynamic equations of motion need to be considered to gain insight into the nucleation and arrest of seismic ruptures (Hughes, 1987; Madariaga and Olsen, 2002; Verruijt, 2010):
   $$\boldsymbol{M}\ddot{u} + \boldsymbol{C}\dot{u} + \mathbf{k}u = \boldsymbol{f}, \quad (1.1)$$
   with u the displacement vector, and $\dot{u}$ and $\ddot{u}$ the velocity and acceleration vector respectively. In most geomechanical evaluations in petroleum engineering, velocity and acceleration are ignored, reducing (1.1) to the equation of static equilibrium, with $\mathbf{k}$ the stiffness matrix and an external force vector $\boldsymbol{f}$. Newton's second law is retrieved by considering point mass ($\boldsymbol{M}$ is the mass matrix) and ignoring internal deformations ($u = \dot{u} = 0$). The damping matrix $\boldsymbol{C}$ accounts for internal friction. Evaluation of the dynamic equation of motion in (1.1) requires additional degrees-of-freedom in every node of a finite-element model and significantly increased computational effort. This is enhanced by the fact that the initial boundary value problem needs to be solved, rather than the harmonious solution.

In principle, the technology is available to evaluate three-dimensional, non-linear, time-dependent and dynamic problems. Appropriate tools are available to develop realistic 3D models of the Groningen field including the fault structure (APPENDIX 1; Sanz et al., 2015). A wide range of plasticity and creep models are available to describe non-linear and time-dependent formation behaviour (e.g. Aki and Richards, 2002). Also, slip- and velocity-weakening relationships are available to simulate fault behaviour (e.g. Scholz, 2002; Madariaga and Olsen, 2002). Furthermore, the availability of sophisticated solution algorithms to solve large non-linear sets of equations is equally important (de Borst, 1987). However, concessions are essential to arrive at a model that can be evaluated within a reasonable timeframe and with acceptable costs.

1.3. Approach

The challenge is to understand and model the main physical processes induced by gas production that cause earthquakes, while acknowledging the variability and uncertainty of the subsurface properties at different scales. The complexity of the problem of induced seismicity calls for a modelling approach that starts simple and adds complexity in a step-wise fashion, building on previous work. Simple assumptions can often be verified analytically, while gradually adding complexity helps to develop an understanding of the impact, behaviour and relevance of individual aspects. A selection of the modelling complexities for this study was made based on previous work.

Roest and Kuilmans (1994) conducted 2D evaluations of slip along multiple faults as a result of depletion in the Eleveld gas reservoir. Fault slip was described by an elastic-perfect-plastic Mohr-Coulomb friction law. Glab and Van Eijs (2001) and Mulders (2003) also considered a number of 3D configurations. Hager and Toksöz (2008) concluded that no maximum magnitude could be estimated using static modelling approaches in their review of the underground storage facility in Bergermeer. The influence of reservoir offset was found in a number of these studies (Mulder, 2003; Orlic and Wassing, 2012), but Van den Bogert (2015) quantified the influence of reservoir offset normalised for reservoir thickness on the pressure depletion required to cause onset of fault slip. However, none of these studies actually demonstrated nucleation of seismic rupture by a loss of equilibrium. Cappa and Rutqvist (2011, 2012) conducted static and dynamic rupture simulations of fault stability under CO2 injection conditions, by assuming a linear fault slip-weakening relationship and a linear-elastic subsurface. Their modelling approach allowed the determination of the injection pressure that causes onset of seismic rupture.

It was decided to include two modelling aspects that are required to simulate nucleation and arresting of seismic rupture which are missing in the study by Van den Bogert (2015), namely

- the evaluation of the dynamic equations of motion (1.1). This means that the static analysis used by Van den Bogert (2015) are replaced by dynamic rupture simulation as used by Madariaga and Olsen (2002), Cappa and Rutqvist (2012) and Buijze et al. (2015) in a so-called dynamic rupture simulation, and
- slip-weakening behaviour to account for the loss of fault strength after onset of slip.

The FAULT module of the DIANA general purpose finite-element software was extended with dynamic rupture capabilities. This module has been developed in the previous study (van den Bogert, 2015). Buijze et al. (2015) investigated requirements for element and time step size with this updated module to obtain reliable and accurate results. They also benchmarked the 2D DIANA results against case TPV 210-2D of the Southern California Earthquake Catalogue (SCEC, Harris, 2009) with a positive result. That is, the dynamic rupture simulation capability of DIANA delivers the same results as other codes used for the simulation of "triggered seismicity" in natural earthquakes. Furthermore, Buijze et al. (2015) started exploring the seismic rupture response along a fault plane that offsets a depleting reservoir using a linear fault slip-weakening relationship. The current study is a continuation of that work.

The main objective of the present study is to develop an understanding of

- the conditions under which fault slip and seismic rupture occurs in a normal faulting environment, with the ambition to develop a fault-based seismological model for the Groningen field.
- the impact of reservoir depletion, reservoir thickness and reservoir offset (in a normal faulting environment) on the occurrence of fault instability and on the magnitude of the simulated seismic rupture.
- the mechanical response of the fault zone imposed by assuming a linear fault slip-weakening behaviour. This includes the sensitivity of the various parameters of the linear slip-weakening relationship on the simulated seismic rupture.

Other objectives are:

- to provide hypotheses that may explain the spatial and temporal differences between the observed and predicted activity rate using alternative models for the Groningen field developed by Bourne and Oates (2017).
- to develop a procedure to conduct dynamic rupture simulations that determine the onset of seismic rupture. This includes the development of post-processing tools to follow and check the simulated rupture process and derive moment magnitude, source-time function, wave forms and other response parameters

A large number of known aspects are not addressed in this study. The influence of the fault orientation and the elastic properties (Young's modulus and Poisson's ratio) has been addressed in a previous study (van den Bogert, 2015) and can be easily incorporated in the results of the current study. A 3D modelling approach was deemed inappropriate, because either the element size would be too large or computational effort and costs would explode. Furthermore, convergence of the numerical solution would be more difficult to achieve or even become impossible. Also, non-linear and time-dependent behaviour of the reservoir and overburden formations (Sanz et al., 2015; Pijnenburg et al., 2018) have not been taken into account. The latter may be relevant because of the significant salt body above the Groningen gas reservoir. Furthermore, thermal aspects and (un)drained behaviour of the fault zone and adjacent formations (Zbinden et. al., 2017) may play a role during seismic events in the Groningen field. A 2D modelling environment is preferred for its computational efficiency, thereby enabling the evaluation of a larger number of cases and the influence of all slip weakening parameters compared to a 3D modelling approach. Aforementioned non-linear aspects and in-homogeneities may be incorporated in subsequent work. This study focusses on the influence of the parameters of the linear slip-weakening relationship and reservoir offset.

1.4. Structure of the report

The report describes the main results of the study, while detailed geomechanical evaluations and evidence of some of the statements is provided in the appendices. Chapter 2 describes the modelling assumptions and default parameters used throughout this report, following the approach outlined in the previous section. The reservoir and fault configuration is representative for the Groningen field (APPENDIX 1), but not tuned to a particular location. The default parameters for the linear slip-weakening relationship for the fault behaviour are specified, as well as the uniform linear-elastic properties for the overburden, reservoir and basement formations. Furthermore, the in-situ stress condition and the procedure for simulating reservoir depletion and seismic rupture is described. Also, specific finite-element modelling aspects are explained in this chapter.

Chapter 3 presents the simulation results for a fault dipping under 66 degrees, which offsets a 200 m thick reservoir by 80 m. The results are shown for a number of cases with decreasing value for the residual friction coefficient (APPENDIX 2 provides a list of all cases evaluated as part of this study). The cases reveal three different rupture mechanisms with characteristic features that might be observable from actual seismic events in the Groningen field. One case – the Base Case – is discussed in detail in APPENDIX 3. The reservoir depletion pressure that causes onset of seismic rupture in the Base Case is evaluated in detail by considering the equilibrium condition of the entire fault in APPENDIX 4, and by a so-called post-bifurcation analysis in APPENDIX 5. Detailed results of the other cases in Chapter 3 and their associated rupture mechanism are presented in APPENDIX 6.

The influence of a number of modelling parameters on the simulated seismic rupture and rupture mechanism is presented in Chapter 4. Section 4.1 shows that the same three rupture mechanisms introduced in Chapter 3 are obtained by varying the reservoir offset. The associated detailed geomechanical evaluations are found in APPENDIX 7. Section 4.2 shows how the residual friction coefficient influences the rupture mechanism and moment magnitude as a function of reservoir offset. The influence of reservoir thickness on the reservoir depletion that causes onset of seismic rupture and on the moment magnitude is addressed in section 4.3, while the in-depth geomechanical evaluation of the cases is provided in APPENDIX 8. The influence of the slope of the descending branch of the linear slip-weakening relationship on the onset of seismic rupture and the moment magnitude is discussed in section 4.4 and the associated detailed evaluation in APPENDIX 9. Finally, in section 4.5, scaling relationships are presented between the moment magnitude on one hand and the size of the slip patch and the maximum relative slip displacement on the other hand. The scaling relationships are derived from all dynamic rupture simulations in this study and provide a quick estimate for these parameters for any (observed) moment magnitude between 0.5 and 4.0. Some additional relationships are provided in APPENDIX 11. An interpretation of the results is given in Chapter 5, while the conclusions are given in Chapter 6, and recommendation in Chapter 7.

2. Model description

This chapter describes the modelling assumptions and default parameters used throughout this study. All parameters are representative for the Groningen field, but not tuned to a particular location. In subsequent chapters, the impact of one or two modelling parameters on the simulated seismic rupture is evaluated at a time, while using the default values for all other modelling parameters as presented in this chapter. The geometrical modelling assumptions are described in section 2.1, the formation and fault properties in section 2.2, and the initial stress, pore pressure and reservoir depletion conditions are discussed in section 2.3. Finally, the followed analysis procedure is described in section 2.4

2.1. Geometrical model

This study uses two-dimensional finite-element (FE) models with a size of 6000 m by 6000 m, and four horizontal layers (Figure 2.1a). The top of the 200 m thick depleting foot wall reservoir formation is at 2910 m depth (red layer), with an overlying 85 m thick top-seal. The reservoir thickness is representative for the Groningen field, which varies from less than 100 m in the South-East to 220 m in the North-West. The thickness of the top-seal is not relevant in the current study, because elastic properties and initial stress in the top-seal and overburden layers are assumed the same in all cases evaluated in this study.

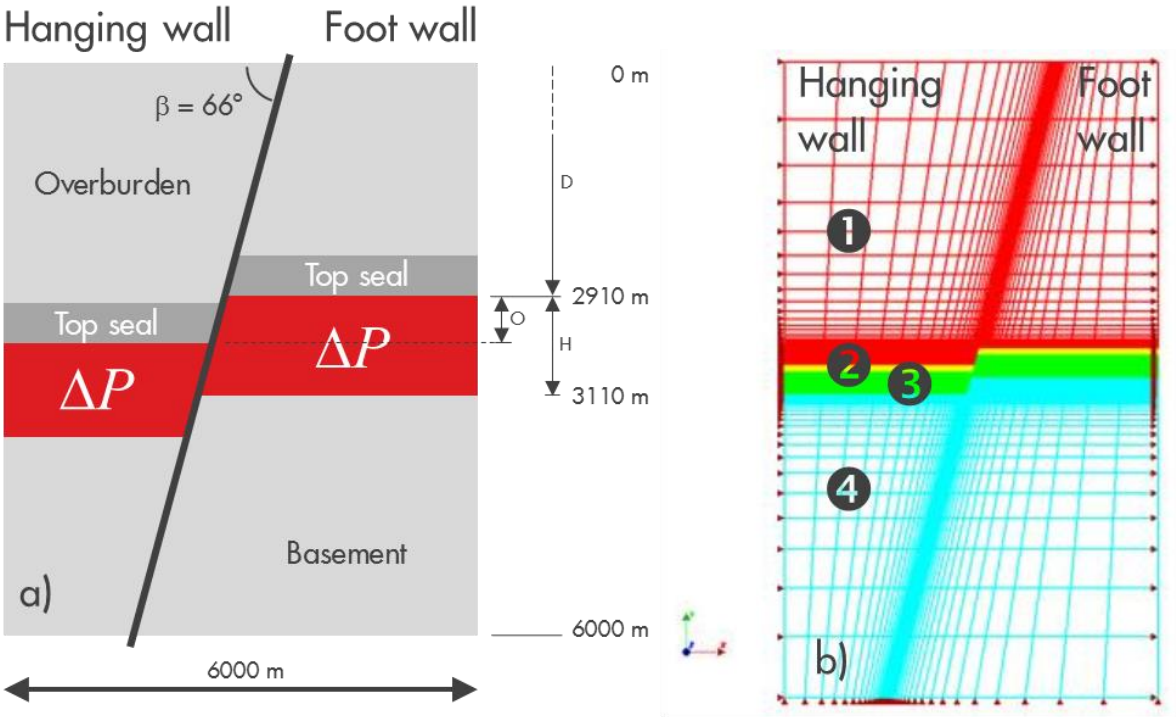

Figure 2.1: *a) The top of the 6000 m wide model (not to scale) is the stress free earth surface and the bottom of the model is at 6000 m depth. The foot wall reservoir is at a depth D of 2910 m with a thickness H of 200 m. In this study, the hanging wall reservoir is taken the same thickness as the foot wall reservoir, while the offset O is variable. The fault dip angle β is 66°. Reservoir depletion is simulated in the third layer only (red color). b) Typical finite-element mesh with the four different layers indicated by different colors. Reservoir offset along the normal fault is modelled by increasing the overburden thickness of the hanging wall, while reducing the basement thickness proportionally.*

The fault is assumed to be a straight plane dipping under 66 degrees with the horizontal surface in all analysis of this study. This is at the low-end of the spectrum of interpreted dip angles in the Groningen field, which is predominantly between 75 and 85 degrees (APPENDIX 1). The small fault dip angle constitutes a conservative assumption, because steeper faults require a larger reservoir depletion pressure to cause onset of fault slip for the same fault slip properties (van den Bogert, 2015).

Reservoir offset O in the Groningen field is predominantly between 0 and about 50% of the reservoir thickness H, although offsets larger than reservoir thickness also occur, notably in the South-East of the field. In this study, reservoir thickness is varied between 140 and 300 m, and the normalised reservoir offset $\bar{O}$, which is defined by the absolute offset O divided by the reservoir thickness H, is varied between 0 and 2. The reservoir thickness is varied, while keeping the top of the foot wall reservoir at the same height. The normalised reservoir offset is varied by adjusting the depth of the hanging wall reservoir.

The two-dimensional DIANA plane-strain FE models include two types of elements (Diana FEA, 2016): i) one-dimensional linear interface elements simulate the behaviour of the fault, and ii) linear continuum elements to simulate the behaviour of the formations. The length of the interface elements is set to 0.3 m over the reservoir interval to accurately calculate the development of critical stress conditions for a normalised reservoir offset between 0 and 2 (Buijze et al., 2015). The size of the *linear continuum elements* next to the interface elements are also 0.3 m, but increase towards the boundaries. Figure 2.1b shows a typical FE mesh, in which the formations are represented by the different colors. The fault zone is the region with small elements in the middle of the model. Note that the vertical size of the interface and continuum elements increase above the foot wall and below the hanging wall reservoir formation. Dedicated element meshes are generated for cases with different foot wall reservoir depth D, reservoir height H, offset O and dip angle β, as well as the total model width and height. In this study, only reservoir thickness H and offset O are varied.

The top surface of the model represents the earth surface and has a zero stress boundary condition, while the normal displacements of the nodes along the two vertical sides and at the bottom of the model are prohibited. This means that a uniaxial deformation and stress condition is prescribed in the model. The zero normal displacements at three of the four model boundaries also implies that velocity waves are reflected in the dynamic rupture simulation, and that energy is contained within the model. The origin of the coordinate system is located in the middle of the top surface of the model, with the positive X-axis in horizontal direction to the right, and the positive Y-axis in vertical direction upwards. Hence, subsurface depth is negative. Furthermore, positive stress and strain correspond with elongation. Thus, compressive stress is negative in this report, unless stated otherwise.

2.2. Formation and fault properties

One of the study objectives is to gain insight into the impact of reservoir depletion on the fault slip behaviour and seismic rupture. Uniform and linear-elastic behaviour is assumed for all formations so that results are not impacted by any property contrasts across the fault in cases with reservoir offset (van den Bogert, 2015). Therefore, Young's modulus E is 10 GPa and Poisson's ratio ν is 0.25 (shear modulus G=6.67 GPa) for all formations, and the Biot-Willis coefficient α is assumed to be 1. The presence of salt in

the Groningen subsurface is ignored in the current study. This means that the subsurface is represented by a homogenous linear-elastic half-space. This simplifies the interpretation of the dynamic rupture analyses and facilitates evaluating the impact of reservoir offset separately.

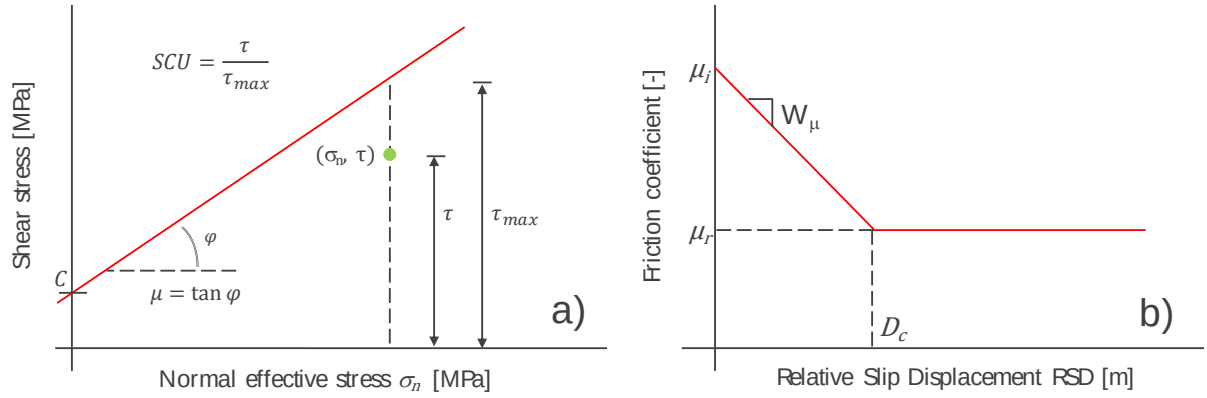

Figure 2.2: a) Mohr-Coulomb shear failure criterion, specified by Cohesion stress C and friction angle φ, is used to determine onset of irrecoverable slip (plasticity), b) linear slip-weakening relationship expresses the reducing friction coefficient μ as a function of the plastic relative slip displacement.

The fault slip behaviour is described by a Mohr-Coulomb friction law (Figure 2.2a) with linear slip-weakening relationship in the interface elements of the model (Figure 2.2b; Madariaga and Olsen, 2002). A material point on the fault plane will start slipping if the local shear stress τ is equal to the local shear strength τ_{max} which is defined by a Mohr-Coulomb frictional slip criterion:

$$\tau_{max} = C + \sigma_n \tan\varphi. \tag{2.1}$$

Herein, C is the cohesion stress, φ is the angle of internal friction, and σ_n is the normal effective stress in the material point on the fault plane (Figure 2.2a). Furthermore, the Shear Capacity Utilisation SCU is defined as a dimensionless metric that indicates the onset of fault slip:

$$SCU = \frac{\tau}{\tau_{max}}. \tag{2.2}$$

Relative displacement across the fault interface are recoverable (elastic) if SCU < 1. Irrecoverable slip displacement along the fault interface is accumulated if SCU=1, whereas a value larger than 1 is not possible. Furthermore, it is assumed that the friction coefficient μ of each point along the fault plane reduces from an initial value μ_i at the onset of fault slip to a residual value μ_r when the relative slip displacement in that point reaches the critical slip displacement D_c (Figure 2.2b). The slope W_μ expresses the reduction of the friction coefficient per millimetre of relative slip displacement across the fault. A (linear) slip-weakening relationship may be combined or replaced with a slip rate friction law as outlined by Madariaga and Olsen (2002).

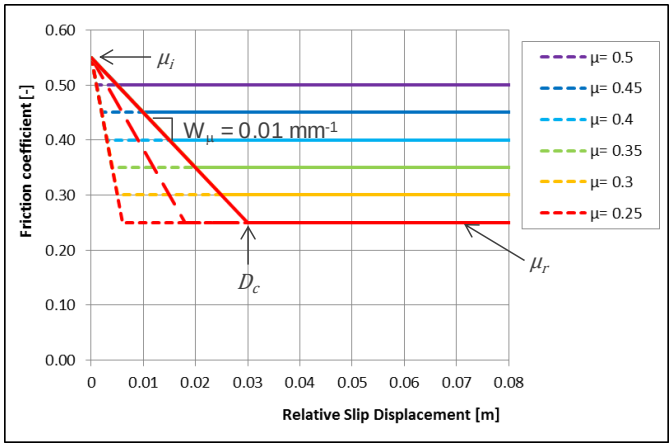

Figure 2.3: *Linear slip-weakening diagram for an initial friction coefficient is 0.55 and a residual friction coefficient between 0.50 and 0.25, and a default slope W_μ = 0.010 mm^{-1} (solid lines). Alternative slopes with W_μ=0.020 mm^{-1} (long-dashed lines) and W_μ=0.050 mm^{-1} (short- dashed lines) are evaluated in Chapter APPENDIX 8.*

Again, the objectives of this study is to develop a *qualitative* understanding of the impact of the fault slip parameters on the simulated a-seismic and seismic slip behaviour along normal faults. The challenge of quantifying fault friction is well described by Spiers et. al. (2017) who are executing an extensive NAM funded experimental program into the behaviour of rock and faults in the Groningen gas field. The cohesion stress C is assumed to be negligible (C = 0 MPa) in accordance with previous experimental and modelling studies (Byerlee, 1978; Streit and Hillis, 2004; Zoback, 2007). The initial friction coefficient μ_i=tan φ_i is assumed to be 0.55 (φ=28.8°), which is in the range measured by Hunfeld et al. (2017) in direct shear experiments conducted on gouges of different mixtures of the members in the stratigraphic column in the Groningen field. The residual friction coefficient has been varied between 0.50 and 0.25 (Di Torro et al., 2011, Rutqvist et al., 2013). However, no appropriate literature data is available to constrain the slope W_μ of the descending branch of the linear slip-weakening relationship. Madariaga and Olsen (2002) quote values for D_c in the order of 10 cm for natural earthquakes with a moment magnitude as large as M_w = 8. The smaller earthquakes in the Groningen field are expected to have a smaller reduction of the friction coefficient (μ_i - μ_r) and smaller value for D_c to arrive at the same slope W_μ. In this study, the default value W_μ = 0.01 mm^{-1} is taken similar as in the study by Buijze et al. (2015), which leads to D_c = 0.03 m if μ_i = 0.55 and μ_r = 0.25 (Figure 2.3). The slope W_μ is varied in section 4.4. All three fault friction parameters, the initial and residual friction coefficient μ_i - μ_r and , are subject to Finally, the fault slip model incorporates a so-called dilatancy angle ψ, which expresses the ratio of the normal over the slip displacement after the onset of slip (Diana FEA, 2016). The dilatancy angle is set to 0° for all simulations in this study.

2.3. Initial stress and depletion conditions

The initial total vertical stress is determined by the density of the subsurface formations (Table 2.1). The ratio of the total minimum horizontal stress to the total vertical stress k_{0min} is set to 0.748 and the ratio of the total maximum horizontal stress to the total vertical stress k_{0max} is 0.798. The maximum horizontal stress azimuth is assumed 160 degrees East of North (Van den Bogert, 2015). These values are summarised in Table 2.1. The update of the initial stress condition of Groningen field by Van Eijs (2015) is not incorporated, because it became available after the start of this study and the

difference with the data used here is rather small. Incorporating the updated initial stress model would require re-evaluating numerous cases to ensure that all cases have the same initial stress condition. Also, this study is not intended to calibrate any model parameter to observed seismic events in the Groningen field.

The initial pore pressure in the overburden and top seal is taken hydrostatically with a pressure gradient of 10 kPa/m (1.0 bar/10m). The pressure gradient in the basement is somewhat larger at 11.66 kPa/m due to the saline aquifer. In the reservoir formation, a gas density of 1.8 g/cm^3 (1.8 kPa/m, 0.18 bar/10m) is taken. Furthermore, the initial pressure at the Gas-Water Contact at 2995 m TVD is 35.2 MPa (352 bar). This pressure point is used to construct the pressure-depth relationship for the reservoir and basement formations. The initial stress condition in the reservoir at 2875 m TVD is summarised in Table 2.2.

Table 2.1: Data used to determine the initial stress condition.

	Density	**k_{0max}**	**k_{0min}**
Formation	[kg/m^3]	[-]	[-]
Overburden	2172	0.795	0.748
Top seal	2450	0.795	0.748
Reservoir	2450	0.795	0.748
Basement	2700	0.795	0.748

Table 2.2: Initial pore pressure and stress condition in the reservoir at 2875 m TVD

Parameter	**Gradient [bar/10m]**	**Pressure [bar]**
Pore pressure gradient (gas density)	0.18	350
Vertical stress gradient	2.14	615
Min. Horizontal stress gradient	1.60	460
Max. Horizontal stress gradient	1.71	491
Max./Min. horizontal stress ratio [-]	1.07	
Max. horizontal stress azimuth [deg]	160	

The initial stress condition is applied to the models in an initialisation step (Diana FEA, 2016), in which model equilibrium is established in an iterative manner if necessary, while adhering to the boundary conditions. The stress condition after the initialisation step is used as reference configuration in the remainder of the analysis. The displacements introduced by the stress initialisation are ignored.

Uniform reservoir depletion is simulated by lowering the pore pressure in layer 3 (red color in Figure 2.1) on both sides of the fault by an equal amount. No pressure depletion is simulated in the other formation layers. The pore pressure in the fault is assumed to follow the pore pressure in the adjacent formations. That is, pore pressure in an interface element is reduced in conjunction with the reservoir pressure if it is in

contact with the foot wall or hanging wall reservoir formation. The pore pressure is not changed if it is not exposed to reservoir depletion on either side of the fault.

2.4. Analysis procedure

The finite-element simulations in this study evaluate the dynamic equations of motion, which read (Hughes, 1987; Verruijt, 2010; Diana, 2016):

$$\boldsymbol{M}\ddot{u} + \boldsymbol{C}\dot{u} + \mathbf{k}u = \boldsymbol{f}, \tag{2.3}$$

with u the displacement vector, and $\dot{u}$ and $\ddot{u}$ the velocity and acceleration vector respectively. Furthermore, $\boldsymbol{M}$ is the mass matrix, $\boldsymbol{C}$ is the damping matrix, $\mathbf{k}$ is the stiffness matrix, and $\boldsymbol{f}$ is the external force vector. The equation of static equilibrium is obtained if the velocity and acceleration vectors are very small and can be ignored:

$$\mathbf{k}u = \boldsymbol{f}. \tag{2.4}$$

The subsurface stress and strain distribution due to reservoir depletion is virtually always evaluated in a static analysis considering equation (2.4), despite the time-dependent character of the reservoir depletion process (hence, the term 'quasi-static analysis' is sometimes used). This is acceptable, because the inertia force $\boldsymbol{M}\ddot{u}$ and internal friction force $\boldsymbol{C}\dot{u}$ remain very small compared to the internal forces $\mathbf{k}u$, even if time-dependent processes, such as salt creep, are included. This approach is also followed in the first stage of the analysis, in which reservoir depletion is simulated until onset of seismic rupture occurs (Figure 2.4a). In the second stage, seismic rupture is simulated considering the dynamic equations of motion (2.3). This approach is identical to the study by Buijze et al. (2015).

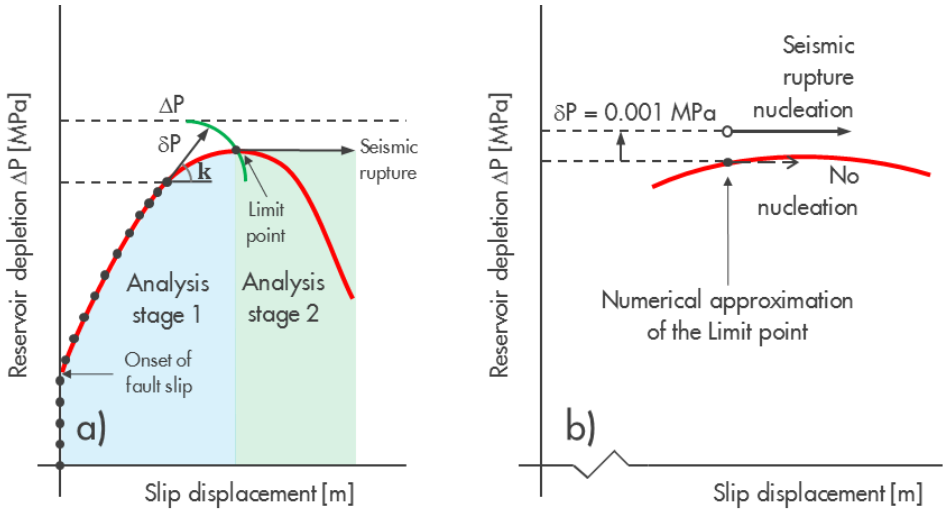

Figure 2.4: *a) Convergence of the numerical solution is not achieved if the incremental reservoir depletion δP exceeds the maximum in the limit point. The arc-length method (Riks, 1979; de Borst, 1987; Diana FEA, 2016) is indicated by the green line and seeks an equilibrium solution by adjusting δP. The (tangential) stiffness matrix $\boldsymbol{k}$ in equation (2.4) is represented by the slope of the red curve. Seismic rupture occurs if no incremental reservoir depletion δP is required to increase the slip displacement. The static analysis in stage 1 is indicated by the blue background color, whereas the seismic rupture analysis in stage 2 is indicated in green. Irreversible (plastic) slip displacement occurs after onset of fault. b) The arc-length method provides an equilibrium solution that approximates the limit point within 0.001 MPa. This implies that a maximum incremental reservoir depletion of 0.001 MPa is sufficient to nucleate a seismic rupture in stage 2 of the simulation.*

In the first stage, the initial stress condition is applied as described in the previous section and reservoir depletion ΔP is increased in steps δP of 1 MPa until onset of *fault slip* is reached. Onset of fault slip is defined by SCU = 1 in any interface element of 0.3 m along the fault plane as described in section 2.2. The same size of interface elements has been used throughout this study so that peak stresses along the fault plane are described with the same accuracy, and onset of fault slip is consistent for all cases evaluated in this study. The incremental depletion steps δP are gradually reduced from 1 MPa in the linear-elastic regime to 0.001 MPa close to the onset of seismic rupture. The reduction of step size is applied manually for every case in this study to accurately capture the depletion pressure ΔP at which onset of seismic rupture occurs (the limit point in Figure 2.4).

Seismic rupture constitutes a so-called limit point in the static analysis, because no incremental reservoir depletion is required to increase the slip displacement along the fault plane (Figure 2.4a). Determination of the limit point is a general problem in numerical simulations when considering strain-softening material behaviour, such as the linear fault slip-weakening relationship in Figure 2.3. Divergence of the numerical solution occurs if the reservoir depletion ΔP exceeds the value in the limit point after increment δP (Figure 2.4a). Fundamentally, divergence is caused by the occurrence of one or more zero values on the main diagonal of the tangential stiffness matrix $\mathbf{k}$ in equation (2.4) (Hill, 1959). This means that no unique solution exists for the system of equations. The so-called arc-length method (Riks, 1979; de Borst, 1987; Rots and de Borst, 1989; Diana FEA, 2016) seeks an equilibrium solution by adjusting (lowering) the incremental depletion pressure δP as indicated by the green line in Figure 2.4a. In this study, the arc-length method is applied to determine the reservoir depletion that causes onset of seismic rupture with an accuracy of 0.001 MPa or smaller.

The dynamic rupture analysis of stage 2 covers a period of 2 seconds (2000 steps of 0.001 s), while reservoir depletion is kept the same. The analyses are conducted using an implicit solution scheme in the DIANA finite-element software (Diana FEA, 2016). A small unbalance is introduced to bring the model out of equilibrium at the start of the dynamic rupture simulation (Figure 2.4b). This is required because analysis stage 1 ends at a converged equilibrium solution within 0.001 MPa reservoir depletion of the limit point. Imposing an incremental reservoir depletion δP = 0.001 MPa at the start of the dynamic rupture simulations therefore ensures that the depletion level exceeds the value at the limit point and that seismic rupture nucleates. This analysis procedure is developed in collaboration with TNO (Buijze et al., 2015, 2017).

3. Influence of the residual friction coefficient

In this chapter, the results of six cases are presented which are fully identical except for the residual friction coefficient in the linear slip-weakening relationship. The subsurface is modelled as a homogenous elastic medium with a straight, dipping fault that intersects a reservoir with offset, and that exhibits linear slip-weakening behaviour as described in Chapter 2. The main common parameters of the six cases are (Figure 3.1a):

- Top foot wall reservoir at D = 2910 m TVD.
- Reservoir thickness H = 200 m.
- Offset hanging wall reservoir O = 80 m.
- Fault dip angle β = 66 degree.
- Fault cohesion C = 0 MPa.
- Initial friction coefficient μ_i = 0.55.
- Slip-weakening slope W_μ = 0.01 mm^{-1}.

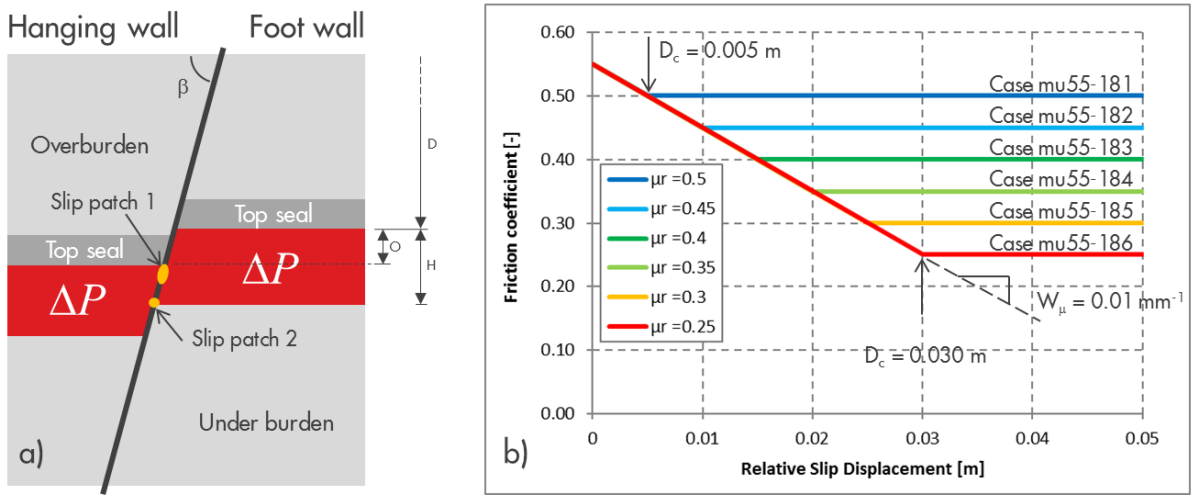

Figure 3.1: *a) The top of the foot wall reservoir is at 2910 m TVD, the reservoir thickness H is 200 m, the offset O is 80 m and fault dip angle β is 66 degrees for all cases in this chapter. b) The linear slip-weakening relationship for the cases in Table 3.1.*

Table 3.1: *The parameters of the linear slip-weakening relationship for the cases discussed in this chapter. Case mu55-182 (bold print) is considered the Base Case in this study.*

Case	Initial friction coefficient μ_i	Residual friction coefficient μ_r	Critical slip displacement D_c	Discussed in
Mu55-181	0.55	0.50	0.005 m	Section 3.1
Mu55-182	**0.55**	**0.45**	**0.010 m**	**Section 3.2**
Mu55-183	0.55	0.40	0.015 m	Section 3.3
Mu55-184	0.55	0.35	0.020 m	Section 3.4
Mu55-185	0.55	0.30	0.025 m	Section 3.4
Mu55-186	0.55	0.25	0.030 m	Section 3.4

The linear slip-weakening diagram for the six cases is given in Figure 3.1b and the corresponding parameter values are given in Table 3.1. The values for the initial friction coefficient μ_i and the slope W_μ of the slip-weakening relationship are based on preliminary experimental results (Hunfeld et al., 2017). Note that the critical slip displacement D_c is adjusted to keep slope W_μ the same in all cases, while reducing the residual friction coefficient from 0.50 in case mu55-181 to 0.25 in case mu55-186. The slope W_μ has the dimension mm^{-1} and expresses the reduction of the friction coefficient per millimeter of slip displacement. The influence of the slope W_μ on the fault slip behaviour is evaluated in Chapter 4. Depletion is simulated by a step-wise and equal decrease of the pore pressure in the foot wall and hanging wall reservoir formations (red areas in Figure 3.1a) up to 30 MPa. This is close to the expected average reservoir depletion at the end of the Groningen field life. Incremental reservoir depletion is reduced from 1 MPa at the start of the analysis to 0.001 MPa at the onset of seismic rupture as described in section 2.4.

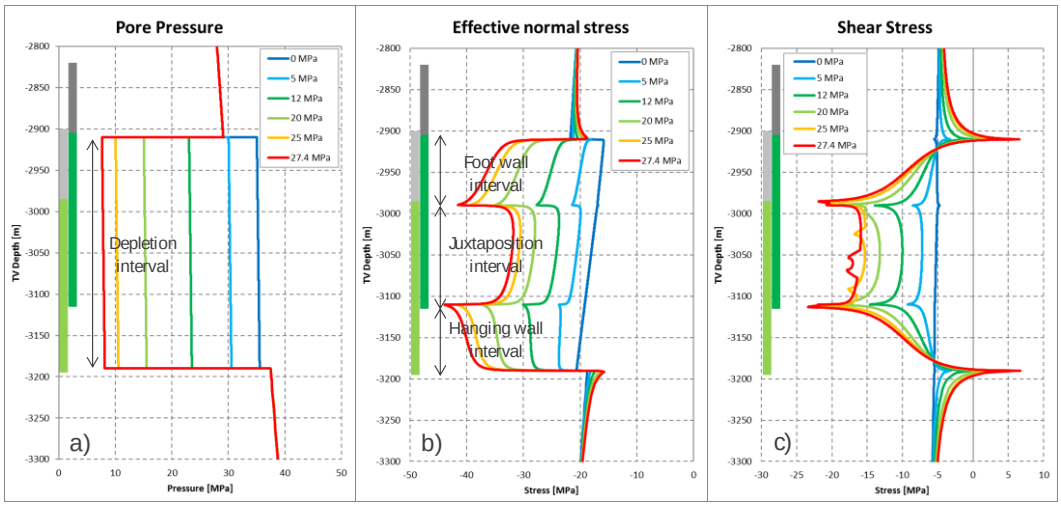

Figure 3.2: *a) The pore pressure, b) the effective normal stress, and c) the shear stress distribution along the fault plane as a function of depth for different levels of reservoir depletion.*

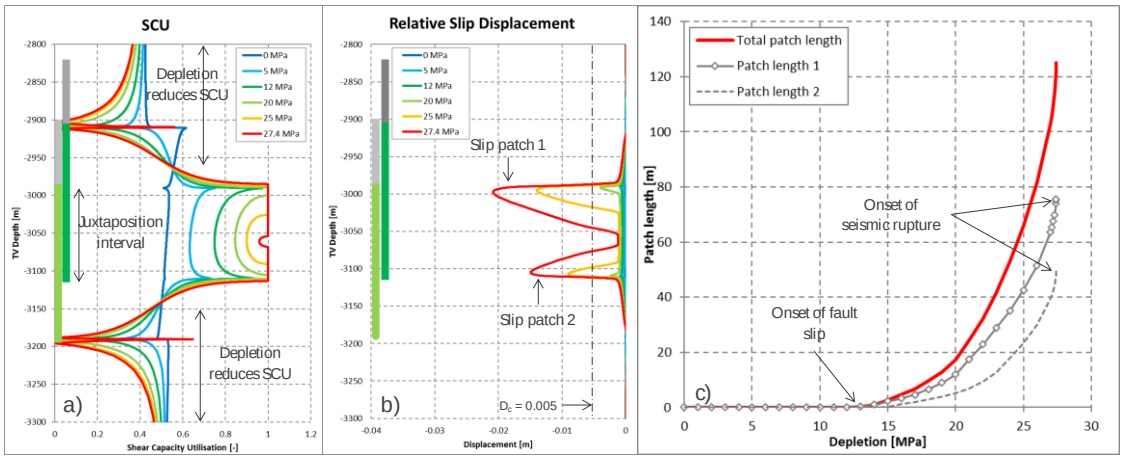

Figure 3.3: *a) The Shear Capacity Utilisation (SCU), and b) the Relative Slip Displacement along the fault plane as a function of depth for different reservoir depletion; c) the length of the two slip patches as a function of reservoir depletion for case mu55-181 (Figure 3.1b).*

3.1. Residual friction coefficient μ_r = 0.50

The first case presented in this chapter has a residual friction coefficient μ_r of 0.50 (case mu55-181, Table 3.1). First, the consequences of reservoir depletion on the stress distribution along the fault plane from the static analysis results of Analysis stage 1 are discussed.

The pore pressure in the fault (Figure 3.2a, and section 2.3) reduces uniformly due to reservoir depletion between the top of the foot wall at 2910 m depth and the bottom of the hanging wall at 3190 m depth. The offset and thickness of the depleting reservoirs are indicated by the green bars at the left-hand side of the graphs. The effective normal stress along the fault plane (Figure 3.2b, compressive stress is negative) increases significantly less over the juxtaposition interval compared to the intervals that are exposed to reservoir depletion on one side only. The effective normal stress along the fault plane does not change significantly across the overburden and basement formations, because the pore pressure in the fault is assumed not to change. The shear stress induced by reservoir depletion (Figure 3.2c) increases most over the juxtaposition interval with peak values at the top of the hanging wall and the bottom of the foot wall reservoir. Negative values indicate a downward directed shear stress exerted on the foot wall reservoir formation (normal faulting environment). Note that the (negative) shear stress reduces at the top and bottom of the depletion interval and becomes positive if the depletion pressure is sufficiently large. This means that the shear stress on the foot wall formations is reversed and directed upwards (see also Van den Bogert, 2015).

The Shear Capacity Utilisation (SCU) in Figure 3.3a is derived from the effective normal and shear stress distribution shown in Figure 3.2 using equations (2.1) and (2.2). The SCU increases over the juxtaposition interval in accordance with the increase of shear stress (Figure 3.2c) with peak values at the top of the hanging wall at 2990 m depth and at the bottom of the foot wall reservoir at 3110 m depth. The SCU along the fault plane is reduced by reservoir depletion over the top part of the foot wall reservoir and upwards into the overburden, and over the bottom part of the hanging wall reservoir and into the basement. This is caused by the reduction of shear stress (Figure 3.2c) *and* the increased normal effective stress. The latter implies an increase of the fault strength τ_{max} according to the Mohr-Coulomb friction law in equation (2.1). The reverse (positive) shear stress peak values at the top and bottom of the depletion interval shown in Figure 3.2c also cause peak values in the SCU (Figure 3.3a). Note that the SCU is always positive (between 0 and 1). A SCU value smaller than 1 means that the Mohr-Coulomb shear failure condition is not satisfied (section 2.2) and that the relative slip displacement along the fault plane is elastic and recoverable (Figure 3.3b).

Onset of fault slip is found at slip patch 1 (top of the hanging wall reservoir) where the SCU=1 after 12.74 MPa reservoir depletion (Figure 3.3c). The length of the slip patch is defined by the interval where SCU=1 and increases with increasing reservoir depletion. The SCU cannot be larger than 1, because the shear stress cannot exceed the shear strength of the fault. Incremental shear stress caused by incremental depletion is carried by parts of the fault where SCU<1. This is the reason why slip patch 1 propagates downwards across the juxtaposition interval if reservoir depletion is increased. Propagation of slip patch 1 above the juxtaposition interval hardly occurs,

because the SCU is significantly smaller than 1 and even reduces due to reservoir depletion. For the same reason, slip patch 2, which occurs at the bottom of the foot wall after almost 15 MPa reservoir depletion, propagates upwards across the juxtaposition interval.

The propagation of slip patch 1 and 2 across the juxtaposition interval is also seen from the Relative Slip Displacement (RSD) in Figure 3.3b. Note that negative values for the RSD indicate a downward displacement of the hanging wall relative to the foot wall. The RSD and length of slip patch 1 is larger than of slip patch 2 (Figure 3.3c). The slip displacement is a-seismic, because incremental reservoir depletion is required to increase the RSD and the size of the slip patch. Both slip patches grow faster with incremental depletion until 27.40 MPa reservoir depletion, when no further depletion is required to increase the length of both slip patches. This is indicative for the *onset of seismic rupture*.

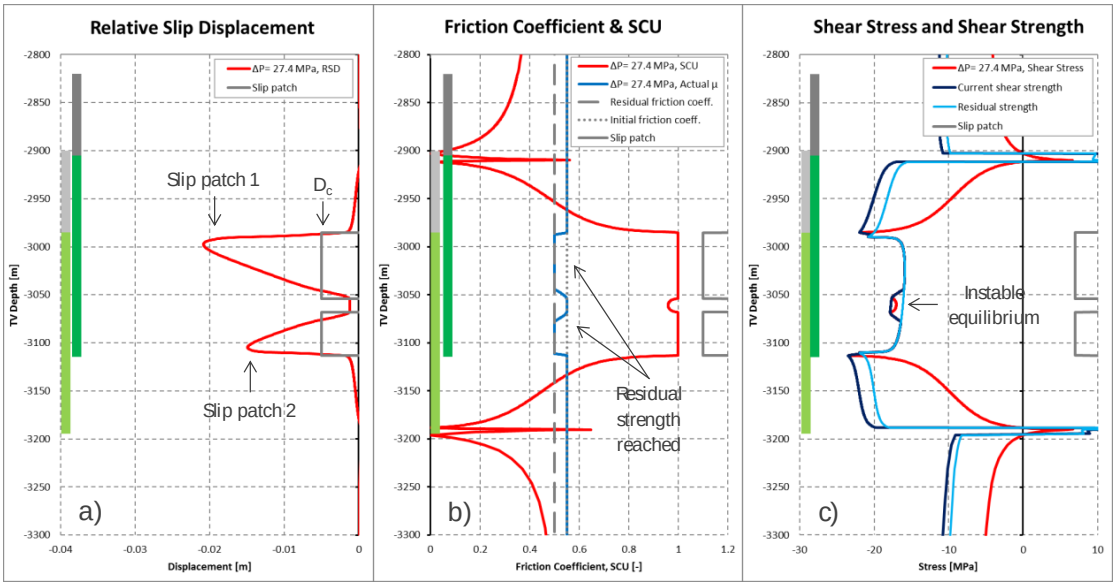

Figure 3.4: *a) the Relative Slip Displacement (RSD), b) the Friction Coefficient and Shear Capacity Utilisation (SCU), and c) the Shear Stress and Shear Strength as a function of depth along the fault plane at the onset of seismic rupture after 27.40 MPa depletion for the case with $\mu_r = 0.50$.*

Figure 3.4 shows the condition of the fault after 27.40 MPa reservoir depletion in more detail. The RSD (red line in Figure 3.4a) is larger than the critical slip displacement D_c = 0.005 m over almost the entire area of slip patch 1 and 2. The vertical size of the grey boxes indicate the length of the two slip patches (as shown in Figure 3.3c) and is based on the interval where SCU=1 (red line in Figure 3.4b). The friction coefficient reduces (blue line in Figure 3.4b) with increasing slip displacement adhering to the prescribed slip-weakening relationship for case mu55-181 in Figure 3.1b. This is the reason why the actual friction angle along the fault plane has reduced to the residual friction coefficient over the intervals where the RSD is larger than D_c. On those intervals, no further slip-weakening occurs if the RSD increases upon further reservoir depletion. The critical slip displacement D_c = 0.005 m is reached on slip patch 1 after 20.45 MPa reservoir depletion and after a somewhat larger reservoir depletion also on slip patch 2 (Figure 3.3b).

Figure 3.4c shows the shear stress distribution after 27.40 MPa reservoir depletion (red line) relative to the residual shear strength (light-blue line). The latter is based on the residual friction coefficient μ_r = 0.50. The shear stress is equal to the residual strength

over the intervals where D_c is exceeded (because the residual strength is reached). The residual strength is not reached and is smaller than the shear stress after 27.40 MPa depletion over a small interval between the two slip patches. This constitutes an unstable condition as the shear stress cannot be carried over this interval if slip displacement increases. The fault above and below the juxtaposition interval is stable, because the SCU < 1 and the residual strength is larger than the shear stress after 27.40 MPa depletion. So, the shear stress can be carried even if slip displacement increases and frictional strength reduces to the residual value.

Seismic rupture nucleates after 27.40 MPa reservoir depletion, because

- no incremental reservoir depletion is required to propagate the slip patches, and
- the residual fault strength between the slip patches is smaller than the actual shear stress.

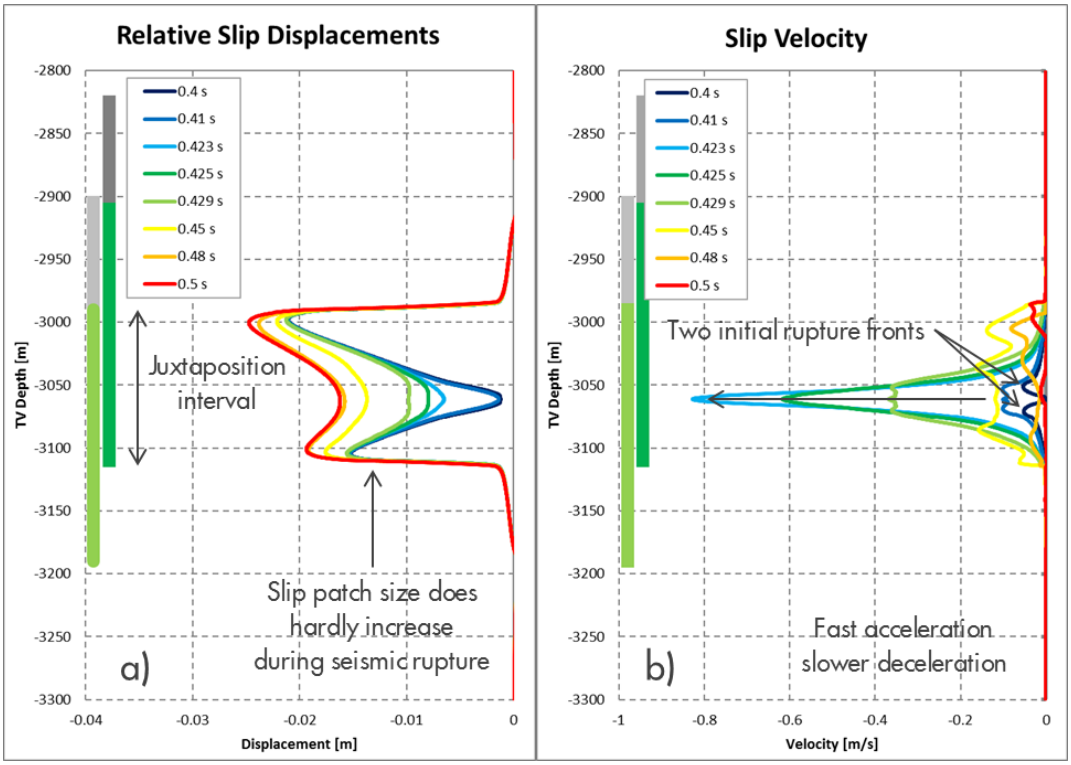

Figure 3.5: *a) The Relative Slip Displacement, and b) the relative slip velocity as a function of depth along the fault plane at various moments during the seismic rupture process for $\mu_r = 0.50$ (case mu55-181, Table 3.1)*

In Analysis stage 2, the dynamic equations of motion (2.3) are evaluated according to the procedure outlined in section 2.4. This includes an incremental depletion δP of 0.001 MPa at the start of the stage 2 analysis to bring the fault out of equilibrium and allow the rupture to nucleate. The slip patch does not extend and the slip velocity remains negligible until 0.4 s (Figure 3.5). This confirms that no initial slip velocity is introduced by the incremental depletion δP at the start of the dynamic rupture simulation. This would constitute an inaccurate representation of the actual fault condition and would provide an over-estimation of the seismic rupture.

Figure 3.5 shows that seismic rupture occurs by merging of the two slip patches in case mu55-181. This is demonstrated by the two peak values of the relative slip velocity in Figure 3.5b at the start of the seismic rupture after 0.4 s: one at the bottom of slip patch 1 and one at the top of slip patch 2. The maximum (absolute) relative slip velocity of

about 0.83 m/s is reached after 0.423 s and is exactly located between the two slip patches. Note that the RSD (Figure 3.5a) does not significantly increase over most of the two initial slip patches until this point in time. Deceleration of the seismic rupture occurs more gradual, while the slip velocity occurs over the entire area of the two merged slip patches. The merged slip patch remains confined to the juxtaposition interval where the fault is exposed to reservoir depletion on both sides. The seismic rupture stops after a little more than 0.5 s when the slip velocity is negligible again and the RSD and size of the slip patch do not further increase.

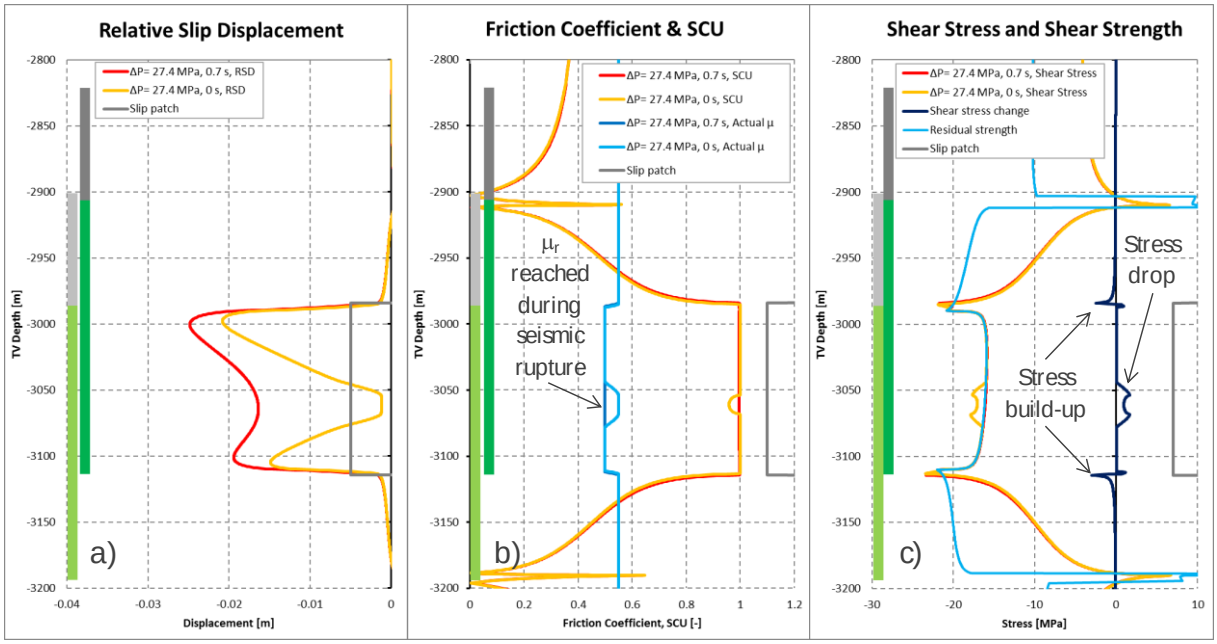

Figure 3.6: *a) Relative Slip Displacement, b) the friction coefficient and Shear Capacity Utilisation (SCU), and c) the shear stress, shear strength, and change of shear stress as a function of depth along the fault plane before (orange lines) and after the seismic rupture (red lines) after 27.40 MPa reservoir depletion for mu55-181.*

Figure 3.6a shows the a-seismic slip displacement induced by 27.40 MPa reservoir depletion (yellow line) and the total slip displacement after the seismic rupture (red line and covers the entire juxtaposition interval. The incremental seismic slip displacement along the fault plane is represented by the difference between the two lines. The friction coefficient is reduced to its residual value over a small interval between the two original slip patches as a result of the seismic rupture (Figure 3.6b). The reduction of shear stress or 'stress drop' therefore only occurs between the two slip patches (Figure 3.6c). Note that the initial shear stress as well as the depletion-induced shear stress is directed downward and is represented by negative values. This means that 'stress drop' is represented by a positive change of shear stress along the fault plane. The maximum shear stress reduction is about 1.7 MPa, but the average 'stress drop' is only 0.31 MPa, because no change of shear stress occurs along a significant part of the seismic slip patch. The assumption of a linear fault slip-weakening relationship implies that 'stress drop' is limited to intervals where the residual friction coefficient is not reached prior to the seismic rupture.

The shear stress reduction goes together with a shear stress build-up at the top and bottom of the seismic slip patch (Figure 3.6c). The integrated shear stress over the entire fault (the total shear force) is the same before and after the seismic rupture because the reservoir depletion does not change. So, the shear stress is re-distributed

to locations where the shear strength is not reached yet (SCU<1) as a results of the seismic rupture. The steep decline of the SCU at the top and bottom of the reservoir juxtaposition interval (Figure 3.6b) implies that significant capacity is available to carry shear stress released from the seismic slip patch. This is also the reason why the seismic slip patch hardly expands in upward and downward direction along the fault plane. So, intervals with a small SCU provide a barrier to rupture propagation as demonstrated in other work (Buijze et al., 2015, 2017).

3.2. Residual friction coefficient μ_r = 0.45

The second case presented in this chapter has a residual friction coefficient μ_r of 0.45 (case mu55-182, Table 3.1) and is considered the Base Case of this study. All parameters are the same as in the previous case, except for the critical slip displacement D_C = 0.01 m, which is adjusted to maintain a slope W_μ = 0.010 mm^{-1} of the descending branch of the linear slip-weakening relationship (Figure 3.1b). A more detailed evaluation of the results is provided in APPENDIX 3, whereas the conditions that causes onset of seismic rupture are presented in APPENDIX 4 by considering the stress redistribution along the fault plane induced by the stress drop over the slip patches, and in APPENDIX 5 by a so-called post-failure analysis.

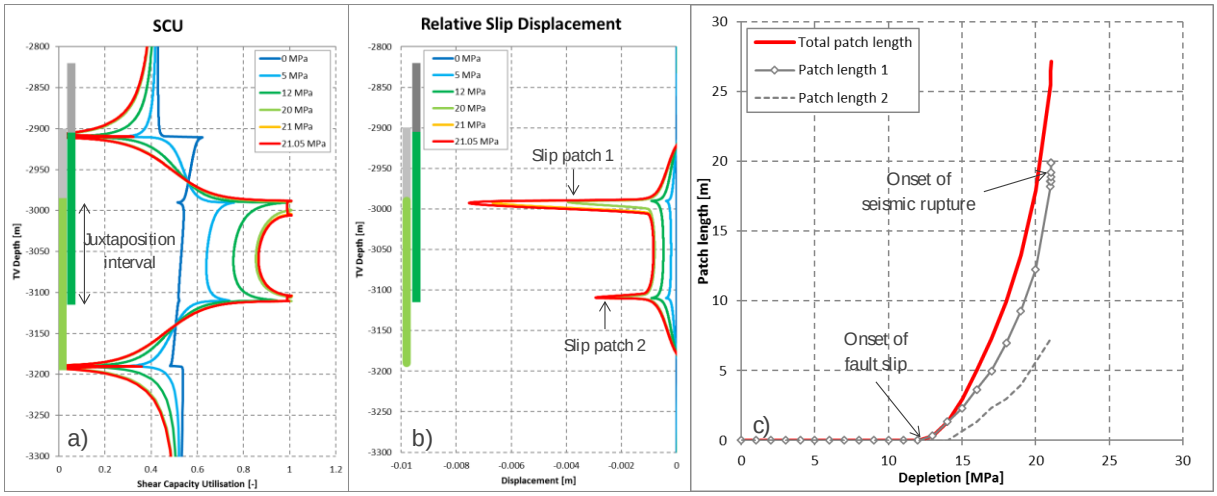

Figure 3.7: a) The Shear Capacity Utilisation (SCU), and b) the Relative Slip Displacement (RSD) along the fault plane as a function of depth for different reservoir depletion; c) the length of the two slip patches as a function of reservoir depletion for the case with μ_r = 0.45.

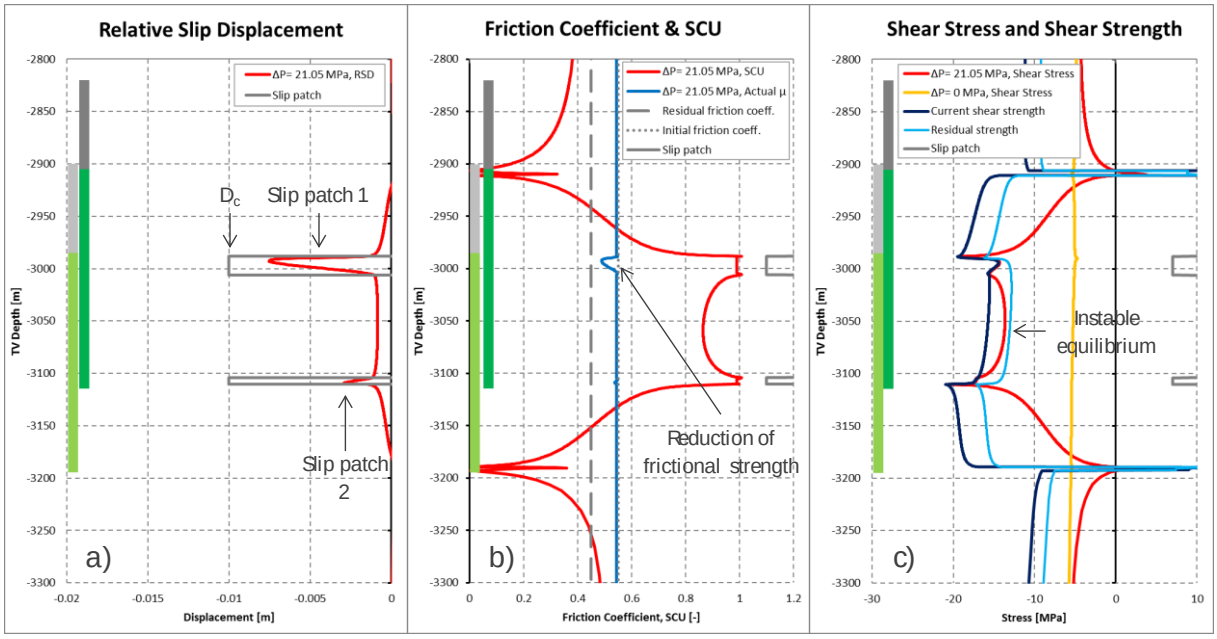

Figure 3.8: *a) the Relative Slip Displacement, b) the Friction coefficient and Shear Capacity Utilisation (SCU), and c) the shear stress and shear strength as a function of depth along the fault plane at the onset of seismic rupture after 21.05 MPa depletion for the case with μ_r = 0.45.*

The simulated slip displacement for this case in Analysis stage 1 is identical to the case with μ_r = 0.50 up to 20.45 MPa reservoir depletion. *Onset of fault slip* occurs also after 12.74 MPa reservoir depletion (Figure 3.7) at the top of the hanging wall (slip patch 1), because the initial friction coefficient μ_i is the same as in the previous case. The slip displacement and associated reduction of the friction coefficient is identical, because the slope W_μ = 0.010 mm^{-1} is the same. Also slip patch 2 occurs at the same reservoir depletion, somewhat below 15 MPa. The deviation starts to occur for a depletion larger than 20.45 MPa when the maximum slip displacement over slip patch 1 reaches the critical slip displacement D_c of 0.005 m for the case in the previous section (case mu55-181 with μ_r = 0.50). This means that the fault strength *does not* further reduce with increasing depletion in case mu55-181, whereas it *does* reduce further in the current case due to the larger critical slip displacement D_c of 0.010 m and smaller the residual friction coefficient μ_r = 0.45.

Onset of seismic rupture occurs after 21.05 MPa reservoir depletion before the critical slip displacement and residual friction coefficient is reached. The largest slip displacement of about 0.0075 m is smaller than the critical slip displacement D_c of 0.010 m and occurs over slip patch 1 (Figure 3.8a). The size of slip patch 1 is about 19.9 m and slip patch 2 is about 7.3 m at this reservoir depletion. The RSD between the two slip patches is small, but not zero. This is the elastic, recoverable displacement and is caused by the shear modulus (6.67 GPa) assigned to the interface elements.

The friction coefficient (blue line in Figure 3.8b) reduces mainly over slip patch 1 due to the Relative Slip Displacement and adhering to the prescribed slip-weakening relationship for the fault (Figure 3.1b). The residual friction coefficient of 0.45, which is represented by the grey dashed line, is not reached yet. The calculated maximum RSD of about 0.0075 m over slip patch 1 is about 75% of the critical slip displacement D_c, which implies that the friction coefficient is also about 75% down along the descending branch of the linear slip-weakening diagram from 0.55 to 0.45. This yields a minimum value of about 0.475 for the actual friction coefficient over slip patch 1.

The slip displacement and reduction of the friction coefficient over slip patch 2 is negligible after 21.05 MPa reservoir depletion.

Instability of slip patch 1 is the root cause of seismic rupture after 21.05 MPa reservoir depletion, because no incremental depletion is required to propagate slip patch 1 (Figure 3.7c). Furthermore, the reservoir shear stress (red line in Figure 3.8c) is larger than the residual shear strength (light-blue line) over the juxtaposition interval, which indicates an instable equilibrium condition. These two condition are also satisfied at the onset of seismic rupture in the previous case.

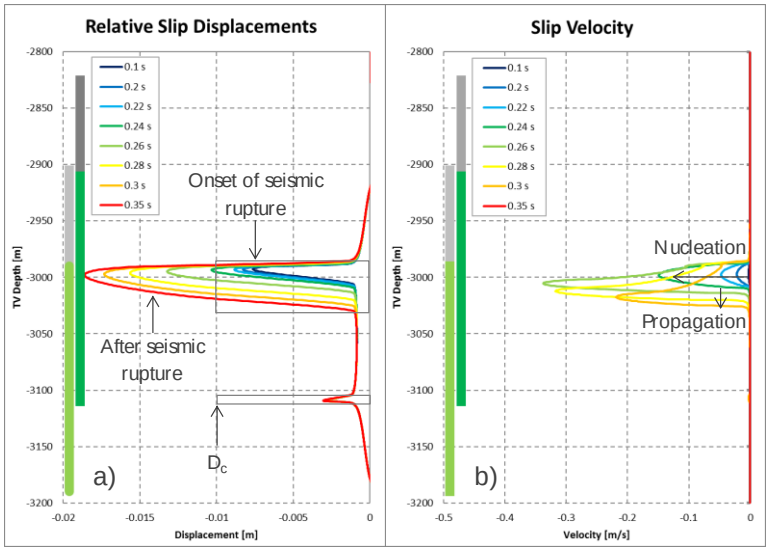

Figure 3.9: *a) The Relative Slip Displacement, and b) the relative Slip Velocity as a function of depth along the fault plane at various moments during the rupture process for case the case with μ_r = 0.45. A negative value indicates a downward movement of the hanging wall relative to the foot wall reservoir.*

The simulated seismic rupture in Analysis stage 2 can be divided into a nucleation phase and a propagation phase. During the nucleation phase until about 0.24s (dark-green line in Figure 3.9b), the a-seismic slip patch turns into a seismic slip patch with increasing relative slip velocity, while the size of the slip patch hardly increases. After 0.24 s, the Relative Slip Displacement reaches the critical slip displacement D_c of 0.010 mm, while the slip patch has marginally extended in downward direction (Figure 3.9a). The slip velocity increases until about 0.26 s and decreases subsequently, until the seismic rupture is arrested after about 0.35 s (red lines) and equilibrium of the fault plane is re-established. The propagation phase is characterised by an extension of the seismic slip patch in downward direction (mainly), while slip patch 2 does not increase in size (and thus does not slip seismically).

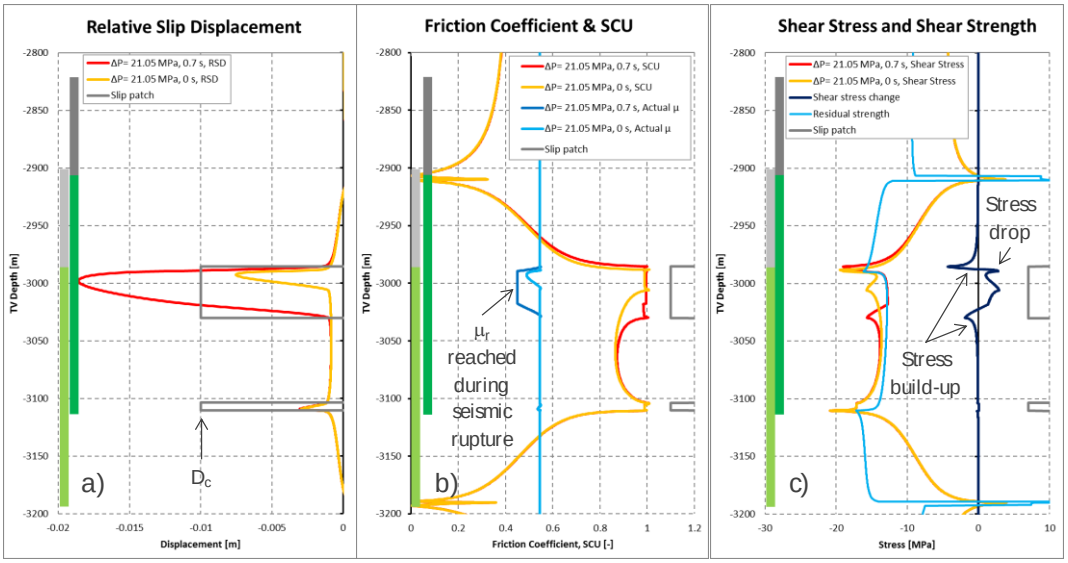

Figure 3.10: *a) Relative Slip Displacement, b) the friction coefficient and Shear Capacity Utilisation (SCU), and c) the shear stress, shear strength, and change of shear stress as a function of depth along the fault plane before (orange lines) and after the seismic rupture (red lines) after 21.05 MPa reservoir depletion for the case with $\mu_r = 0.45$.*

The size of slip patch 1 increases from 19.9 m to about 49 m, while the maximum absolute slip displacement increases from about 0.0075 m to about 0.019 m as a result of seismic rupture (Figure 3.10a). The residual friction coefficient is reached over a large part of the seismic slip patch, and the SCU is increased between the two slip patches (Figure 3.10b). The seismic rupture is arrested because the residual friction coefficient is reached over the seismic slip patch and because the SCU < 1 in the propagation direction below the seismic slip patch. The first reason means that no further strength reduction of the fault is simulated, and the second reason means that the interval below the seismic slip patch can carry incremental shear stress without slipping. The average stress drop over slip patch 1 is 0.98 MPa with a maximum of 2.9 MPa for this case (Figure 3.10c). The shear stress reduction is compensated by shear stress build-up at the top and bottom of the seismic slip patch.

For this case, seismic rupture nucleates after 21.05 MPa, because the residual friction coefficient is not reached yet, and because the size of the slip patch 1 exceeds a critical length. Uenishi and Rice (2003) demonstrated analytically that an a-seismic slip patch becomes instable when its size reaches a critical length L_c when using a linear slip-weakening relationship:

$$L_c = \frac{1.158}{(1-\nu)} \frac{G}{W}, \tag{3.1}$$

with Poisson's Ratio ν, shear modulus G, and the slope W of the descending branch of the linear slip-weakening diagram in [MPa/m]. In this study, the slope of the descending branch in the linear slip-weakening diagram is expressed in terms of the friction coefficient μ rather than the shear strength τ_{max} as done by Uenishi and Rice. Therefore, the slope of the slip-weakening diagram in Figure 3.1b is referred to as W_μ to distinguish it from the slope W defined in terms of shear strength. The value for W is the product of W_μ and the normal effective stress σ_n on the fault plane:

$$W = W_\mu \sigma_n. \tag{3.2}$$

In this study, the normal effective stress and therefore also the critical slip length is not constant along the fault plane. For this reason, the average value of the critical slip length of all interface elements that are part of the slip patch (for which SCU = 1) is calculated using (3.2) and (3.1). The analytical average critical slip length L_c in case mu55-182 with $\mu_r = 0.45$, using the normal effective stress distribution after 21.05 MPa reservoir depletion is 21.1 m. The length of the slip patch 1 after 21.05 MPa reservoir depletion is 19.9 m, or 94% of the analytical value.

3.3. Residual friction coefficient $\mu_r = 0.40$

The third case presented in this chapter has a residual friction coefficient $\mu_r = 0.40$ (case mu55-183, Table 3.1). All other parameters are the same as in the previous two cases, except for the critical slip displacement $D_c = 0.015$ m, so that the slope W_μ of the descending branch of the linear slip-weakening relationship remains the same at 0.010 mm^{-1} (Figure 3.1b).

Also in this case, *onset of fault slip* occurs at the top of the hanging wall (slip patch 1) after 12.74 MPa reservoir depletion (Figure 3.7) and slip patch 2 occurs also after almost 15 MPa reservoir depletion in Analysis stage 1. This is because the initial friction coefficient $\mu_i = 0.55$ is the same as in the previous two cases. The expansion of the slip patch is exactly the same with increasing reservoir depletion, because the slope of the slip-weakening relationship ($W_\mu = 0.010$ mm^{-1}) is the same as in the previous case. This is the reason why also *onset of seismic rupture* occurs at the same depletion level for the cases with $\mu_r = 0.45$ and $\mu_r = 0.40$. Actually, seismic rupture nucleates after 21.05 MPa reservoir depletion for all $\mu_r < 0.475$ provided that the critical slip displacement D_c is adjusted such that $W_\mu = 0.010$ mm^{-1}. This threshold value for the residual friction coefficient is based on the maximum slip displacement – and thus the minimum friction coefficient reached – over slip patch 1 at the onset of seismic rupture after 21.05 MPa reservoir depletion. In the previous two sections it is demonstrated that seismic rupture by instability of slip patch 1 is suppressed if the residual friction coefficient is reached before reaching the critical length of the slip patch. The maximum slip displacement for the case with $\mu_r = 0.45$ is 0.0075 m, and the fiction coefficient is 0.475 according to the assumed linear slip-weakening relationship. This implies that seismic rupture nucleates under the same conditions for all $\mu_r < 0.475$ after 21.05 MPa reservoir depletion.

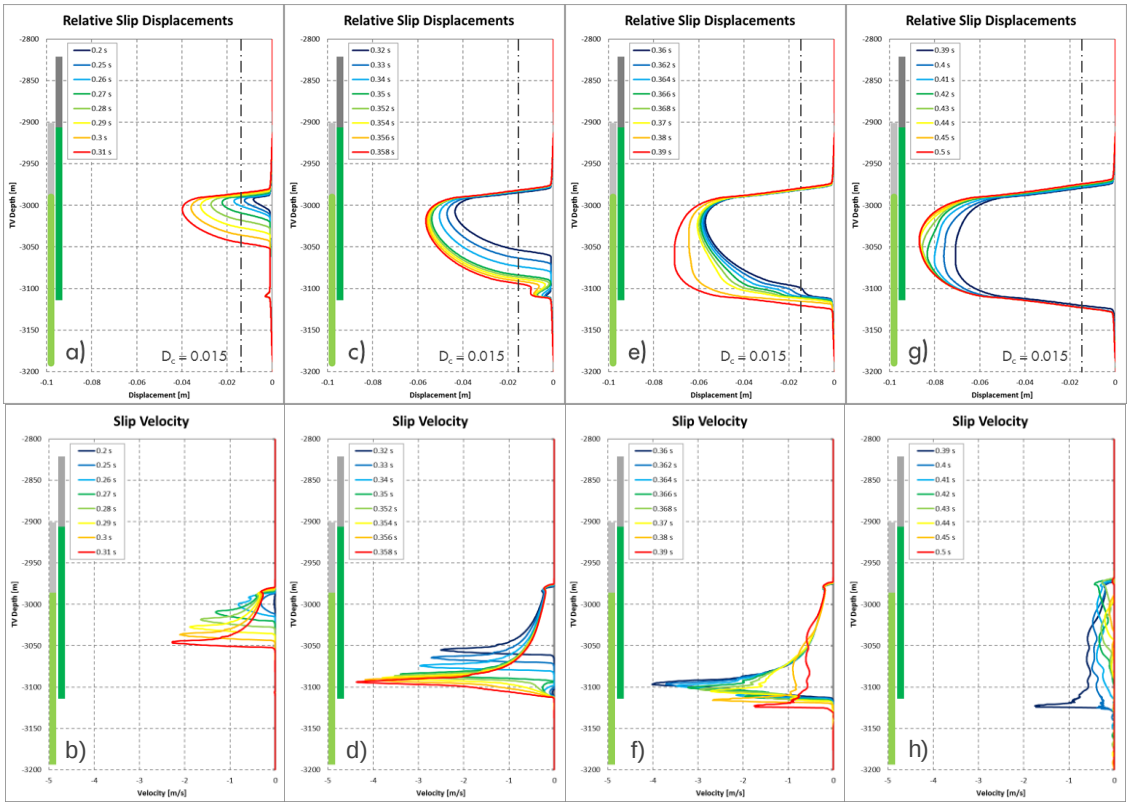

Figure 3.11: The Relative Slip Displacement (top), and Relative Slip Velocity (bottom) as a function of depth along the fault plane at various moment in time during the seismic rupture for the case with μ_r = 0.40.

In analysis stage 2, initially, the seismic rupture propagates from slip patch 1 downwards along the fault plane in exactly the same way as in the precious case with μ_r = 0.45. However, the smaller residual friction coefficient causes the seismic slip patch to accelerate longer and to merge with slip patch 2. The relative slip displacement in Figure 3.11a and the slip velocity in Figure 3.11b until 0.31 s confirms that seismic rupture nucleates at slip patch 1, while slip patch 2 is stable. Slip patch 1 expands predominantly in downwards direction, while the peak slip velocity is increasing. After 0.26 s (light blue line in Figure 3.11b), the slip velocity reduces at the top of the hanging wall at the original location of slip patch 1, because the residual friction coefficient is reached. Figure 3.11c/d shows the accelerating peak velocity at the downward propagating rupture front when it merges with slip patch 2. The shallow rupture front propagates upwards very slowly, while the (downward) slip velocity is virtually constant. The propagation of the deepest rupture front and peak slip velocity is decelerating after 0.36 s (Figure 3.11e/f). This is caused by the significant shear stress capacity left below the juxtaposition interval of the reservoir (see e.g. Figure 3.10b). The slip displacement increases further after 0.39 s (Figure 3.11g/h), while the seismic slip patch slowly expands further in downward direction and the slip velocity significantly reduces. The slip velocity is negligible after about 0.5 s.

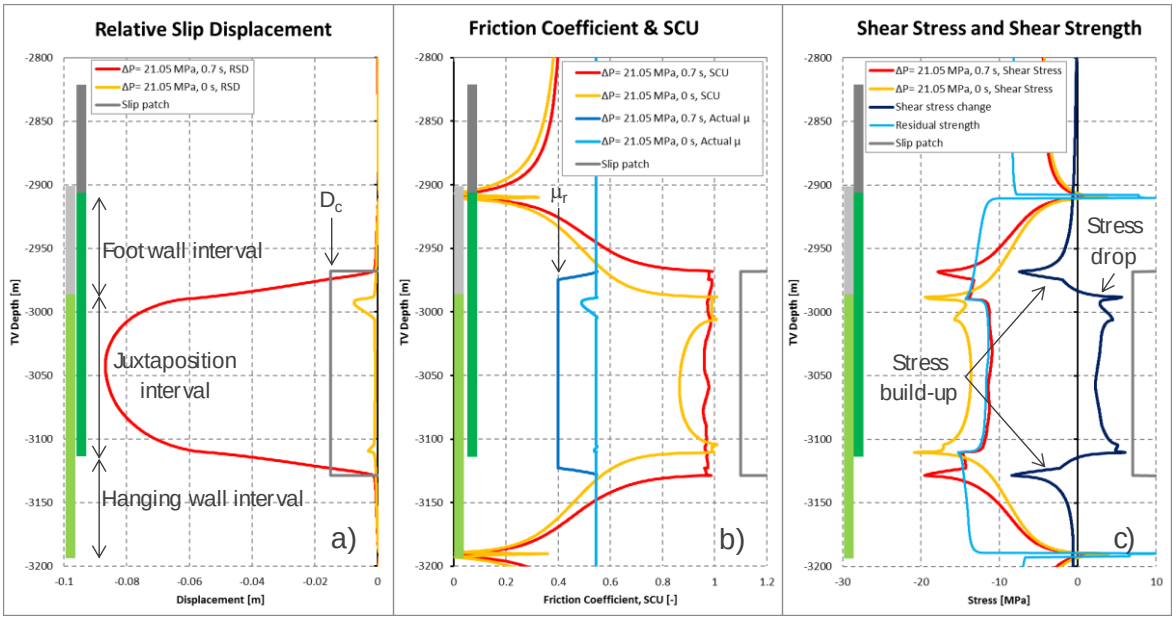

Figure 3.12: *a) Relative Slip Displacement, b) the Friction Coefficient and Shear Capacity Utilisation (SCU), and c) the Shear Stress, Shear Strength, and change of shear stress as a function of depth along the fault plane before (orange lines) and after the seismic rupture (red lines) after 21.05 MPa reservoir depletion for the case with $\mu_r = 0.40$.*

Slip patch 1 expands from 19.9 m before the seismic rupture to about 176 m afterwards, and penetrates into the foot wall and hanging wall intervals of the fault (red line in Figure 3.12a). The seismic slip patch overlaps with a-seismic slip patch 1 and 2 (orange line). The maximum slip displacement increases from 0.0075 m to 0.087 m due to the seismic rupture and exceeds the critical slip displacement of 0.015 m over almost the entire slip patch, which is indicated by the grey box. Consequently, the residual friction coefficient of 0.40 (dark-blue line in Figure 3.12b) is reached over almost the entire slip patch. The rupture is arrested in the foot wall interval above the juxtaposition interval and the hanging wall interval below it. This is explained by the relatively low value of the SCU over these interval, which indicates that these interval have a significant capacity to carry the shear stress released from the seismic slip patch. The redistribution of shear stress from the seismic slip patch to the foot wall and hanging wall intervals is shown by the change of shear stress (dark-blue line in Figure 3.12c). The average stress drop over the seismic slip patch is 1.95 MPa, with a maximum of 6.0 MPa. The maximum build-up of shear stress is 8.4 MPa.

3.4. Moment magnitude and source-time function

In this section, the influence of the residual friction coefficient on the moment magnitude (Hanks and Kanamori, 1979) and the source-time function for all six cases in Table 3.1 are presented and discussed. A source-time function gives the average relative slip velocity over the seismic slip patch as a function of time (APPENDIX 10) and represents the rupture as a seismic point source. First, the results of the three cases with a residual friction coefficient of 0.25, 0.30 and 0.35 are briefly presented (more detailed results are presented in APPENDIX 6). The critical slip displacement D_c has been adjusted such that the slope W_μ of the linear slip-weakening relationship is 0.010 mm^{-1} (Figure 3.1b).

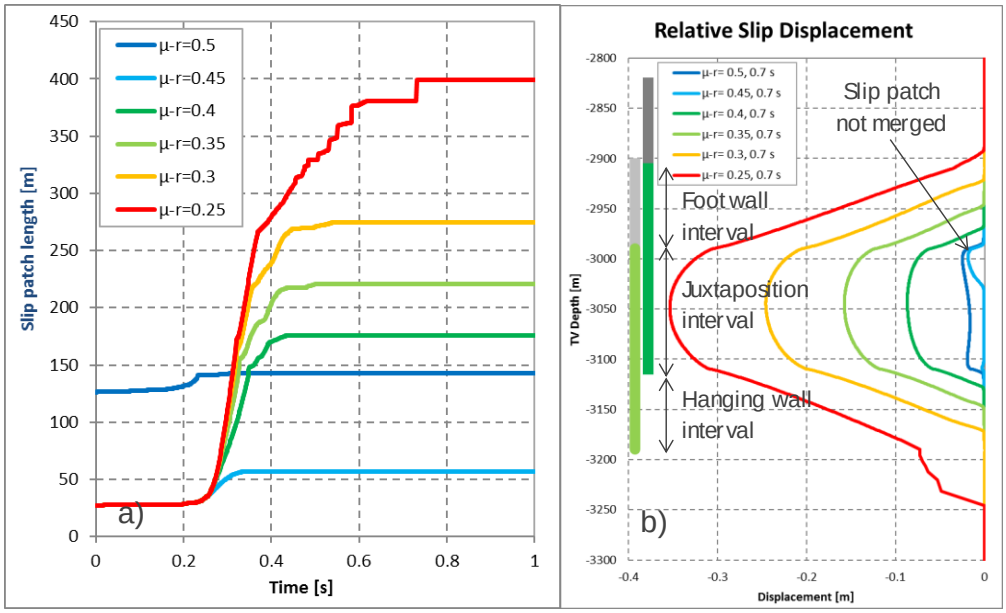

Figure 3.13: *a) Total length of the slip patches as a function of time, and b) the Relative Slip Displacement as a function of depth along the fault plane after the seismic rupture (0.7 s) for the cases in Table 3.1. All seismic rupture occurs after 21.05 MPa reservoir depletion except the case with μ_r = 0.50 (dark blue line), which occurs after 27.40 MPa reservoir depletion.*

The three cases in Table 3.1 with a residual friction coefficient μ_r of 0.25, 0.30 and 0.35 show a similar fault slip behaviour as the case with μ_r = 0.40. That is, onset of fault slip occurs after 12.74 MPa reservoir depletion and seismic rupture occurs after 21.05 MPa depletion by instability of slip patch 1. Figure 3.13a shows an identical increase of the seismic slip patch until about 0.3 s for the cases with $\mu_r \leq 0.45$. This is explained by the identical slope W_μ of the linear slip-weakening relationship which causes an identical acceleration of the slip velocity along the fault plane. The slip velocity accelerates longer (cf. Figure 3.11) and the stress drop over the juxtaposition interval is larger (cf. Figure 3.12c) with decreasing value for the residual friction coefficient. For this reason, the length of the slip patch increases faster and becomes larger for smaller value for the residual friction coefficient (Figure 3.13a). The merging of the two a-seismic slip patches in the case with μ_r = 0.50 (section 3.1) causes a much smaller increase of the slip patch (dank blue line). In this case the slip patch does not expand significantly outside the juxtaposition interval of about 131 m. Except for the case with μ_r = 0.45, all other cases expand (significantly) outside the juxtaposition interval during the seismic rupture.

The expansion of the slip patch outside the juxtaposition interval is more clearly seen in Figure 3.13b, which shows the relative slip displacement after the seismic rupture for all six cases in Table 3.1. The slip patch propagates further upward into the foot wall and further downward into the hanging wall intervals with decreasing value for the residual friction coefficient. These intervals are barriers for seismic slip propagation because of the low value for the SCU (Figure 3.12b). A larger part of that shear stress barrier is required to arrest the seismic rupture as the shear stress reduction over the seismic slip patch is larger with decreasing value for the residual friction coefficient.

The slip patch propagates out of the hanging wall into the basement for the case with $\mu_r = 0.25$[1].

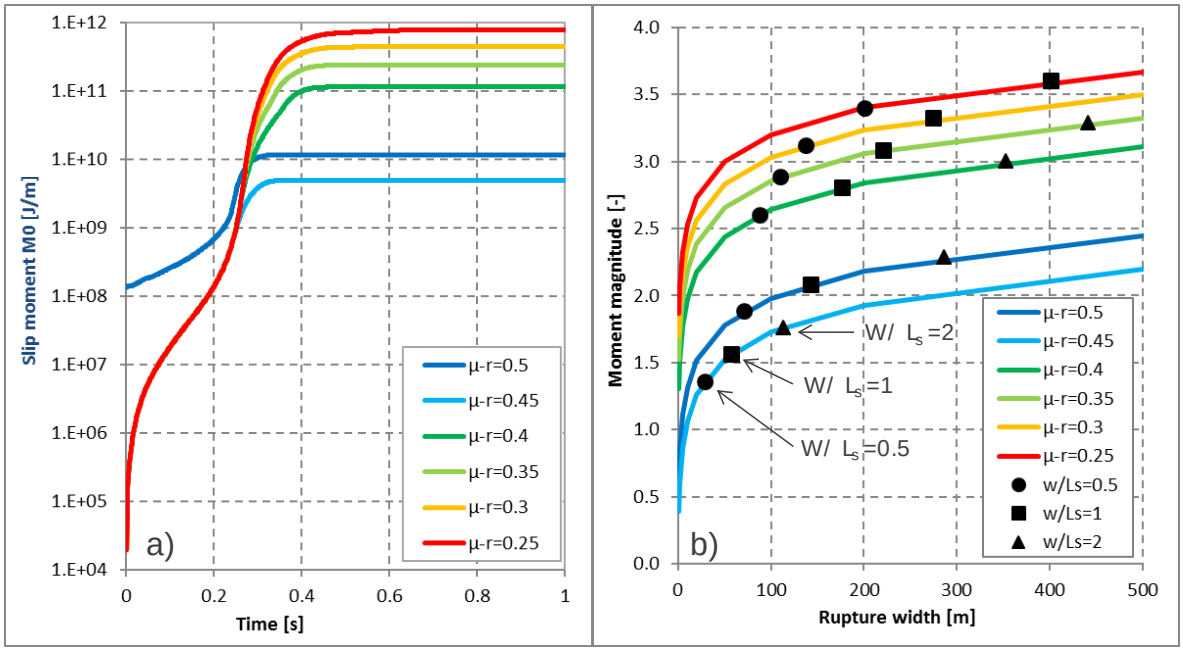

Figure 3.14: *a) Slip moment M_0 on log-scale as a function of time, and b) moment magnitude M_w as function of the assumed rupture width in strike direction of the fault for the cases in Table 3.1. Rupture widths of 0.5, 1 and 2 times the seismic patch length in dip slip direction are indicated.*

The seismic moment M_0 and the moment magnitude M_w (Hanks and Kanamori, 1979) are calculated from the relative slip displacement along the fault plane using the expressions given in APPENDIX 13. The seismic moment M_0 is proportional to the area between the orange and red lines as shown for the case with $\mu_r = 0.40$ in Figure 3.12a. The dimension of the seismic moment in Figure 3.14a is J/m due to the two-dimensional character of the finite-element model. An assumption for the rupture width w in the strike direction along the fault plane is required to calculate the moment magnitude. Figure 3.14b shows the calculated moment magnitude as a function of the assumed rupture width w using the seismic moment M_0 after 1 s for the six cases in Figure 3.14a according to the expression in APPENDIX 13. For instance, the moment magnitude M_w is 1.56 for the case with $\mu_r = 0.45$ if the rupture withdraw in strike direction along the fault is assumed to be equal to the length L_s of the slip patch in dip direction (Figure 3.13a). The moment magnitude M_w increases by about 0.2 each time the aspect ratio is doubled (w/L_s =2, 4, 8, etc). An aspect ratio w/L_s=1 is used throughout this report, unless stated otherwise.

[1] *The large, sudden increases of the slip patch size after about 0.7 s in Figure 3.13a is caused by the increasing size of the interface elements below the hanging wall. This is also reflected by the slip displacement at the bottom of the slip patch in Figure 3.13b.*

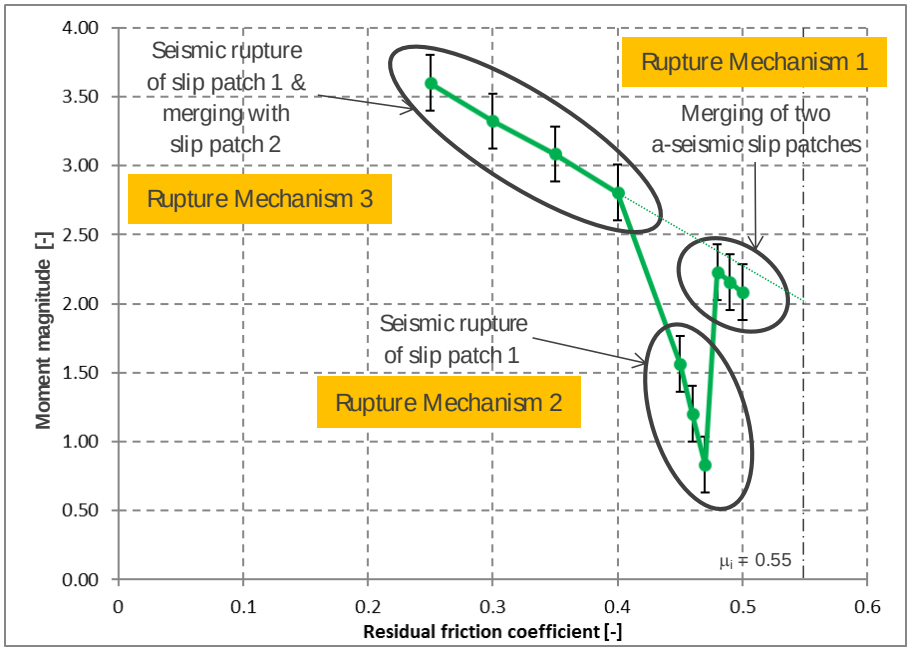

Figure 3.15: *Moment magnitude M_w (assuming w/L_s =1, see Figure 3.14) as a function of the residual friction coefficient for the cases discussed in APPENDIX 6. The error bars indicate the moment magnitude if an aspect ratio w/L_s=0.5 and w/L_s=2 is assumed.*

Figure 3.15 shows the moment magnitude M_w as a function of the residual friction coefficient. The moment magnitude represented by the green line is based on an aspect ratio w/L_s=1 for the seismic slip patch. The error bars indicate a reduction and an increase of about 0.2 for the moment magnitude if an aspect ratio w/L_s=0.5 and w/L_s=2 is assumed respectively. Three rupture mechanisms are observed in the dynamic rupture simulations presented in this chapter:

1. **Merging of the two slip patches for $0.475 \leq \mu_r \leq 0.50$.**
2. **Instability of the shallow slip patch without merging with the deep slip patch for $0.45 \leq \mu_r < 0.475$**
3. **Instability of the shallow slip patch and merging with the deep patch for $0.25 \leq \mu_r \leq 0.40$**

The results of the cases mu55-187 through mu55-190 with a residual friction coefficient $0.46 \leq \mu_r \leq 0.49$ (APPENDIX 2) are included in Figure 3.15 to confirm the transition between rupture mechanism 1 and 2 at about $\mu_r = 0.475$ (see section 3.2). It is seen that Rupture Mechanism 2 generates significantly smaller seismic events in comparison with the other cases. This is attributed to the merging of the two slip patches which releases more kinetic energy than seismic rupture of a single slip patch (Appendix A.6.5). The moment magnitude shows a linear dependency on the residual friction coefficient for each rupture mechanism. Rupture Mechanism 1 and 3 also follow almost the same trendline, albeit that the trendline for Rupture Mechanism 1 is somewhat below that for Rupture Mechanism 3, as indicated by the dotted line. So, the moment magnitude is not only influenced by the reduction of the friction coefficient (μ_i - μ_r), but also by the rupture mechanism.

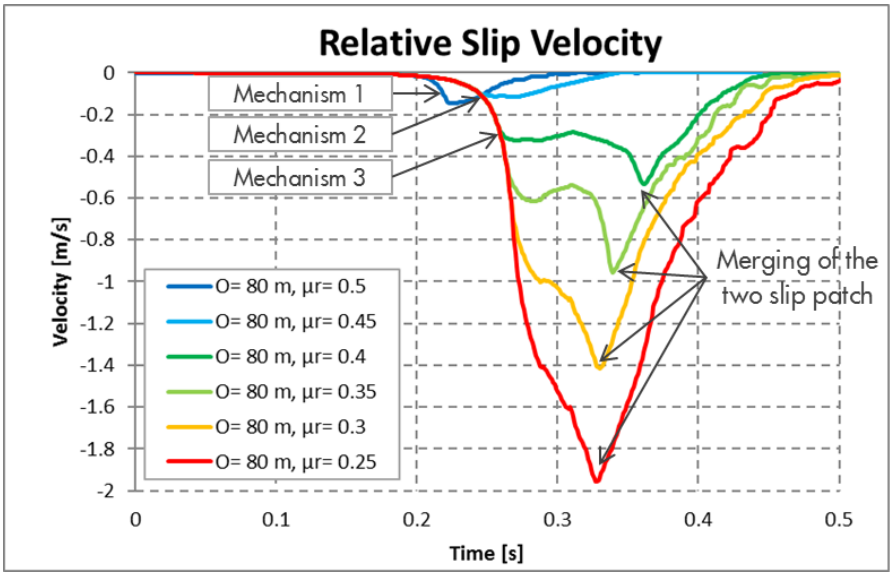

Figure 3.16: Average relative slip velocity as a function of time[2] (source-time function) for different values of the residual friction coefficient and an offset of 80 m ($\bar{O}$ =0.4).

A source-time function gives the average relative slip velocity over the seismic slip patch as a function of time (APPENDIX 10) and represents the rupture as a seismic point source. Figure 3.16 shows the source-time function for the six cases in Table 3.1. A source-time function gives the average relative slip velocity over the slip patch as a function of time (APPENDIX 10) and represents the rupture as a seismic point source. The source-time function for the case with μ_r=0.50 that exhibits Rupture Mechanism 1 (dark-blue line) shows a much faster acceleration (increase of slip velocity) than the more gradual velocity increase seen for the other cases that exhibit Rupture Mechanism 2 or 3 and is caused by instability of slip patch 1. Rupture mechanism 3 is characterised by a second acceleration phase which is caused by the merging of the two slip patches. The larger slip velocity also causes that the peak velocity is reached somewhat earlier with decreasing value for the residual friction coefficient.

The moment magnitude in Figure 3.15 and the source-time functions in Figure 3.16 show that seismic rupture is not only dependent on the residual friction coefficient, but also on the rupture mechanism. The transition between the three rupture mechanisms is clearly seen in Figure 3.15 and occurs at about μ_r = 0.475 between Rupture Mechanism 1 and 2, and between μ_r = 0.40 and μ_r =0.45 for the transition between Rupture Mechanism 2 and 3. Additional analysis would be required to determine the transition between Rupture Mechanism 2 and 3 more accurately.

3.5. Interpretation of the results

In the first three sections of this chapter, the results of three identical cases are presented, except for the residual friction coefficient which is varied between 0.50 and 0.40 (Table 3.1). The critical slip displacement D_c is adjusted to maintain the slope in the slip-weakening diagram W_μ at 0.010 mm^{-1}. In all three cases, onset of fault slip occurs at the top of the hanging wall reservoir after 12.74 MPa reservoir depletion, while a second slip patch occurs at the bottom of the foot wall reservoir after almost 15 MPa reservoir depletion. The loss of fault strength caused by the increasing Relative

[2] *The red line for the case with μ_r=0.25 is covering all other lines except the dark-blue line for μ_r=0.50*

Slip Displacement (RSD) is identical, because the slope W_μ of the descending branch of the linear slip-weakening relationship is the same in all three cases. Uenishi and Rice (2003) demonstrated analytically that seismic rupture occurs if the size of an a-seismic slip patch exceeds a certain critical length L_c when using a linear slip-weakening relationship. In the cases with μ_r = 0.45 (mu55-182) and μ_r = 0.40 (mu55-183), onset of seismic rupture occurs after 21.05 MPa reservoir depletion when the length of slip patch 1 is very close (94%) to the analytical value obtained from expression (3.1). Seismic rupture at slip patch 1 is suppressed in the case with μ_r = 0.50 (mu55-181), because the residual friction coefficient is reached after 20.45 MPa before the critical length of slip patch 1 is exceeded. This means that no further slip weakening occurs on a part of the a-seismic slip patch if the RSD increases upon further reservoir depletion. Absence of slip weakening means that $W_\mu = 0$ and $L_c \rightarrow \infty$ according to Uenishi and Rice's expression (3.1). Therefore, instability of slip patch 1 does not occur and seismic rupture is suppressed.

Slip patch stabilisation may also occur when the residual friction coefficient μ_r is reached during the seismic rupture. This is found in the cases with μ_r = 0.50 and 0.45. In the case with μ_r = 0.50 (section 3.1), seismic rupture nucleates between the two slip patches after 27.40 MPa reservoir depletion (Figure 3.4c) and accelerates over intervals where the residual friction coefficient is not reached yet (Figure 3.4b). The slip velocity reduces shortly after the relative slip displacement exceeds D_c and no further strength reduction occurs (Figure 3.5). The seismic rupture is arrested within the juxtaposition interval, where the residual friction coefficient is reached during the depletion stage through a-seismic slip (Figure 3.6b). So, seismic rupture is arrested if no further slip weakening is present on the seismic slip patch. Also in this case, $W_\mu = 0$ and $L_c \rightarrow \infty$, which means that the condition for seismic rupture is not satisfied anymore.

Slip patch stabilisation also occurs during the seismic rupture in the case with μ_r = 0.45 (section 3.2). Deceleration of the seismic rupture is found once the critical slip displacement is exceeded and the residual friction coefficient is reached (Figure 3.9). The stabilising effect of the residual friction coefficient is also demonstrated in the post-failure analysis in APPENDIX 5. The seismic rupture is arrested before merging of the two slip patches occurs, because the fault shear strength is not reached yet (SCU < 1) between slip patch 1 and slip patch 2 (Figure 3.8b). Obviously, no slip weakening occurs over intervals where the shear strength is not reached yet, so that $W_\mu = 0$ and $L_c \rightarrow \infty$.

Seismic rupture does not decelerate after reaching the critical slip displacement in the case with μ_r = 0.40 and D_c = 0.015 m (Figure 3.11a/b in section 3.3). After nucleation, the seismic rupture accelerates longer and the seismic slip patch grows larger before the residual friction coefficient is reached in this case compared to the case with μ_r = 0.45. The size of the seismic slip patch where RSD < D_c is still larger than the critical slip length L_c when the critical slip displacement D_c is exceeded and the residual friction coefficient μ_r = 0.40 is reached, so that the condition for seismic rupture formulated by Uenishi and Rice is still satisfied. The condition for seismic rupture is not satisfied any longer if the rupture propagates into the foot wall and hanging wall intervals (Figure 3.12a), because SCU < 1 and thus $W_\mu = 0$ and $L_c \rightarrow \infty$.

This leads to the following conclusion:

Seismic rupture nucleates or accelerates if an (a-)seismic slip patch contains an interval that is larger than the critical slip length L_c according

to expression (3.1) formulated by Uenishi and Rice (2003) when using a linear slip-weakening relationship

This conclusion implies that

i) the condition for fault slip is met (SCU=1),
ii) the residual friction coefficient is not reached yet, and that
iii) the slope $W_\mu > 0$ over a sufficiently large interval of the slip patch.

All three parameters of the linear slip-weakening relationship (μ_i, μ_r and W_μ) also determine the rupture mechanism observed in the dynamic rupture simulation. The slope W_μ and the residual friction coefficient μ_r determine if seismic rupture nucleates by merging of the two a-seismic slip patches or if it nucleates by instability of a single slip patch. A single a-seismic slip patch becomes instable if its size reaches a critical length L_c, which corresponds well with the analytical expression (3.1) derived by Uenishi and Rice (2003). Merging of the two a-seismic slip patches occurs if the residual friction coefficient is reached before the critical length L_c. In the latter case, a significantly larger reservoir depletion pressure is required to cause seismic rupture. So, the three parameters of the linear slip-weakening relationship determine if, and at what reservoir depletion seismic rupture occurs, and which of the three observed rupture mechanisms will occur. Other rupture mechanisms may be found when varying other modelling parameters, or when changing the modelling assumption of the current study. However, the good correspondence with the analytical expression by Uenishi and Rice (2003) and the confirmation by the post-failure analysis presented in APPENDIX 5 provides confidence that the models capture the nucleation of seismic rupture in a plausible and mechanically correct way.

4. Influence of Reservoir offset and other modelling parameters

In the previous chapter, three rupture mechanisms are found by varying the residual friction coefficient, while keeping all other model parameters the same. In this chapter, the results of a large number of cases are presented in which also other parameters are changed. Case mu55-182 (section 3.2) is selected as Base Case for this study and is characterised by a fault with a dip angle β = 66 degree with the horizontal, intersecting a reservoir with thickness H = 200 m and an offset $\bar{O}$ = 80 m. The normalised reservoir offset $\bar{O}$ is defined by the absolute offset $\bar{O}$ divided by the reservoir thickness H and is 0.4 for the Base Case. The initial and residual friction coefficient are 0.55 and 0.45 respectively, while the slope of the descending branch of the linear slip-weakening relationship W_μ = 0.01 mm^{-1}. Other parameters are as described in chapter 2. A detailed results description of the Base Case is found in APPENDIX 3.

In section 4.1, the influence of the reservoir offset on the reservoir depletion that causes seismic rupture and the rupture mechanism is discussed. In section 4.2, the same analyses are repeated for a residual friction coefficient between 0.25 and 0.50, while maintaining a slope W_μ = 0.01 mm^{-1} in the slip-weakening diagram. For $\mu_r < 0.25$, the seismic rupture would continue to propagate downwards and upwards along the fault plane under the current in-situ stress conditions. This lower bound is in agreement with experimental values obtained by Di Torro et al. (2011). The influence of reservoir thickness on the onset of seismic rupture and the moment magnitude are discussed in section 4.3, while the slope W_μ is addressed in section 4.4.

4.1. Reservoir offset

This section provides a summary of the results presented in APPENDIX 7 for a number of cases in which the reservoir offset is varied between 0 and 400 m, while taking all other parameters identical to the Base Case (section 3.2 and APPENDIX 3). This means that the normalised reservoir offset is varied between 0 and 2. The normalised reservoir offset in the Groningen field is predominantly between 0 and 0.5, while the normalised offset is larger than 2 for less than 1% of the fault length (APPENDIX 1).

Figure 4.1a shows the impact of the normalised reservoir offset on the reservoir depletion that causes onset of fault slip and the onset of seismic rupture. The *onset of fault slip* (green line) is similar to the result found in a previous study (van den Bogert, 2015). A reservoir with an offset about equal to the reservoir thickness is most prone to *fault slip* due to reservoir depletion, whereas a reservoir without offset is least prone to fault slip. The relationship in Figure 4.1a also implies that reservoir depletion on one side of the fault does not constitute a worst-case scenario, as this condition is represented by the case with a very large offset.

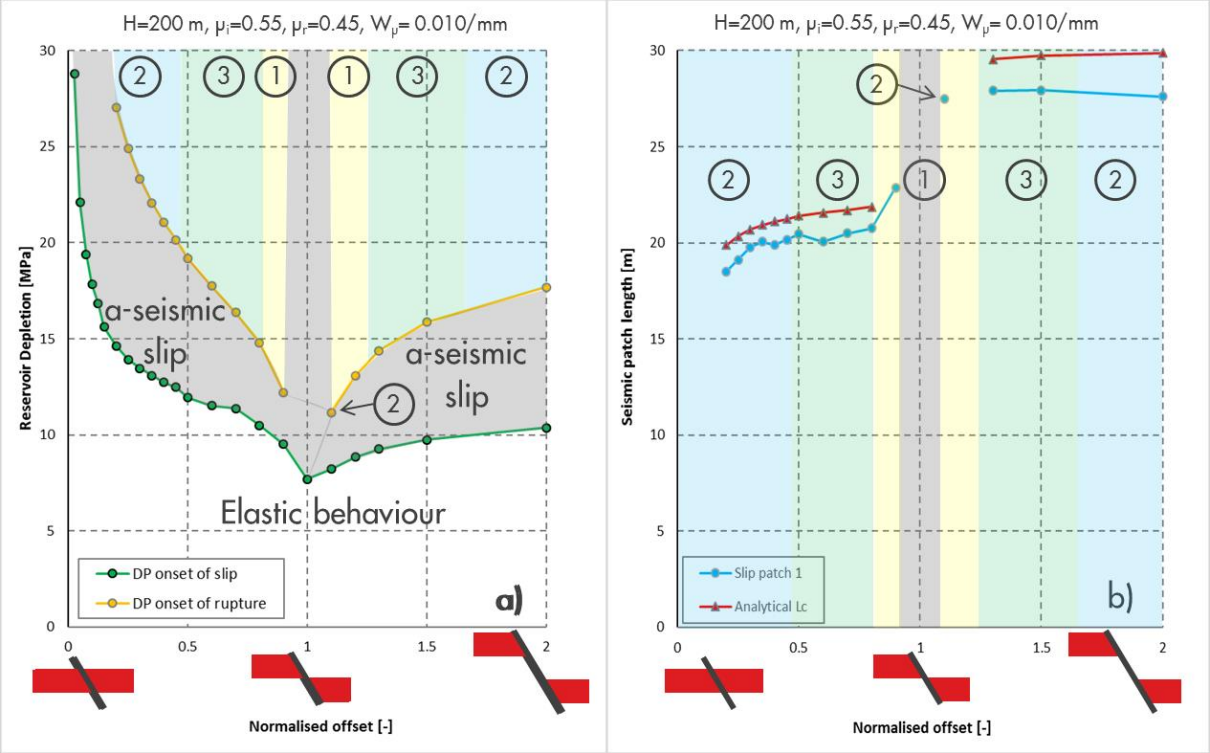

Figure 4.1: *a) Reservoir depletion at the onset of fault slip and the onset of seismic rupture, b) the length of (shallow) slip patch 1 at the onset of seismic rupture as a function of the normalised reservoir offset. The background colour and number refers to Rupture Mechanism 1, 2 or 3.*

Fault slip is accommodated in an a-seismic fashion in the depletion range between the onset of fault slip (green line) and the onset of seismic rupture (yellow line). This depletion range is smallest for an offset of about the reservoir thickness and it is increasing for a smaller and larger offset. Seismic rupture does not occur up to 30 MPa depletion for a small normalised offset. Seismic rupture does also not occur in case of a normalised offset of 1. In this case, only one slip patch occurs, because the top of the hanging wall and bottom of the foot wall reservoir formations coincided. The single slip patch is stabilised, because the residual friction coefficient μ_r = 0.45 is reached before the critical slip length L_s is exceeded, similar as the case discussed in section 3.1.

A large depletion range with a-seismic fault slip – as found for a normalised offset smaller than, say, 0.3 – can be regarded as structurally ductile behaviour, whereas a small depletion range with a-seismic fault slip – with a normalised offset between 0.7 and 1 – can be considered as a brittle response. In this sense, a small (normalised) reservoir offset demonstrates a more ductile structural response, whereas a normalised offset of about 1 demonstrates a more brittle response under the same fault slip-weakening assumptions.

The rupture mechanism that occurs after the onset of seismic rupture is indicated by the background colour in Figure 4.1. Rupture Mechanism 2, which is indicated by the blue areas and is characterised by rupture of the shallow slip patch only (see section 3.4), applies if the distance between the two slip patches is relatively large and instability of the shallow slip patch does not lead to merger with the deep slip patch. For the assumed slip-weakening behaviour this is found for a normalised offset smaller than 0.5, or larger than about 1.5. Rupture Mechanism 3 applies (green areas) if the

distance between the slip patches is sufficiently small to allow the instable shallow slip patch to merge with the deeper slip patch. Merging of the slip patches is the root cause of seismic rupture (Rupture Mechanism 1, yellow area) if the normalised offset is close to 1. An exception is found in the case with 220 m offset, in which case merging of the two slip patches occurs in a stable fashion. Rupture Mechanism 2 is assigned to this case, because fault instability occurs from a single merged slip patch. This case shows that merging of two slip patches not necessarily leads to fault instability. The source-time functions associated with all three rupture mechanisms show the same characteristics as discussed in section 3.4 for different values of the residual friction coefficient (APPENDIX 10). So, the classification of rupture mechanism is valid for any (normalised) reservoir offset.

Figure 4.1b shows that the length of the shallow slip patch (slip patch 1) at the onset of seismic rupture (solid blue line) corresponds well with the critical slip length L_c (red line) calculated using the analytical expression (3.1) by Uenishi and Rice (2003). The length of the slip patch at the onset of seismic rupture is between 93% and 96% of the analytical value of L_c for the cases in APPENDIX 7. The deviation is explained by the fact that L_c is not constant along the fault plane (see section 3.2). The correspondence between the numerical and analytical results provides support for the relationship between normalised offset and onset of seismic rupture in Figure 4.1a, and allows an estimation of the reservoir depletion at which onset of seismic rupture can be expected based on the input parameters of the dynamic rupture simulation.

4.2. Residual friction coefficient

The reservoir depletion at onset of seismic rupture and the rupture mechanisms indicated in Figure 4.1a are valid for the linear slip-weakening parameters as specified in Figure 3.1 (μ_i=0.55, μ_r=0.45, W_μ=0.01 mm^{-1}). Onset of seismic rupture occurs at the same reservoir depletion for $\mu_r \leq 0.47$ provided that the slope in the slip-weakening relationship is the same (APPENDIX 6). However, the transition between Rupture Mechanism 2 to Rupture Mechanism 3 in Figure 3.1 is dependent on the residual friction coefficient: Rupture Mechanism 3 occurs at a smaller normalised offset for $\bar{O}$ <1 (Figure 3.15) and at a larger normalised offset for $\bar{O}$ >1 if μ_r is smaller than 0.45.

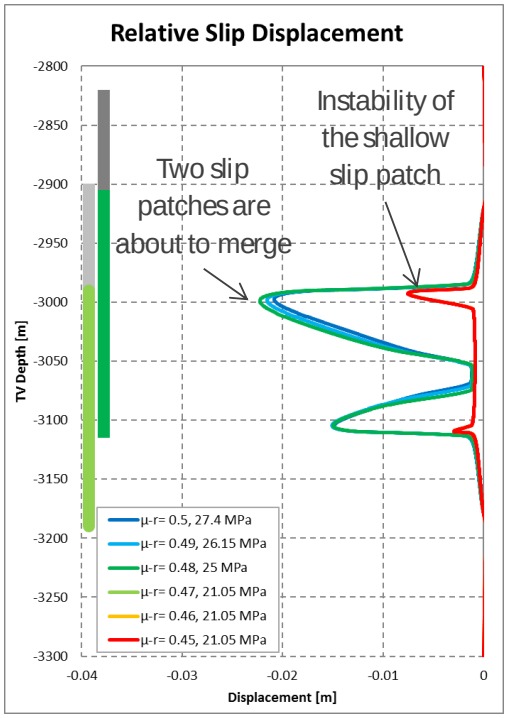

Figure 4.2: *The Relative Slip Displacement (RSD) as a function of depth along the fault plane at the onset of seismic rupture. The residual friction coefficient and the reservoir depletion is indicated in the legend.*

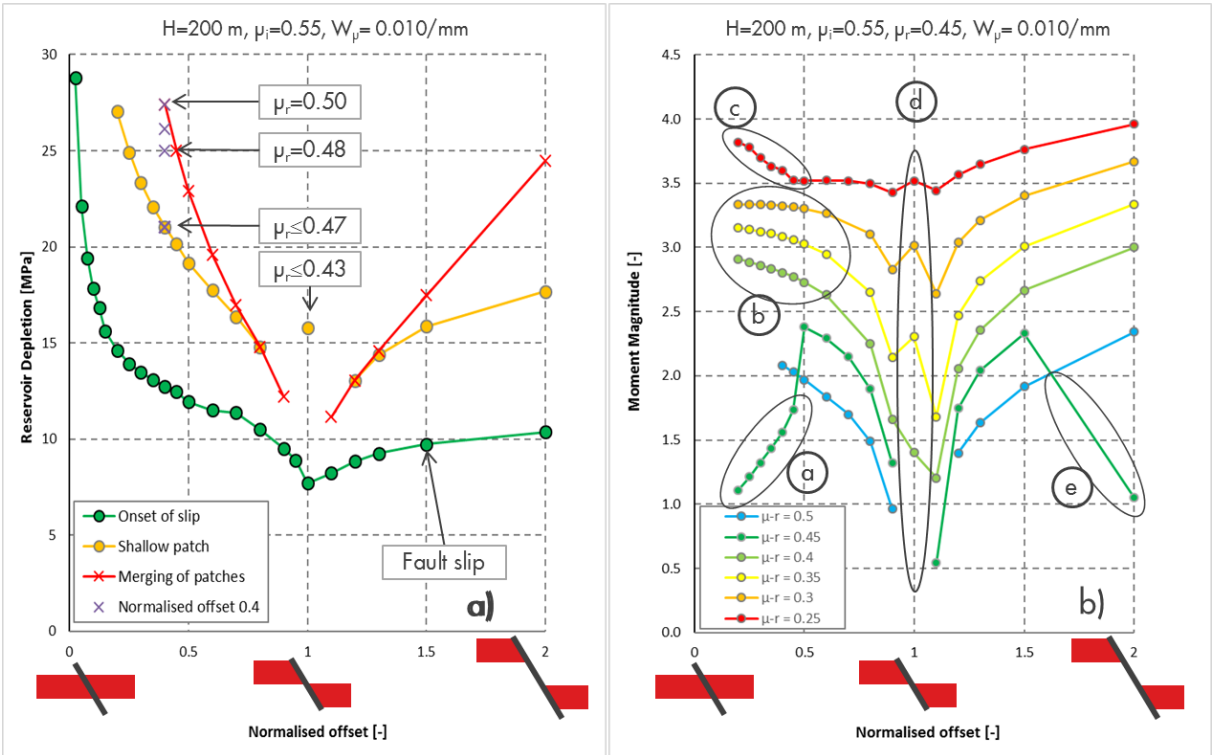

Figure 4.3: *a) Reservoir depletion at the onset of fault slip (green line), and the onset of seismic rupture for μ_r=0.45 (yellow line, Rupture Mechanism 2 or 3) and μ_r=0.50 (red line, Rupture Mechanism 1) as a function of the normalised reservoir offset. b) moment magnitude as a function of normalised reservoir offset for different values of the residual friction coefficient based on a width to length ratio of 1 for the seismic slip patch.*

For μ_r>0.45, Rupture Mechanism 2 or 3 may not occur in favour of Rupture Mechanism 1 (merging of two slip patches) irrespective of the normalised offset. Instability of the shallow slip patch occurs if the RSD reaches the critical slip displacement D_c somewhere on the slip patch. This implies that the residual friction coefficient μ_r is reached and that fault instability and seismic rupture is suppressed (APPENDIX 5 and APPENDIX 6). This also means that fault slip is accommodated a-seismically while increasing reservoir depletion. Figure 4.2 shows much larger and almost merging slip patches for cases with $\mu_r \geq 0.48$. Also, the RSD is much larger, and larger than D_c for each case. The reservoir depletion at the onset of seismic rupture associated with these cases ($\bar{O}$ =0.4) is represented by the crosses in Figure 4.3a. The red line represents the depletion pressure at the onset of seismic rupture for cases with μ_r = 0.50, which all exhibit Rupture Mechanism 1. The threshold value for the residual friction coefficient that marks the transition between Rupture Mechanism 2/3 and Rupture Mechanism 1 is provided in Figure A7.17 of APPENDIX 7.

The following observations are made from Figure 4.3b showing the influence of the normalised reservoir offset and the residual friction coefficient on the moment magnitude:

a. A relatively small moment magnitude is calculated for cases with μ_r=0.45 and $\bar{O}$ <0.5, because the slip patches do not merge (Rupture Mechanism 2).
b. Merging of the slip patches occurs for $\mu_r \leq 0.40$ and $0.20 \leq \bar{O} \leq 0.45$ (Rupture Mechanism 3), resulting into a significantly larger moment magnitude.
c. The rupture extends into the overburden and basement for μ_r=0.25 and $\bar{O} \leq 0.45$ (Figure 3.11). A larger offset implies a larger distance between the overburden and basement formations that provide a barrier for rupture propagation (APPENDIX 6), and explains why the moment magnitude is fairly constant for $0.5 \leq \bar{O} \leq 1.0$.
d. The single slip patch generated for $\bar{O}$ =1 becomes unstable at 15.8 MPa depletion if $\mu_r \leq 0.43$ (Figure 4.3a). A larger residual friction coefficient does not lead to fault instability. The moment magnitude increases for smaller values of the residual friction coefficient. Strictly speaking, these cases exhibit Rupture Mechanism 2.
e. Additional cases are required to establish the transition between rupture Mechanism 2 and 3 and associated moment magnitude for μ_r=0.45 and $\bar{O}$ >1.5. A mirrored trend is expected as described under note a.

4.3. Reservoir thickness

A previous study (van den Bogert, 2015) demonstrated that the onset of *fault slip* is a function of the normalised offset, rather than absolute offset. This section addresses the influence of the normalised offset on the onset of *seismic rupture* by considering a reservoir thickness of 170 and 230 m. The cases discussed in section 4.1 are repeated for a normalised offset between 0 and 0.6. All other parameters are identical to the Base Case (case mu55-182, section 3.2 and APPENDIX 3), including the linear slip-weakening relationship given in Figure 3.1b (μ_i=0.55, μ_r=0.45, W_μ=0.01 mm^{-1}). Detailed analysis results are provided in APPENDIX 8.

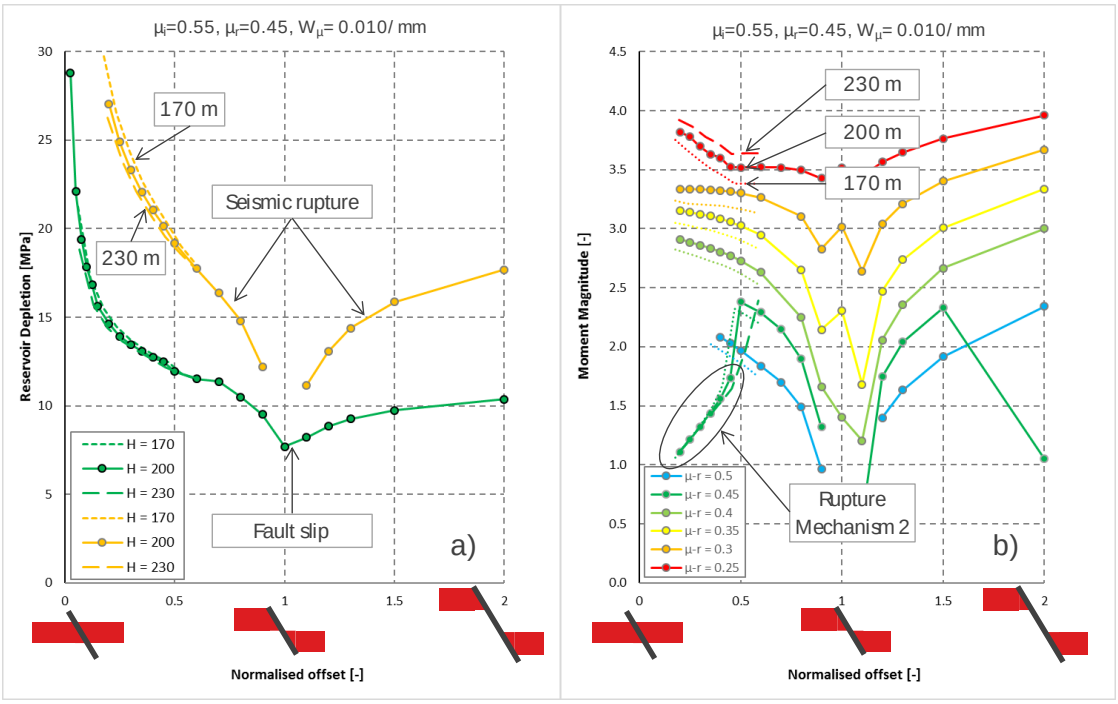

Figure 4.4: *a) Onset of fault slip (green) and onset of seismic rupture (yellow), and b) moment magnitude as a function of normalised reservoir offset Ō for a reservoir thickness of 170 m (short-dashed lines), 200 m (solid lines) and 230 m (long-dashed lines).*

The green lines in Figure 4.4a confirm that reservoir thickness does not influence the *onset of fault slip* for a given normalised offset. The slight difference in depletion pressure for 170, 200 and 230 m thickness is attributed to the somewhat larger depth of the hanging wall – where onset of fault slip occurs – for larger reservoir thickness. The result implies that the shear stress distribution along the fault plane, which is imposed by the reservoir offset, can be scaled with the reservoir thickness.

Close examination reveals that *onset of seismic rupture* for 170 m reservoir thickness (yellow short-dashed line in Figure 4.4a) occurs at slightly larger depletion pressure, and for 230 m thickness (yellow long-dashed line) at a slightly lower depletion pressure compared to 200 m reservoir thickness (yellow solid line). This is explained by the fact that the stress distribution scales with reservoir thickness, but that onset of seismic rupture occurs if a critical length of the slip patch is reached (Figure 4.1). The scaling of the stress distribution implies that the critical stress area and the slip patch length increases with reservoir thickness for the same reservoir depletion, while the critical length of the slip patch is the same for all cases. The depletion level at which a certain critical slip length L_c is reached is therefore reducing with increasing reservoir thickness (APPENDIX 8).

Moment magnitude increases with reservoir thickness for the same normalised offset and fault slip properties for Rupture Mechanism 1 and 3 (Figure 4.4b). The moment magnitude for 170 m reservoir thickness and μ_r =0.25 (red short-dashed line) is smaller, and for 230 m reservoir thickness and μ_r=0.25 (red long-dashed red line) is larger than for 200 m reservoir thickness (red solid line). The same is found for a residual friction coefficient of 0.30, 0.35 and 0.40, which all exhibit Rupture Mechanism 3 (Appendix A.7.3.4). Moment magnitude also reduces with reservoir thickness for cases with μ_r=0.50 (light-blue dashed and solid lines in Figure 4.4b), which exhibit Rupture Mechanism 1. However, the moment magnitude is the same for different reservoir thickness in case of Rupture Mechanism 2, which is characterised by rupture of the

shallow slip patch only. This is found for cases with μ_r =0.45 and $\bar{O}$ < 0.45 (dark-green lines in Figure 4.4b). In these cases, the size of the slip patch and the RSD are identical at the onset of seismic rupture and also the moment magnitude is the same, but the depletion pressure that causes the seismic rupture is reducing with increasing reservoir thickness (APPENDIX 8).

4.4. Slope of the slip-weakening relationship

In section 4.1 (Figure 4.1), it is demonstrated that onset of seismic rupture occurs if the size of the shallow slip patch reaches the critical length L_c. The analytical expression for L_c is dependent on the slope W_μ of the descending branch of the linear slip-weakening diagram as discussed in section 2.2. In this section, the onset of seismic rupture and moment magnitude is discussed for a slope W_μ between 0.01 mm^{-1}, as used in all cases discussed so far, and 0.1 mm^{-1}. The reservoir thickness (200 m) and the initial and residual friction coefficient (0.55 and 0.45 respectively) are the same as in the Base Case (section 3.2). The normalised reservoir offset is varied between 0 and 0.98. This section provides a summary of the detailed evaluations given in APPENDIX 9.

Figure 4.5a shows that the reservoir depletion at the *onset of seismic rupture* reduces, and approaches the depletion at the *onset of fault slip* for an increasing slope W_μ of the linear slip-weakening diagram. The grey line, which represents the reservoir depletion at *the onset of fault slip* for μ_i =0.55, and the blue line for W_μ = 0.01 mm^{-1} are the same as the green and yellow lines in Figure 4.1a respectively. The depletion range between onset of fault slip and onset of seismic rupture is smaller for all values of W_μ if the normalised offset approaches 1. A larger value of W_μ implies a steeper slope in the slip-weakening diagram and allows less a-seismic slip before seismic rupture occurs and yields a more brittle fault slip response. In the extreme case of an infinitely steep slope (D_c=0), seismic rupture occurs at the same reservoir depletion as onset of fault slip.

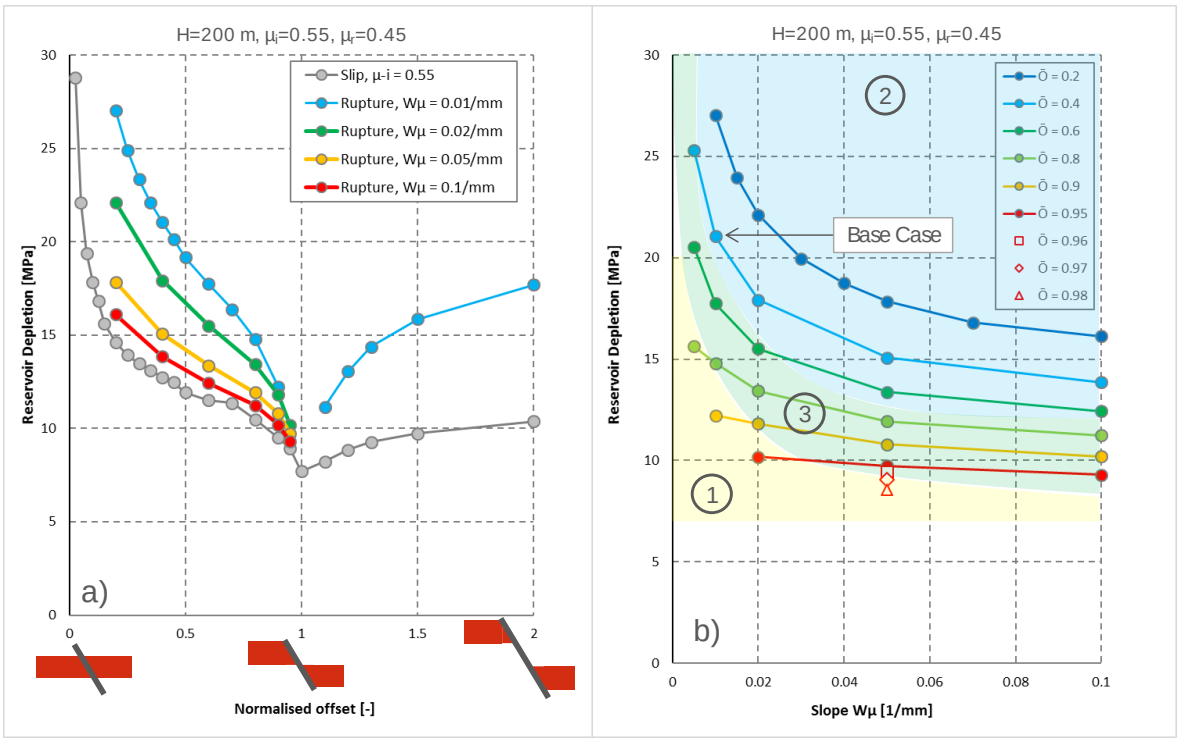

Figure 4.5: *Reservoir depletion at the onset of seismic rupture as a function of normalised reservoir offset (a) and as function of the slope W_μ (b). The background color refers to the simulated rupture mechanism. The Base Case is discussed in section 3.2.*

The influence of W_μ on the rupture mechanism is indicated by the background colour in Figure 4.5b. Rupture Mechanism 2 (blue back ground) is found for $\bar{O}$ = 0.2 (dark-blue line) and all considered values for W_μ (in combination with μ_i =0.55 and μ_r =0.45). For this relatively small normalised offset, the distance between two slip patches is sufficiently large and the reduction of the friction coefficient (μ_i - μ_r) sufficiently small to prevent merging of the slip patches during the seismic rupture. Rupture Mechanism 2 is also found for a larger normalised offset provided that the slope in the slip-weakening diagram is sufficiently steep (i.e. W_μ sufficiently large). This corresponds to relatively brittle fault slip behaviour. For smaller values for W_μ (more ductile fault slip behaviour), the shallow slip patch merges with the deep slip patch at larger depletion pressure (Rupture Mechanism 3) as indicated by the green back ground colour in Figure 4.5b. Rupture Mechanism 3 is prevailing for a normalised offset approaching 1. Rupture Mechanism 1 is found for small values of W_μ or if the normalised offset is close to 1. A small values of W_μ corresponds with ductile fault slip behaviour and a very large critical slip length L_c that prevents the shallow slip patch to become instable, while a normalised offset close to 1 implies that the distance between the two slip patches is so small that merging occurs at a smaller reservoir depletion than instability of the shallow slip patch. Only very brittle fault slip behaviour with a large value for W_μ can cause Rupture Mechanism 2 for $\bar{O} \approx 1$.

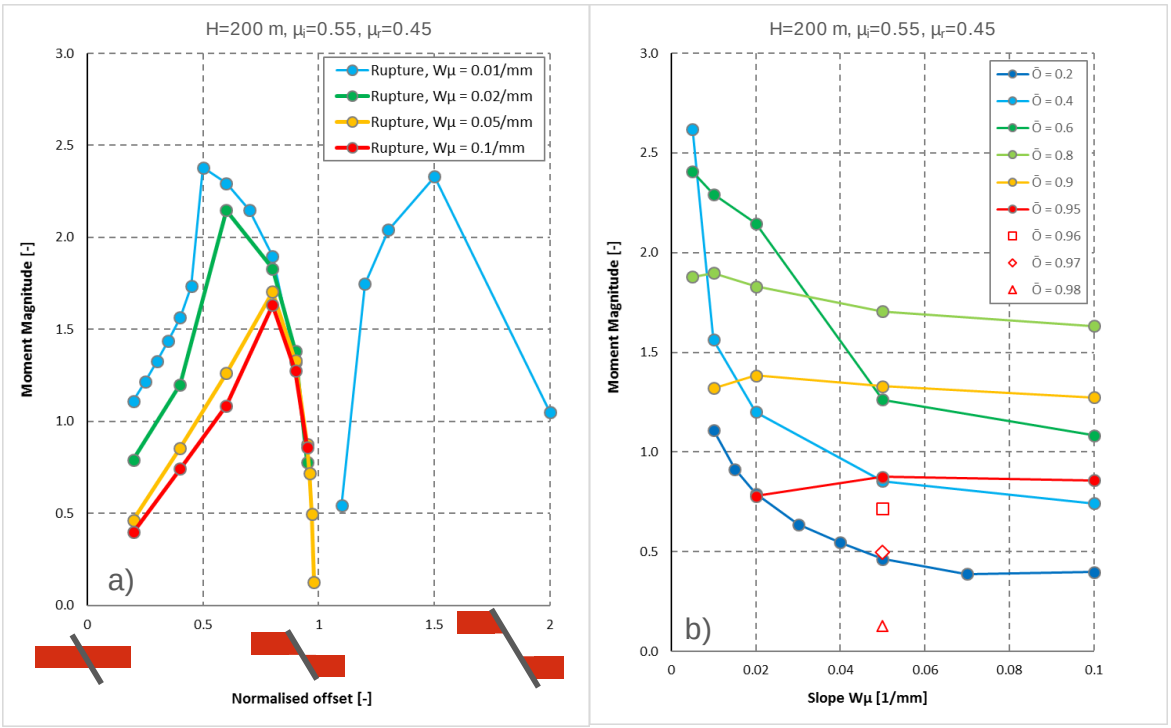

Figure 4.6: *Moment Magnitude a) as a function of normalised reservoir offset, and b) as function of the slope W_μ. Note that b) includes results for W_μ=0.005/mm that are not in a).*

Figure 4.6 shows the results of the same cases as in Figure 4.5, except that the moment magnitude is plotted as function of the normalised offset and the slope W_μ. The light-blue line in Figure 4.6a for W_μ=0.010/mm is the same as the dark-green line in Figure 4.3b. Figure 4.6a shows that the moment magnitude reduces with increasing slope of

the slip-weakening diagram. This is primarily caused by the smaller reservoir depletion at which seismic rupture nucleates for increasing slope W_μ (Figure 4.5a). A smaller reservoir depletion means that less (compaction) strain energy is stored in the reservoir formations, and that less energy is available for seismic rupture (see APPENDIX 12 for the definition of energy balance equation, and Appendix A.3.2 for a discussion on the evolution of all energy component during seismic rupture in the Base Case). The largest moment magnitude for each value of the slope W_μ is found roughly for $0.5< \bar{O} <0.8$ and $1.2< \bar{O} <1.5$ and all exhibit Rupture Mechanism 3.

Figure 4.6b shows that the slope W_μ does not influence the moment magnitude for a normalised offset $0.8\leq \bar{O} \leq 0.98$ as much as for $\bar{O} \leq 0.6$. Figure 4.6a/b also shows that the moment magnitude is smaller for the normalised offset $\bar{O}$ approaching 1. This is consistent with the reservoir depletion in Figure 4.5a which is reducing and converging to the same value for $\bar{O} \rightarrow 1$. All cases exhibit merging of the two slip patches in Rupture Mechanism 1 or 3 (Figure 4.5b) with the slip patch confined to the juxtaposition interval, similar as shown in section 3.1 (APPENDIX 9). The moment magnitude is smaller for $\bar{O} \rightarrow 1$, because i) the juxtaposition interval is smaller, ii) the Relative Slip Displacement after the seismic rupture is smaller, and iii) seismic rupture occurs after a smaller reservoir depletion.

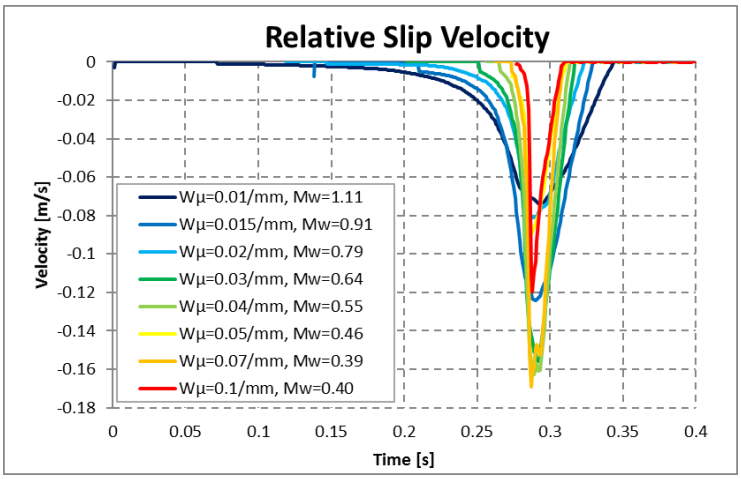

Figure 4.7: *Average relative slip velocity as a function of time (source-time function) for an offset of 40 m ($\bar{O}$ = 0.2) and different values of the slope W_μ (H=200m, μ_i =0.55 and μ_r =0.45). All cases exhibit Rupture Mechanism 2. Time shifts have been applied to align the peak velocity.*

Figure 4.7 shows the source-time function for the cases with an offset of 40 m ($\bar{O}$ = 0.2) and $0.01 \leq W_\mu \leq 0.1$ mm^{-1}. The reservoir depletion at which seismic rupture occurs for the different cases is represented by the dark-blue line Figure 4.5b, and the associated moment magnitude by the dark-blue line in Figure 4.6b. All cases exhibit Rupture Mechanism 2 which means that no merging of the slip patches occurs. It is seen that the slope W_μ of the descending branch of the linear slip-weakening diagram influences the acceleration phase of the seismic rupture. This is reflected by the shorter period required to reach peak velocity after the onset of seismic rupture, which is defined when the average velocity in the source-time function exceeds 0.001 m/s. Also, the deceleration phase after the peak velocity is shorter for an increasing slope W_μ. So, for Rupture Mechanism 2, the duration of the seismic rupture is shorter for increasing value for the slope W_μ. The slope W_μ is the only parameter investigated in this study that influences the duration of the (acceleration phase of the) seismic rupture (APPENDIX 10).

4.5. Scaling relationships

The simulation results of all analyses in this study (APPENDIX 2) have been collected to test relationships between moment magnitude and different response parameters, such as the length of the seismic slip patch (along the fault dip direction, Figure 4.8a) and the Relative Slip Displacement (Figure 4.8b). In the calculation of the moment magnitude (APPENDIX 13) it is assumed that the rupture width w (in the fault strike direction) is equal to the length L_s of the slip patch in dip direction obtained from the 2D simulation results. So, the aspect ratio w/L_s of the seismic slip patch is assumed to be 1. The moment magnitude increase with about 0.2 each time the assumption for the aspect ratio is doubled (see also section 3.4), while it increases with about 0.5 if $w/L_s = 6$ is assumed.

Stock and Smith (2000) conducted a study into the relationship between the length and width of the seismic slip patch and the moment magnitude of more than 550 events. They found that the aspect ratio of the seismic slip patch was similar for all earthquakes in a normal and reverse faulting environment (Figure 4.9), irrespective of their moment magnitude. This was not the case in strike-slip events, as the thickness of the seismogenic layer seems to limit the height of the rupture area in dip direction (referred to as L_s in this study). In a normal faulting environment such as the Groningen field, an aspect ratio w/L_s between 1 and 2 is most common, while $w/L_s > 6$ is hardly observed. This means that the moment magnitude reported this study should be increased by about 0.5 to obtain a realistic upper-bound for the moment magnitude.

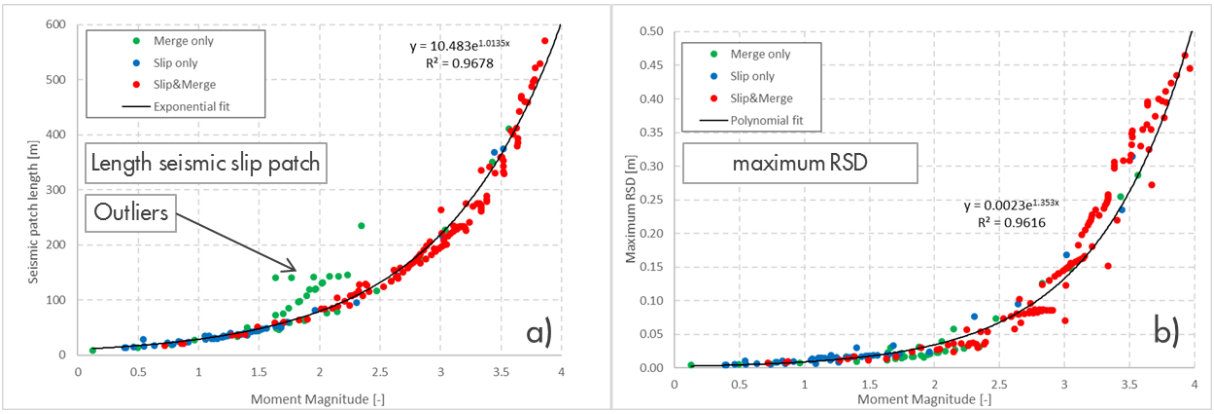

Figure 4.8: *a) The total length of the seismic slip patches and b) the maximum Relative Slip Displacement (RSD) as a function of moment magnitude M_w and rupture mechanism for all cases in this report (APPENDIX 2). Green markers indicates occurrence of Rupture Mechanism 1, blue indicates Rupture Mechanism 2 and red indicates Rupture Mechanism 3.*

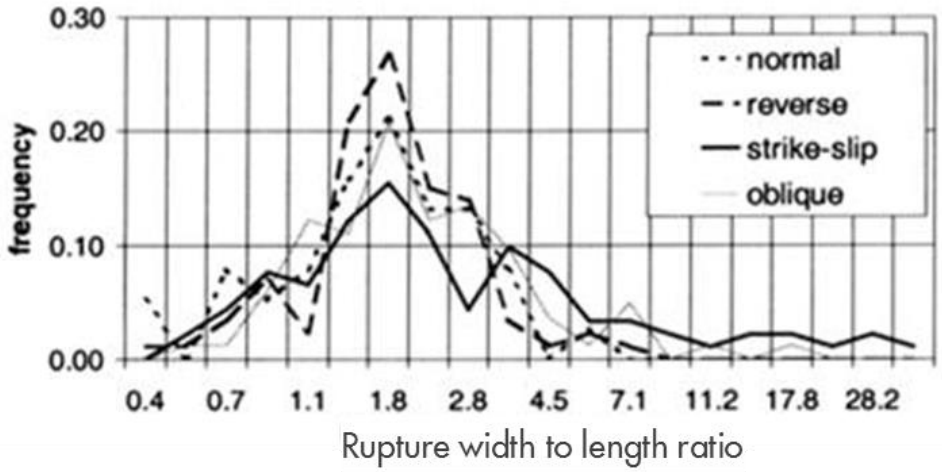

Figure 4.9: Distribution of the seismic patch aspect ratio of earthquakes in different faulting environments (Stock and Smith, 2000).

Each marker in Figure 4.8 shows the result of a single dynamic rupture simulation. The marker colour indicates the simulated rupture mechanism as introduced in section 3.4. These case studies include variations of the residual friction coefficient, the slope W_μ of the slip-weakening relationship, the reservoir thickness and reservoir offset. Other parameters, such as the in-situ stress condition, the fault dip and azimuth angle, the initial friction coefficient, Young's modulus and Poisson's ratio have been addressed in a previous study (van den Bogert, 2015). So, also the shear modulus G, which appears in the expression of the moment magnitude, is the same for all analyses in this study. Different relationships should be expected if parameter values are considered outside the ranges used in this study, in particular for a different value of the shear modulus. The correlations presented in this section and in APPENDIX 11 are valid for the parameter ranges applied in this study.

Moment magnitude, assuming $w/L_s = 1$, remains smaller than 4.0 for all cases in this study with $\mu_r \geq 0.25$ (APPENDIX 2). The largest moment magnitude is found in cases with a small normalised reservoir offset (cases mu55-36, -146, -156, -336, -356, and -366 in APPENDIX 2) or with a large normalised offset (of 1.5 and 2.0 for cases mu55-286 and mu55-296 respectively). A larger moment magnitude is possible for the current fault dip and azimuth angle if $\mu_r < 0.25$ (cases mu55-87, -97, 297 and -298). However, this may result in a progressive seismic rupture (case mu55-298) that does not stop under the current modelling assumptions. These type of seismic events have not occurred in the Groningen field so far, which implies that the reduction of friction coefficient ($\mu_i - \mu_r$) is probably not much larger than (0.55 - 0.25) = 0.30 in most instances. The maximum reduction of the friction coefficient that generates finite seismic rupture is also influenced by the fault orientation, in-situ stress condition and shear modulus.

Figure 4.8 shows that the total length of the slip patches and the RSD adhere quite well to power-law relationships for the cases in this study. Rupture Mechanism 3 tends to generate the largest seismic ruptures and Rupture Mechanism 2 the smallest, but both adhere to the same power-law relationship. The patch size is significantly larger than the correlation function for some cases that exhibit Rupture Mechanism 1, indicated as "outliers". In these cases, seismic rupture occurs over an area where the residual friction coefficient has been reached due to a-seismic slip. This area has a reduced strength and is therefore less effective in arresting the seismic rupture

compared to cases that exhibit Rupture Mechanism 2 or 3, in which the rupture propagates over a fault area with the larger initial friction coefficient.

All cases with $M_w < 3.0$ have a seismic slip patch smaller than about 200 m that remains within the reservoir depth range. The seismic slip patch propagates outside the reservoir bounds for an increasing number of cases with increasing moment magnitude above 3.0. For $M_w > 3.7$, the seismic slip patch propagates outside the reservoir bounds in all cases evaluated in this study. In these cases, the seismic slip patch is larger than about 460 m in dip direction of the fault, and an equal size along strike of the fault ($w/L_s = 1$). These moment magnitude bounds should be increased by 0.5 if $w/L_s = 6$ is assumed. The modelling assumptions and parameter values used in this study are not calibrated against Groningen field data, so that no conclusions can be drawn at this stage whether or not the seismic slip patch propagates outside the reservoir bounds for observed seismic events with $M_w > 3.7$. In-situ stress contrasts between reservoir and overburden and basement, which are not incorporated in the current study, may redirect propagation of the seismic slip patch along the strike direction of the fault rather than the dip direction considered here. Also, a different value for the shear modulus is expected to change the resulting moment magnitude reported in this study. The correlation functions (APPENDIX 11) should therefore be treated with great care, in particular when parameter values are used outside the ranges in this study.

5. Interpretation

In this study, the influence of the normalised reservoir offset (section 4.1), the residual friction coefficient (section 4.2), the reservoir thickness (section 4.3), and the slope of the descending branch of the linear slip-weakening diagram (section 4.4) on the simulated seismic rupture has been investigated. The results can be separated into two categories: one about the *conditions* under which seismic rupture occurs, and one about the *characteristics* of the simulated seismic rupture. Three findings fall into the first category:

- Reservoir offset strongly influences the onset of fault slip and also the onset of seismic rupture (Figure 4.5a). Reservoirs with a normalised offset of about 1 are most prone to fault slip and seismic rupture, while reservoirs with a small normalised offset ($\bar{0} < 0.2$) sustain a significantly larger reservoir depletion before onset of seismic rupture occurs (assuming the same in-situ stress and fault slip properties). Onset of fault slip is also influenced by the initial friction coefficient μ_i and the orientation of the fault (dip and azimuth angle) relative to the assumed in-situ stress condition (van den Bogert, 2015).
- The slope of the descending branch of the linear slip-weakening diagram W_μ strongly influences the onset of seismic rupture (Figure 4.5a). A steeply descending branch (large value for W_μ) causes individual slip patches to become unstable at a relatively small size, which means that seismic rupture follows onset of fault slip after a small incremental reservoir depletion. This is referred to as relatively brittle failure behaviour. Inversely, a gently descending branch requires a larger a-seismic slip patch and a larger incremental reservoir depletion to cause seismic rupture, and is referred to as a ductile response. Seismic rupture does not occur if the size of the a-seismic slip patch is larger than the length of the juxtaposition interval. Also, seismic rupture cannot occur if the depletion pressure for seismic rupture is larger than the initial reservoir pressure. This is most relevant for reservoirs with small normalised offset ($\bar{0} < 0.2$).
- The size of the slip patch at the onset of seismic rupture obtained from the dynamic rupture simulations corresponds well with the analytical expression derived by Uenishi and Rice (2003). The simulation results are less than 10% smaller than the analytical values (APPENDIX 7).

Five other findings relate to the character of the simulated seismic rupture, namely

- All simulated seismic ruptures conducted in this study (APPENDIX 2) can be classified into three rupture mechanisms:
  1. *Merging of the two slip patches* is the root cause of seismicity if the slip patches are relatively close (e.g. if reservoir offset is about equal to the reservoir thickness, Figure 4.1, or in case of a relatively thin depleting reservoir), if the slope in the slip-weakening diagram is not so steep (e.g. in case of rather ductile fault gouge material, Appendix A.9.1) or if the reduction in frictional strength is limited (difference between initial and residual friction coefficient (μ_i - μ_r) is small, Appendix A.6.2).
  2. *Instability of a single slip patch* occurs if the slip patches are sufficiently spatially separated (e.g. locations with limited reservoir offset, Figure 4.1), if the slope in the slip-weakening diagram is sufficiently steep (in case of brittle fault gouge material, Appendix A.9.1) and/or the reduction in frictional strength (μ_i - μ_r) is sufficiently large (Appendix A.6.3).

3. *Instability of a single slip patch and merging with an adjacent slip patch* occurs if the two slip patches are not sufficiently separated (because of reservoir offset, Figure 4.1) or if the reduction in frictional strength is relatively large (Appendix A.6.4).

   This study has demonstrated that any of the three rupture mechanisms can occur on any fault configuration by selecting appropriate fault slip parameters. However, fault slip parameters can be significantly constrained if actual seismic events can be located on known natural faults and if the associated rupture mechanism can be identified.

- The source-time function has distinctively different characteristics for each rupture mechanism, which may provide the opportunity to identify the rupture mechanism of observed seismic events in the Groningen field. The slope W_μ of the descending branch of the linear slip-weakening relationship is the only parameter in this study that influences the acceleration of the slip velocity in the source-time function (section 4.4 and APPENDIX 10). Again, this may provide the opportunity to estimate the slope W_μ from observed seismic events by comparison of actual and simulated wave forms.
- A seismic rupture with a moment magnitude in the range between M_w=0.5 and M_w=4.0 can be generated by any of the rupture mechanisms, albeit that Rupture Mechanism 2 tends to generate events with a somewhat smaller moment magnitude, whereas Rupture Mechanism 3 tends to generate the largest seismic event for similar fault properties (Figure 3.15 and Figure 4.4). Seismic ruptures with M_w < 3.0 have a rupture length (along fault dip) smaller than 200 m and remain contained within the reservoir depth range, whereas all ruptures with M_w > 3.7 extend outside the reservoir bounds. The moment magnitude mentioned in this study, which is based on an aspect ratio of the seismic slip patch w/L_s = 1, should be increased by 0.5 if a realistic maximum w/L_s = 6 is considered.
- A slip patch is stabilised if the residual friction coefficient is reached (section 3.5 and APPENDIX 5). This is found for a-seismic as well as seismic slip patches. Seismic slip requires a reduction of the friction coefficient, which is not the case if the residual friction coefficient is reached for RSD > D_c. A seismic rupture is decelerating as soon as the residual friction coefficient is reached somewhere on the seismic slip patch. The reduction of the friction coefficient (μ_i - μ_r) influences the moment magnitude of the seismic rupture (APPENDIX 11). Seismic rupture is suppressed if the residual friction coefficient is reached on an a-seismic slip path. Seismic rupture may still occur by merging of the two slip patches at an elevated depletion pressure (Appendix A.6.2).
- The size of the seismic slip patch and the maximum relative slip displacement adhere to a power-law relationship with the moment magnitude for 0.5 < M_w < 4.0 (with w/L_s = 1) irrespective of the rupture mechanism (section 4.5 and APPENDIX 11).

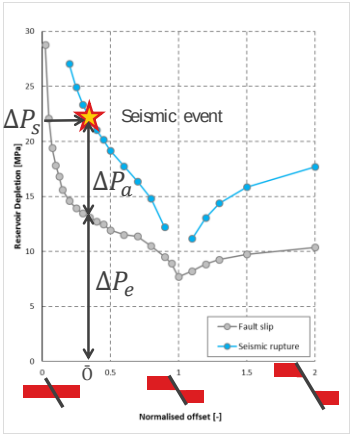

Figure 5.1: *The reservoir depletion $\boldsymbol{\Delta P_s}$ at the occurrence of every observed seismic event can be decomposed into a component $\boldsymbol{\Delta P_e}$ that is causing reversible, elastic displacement along the fault plane, and a component $\boldsymbol{\Delta P_a}$ that is causing a-seismic slip. The normalised reservoir offset can be taken from the subsurface model at the interpreted seismic event fault location.*

The parameters in the linear slip-weakening relationship (μ_i, μ_r and W_μ) can be constrained by seismic events in the Groningen field using these findings. Seismic events in the Groningen field are located with increasing confidence on known, natural faults, due to improved monitoring and interpretation techniques (Willacy et al., 2018), while enhanced geological interpretation is instrumental in providing the fault orientation and reservoir thickness and offset more accurately. This allows estimating the normalised reservoir offset at the seismic event location. The dynamic reservoir model of the field, calibrated against decades of production data, provides a relatively good estimate of the local reservoir depletion at the time of each seismic event. So, every observed seismic event that can be located on a known natural fault provides the normalised reservoir offset $\bar{O}$ and the depletion pressure ΔP_s at which seismicity occurs (Figure 5.1). This depletion pressure can be separated into two parts:

$$\Delta P_s = \Delta P_e + \Delta P_a,$$

with ΔP_e the depletion pressure that accommodates deformation along the fault plane elastically and leads to onset of fault slip, and ΔP_a the depletion pressure that induces a-seismic fault slip and leads to seismic rupture. In this study, the slope W_μ is found to be the only parameter that influences ΔP_a, while various parameter influence ΔP_e, such as the initial friction coefficient, Poisson's ratio of the reservoir formation, the initial stress condition and the fault orientation. The fault dip and azimuth can be constrained by the improved geological interpretations, whereas Poisson's ratio is available from lab experiments and from reservoir compressibility obtained by subsidence inversion. The total stress $\underline{S_0}$ at virgin reservoir condition and the initial friction coefficient are the main factors influencing ΔP_e at a given fault event location. So,

$$\Delta P_s = \Delta P_e\left(\underline{S_0}, \mu_i\right) + \Delta P_a\left(W_\mu\right). \tag{5.1}$$

Herein, $\underline{S_0}$ describes the initial stress condition, taking into account the total vertical stress S_v, the total maximum and minimum horizontal stress S_H and S_h respectively, the maximum horizontal stress azimuth ψ_H and the initial reservoir pore pressure P_p. Again, the initial vertical stress and pore pressure are well constrained by field data, but the magnitude and orientation of the horizontal stress components are considered most

variable and uncertain across the Groningen field (van Eijs, 2015). Using the current understanding of the initial stress in the Groningen field (Van Eijs, 2015) in expression (5.1), a relationship between the initial friction coefficient μ_i and the slope W_μ can be formulated at every seismic event location with known fault orientation and reservoir offset. Assuming a larger value for the slope W_μ – for instance – would reduce ΔP_a and would imply a larger value for the initial friction coefficient to increase ΔP_e. Multiple seismic events recorded in close vicinity could provide information on the variability of the fault friction parameters, but could possibly also provide constraints for the initial stress condition $\underline{S_0}$.

The absence of seismic events at a particular reservoir depletion pressure also provides constraints for the slip-weakening parameters. Absence of seismic events may be explained by:

i) a sufficiently large value for the initial friction coefficient,
ii) a relatively small reduction of the friction coefficient (μ_i - μ_r), or
iii) a small value for W_μ so that the critical slip length L_c is larger than the reservoir thickness.

The fault slip properties vary across the Groningen field and are part of the explanation why – to date – seismic events are observed in particular locations and why not in other locations.

The residual friction coefficient μ_r in the linear slip-weakening relationship can be constrained from the moment magnitude of observed seismic events. However, moment magnitude is not only dependent on geometrical properties such as the normalised reservoir offset and thickness (Figure 4.4), but also on the fault friction properties W_μ (Figure 4.6) and the initial friction coefficient μ_i. The residual friction coefficient is therefore best constrained after developing the relationship between μ_i and W_μ as outlined above, and expressed relative to the friction coefficient (μ_i - μ_r). The Rupture Mechanism, which influences the moment magnitude (Figure 4.3), is not an independent parameter as it is impacted by the fault friction parameters.

Expression (5.1) and the insights developed in this study could be used in a stochastic approach as followed by Dempsey and Suckale (2017) to forecast future seismicity in the Groningen field. This should include constraining the parameters in the linear slip-weakening relationship (μ_i, μ_r and W_μ) based on observed seismic events for different parts of the field (as field data permits). A fast algorithm that can compute the onset of seismic rupture for any fault orientation, reservoir offset and thickness, and fault friction parameters would be an important requirement for such an approach. An analytical solution would be best suited for this purpose. Possibly, the analytical solution developed by Nowacki (1986) and employed by Lehner and Leroy (1995) could be adjusted to calculate the normal and shear stress distribution along an arbitrarily oriented fault plane. Further work would be required to evaluate this option.

The distinctly different character of the source-time function may provide an opportunity to associate a particular rupture mechanism to an observed seismic events in the Groningen field. Also, the slope W_μ of the linear slip-weakening diagram has a clear impact on the source-time function (Figure 4.7). Determination of the rupture mechanism and calibration of W_μ from event data would also reduce uncertainty of the initial friction coefficient as discussed above. However, the current two-dimensional modelling approach includes a number of limitations that may hamper a successful outcome, such as

i) the size of the seismic slip patch along the strike of the fault is not taken into account,
ii) only wave forms perpendicular to the fault are simulated,
iii) reflections by normal and shear wave velocity contrasts are not taken into account.

Three-dimensional dynamic rupture simulations can resolve some of these limitations, but is computationally expensive. The opportunity to constrain or possibly calibrate the slope W_μ from recorded wave form data would increase the reliability of all frictional parameters, because it would be obtained from an independent data source. Identification of a seismic event's rupture mechanism would provide insight into the local stress condition of the fault, and would enable building hypotheses of future seismic events on the same location or elsewhere in the Groningen field. For these reasons, it would be worth further investigating the impact of the Rupture Mechanism and the fault friction properties on the recorded wave forms.

6. Conclusions

The in-depth evaluation of the large number of dynamic rupture simulations leads to the following conclusions:

- In-house technology and expertise is developed to simulate depletion-induced seismic events along fault planes in 2D with realistic duration and moment magnitude under realistic conditions using commercially available software. The impact of fault slip parameters on the depletion level at which seismic rupture occurs, as well as the moment magnitude has been quantified.
- Complex fault slip responses are found even when using relatively simple two-dimensional geomechanical models:
  - The subsurface is a homogenous linear-elastic half-space, incorporating a horizontal homogenously depleting reservoir with offset.
  - The fault is straight and behaves according to a Mohr-Coulomb friction law with linear slip-weakening relationship.
  - Three different rupture mechanisms are found with distinctly different characteristics, which may be recognisable in actually observed seismic events.
- The complex fault slip responses found in the dynamic rupture simulations provide support to the strategy of incorporating more realistic modelling assumptions one-by-one (e.g. non-linear and time-dependent behaviour of formations). This strategy should be continued in potential further work.
- Seismic rupture may occur by instability of a single slip patch or by merging of two a-seismic slip patches. In particular,
  - seismic rupture nucleates at a single slip patch if its size exceeds a critical length L_c which adheres to the analytical expression derived by Uenishi and Rice (2003)
  - seismic rupture may also occur by merging of two slip patches generating seismic events with larger moment magnitude than events caused by rupture of a single a-seismic slip patch.
  - the size of the seismic slip patch and the maximum relative slip displacement for seismic events in the Groningen field can be estimated from observed moment magnitude, because all three rupture mechanisms adhere to the same scaling rules (for the parameters considered in this study).
- Seismic rupture is preceded by a-seismic slip in all cases evaluated in this study. The slip-weakening relationship and the reservoir offset influences the incremental depletion ΔP_a required to bring the fault to seismic rupture. The larger the incremental reservoir depletion, the more ductile the structural response to reservoir depletion.
- The reservoir depletion at which seismic rupture occurs is strongly influenced by
  - the normalised reservoir offset (absolute reservoir offset divided by reservoir thickness), as well as
  - all three parameters of the linear slip-weakening relationship (initial and residual friction coefficient μ_i and μ_r respectively, and the slope W_μ).
- A fault- and stress-based seismological model for the Groningen field can be developed that
  - may explain the spatial differences between observed and predicted seismic activity rate in the Groningen field by different slip-weakening behaviour along the faults across the field.

- derives the parameters of the linear fault slip-weakening relationship from observed seismic events, which are mapped on interpreted natural faults.

7. Recommendations

Based on the results and insights developed in this study, it is recommended to

- develop a fault-based seismological model using the fault location and moment magnitude of historical seismic events in the Groningen field. Also, deployment of the analytical solution provided by Nowacki (1986) for a fast representation of the relationships provided in Figure 4.4 and Figure 4.5 should be investigated. If so, a stochastic approach as used by Dempsey and Suckale (2017) could be pursued providing probabilistic assessment of future seismic events in the Groningen field.
- investigate if the three different rupture mechanisms found in this study can be identified in recorded wave forms of actual seismic events in the Groningen field. This includes investigating the impact of various assumptions and limitations underlying the current dynamic rupture simulations, such as the 2D character of the current study and the representation of seismic events by a single source-time function. Three-dimensional analysis should be considered to evaluate wave forms arriving at an azimuth angle with the fault plane, and multiple source-time functions should be considered in particular to capture the complexity of the source found for Rupture Mechanism 3.
- investigate if the slope W_μ in the linear slip-weakening relationship can be constrained from recorded seismic wave forms. This would provide an independent source for calibrating one of the fault friction parameters and also increases the reliability of the values estimated for the other friction parameter. This work can be done as part of the investigations mentioned under the previous point.
- conduct similar dynamic rupture simulations in 3D to evaluate the impact of various geometrical and property anisotropies along strike direction of a fault. Particular attention should be paid to the factors that influence the aspect ratio at the seismic slip patch.

The results of this study also provide recommendations for projects in which fault slip stability is evaluated for other purposes than the assessment of the seismic hazard:

- The two-dimensional analysis capability developed as part of this study should be employed instead of
  - a Mohr-circle analysis to advise on the reservoir depletion that causes onset of fault slip and onset of seismic rupture (see also Van den Bogert, 2015).
  - three-dimensional finite-element techniques to assess fault stability in field studies. It is demonstrated that fault slip and seismic rupture are caused by steep shear stress gradients at the boundaries of depleting (and inflating) reservoir formations, which are not captured by the coarse element meshes commonly used in 3D field studies. The most efficient and reliable approach is to obtain the most critically stressed locations using a conventional 3D field model, and evaluate fault slip, and if needed also seismic rupture, using the 2D capability developed as part of this study, incorporating the required non-linear behaviour and small element size.

8. Acknowledgements

This project was not feasible without the continuous support from Jan van Elk and Dirk Doornhof (NAM) in many ways. In particular the trust and space provided to develop new technologies and insights in this complex subject, without the certainty of a positive outcome is much appreciated. Special thanks goes to Rob van Eijs (NAM) for the constructive and challenging discussions, which helped to get the best out of this project. Clemens Visser, Jyotirmoy Mallik, Jose Viota and Ide van der Molen of NAM and Pascal Richard and Peter Swaby (Shell Global Solutions) are thanked for their support in developing the Groningen fault model. Furthermore, I thank Rick Wentinck, Roger Yuan, Peter Schutjens and Nicolas Hummel for their discussions and constructive feedback during the project and their in-depth review of the report. Also, the discussions with Alexander Droujinine, Steve Oates, Sara Minisini, Chris Willacy in Shell, and Loes Buijze and Chris Spiers in University of Utrecht are acknowledged. Furthermore, Diana FEA is thanked for their support conducting the dynamic rupture simulations.

References

Aki, K. and Richards, P.G. *Quantitative Seismology* (2002), 2nd Edition.. University Science Books, Sausalito, California, USA.

Barton, N., and Bandis, S. (1980). *Some Effect of Scale on the Shear Strength of Joints.* Int.. J. Rock Mech. Min. Sci. and Geomech. Abstr., Vol. 17, pp. 69-71.

Bourne, S.J., Oates, S.J., van Elk, J. and Doornhof, D. (2014), *A seismological model for earthquakes induced by fluid extraction from a subsurface reservoir*. Journal of Geophysical Research: Solid Earth, Vol. 119, pp 8991-9015.

Bourne, S. J., Oates, S. J., Bommer, J. J., Dost, B., van Elk, J. and Doornhof, D. (2015). *A Monte Carlo Method for Probabilistic Hazard Assessment of Induced Seismicity due to Conventional Natural Gas Production*. Bulletin of the Seismological Society of America, 105(3), pp. 1721-1738.

Bourne, S. J., and Oates, S. J. (2017). *Extreme threshold failures within a heterogeneous elastic thin sheet and the spatial-temporal development of induced seismicity within the Groningen gas field*. J. Geophysical Research: Solid Earth, 122. https://doi.org/10.1002/2017JB014356

Buijze, L., Orlic, B., Wassing, B.B.T. (2015), *Modelling fault rupture in a depleting gas field*. Report TNO project report 2015 R10844, November 2015.

Candela, T., Renard, F., Schmittbuhl, J. Buchon, M., Brodsky, E.E., (2011), *Fault Slip Distribution and Fault Roughness*. Geophys. J. Int., Vol. 187, pp. 959-968.

Cappa, F., and Rutqvist, J. (2011), *Impact of CO2 geological sequestration on the nucleation of earthquakes*. Geophysical Research Letters, Vol. 38, L17313.

Cappa, F., and Rutqvist, J. (2012), *Seismic Rupture and Ground Acceleration Induced by CO2 injection in the shallow crust*. Geophys. J. Int., Vol. 190, pp. 1784-1789.

de Borst, R. (1986), *Non-linear Analysis of Frictional Materials.* Dissertation. Delft University of Technology, Delft.

de Borst, R. (1987), *Computation of post-bifurcation and post-failure behaviour of strain-softening solids.* Computers and Structures, Vol. 25, pp. 211-224.

Diana FEA bv, Finite-Element Program and User Documentation, version 10.1, 2016, https://dianafea.com/manuals/d101/Diana.html

Di Torro, G., Han, R., Hirose, T., De Paola, N., Nielsen, S., Mizoguchi, K., Ferri, F. Cocco, M. And Shimamoto, T. (2011), *Fault Lubrication during Earthquakes*, Nature, Vol. 471, pp 494-499, doi:10.1038/nature09838

Dost, B., Goutbeek, F. Van Eck, T., Kraaijpoel, D. (2012), *Monitoring induced seismicity in the North of The Netherlands: status report 2010*. KNMI Scientific report WR 2012-03. Available at www.knmi.nl

Dost, B., Ruigrok, E. and Spetzler, J. (2017), *Development of seismicity and probabilistic hazard assessment for the Groningen gas field*. Netherlands Journal of Geoscience – Geologie en Mijnbouw, Vol. 96, Nr. 5, pp 235-245.

Fjaer, E., Holt, R.M., Horsrud, P., Raaen, A.M. and Risnes, R. (2008). *Petroleum related rock mechanics*, 2nd edition. Elsevier. Dev. in Petroleum Science.

Geertsma, J. (1973), *Land subsidence above compacting oil and gas reservoirs*, J. Petrol. Technology, Vol. 25, pp. 734-744.

Glab, M. and Van Eijs. R (2001), *Localisation of Sensitive Reservoir Settings for Induced Seismicity using FEM*, Report TNO-NITG 00-320-A

Grasso, J.-R. (1992). *Mechanics of seismic instabilities induced by the recovery of hydrocarbons*. Pure and Applied Geophysics, Vol. 139, No. 3-4, pp. 507-534.

Hager, B.H. and Toksöz, M.N. (2008) *Technical review of Bergermeer seismicity study – TNO report 2008-U-R1071/B*. Dept. of Earth, Atmospheric and Planetary Sciences, Massachusetts Institute of Technology, Cambridge, MA 02139, USA.

Harris, R.A., Barall, M., Archuleta, R. Dunham, E., Aagaard, B., Ampuero, J.-P., Templeton, E. (2009), *The SCEC/USGS Dynamic Earthquake Rupture Code Verification Exercise*. Seismological Research Letters, Vol. 80, nr. 1, pp. 119-126

Hill, R. (1959), *Some basic principles in the mechanics of solids without a natural time*. J. Mech. Phys. Solids, Vol. 7, pp. 209-225

Hughes, T.J.R. (1987), *The Finite-Element Method; Linear static and Dynamic Finite Element Analysis*. Prentice-Hall Int.

IEAGHG (2015), *Criteria of Fault Geomechanical Stability During a Pressure Build-up*. Techincal Report, April 2015, International Energy Agency Environmental Projects Ltd. (IEAGHG), Cheltenham, U.K.

Kanamori, H. (2001*), Energy budget of earthquakes and seismic efficiency*, Chapter 11 in Earthquake Thermodynamics and Phase Transformation in the Earth's Interior, Academic Press.

Klose, C.D. (2012*), Mechanical and statistical evidence of the causality of human-made mass shifts on the earth's upper crust and the occurrence of earthquakes*, J. Seismology, Vol. 17, pp. 109-135

Lehner, F.K. and Leroy, L. (1995), *On the possibility of fault reactivation in and around the Eleveld field*. Report RKGR.95.009, Shell Global Solutions International B.V.

Madariaga, R. and Olsen, K.B. (2002*), Earthquake Dynamic*, Chapter 12 in Int. Handbook of Earthquake and Eng. Seismology, Vol. 81A, Int'l. Assoc. Seismol. and Phys. Earth's Interior.

Mulders, F.M.M. (2003*), Modeling of stress development and fault slip in and around producing gas reservoirs*, Ph.D. thesis, Delft University of Technology

NAM (2016a), *Technical Addendum to the Winningsplan Groningen 2016, Part III, Hazard (Chapter 7),* Report EP201604259068, https://www.nam.nl/feiten-en-cijfers/onderzoeksrapporten.html#iframe=L2VtYmVkL2NvbXBvbmVudC8/aWQ9b25kZXJ6b2Vrc3JhcHBvcnRlbg

NAM (2016b), *Study and Data Acquisition Plan Induced Seismicity in Groningen, Update post-winningsplan 2016, Progress and Schedule*. Report EP201611206224 , https://www.nam.nl/feiten-en-cijfers/onderzoeksrapporten.html#iframe=L2VtYmVkL2NvbXBvbmVudC8/aWQ9b25kZXJ6b2Vrc3JhcHBvcnRlbg==

NAM (2018), https://www.nam.nl/english-information.html

Nowacki, W. (1986), *Thermoelasticity,* 2nd Edition, PWN – Polish Scientific Publishers, Warsaw, Pergamon Press, Oxford, pp. 539.

Orlic, B. and Wassing, B.B.T. (2012*), Modeling stress development and fault slip in producing hydrocarbon reservoirs overlain by rock salt caprocks*, ARMA 12-145, 46th US Rock Mechanics / Geomechanics Symposium, Chicago, Il, USA, 24-27 June 2012.

Pijnenburg, R.P.J., Verberne, B.A., Hangx, S.J.T., and Spiers, C.J. (2018). *Deformation behavior of sandstones from the seismogenic Groningen gas field: Role of inelastic versus elastic mechanisms*. Journal of Geophysical Research: Solid Earth, 123. https://doi.org/10.1029/2018JB015673

Pruiksma, J.P., Breunese, J.N., van Thienen-Visser, K., de Waal, J.A. (2015), *Isotach formulation of the rate type compaction model for sandstone*. Int. J. Rock Mech. & Min. Sci., Vol. 78, pp 127-132

Roest, J.P.A., Kuilman, W. (1994), *Geomechanical analysis of small earthquakes at the Eleveld gas reservoir. SPE 28097, SPE/ISRM Rock Mechanics in Petroleum Eng. Conference, Delft, The Netherlands, 29-31 August 1994*.

Riks, E. (1979), *An incremental approach to the solution of snapping and buckling problems*. Int. J. Solids & Structures, Vol. 15, pp. 529-551.

Ripperger, J., Ampuero, J.-P., , Mai, P.M., and Giardini, D. *(2007). Earthquake Source Characteristics from Dynamic Rupture with Constrained Stochastic Fault Stress*. Journal of Geophysical Research, 112.

Rots, J.G. and de Borst, R. (1989), *Analysis of Concrete Fractuer in "Direct" tension*. Int. J. Solids & Structures, Vol. 25, No. 12, pp. 1381-1394.

Rutqvist, J., Rinaldi, A.P., Cappa, F., and Moridis, G.J. *(2013). Modelling of fault reactivation and induced seismicity during hydraulic fracturing of shale-gas reservoirs.* J. Petroleum Sci. and Eng., Vol. 107, pp. 31-44.

Sanz, P.F., Lele, S.P., Searles, K.H., Hsu, S.-Y., Garzon, L., Burdette, J.A., Kline, W.E., Dale, B. A., and Hector, P.D. (2015), *Geomechanical Analysis to Evaluate Production-Induced Fault Reactivation at Groningen Gas Field*. SPE-174942-MS, SPE Annual Technical Conference and Exhibition, Houston, Texas, USA, 28-30 September 2015.

Santarelli, F.J., Tronvoll, J.T., Svennekjaer, M., Skeie, H., Henriksen, R. and Bratli, R.K. (1998), *Reservoir stress path: The depletion and the Rebound*. SPE/ISRM 47350, Eurock '98 Conference, Trondheim (Norway), 8-10 July 1998.

Scholz, C.H. (1998), *Earthquakes and Friction Laws*. Nature, Vol. 391, pp. 37-41.

Scholz, C.H. (2002), *The Mechanics of earthquakes and faulting*. Cambridge University Press, New York (NY), ISBN 521652235

Segall, P. (1989). *Earthquakes triggered by fluid extraction*. Geology, Vol. 17, pp. 942-946.

Segall, P., Grasso, J.-R. & Mossop, A., (1994). *Poroelastic stressing and induced seismicity near the Lacq gas field, southwestern France*. Journal of Geophysical Research, 99(B8), pp.15,423–15,438.

Shirzaei, M., Ellsworth, W.L., Tiampo, K.F., González, P.J., Manga, M. (2016), *Surface Uplift and time-dependent seismic hazard due to fluid injection in Eastern Texas*. Science, Vol. 353, Issue 6306 pp. 1416-1419.

Spiers, C.J., Hangx, S.J.T., Niemeijer, A.R. (2017), *New Approaches in experimental research on rock and fault behaviour in the Groningen gas field*. Netherlands Journal of Geoscience – Geologie en Mijnbouw, Vol. 96, Nr. 5, pp 55-69

Stock, C. and Smith, E.G.C. (2000), *Evidence for Different Scaling of Earthquake Source Parameters for Large Earthquakes Depending on Fault Mechanism*, Geophysics J. Int., Vol. 143, pp. 157-162

Streit, J.E and Hillis, R.R. (2004), *Estimating fault stability and sustainable fluid pressure for underground storage of CO2 in porous rock*, Energy, Vol. 29, pp. 1445-1456.

Templeton, E.L. and Rice, J. R. (2008), *Off-fault plasticity and earthquake rupture dynamics: 1. Dry materials or neglect of fluid pressure change*, J. Geophys. Res., Vol. 113, B09306, doi:10.1029/2007JB005529.

Uenishi, K. and Rice, J. R. (2003), *Universal nucleation length for slip-weakening rupture instability under nonuniform fault loading*, J. Geophys. Res., 108(B1), 2042, doi:10.1029/2001JB00168.

Van den Bogert, P.A.J. (2015), *Impact of various modelling options on the onset of fault slip and fault slip response using 2-dimensional Finite-Element Modelling*. Report SR.15.11455, Shell Global Solutions International B.V.

Van Eck, T., Goutbeek, F. Haak, H., Dost, B. (2004), *Seismic Hazard due to small shallow induced earthquakes*. KNMI Scientific report WR 2004-01. Available at www.knmi.nl.

Van Eijs, R.M.H.E., Mulders, F.M.M., Nepveu, M., Kenter, C. en Scheffers, B.C. (2006), *Correlation between hydrocarbon reservoir properties and induced seismicity in the Netherlands.* Engineering Geology, 84, 99-111. 2006

Van Eijs, R.M.H.E. (2015), *Neotectonic Stresses in the Permian Slochteren Formation of the Groningen Field.* NAM report EP201510210531, https://nam-feitenencijfers.data-app.nl/download/rapport/b7a3cb12-46c3-4783-86f0-5905882cb0f6?open=true

Van Thienen-Visser, K. Nepveu, M., Hettelaar, J., *Deterministische hazard analyse voor geinduceerde seismicitiet in Nederland.* (in Dutch). TNO-rapport 2012 R1-198, 2012.

Verruijt, A. (2010). *An introduction to Soil Dynamics*. Springer. DOI: 10.1007/978-3-319-61185-3

Visser, C. (edt.), *Groningen Field Review 2012, Static Modelling and Hydrocarbon Volume Determination*, Document number: EP201203204663

Willacy, C., van Dedem, E. , Minisini, S. , Li, J., Blokland, J. W., Das, I. and Droujinine, A. (2018), *Application of Full Waveform Event Location and Moment Tensor Inversion for Groningen Induced Seismicity,* The Leading Edge, 37(2), 92–99.

World Stress Map Project, http://dc-app3-14.gfz-potsdam.de/pub/introduction/introduction_frame.html

Zbinden, D., Rinaldi, A.P., Urpi, L., and Wiemer, S. (2017), *On the physics-based processes behind production-induced seismicity in natural gas field,* Journal of Geophysical Research: Solid Earth, April 2017, *https://doi.org/10.1002/2017JB014003.*

Zheng, Y. and Guises, R. (2014), *Dynamic Geomechanical Modelling to Assess and Minimize the Risk of Fault Slip during reservoir depletion of the Groningen Field – 1D Geomechanical Model,* Baker RDS NAM0001 Final Report.

Zoback, M.D. (2007), *Reservoir Geomechanics,* Cambridge University Press, ISBN 9780511586477, https://doi.org/10.1017/CBO9780511586477

APPENDIX 1. THE GRONINGEN FAULT MODEL

Seismic events in the Groningen gas field are mapped on known, natural faults with increasing confidence, while the observed slip direction (the derived moment tensor) is often well aligned with the local fault orientation (Willacy et al., 2018). Therefore, it is prudent to consider the fault map of the field to determine the main geometrical features that may influence the stress changes induced by reservoir depletion. Figure AError**! No text of specified style in document.**.1 shows the interpreted faults and the depth of the bottom of the reservoir formations, consisting of the Ten Boer Claystone (ROCLT) and the Slochteren Sandstone (ROSL) formations (Visser, 2012). The insert on the right-hand side shows a representative geometrical configuration of a fault (green) that offsets the depleting formations. Ten Boer and Slochteren formations are slightly dipping downward from the South-East to the North-West, with the initial Gas-Water contact at 2995 m depth throughout the field. The combined thickness of the Ten Boer and Slochteren formations increase from less than 100 m in the South-East to more than 300 m in the North-West of the field. The gas reservoir is overlain by thick packages of salt in the Permian Zechstein Group with very stiff anhydrites and carbonates in the Z1 formation (ZEZ1), directly above the Ten Boer formation (not shown). In this study, we are interested in the impact of the reservoir offset on fault slip and seismic rupture. In particular, the reservoir offset normalised for the reservoir thickness is important for the evaluation of fault slip and seismic rupture (Van den Bogert, 2015, and section 4.1).

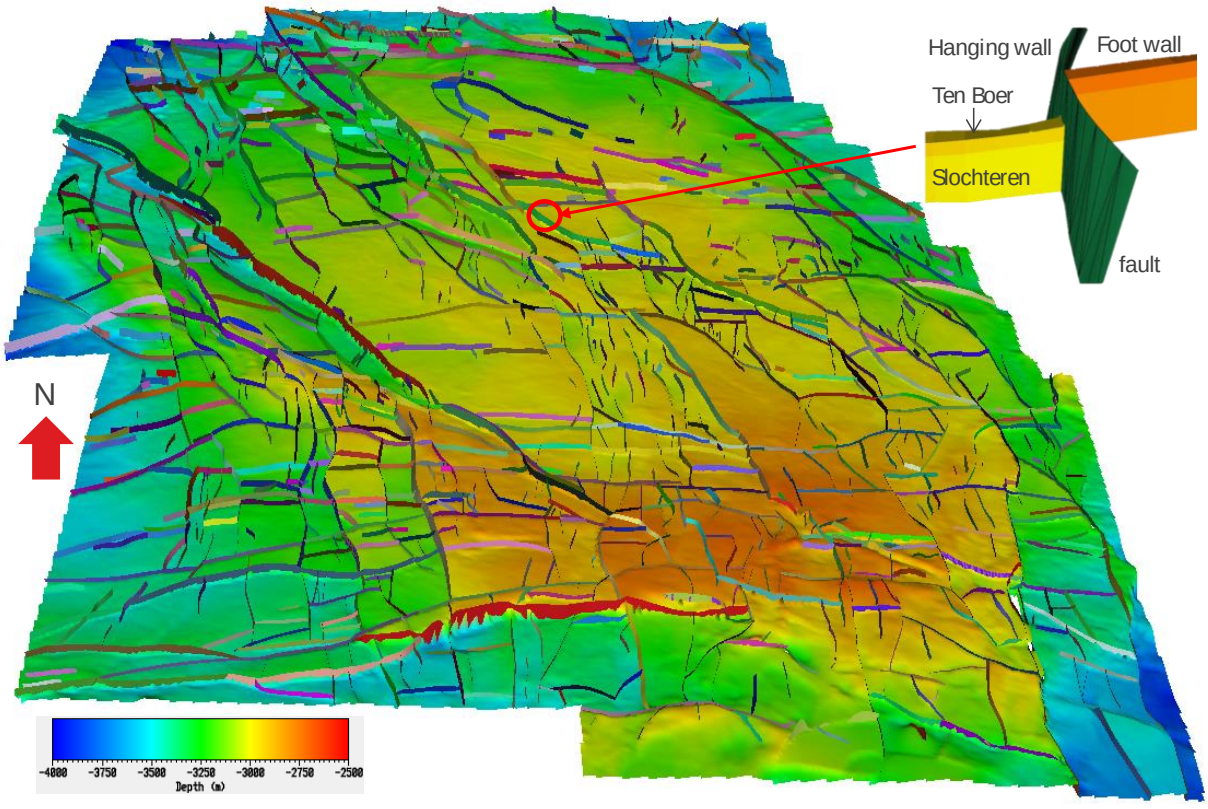

*Figure A**Error! No text of specified style in document.**.1: The interpreted faults intersecting the bottom of the Groningen gas reservoir formation (Slochteren). Colours indicate depth [m]. The map covers an area of about 20x30 km². The Slochteren formation is overlain by Ten Boer Claystone (see insert) and Zechstein salt sediments (Visser, 2012).*

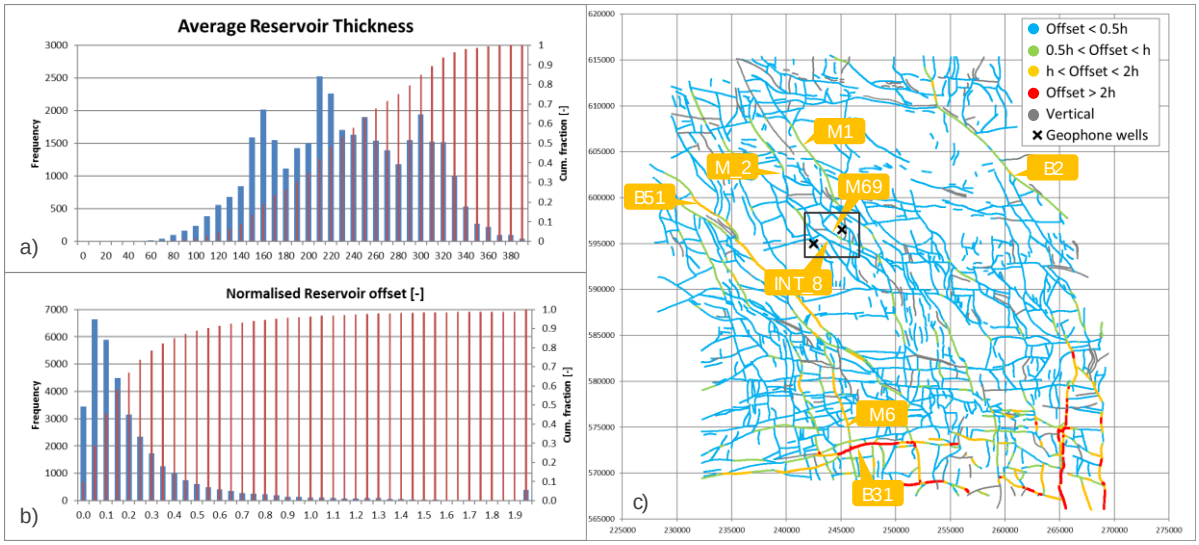

*Figure A**Error! No text of specified style in document.**.2: The (cumulative) frequency distribution of a) the average reservoir thickness, and b) the normalised reservoir offset in more than 35,000 cross-sections; c) the Groningen fault map represented by more than 35,000 points (cross-section locations) in which the color indicates the normalised reservoir offset (offset O divided by the reservoir thickness h). The rectangle indicates the Loppersum area, where the largest earthquakes have occurred so far, while the two crosses indicate the location of two wells with down-hole geophones at reservoir depth (about 3000 m).*

The Groningen field is located in a normally faulted environment. More than 35,000 cross-sections of Ten Boer and Slochteren formations are generated along the faults in the Groningen field, similar to the example shown in the insert of Figure AError**! No text of specified style in document.**.1. For each cross-section, the fault dip and azimuth angle was determined in conjunction with the depth and thickness of the Ten Boer and Slochteren formations on both sides of the fault. The normalised reservoir offset was calculated by dividing the absolute offset of the Slochteren formation by the average depleting reservoir interval (Ten Boer and Slochteren formations) on both sides of the fault. The offset is defined positive if the hanging wall is deeper than the foot wall. The cumulative frequency distribution (Figure AError**! No text of specified style in document.**.2b) shows that the normalised reservoir offset in almost 90% of the cross-sections is between 0 and 0.5. This is also reflected in Figure AError**! No text of specified style in document.**.2c, which shows the fault lines in map view with a color code that represents the normalised offset. It is seen that a normalised reservoir offset larger than 2 is only found in the South-East of the field (red dots).

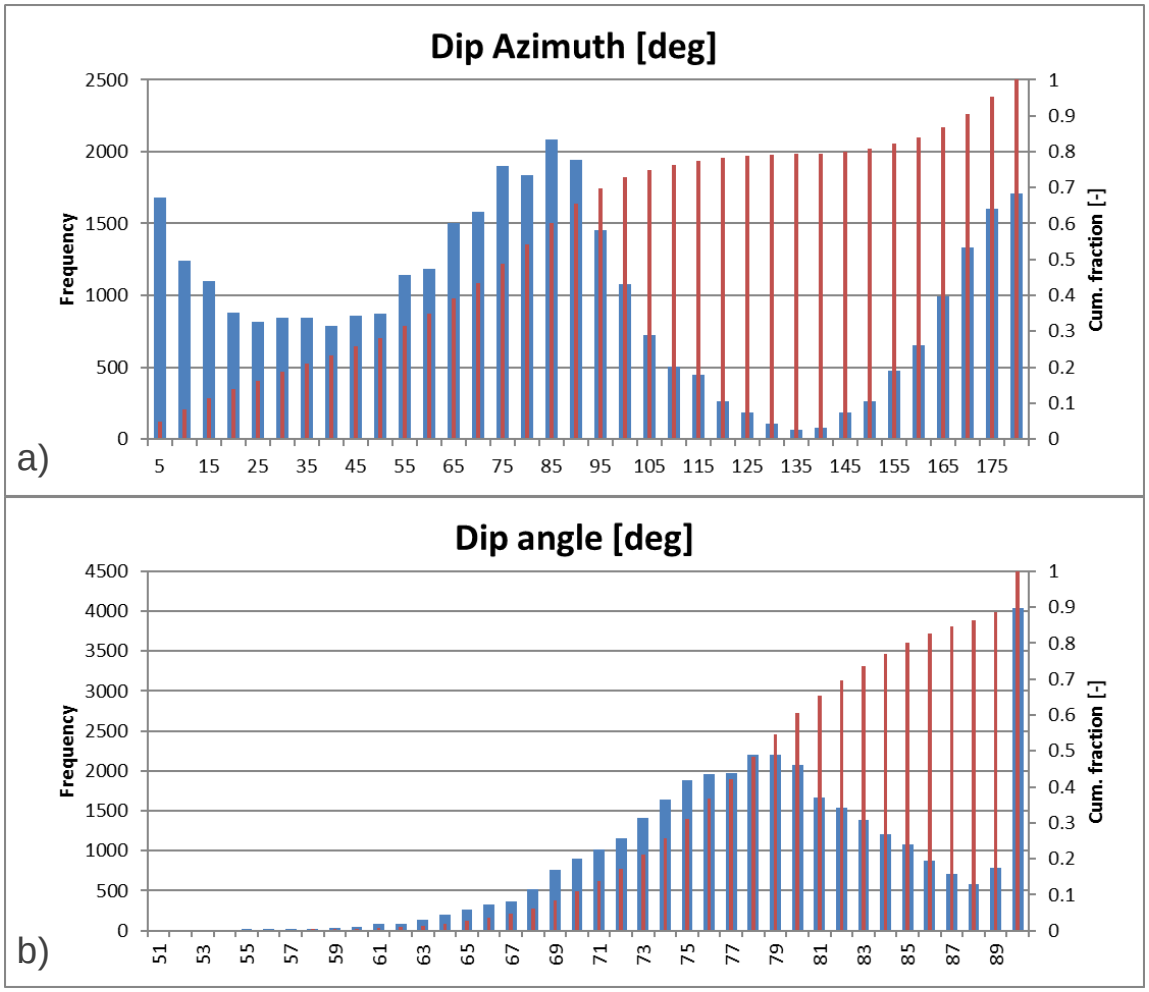

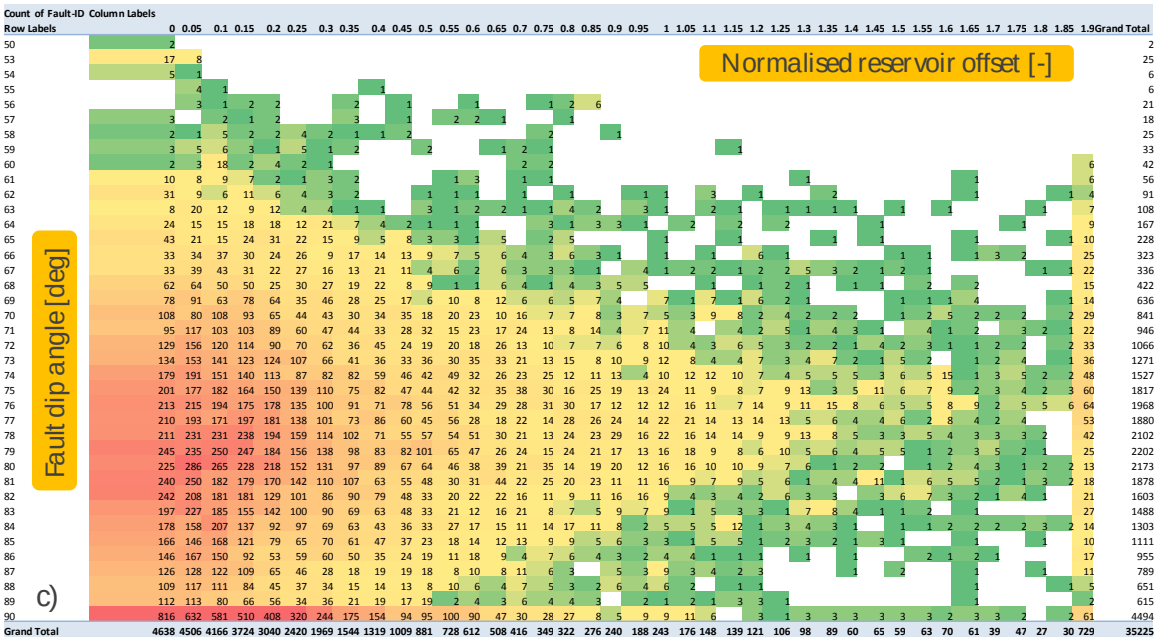

*Figure A**Error! No text of specified style in document.**.3: a) the (cumulative) frequency distribution of the fault azimuth angle, b) the (cumulative) frequency distribution of the fault dip angle, and c) a heat map showing the number of cross-sections with a particular combination for the fault dip angle (vertically, between 50 and 90 degrees) and the normalised reservoir offset (horizontally, between 0 and 2).*

The azimuth angles were derived from the normal vector of the fault plane in every cross-section. The azimuth angle was defined as the angle between 0 and 180 degrees in a horizontal plane between the normal vector and the geographic North (East of North). The frequency distribution of the azimuth angle in Figure A**Error! No text of specified style in document.**.3a shows two dominating fault sets: one with an azimuth angle between 65 and 95 degrees (East of North), and one between 170 and 185 (5) degrees. The dip angle was defined as the angle between the fault dip direction and a horizontal plane (Figure 2.1a), and was found mostly between about 75 and 80 degrees (Figure A**Error! No text of specified style in document.**.3b). The subsurface model assumes vertical faults in cases where the fault dip angle could not be determined. This is the case in about 10% of the cross-sections. The heat map in Figure A**Error! No text of specified style in document.**.3c shows a consistent distribution of the dip angle for the entire range of observed normalised reservoir offsets.

APPENDIX 2. OVERVIEW OF ANALYSES CONDUCTED IN THIS STUDY

Table A**Error! No text of specified style in document.**.1 below provides an overview of all analyses conducted in support of the conclusions of this report. A selection of the analyses relevant for each section in this report is provided when relevant. In total 208 cases have been evaluation: 39 exhibit Rupture Mechanism 1 (black M_w Table A**Error! No text of specified style in document.**.1), 52 exhibit Rupture Mechanism 2 (blue M_w) and 117 show Rupture Mechanism 3 (red M_w)

*Table A**Error! No text of specified style in document.**.1: Overview of cases conducted in this study. The initial friction coefficient is 0.55 and the fault dip angle is 66 degree for all cases. Onset of fault slip and onset of seismic rupture is only provided if occurring at a reservoir depletion smaller than 30 MPa. Moment Magnitude is color coded: black = Rupture Mechanism 1, blue = Rupture Mechanism 2, red = Rupture Mechanism 3.*

Case	Offset	Res. thick-ness H	Norm. offset $\bar{O}$	Residual friction μ_r	Slope W_μ	ΔP at fault slip	ΔP at seismic rupture	M_w
	[m]	[m]	[-]	[-]	[mm^{-1}]	[MPa]	[MPa]	[-]
Mu55-2	0	170	0	0.50	0.010	95.66	-	-
Mu55-12	10	170	0.059	0.45	0.010	21.26	-	-
Mu55-22	20	170	0.118	0.40	0.010	17.22	-	-
Mu55-32	30	170	0.176	0.45	0.010	15.49	29.73	1.06
Mu55-33	30	170	0.176	0.40	0.010	15.49	29.73	2.82
Mu55-34	30	170	0.176	0.35	0.010	15.49	29.73	3.05
Mu55-35	30	170	0.176	0.30	0.010	15.49	29.73	3.24
Mu55-36	30	170	0.176	0.25	0.010	15.49	29.73	3.75
Mu55-41	40	170	0.235	0.50	0.010	14.49	-	-
Mu55-42	40	170	0.235	0.45	0.010	14.49	26.54	1.19
Mu55-43	40	170	0.235	0.40	0.010	14.49	26.54	2.79
Mu55-44	40	170	0.235	0.35	0.010	14.49	26.54	3.03
Mu55-45	40	170	0.235	0.30	0.010	14.49	26.54	3.21
Mu55-46	40	170	0.235	0.25	0.010	14.49	26.54	3.67
Mu55-51	50	170	0.294	0.50	0.010	13.76	-	-
Mu55-52	50	170	0.294	0.45	0.010	13.76	24.34	1.32
Mu55-53	50	170	0.294	0.40	0.010	13.76	24.34	2.76
Mu55-54	50	170	0.294	0.35	0.010	13.76	24.34	3.01
Mu55-55	50	170	0.294	0.30	0.010	13.76	24.34	3.21
Mu55-56	50	170	0.294	0.25	0.010	13.76	24.34	3.58
Mu55-61	60	170	0.353	0.50	0.010	13.26	29.45	2.02

Case	Offset	Res. thick-ness H	Norm. offset $\bar{O}$	Residual friction μ_r	Slope W_μ	ΔP at fault slip	ΔP at seismic rupture	M_w
	[m]	[m]	[-]	[-]	[mm^{-1}]	[MPa]	[MPa]	[-]
Mu55-62	60	170	0.353	0.45	0.010	13.26	22.69	1.47
Mu55-63	60	170	0.353	0.40	0.010	13.26	22.69	2.73
Mu55-64	60	170	0.353	0.35	0.010	13.26	22.69	2.99
Mu55-65	60	170	0.353	0.30	0.010	13.26	22.69	3.2
Mu55-66	60	170	0.353	0.25	0.010	13.26	22.69	3.51
Mu55-71	70	170	0.412	0.50	0.010	12.80	26.23	1.96
Mu55-72	70	170	0.412	0.45	0.010	12.80	21.35	1.69
Mu55-73	70	170	0.412	0.40	0.010	12.80	21.35	2.69
Mu55-74	70	170	0.412	0.35	0.010	12.80	21.35	2.96
Mu55-75	70	170	0.412	0.30	0.010	12.80	21.35	3.19
Mu55-76	70	170	0.412	0.25	0.010	12.80	21.35	3.45
Mu55-81	80	170	0.471	0.50	0.010	12.46	23.63	1.9
Mu55-82	80	170	0.471	0.45	0.010	12.46	20.22	2.32
Mu55-83	80	170	0.471	0.40	0.010	12.46	20.22	2.65
Mu55-84	80	170	0.471	0.35	0.010	12.46	20.22	2.92
Mu55-85	80	170	0.471	0.30	0.010	12.46	20.22	3.18
Mu55-86	80	170	0.471	0.25	0.010	12.46	20.22	3.38
Mu55-87	80	170	0.471	0.20	0.010	12.46	20.22	4.07
Mu55-91	90	170	0.592	0.50	0.010	11.85	21.37	1.83
Mu55-92	90	170	0.592	0.45	0.010	11.85	19.02	2.27
Mu55-93	90	170	0.592	0.40	0.010	11.85	19.02	2.59
Mu55-94	90	170	0.592	0.35	0.010	11.85	19.02	2.88
Mu55-95	90	170	0.592	0.30	0.010	11.85	19.02	3.16
Mu55-96	90	170	0.592	0.25	0.010	11.85	19.02	3.38
Mu55-96	90	170	0.592	0.20	0.010	11.85	19.02	4.01
Mu55-101	100	170	0.588	0.50	0.010	11.57	19.52	1.75
Mu55-102	100	170	0.588	0.45	0.010	11.57	18.10	2.21
Mu55-103	100	170	0.588	0.40	0.010	11.57	18.10	2.53
Mu55-104	100	170	0.588	0.35	0.010	11.57	18.10	2.83
Mu55-106	100	170	0.588	0.30	0.010	11.57	18.10	3.13
Mu55-106	100	170	0.588	0.25	0.010	11.57	18.10	3.38
Mu55-111	68	170	0.4	0.45	0.010	13.28	21.60	1.63

Case	Offset	Res. thick-ness H	Norm. offset $\bar{O}$	Residual friction μ_r	Slope W_μ	ΔP at fault slip	ΔP at seismic rupture	M_w
	[m]	[m]	[-]	[-]	[mm^{-1}]	[MPa]	[MPa]	[-]
Mu55-112	56	140	0.4	0.45	0.010	13.52	22.36	2.26
Mu55-113	92	230	0.4	0.45	0.010	13.04	20.64	1.53
Mu55-114	104	260	0.4	0.45	0.010	12.74	20.14	1.49
Mu55-115	120	300	0.4	0.45	0.010	12.73	19.86	1.48
Mu55-116	28	140	0.2	0.45	0.010	16.09	29.94	1.13
Mu55-117	34	170	0.2	0.45	0.010	15.50	28.29	1.12
Mu55-118	46	230	0.2	0.45	0.010	14.74	26.08	1.11
Mu55-119	52	260	0.2	0.45	0.010	14.51	25.31	1.12
Mu55-120	60	300	0.2	0.45	0.010	14.28	24.49	1.13
Mu55-121	0	200	0.000	0.45	0.010	90.99	-	-
Mu55-122	5	200	0.025	0.45	0.010	28.78	-	-
Mu55-123	10	200	0.050	0.45	0.010	22.10	-	-
Mu55-124	15	200	0.075	0.45	0.010	19.40	-	-
Mu55-125	20	200	0.100	0.45	0.010	17.85	-	-
Mu55-126	25	200	0.125	0.45	0.010	16.83	-	-
Mu55-132	30	200	0.15	0.45	0.010	15.61	-	-
Mu55-141	40	200	0.20	0.50	0.010	14.63	-	-
Mu55-142	40	200	0.20	0.45	0.010	14.63	27.05	1.11
Mu55-143	40	200	0.20	0.40	0.010	14.63	27.05	2.91
Mu55-144	40	200	0.20	0.35	0.010	14.63	27.05	3.16
Mu55-145	40	200	0.20	0.30	0.010	14.63	27.05	3.34
Mu55-146	40	200	0.20	0.25	0.010	14.63	27.05	3.82
Mu55-151	50	200	0.25	0.50	0.010	-	-	-
Mu55-152	50	200	0.25	0.45	0.010	13.93	24.92	1.21
Mu55-153	50	200	0.25	0.40	0.010	13.93	24.92	2.89
Mu55-154	50	200	0.25	0.35	0.010	13.93	24.92	3.14
Mu55-155	50	200	0.25	0.30	0.010	13.93	24.92	3.34
Mu55-156	50	200	0.25	0.25	0.010	13.93	24.92	3.78
Mu55-161	60	200	0.30	0.50	0.010	13.47	-	-
Mu55-162	60	200	0.30	0.45	0.010	13.47	23.34	1.32
Mu55-163	60	200	0.30	0.40	0.010	13.47	23.34	2.86
Mu55-164	60	200	0.30	0.35	0.010	13.47	23.34	3.13
Mu55-165	60	200	0.30	0.30	0.010	13.47	23.34	3.33

Case	Offset	Res. thick-ness H	Norm. offset $\bar{O}$	Residual friction μ_r	Slope W_μ	ΔP at fault slip	ΔP at seismic rupture	M_w
	[m]	[m]	[-]	[-]	[mm^{-1}]	[MPa]	[MPa]	[-]
Mu55-166	60	200	0.30	0.25	0.010	13.47	23.34	3.70
Mu55-171	70	200	0.35	0.50	0.010	13.10	-	-
Mu55-172	70	200	0.35	0.45	0.010	13.10	22.09	1.44
Mu55-173	70	200	0.35	0.40	0.010	13.10	22.09	2.83
Mu55-174	70	200	0.35	0.35	0.010	13.10	22.09	3.11
Mu55-175	70	200	0.35	0.30	0.010	13.10	22.09	3.33
Mu55-176	70	200	0.35	0.25	0.010	13.10	22.09	3.63
Mu55-181	80	200	0.40	0.50	0.010	12.74	27.41	2.08
Mu55-182	80	200	0.40	0.45	0.010	12.74	21.05	1.56
Mu55-183	80	200	0.40	0.40	0.010	12.74	21.05	2.81
Mu55-184	80	200	0.40	0.35	0.010	12.74	21.05	3.08
Mu55-185	80	200	0.40	0.30	0.010	12.74	21.05	3.32
Mu55-186	80	200	0.40	0.25	0.010	12.74	21.05	3.60
Mu55-187	80	200	0.40	0.49	0.010	12.74	26.15	2.16
Mu55-188	80	200	0.40	0.48	0.010	12.74	25.00	2.23
Mu55-189	80	200	0.40	0.47	0.010	12.74	21.05	0.83
Mu55-190	80	200	0.40	0.46	0.010	12.74	21.05	1.20
Mu55-191	90	200	0.45	0.50	0.010	12.47	25.02	2.03
Mu55-192	90	200	0.45	0.45	0.010	12.47	20.15	1.73
Mu55-193	90	200	0.45	0.40	0.010	12.47	20.15	2.77
Mu55-194	90	200	0.45	0.35	0.010	12.47	20.15	3.06
Mu55-195	90	200	0.45	0.30	0.010	12.47	20.15	3.32
Mu55-196	90	200	0.45	0.25	0.010	12.47	20.15	3.52
Mu55-201	100	200	0.50	0.50	0.010	11.94	22.91	1.97
Mu55-202	100	200	0.50	0.45	0.010	11.94	19.17	2.38
Mu55-203	100	200	0.50	0.40	0.010	11.94	19.17	2.73
Mu55-204	100	200	0.50	0.35	0.010	11.94	19.17	3.03
Mu55-205	100	200	0.50	0.30	0.010	11.94	19.17	3.30
Mu55-206	100	200	0.50	0.25	0.010	11.94	19.17	3.52
Mu55-211	120	200	0.60	0.50	0.010	11.52	19.60	1.84
Mu55-212	120	200	0.60	0.45	0.010	11.52	17.75	2.29
Mu55-213	120	200	0.60	0.40	0.010	11.52	17.75	2.63
Mu55-214	120	200	0.60	0.35	0.010	11.52	17.75	2.95

Case	Offset	Res. thick-ness H	Norm. offset $\bar{O}$	Residual friction μ_r	Slope W_μ	ΔP at fault slip	ΔP at seismic rupture	M_w
	[m]	[m]	[-]	[-]	[mm^{-1}]	[MPa]	[MPa]	[-]
Mu55-215	120	200	0.60	0.30	0.010	11.52	17.75	3.26
Mu55-216	120	200	0.60	0.25	0.010	11.52	17.75	3.52
Mu55-217	140	200	0.70	0.50	0.010	11.37	16.96	1.70
Mu55-218	140	200	0.70	0.45	0.010	11.37	16.38	2.15
Mu55-219	140	200	0.70	0.25	0.010	11.37	16.38	3.52
Mu55-221	160	200	0.80	0.50	0.010	10.49	14.8	1.49
Mu55-222	160	200	0.80	0.45	0.010	10.49	14.8	1.90
Mu55-223	160	200	0.80	0.40	0.010	10.49	14.8	2.25
Mu55-224	160	200	0.80	0.35	0.010	10.49	14.8	2.65
Mu55-225	160	200	0.80	0.30	0.010	10.49	14.8	3.10
Mu55-226	160	200	0.80	0.25	0.010	10.49	14.8	3.50
Mu55-231	180	200	0.90	0.50	0.010	9.51	12.22	0.96
Mu55-232	180	200	0.90	0.45	0.010	9.51	12.22	1.32
Mu55-233	180	200	0.90	0.40	0.010	9.51	12.22	1.66
Mu55-234	180	200	0.90	0.35	0.010	9.51	12.22	2.15
Mu55-235	180	200	0.90	0.30	0.010	9.51	12.22	2.83
Mu55-236	180	200	0.90	0.25	0.010	9.51	12.22	3.43
Mu55-241	200	200	1.0	0.50	0.010	7.70	-	-
Mu55-242	200	200	1.0	0.45	0.010	7.70	-	-
Mu55-243	200	200	1.0	0.40	0.010	7.70	15.78	1.40
Mu55-244	200	200	1.0	0.35	0.010	7.70	15.78	2.31
Mu55-245	200	200	1.0	0.30	0.010	7.70	15.78	3.02
Mu55-246	200	200	1.0	0.25	0.010	7.70	15.78	3.52
Mu55-251	220	200	1.1	0.50	0.010	8.22	-	-
Mu55-252	220	200	1.1	0.45	0.010	8.22	11.16	0.54
Mu55-253	220	200	1.1	0.40	0.010	8.22	11.16	1.21
Mu55-255	220	200	1.1	0.35	0.010	8.22	11.16	1.68
Mu55-255	220	200	1.1	0.30	0.010	8.22	11.16	2.64
Mu55-256	220	200	1.1	0.25	0.010	8.22	11.16	3.44
Mu55-261	240	200	1.2	0.50	0.010	8.85	13.06	1.40
Mu55-262	240	200	1.2	0.45	0.010	8.85	13.06	1.75
Mu55-263	240	200	1.2	0.40	0.010	8.85	13.06	2.06
Mu55-265	240	200	1.2	0.35	0.010	8.85	13.06	2.47

Case	Offset	Res. thick-ness H	Norm. offset $\bar{O}$	Residual friction μ_r	Slope W_μ	ΔP at fault slip	ΔP at seismic rupture	M_w
	[m]	[m]	[-]	[-]	[mm^{-1}]	[MPa]	[MPa]	[-]
Mu55-265	240	200	1.2	0.30	0.010	8.85	13.06	3.04
Mu55-266	240	200	1.2	0.25	0.010	8.85	13.06	3.57
Mu55-271	260	200	1.3	0.50	0.010	9.27	14.59	1.63
Mu55-272	260	200	1.3	0.45	0.010	9.27	14.38	2.04
Mu55-273	260	200	1.3	0.40	0.010	9.27	14.38	2.36
Mu55-275	260	200	1.3	0.35	0.010	9.27	14.38	2.74
Mu55-275	260	200	1.3	0.30	0.010	9.27	14.38	3.21
Mu55-276	260	200	1.3	0.25	0.010	9.27	14.38	3.65
Mu55-281	300	200	1.5	0.50	0.010	9.74	17.49	1.92
Mu55-282	300	200	1.5	0.45	0.010	9.74	15.86	2.33
Mu55-283	300	200	1.5	0.40	0.010	9.74	15.86	2.66
Mu55-285	300	200	1.5	0.35	0.010	9.74	15.86	3.01
Mu55-285	300	200	1.5	0.30	0.010	9.74	15.86	3.40
Mu55-286	300	200	1.5	0.25	0.010	9.74	15.86	3.77
Mu55-291	400	200	2.0	0.50	0.010	10.38	24.47	2.34
Mu55-292	400	200	2.0	0.45	0.010	10.38	17.69	1.05
Mu55-293	400	200	2.0	0.40	0.010	10.38	17.69	3.00
Mu55-294	400	200	2.0	0.35	0.010	10.38	17.69	3.34
Mu55-295	400	200	2.0	0.30	0.010	10.38	17.69	3.67
Mu55-296	400	200	2.0	0.25	0.010	10.38	17.69	3.96
Mu55-297	400	200	2.0	0.20	0.010	10.38	17.69	4.38
Mu55-298	400	200	2.0	0.15	0.010	10.38	17.69	4.80[3]
Mu55-302	0	230	0	0.45	0.010	86.70	-	-
Mu55-312	15	230	0.065	0.45	0.010	18.81	-	-
Mu55-322	30	230	0.130	0.45	0.010	15.70	-	-
Mu55-332	45	230	0.196	0.45	0.010	14.40	26.28	1.11
Mu55-336	45	230	0.196	0.25	0.010	14.40	26.28	3.93
Mu55-342	60	230	0.261	0.45	0.010	13.62	23.80	1.24
Mu55-346	60	230	0.261	0.25	0.010	13.62	23.80	3.86
Mu55-352	75	230	0.326	0.45	0.010	13.12	22.09	1.38

[3] *Progressive rupture: No arrest of the seismic rupture found within simulation period*

Case	Offset	Res. thick-ness H	Norm. offset $\bar{O}$	Residual friction μ_r	Slope W_μ	ΔP at fault slip	ΔP at seismic rupture	M_w
	[m]	[m]	[-]	[-]	[mm^{-1}]	[MPa]	[MPa]	[-]
Mu55-356	75	230	0.326	0.25	0.010	13.12	22.09	3.78
Mu55-362	90	230	0.391	0.45	0.010	12.70	20.80	1.51
Mu55-366	90	230	0.391	0.25	0.010	12.70	20.80	3.72
Mu55-372	105	230	0.457	0.45	0.010	12.16	19.55	1.65
Mu55-376	105	230	0.457	0.25	0.010	12.16	19.55	3.64
Mu55-382	120	230	0.522	0.45	0.010	11.85	18.65	1.96
Mu55-386	120	230	0.522	0.25	0.010	11.85	18.65	3.64
Mu55-392	135	230	0.587	0.45	0.010	11.61	17.82	2.39
Mu55-396	135	230	0.587	0.25	0.010	11.61	17.82	3.64
Mu55-402	0	140	0	0.45	0.010	88.51	-	-
Mu55-412	30	140	0.214	0.45	0.010	15.33	29.09	1.16
Mu55-422	50	140	0.357	0.45	0.010	14.27	25.79	1.35
Mu55-432	80	140	0.571	0.45	0.010	11.94	18.86	2.10
Mu55-442	110	140	0.786	0.45	0.010	10.39	14.63	1.64
Mu55-452	130	140	0.929	0.45	0.010	8.72	-	-
Mu55-462	140	140	1	0.45	0.010	7.68	-	-
Mu55-472	150	140	1.071	0.45	0.010	8.12	-	-
Mu55-482	170	140	1.215	0.45	0.010	9.20	13.27	1.49
Mu55-492	200	140	1.429	0.45	0.010	9.90	16.10	2.02
Mu55-531	40	200	0.2	0.45	0.001	15.09	-	-
Mu55-532	40	200	0.2	0.45	0.002	15.09	-	-
Mu55-533	40	200	0.2	0.45	0.005	15.09	-	-
Mu55-534	40	200	0.2	0.45	0.020	15.09	22.11	0.79
Mu55-535	40	200	0.2	0.45	0.050	15.09	17.84	0.46
Mu55-536	40	200	0.2	0.45	0.100	15.09	16.12	0.40
Mu55-537	40	200	0.2	0.45	0.015	15.09	23.94	0.91
Mu55-538	40	200	0.2	0.45	0.030	15.09	19.96	0.64
Mu55-539	40	200	0.2	0.45	0.040	15.09	18.74	0.55
Mu55-540	40	200	0.2	0.45	0.070	15.09	16.8	0.39
Mu55-551	80	200	0.4	0.45	0.001	13.35	-	-
Mu55-552	80	200	0.4	0.45	0.002	13.35	-	-

Case	Offset	Res. thick-ness H	Norm. offset $\bar{O}$	Residual friction μ_r	Slope W_μ	ΔP at fault slip	ΔP at seismic rupture	M_w
	[m]	[m]	[-]	[-]	[mm^{-1}]	[MPa]	[MPa]	[-]
Mu55-553	80	200	0.4	0.45	0.005	13.35	25.30	2.62
Mu55-554	80	200	0.4	0.45	0.020	13.35	17.92	1.2
Mu55-555	80	200	0.4	0.45	0.050	13.35	15.07	0.85
Mu55-556	80	200	0.4	0.45	0.100	13.35	13.86	0.74
Mu55-573	120	200	0.6	0.45	0.005	11.82	20.51	2.41
Mu55-574	120	200	0.6	0.45	0.020	11.82	15.51	2.15
Mu55-575	120	200	0.6	0.45	0.050	11.82	13.38	1.26
Mu55-576	120	200	0.6	0.45	0.100	11.82	12.44	1.08
Mu55-591	160	200	0.8	0.45	0.001	10.76	-	-
Mu55-592	160	200	0.8	0.45	0.002	10.76	-	-
Mu55-593	160	200	0.8	0.45	0.005	10.76	15.62	1.88
Mu55-594	160	200	0.8	0.45	0.020	10.76	13.44	1.83
Mu55-595	160	200	0.8	0.45	0.050	10.76	11.93	1.71
Mu55-596	160	200	0.8	0.45	0.100	10.76	11.24	1.63
Mu55-601	180	200	0.9	0.45	0.0010	9.77	-	-
Mu55-602	180	200	0.9	0.45	0.0020	9.77	-	-
Mu55-603	180	200	0.9	0.45	0.0050	9.77	-	-
Mu55-604	180	200	0.9	0.45	0.0200	9.77	11.81	1.38
Mu55-605	180	200	0.9	0.45	0.0500	9.77	10.79	1.33
Mu55-606	180	200	0.9	0.45	0.1000	9.77	10.19	1.27
Mu55-611	190	200	0.95	0.45	0.0010	8.92	-	-
Mu55-612	190	200	0.95	0.45	0.0020	8.92	-	-
Mu55-613	190	200	0.95	0.45	0.0050	8.92	-	-
Mu55-614	190	200	0.95	0.45	0.0200	8.92	10.18	0.78
Mu55-615	190	200	0.95	0.45	0.0500	8.92	9.73	0.88
Mu55-616	190	200	0.95	0.45	0.1000	8.92	9.29	0.86
Mu55-617	190	200	0.95	0.45	0.0100	8.92	-	-
Mu55-625	192	200	0.96	0.45	0.0500	8.75	9.42	0.72
Mu55-635	194	200	0.97	0.45	0.0500	8.47	9.05	0.50
Mu55-645	196	200	0.98	0.45	0.0500	8.13	8.53	0.13
Mu55-754	80	200	0.4	0.50	0.020	13.01	26.33	1.95
Mu55-755	80	200	0.4	0.50	0.050	13.01	25.43	1.77

Case	Offset	Res. thick-ness H	Norm. offset $\bar{O}$	Residual friction μ_r	Slope W_μ	ΔP at fault slip	ΔP at seismic rupture	M_w
	[m]	[m]	[-]	[-]	[mm^{-1}]	[MPa]	[MPa]	[-]
Mu55-756	80	200	0.4	0.50	0.100	13.01	25.01	1.64

APPENDIX 3. BASE CASE

The results of the Base Case, which are discussed in detail in this Appendix, act as a reference throughout this report. Case mu55-182 is selected as Base Case, because it is representative for the fault configuration in the Loppersum area of the Groningen field, but also because meaningful and realistic results are obtained if different values for various relevant model parameters are used. This facilitates evaluation of the impact of individual modelling parameters on the simulated seismic rupture. The main parameters of the Base Case are (Figure A3.1):

- Top foot wall reservoir at D = 2910 m TVD.
- Reservoir thickness H = 200 m.
- Offset hanging wall reservoir O = 80 m.
- Fault dip angle β = 66 degree.
- Fault cohesion C = 0 MPa.
- Initial friction coefficient μi = 0.55.
- Slip-weakening slope Wμ = 0.01 mm-1.

The normalised reservoir offset $\bar{0}$ is defined by the absolute offset O divided by the reservoir thickness H and is 0.4 for the Base Case. The assumed linear slip-weakening diagram for the Base Case is given in the right-hand side of Figure A3.1. All other model parameters are described in Chapter 2.

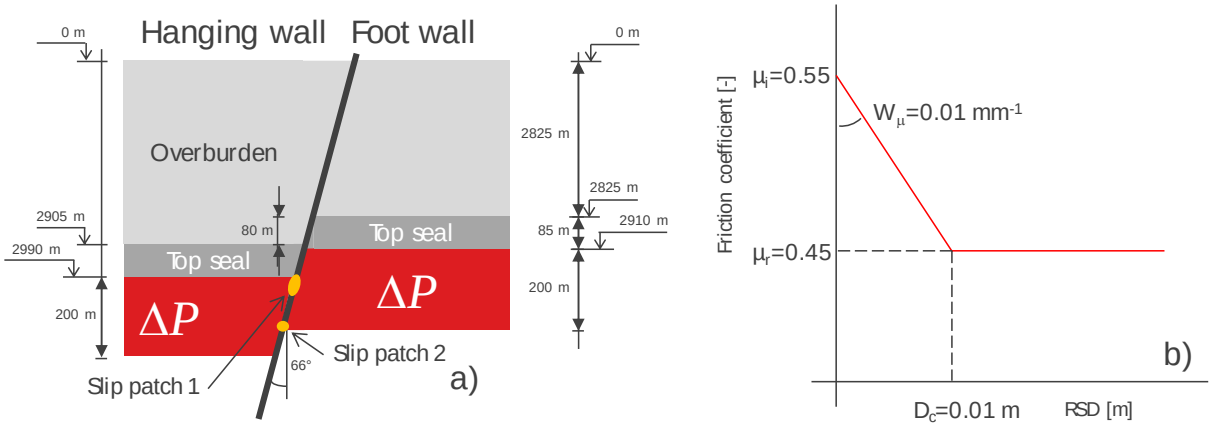

Figure A3.1: a) Base Case configuration with an offset of 80 m (case mu55-182), and b) The linear-slip weakening relationship assumed for the friction coefficient.

In section A.3.1 and in accordance with the procedure described in section 2.4, the results of the depletion stage 1 are presented until the onset of seismic rupture is reached. In section A.3.2, the dynamic rupture simulation results are presented (stage 2).

Special attention is paid to the correctness of this so-called limit point that causes fault instability and seismic rupture. In APPENDIX 4, the onset of seismic rupture is explained by considering the stress redistribution along the fault plane induced by the stress drop over the slip patches. In APPENDIX 5, a post-failure analysis is conducted to proof the existence of a limit point at the onset of seismic rupture.

A.3.1. Instable equilibrium

Onset of *fault slip* is found at slip patch 1 (Figure A3.1) at the top of the hanging wall after 12.74 MPa reservoir depletion as indicated in Figure A3.2a. Slip patch 2 occurs at the bottom of the foot wall between 14 and 15 MPa reservoir depletion. The markers in the line for slip patch 1 indicate that the incremental depletion steps of 1 MPa initially, are reduced to 0.001 MPa towards onset of seismic rupture. The length of slip patch 1 accelerates with incremental depletion and shows a vertical gradient at 21.05 MPa depletion. This implies that no further depletion is required to increase the length of slip patch 1, and is indicative for the onset of seismic fault rupture.

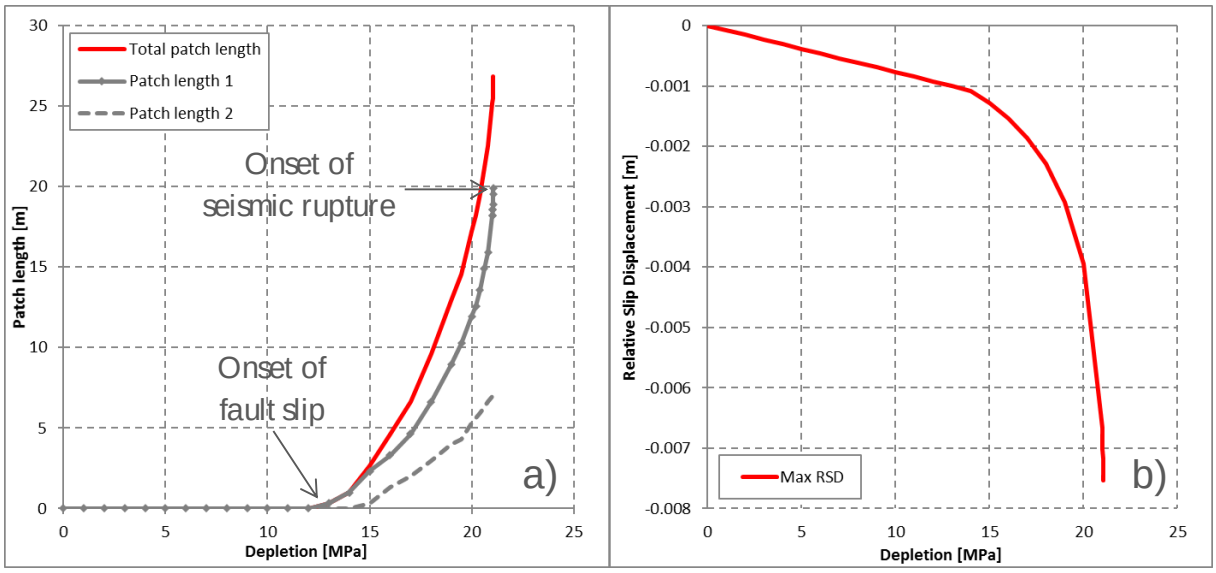

Figure A3.2: a) Length of the slip patches and b) the maximum Relative Slip Displacement (RSD) as a function of reservoir depletion. Slip patch 1 is the shallow slip patch, while slip patch 2 is the deepest slip patch in Figure 3.1a.

Figure A3.3 shows the instable equilibrium condition of the fault in the Base Case at 21.05 MPa reservoir depletion. The red line in Figure A3.3a shows the downward (negative) Relative Slip Displacement (RSD) of the hanging wall relative to the foot wall. The offset of the reservoir formations is represented by the green bars at the left-hand side of the graph. The grey bars represent the reservoir seal. The two grey boxes indicate the location of the two slip patches. The vertical size represents the length of the slip patch, while the horizontal size indicates the critical relative slip displacement D_C. The shallow patch occurs at the top of the hanging wall reservoir, and is larger than the deep slip patch that occurs at the bottom of the foot wall reservoir. Also, the RSD is larger over the shallow slip patch. The RSD between the two slip patches is small, but not zero. This is the elastic, recoverable displacement and is caused by the shear modulus (6.67 GPa) assigned to the interface elements. The absolute RSD over the shallow slip patch of 0.0075 m remains smaller than the critical slip displacement D_C of 0.010.

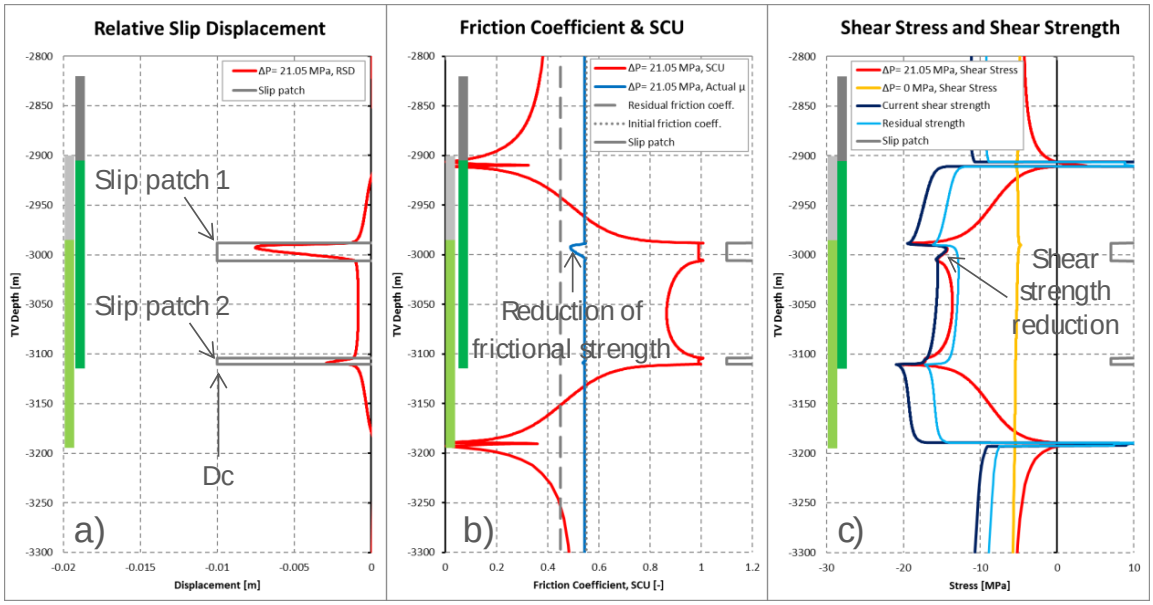

Figure A3.3: *a) the Relative Slip Displacement (RSD), b) the Friction coefficient and Shear Capacity Utilisation, and c) the Shear stress and Shear strength as a function of depth along the fault plane at the onset of seismic rupture at 21.05 MPa depletion.*

The size and location of the two slip patches is determined by the distribution of the Shear Capacity Utilisation (SCU) along the fault plane (red line in Figure A3.3b). The SCU, defined by expression (2.2), indicates how close the actual shear stress τ (red line in Figure A3.3c) is to the shear strength τ_{max} (expression (2.1), dark-blue line in Figure A3.3c). The fault slips if SCU=1. The length of the slip patches in Figure A3.3 is determined by the length of the intervals with SCU=1.

The actual friction coefficient (blue line in Figure A3.3b) indicates the fault strength at 21.05 MPa depletion. The actual friction coefficient coincides with initial friction coefficient of 0.55 (dotted line) over most of the depth range and drops to about 0.48 over the shallow slip patch adhering to the prescribed slip-weakening relationship for the fault. The residual friction coefficient of 0.45 is represented by the grey dashed line. The calculated maximum RSD of about 0.0075 m over the shallow slip patch is about 75% of the critical slip displacement D_c, which implies that the friction coefficient is also about 75% down on the descending branch of the linear slip-weakening diagram from 0.55 to 0.45. This yields a value 0.475 for the actual friction coefficient as indicated by the blue line at the location of the shallow slip patch.

The interval between the two slip patches is susceptible to seismic rupture, because the shear stress (red line in Figure A3.3c) is larger than the residual shear strength (light blue line). Note that negative shear stress values represent a downward shear stress on the foot wall formations. The residual shear strength at 21.05 MPa reservoir depletion is calculated based on the residual friction coefficient of 0.45. Intervals with a residual strength larger than the shear stress are stable under any slip condition at this depletion level. The shear stress (red line) is equal to the actual shear strength (dark blue line) over the two slip patches, as per definition.

A.3.2. Simulating fault rupture

In this section, the dynamic rupture analysis for the Base Case is discussed, which is conducted after reaching the limit point and instable equilibrium at 21.05 MPa

reservoir depletion. The dynamic rupture simulation is conducted using 2000 time steps of 0.001 s considering mass inertia and Rayleigh damping (Buijze et al, 2016).

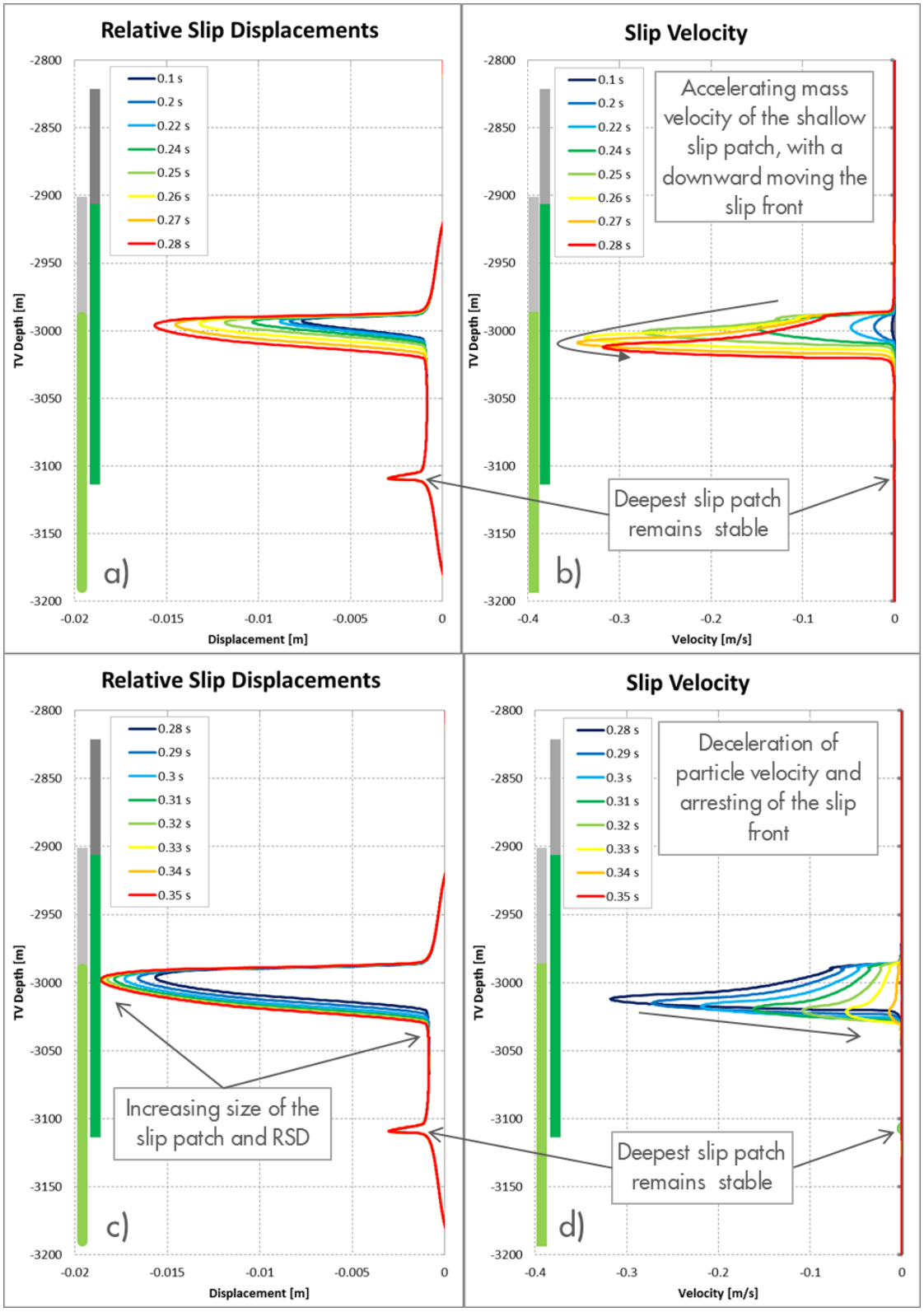

Figure A3.4: a) and c) Relative Slip Displacement, and b) and d) Slip Velocity as a function of depth along the fault plane at various moments during the rupture process for case mu55-182. Slip displacement and slip velocity are oriented tangential to the fault plane and are

given for the hanging wall relative to the foot wall. Slip displacement and slip velocity in normal direction are negligible.

The rupture process in Figure A3.4 is described by the RSD (left-hand side) and the relative slip velocity (right-hand side). The acceleration phase – until the maximum slip velocity is reached – is given in Figure A3.4a/b and the deceleration phase is given in Figure A3.4c/d. The slip velocity is increasing with a parabolic distribution over the slip patch up to about 0.24 s (dark green line in Figure A3.4b. After 0.24 s, the maximum slip velocity is found at an increasing depth, with a highest value of about 0.35 m/s after about 0.27 s, marking the end of the acceleration phase, as indicated by the arrow. Thereafter, the maximum relative slip velocity is reducing steadily, while the size of the slip patch increases slightly in downward direction, until equilibrium on the fault plane is re-established after about 0.35 s and the seismic rupture is ended. The shallow slip patch at the top of the hanging wall is extended mainly in downward direction, while the deeper slip patch does not change in size.

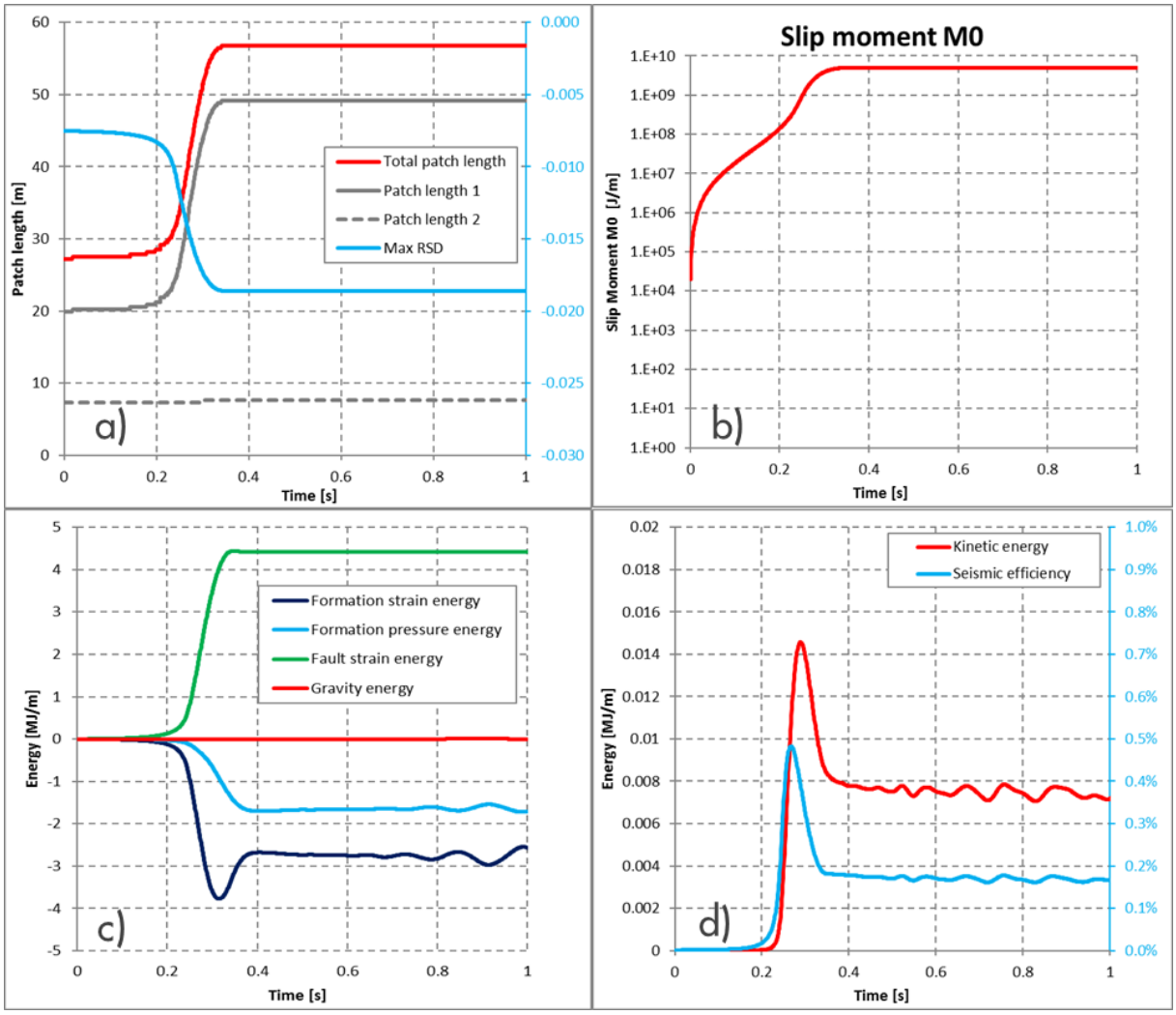

Figure A3.5: a) Total length of the two slip patches (Left-hand scale) and the maximum Relative Slip Displacement (right-hand scale); b) Slip moment on log-scale; c) Change of formation

strain and pressure energy, as well as gravity energy, and energy dissipated by fault slip; d) kinetic energy and seismic efficiency for case mu55-182 as a function of time.

The (shallow) slip patch 1 is extended from about 20 m to about 46 m, while the maximum RSD increases from -0.0075 m to -0.0186 m (right-hand side, Figure A3.5a). The extension of slip patch 2 is considered negligible, because it concerns slip of only one additional interface element of 0.3 m length. The calculation of the slip moment in Figure A3.5b is based on the incremental slip displacement over the slip patch during the dynamic rupture simulation as described in APPENDIX 13. The seismic slip moment excludes the a-seismic slip displacement induced by reservoir depletion. The slip moment does not further increase after about 0.4 s.

The energy components in Figure A3.5c and Figure A3.5d is calculated for the entire finite-element model as specified in APPENDIX 12. That is, the change of each energy component is shown relative to the start of the rupture simulation. During the seismic event, the release of formation strain ΔE_ε and formation pressure energy ΔE_p (negative values) is mainly dissipated by fault slip (fault strain energy ΔE_{fs}) and – for a small part – converted into kinetic energy ΔE_k (red line in Figure A3.5d). The kinetic energy in the model after the seismic event (0.4 s) represents the seismic wave energy that is partly transmitted to the surface. The change of gravitational energy ΔE_g is negligible, which implies that the net vertical displacement of mass in the subsurface is negligible. The change of fault pressure energy ΔE_{fp} is not shown, because it is negligible throughout the two analysis stages (depletion and dynamic rupture).

The sum of all energy components in Figure A3.5c and Figure A3.5d is exactly zero throughout the dynamic rupture simulation, thereby satisfying the energy balance equation (APPENDIX 12). The seismic efficiency in Figure A3.5d is calculated by (APPENDIX 12)

$$\eta = \Delta E_k / \left(\Delta E_e + \Delta E_g - \Delta E_k\right) = \Delta E_k / \left(\Delta E_\varepsilon + \Delta E_p + \Delta E_g - \Delta E_k\right)$$

and represents the fraction of the released energy that is transmitted as seismic waves. So, formation strain and formation pressure energy is released and for the largest part dissipated by fault slip and for a small fraction radiated in seismic waves.

The dynamic rupture analysis for the Base Case is executed correctly, because the simulation starts with negligible kinetic energy and with a negligible kinetic energy increase rate. This implies that the unbalance introduced by an incremental 0.001 MPa reservoir depletion at the start of the rupture simulation is not influencing the outcome of the analysis. It takes about 0.2 s before kinetic and other energy components start to change. This is consistent with the slip velocity shown in Figure A3.4b. It is important to select the unbalance at the start of the dynamic rupture analysis as small as possible to obtain representative results (Ripperger et. al., 2007).

The moment magnitude M_w is calculated from the seismic slip moment M_0 at the end of seismic rupture (0.7s) as described in APPENDIX 13. However, the 2-D analysis results require an assumption about the width of the rupture area along the strike of the fault. Figure A3.6 shows the calculated moment magnitude as a function of the assumed width of a rectangular slip patch. The moment magnitude M_w is 1.56 when assuming a width to length ratio (w/L_s) of 1. That is, the rupture width in strike direction is assumed equal to the rupture length in dip direction as given in Figure A3.5a. The moment

magnitude increases by about 0.2 every time the w/L_s ratio is doubled (to 2, 4, 8 etc). In the remainder of this report a rupture w/L_s ratio of 1 is assumed, unless specified otherwise.

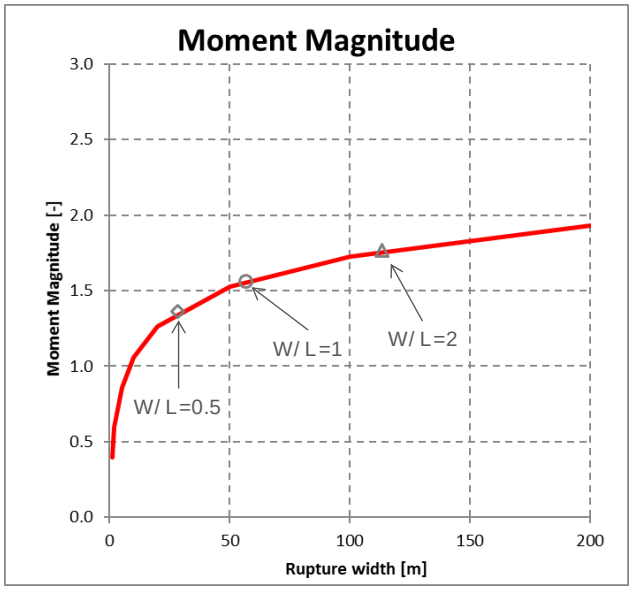

Figure A3.6: *Moment Magnitude for the Base Case as function of the assumed rupture width in the 2-D finite-element model. Rupture widths of 0.5, 1 and 2 times the rupture length in dip slip direction are indicated.*

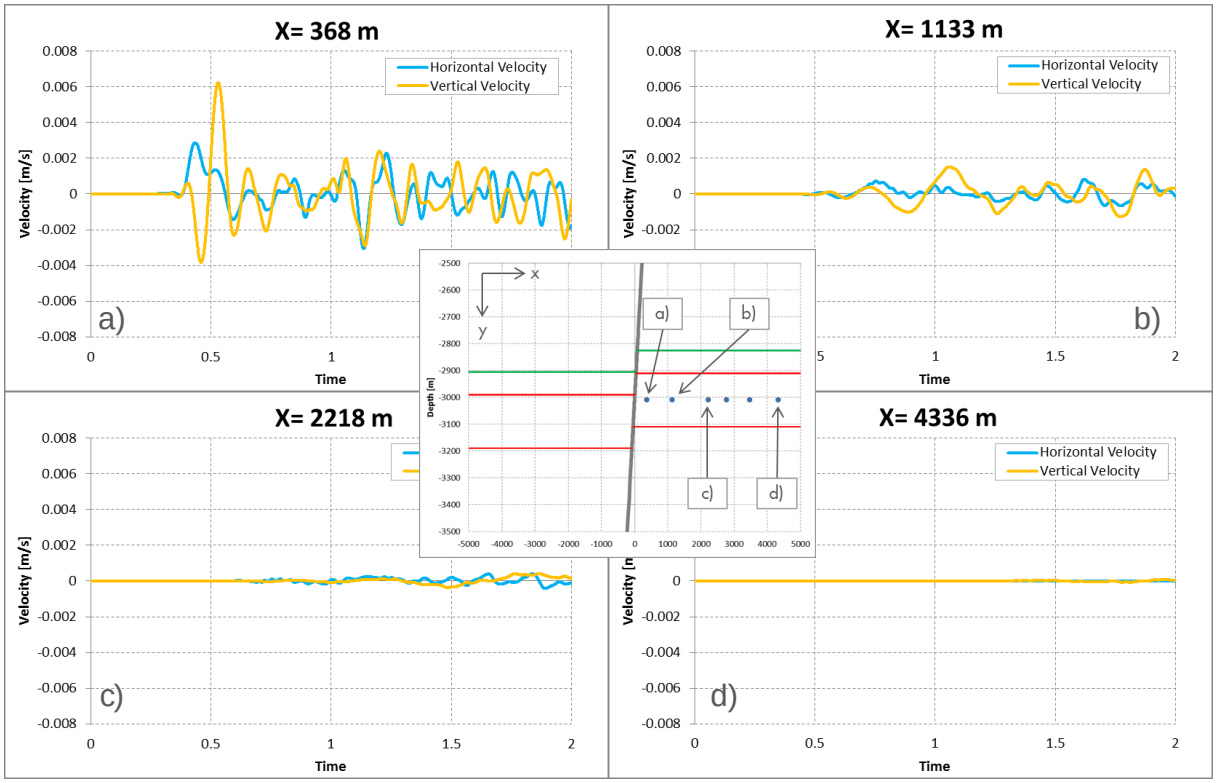

Figure A3.7: *Horizontal and vertical velocity as a function of time at different seismic stations in the foot wall reservoir (3010 m depth, see insert) for case mu55-182. The source at the fault is located at about X=0 m.*

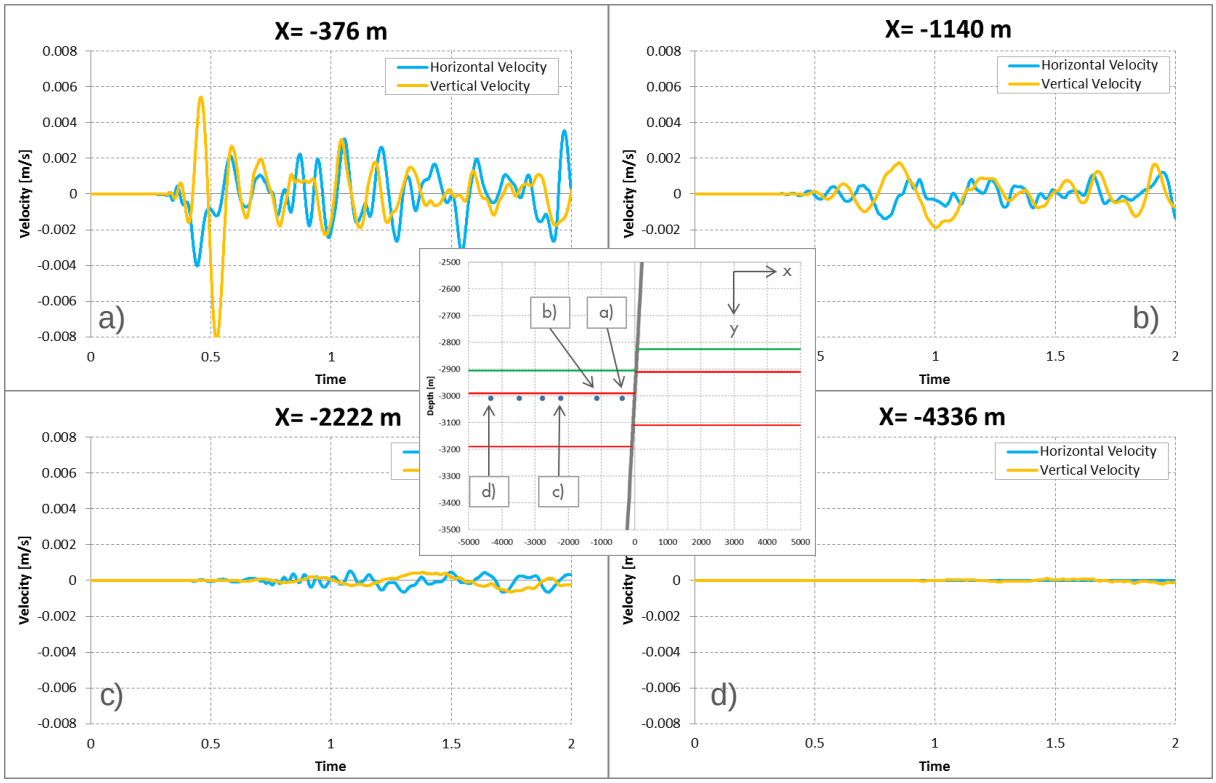

Figure A3.8: Horizontal and vertical velocity as a function of time at different seismic stations in the hanging wall reservoir (3010 m depth, see insert) for the Base Case. The fault is located at about X=0 m.

The horizontal and vertical velocity in the foot wall and hanging wall reservoir formations reduces quickly with increasing distance from the fault. Figure A3.7 and Figure A3.8 show the velocity (at the same scale) as a function of time at eight seismic stations at 3010 m depth (see inserts). It is seen that the peak velocity reduces with increasing distance to the fault, and appears to be somewhat larger in the hanging wall than in the foot wall at the same distance of the fault: At X=-376m in the hanging wall (Figure A3.8a), the peak velocity is -0.0081 m/s, whereas at X=368 m in the foot wall (Figure A3.7a), the peak velocity is +0.0063 m/s both after 0.52 seconds. This suggests that more energy is radiated in the hanging wall formations than in the foot wall formations. It is noted that the peak relative slip velocity at about 370 m from the fault is only a few percent of the peak velocity at the fault plane (0.0081 m/s versus 0.35 m/s, Figure A3.4b). Also, note that the displacement and velocity in Figure A3.4 are tangential to the fault plane, whereas orthogonal x- and y- components are presented in Figure A3.7 and Figure A3.8.

Furthermore, it seems that the wave length of – in particular – the vertical velocity is reducing with increasing distance to the fault. This is most clearly seen in Figure A3.7c and Figure A3.8c in the seismic stations at about 2200m on either side of the fault. Further study and comparison with actually observed seismic events in the Groningen field is required to derive meaningful conclusions.

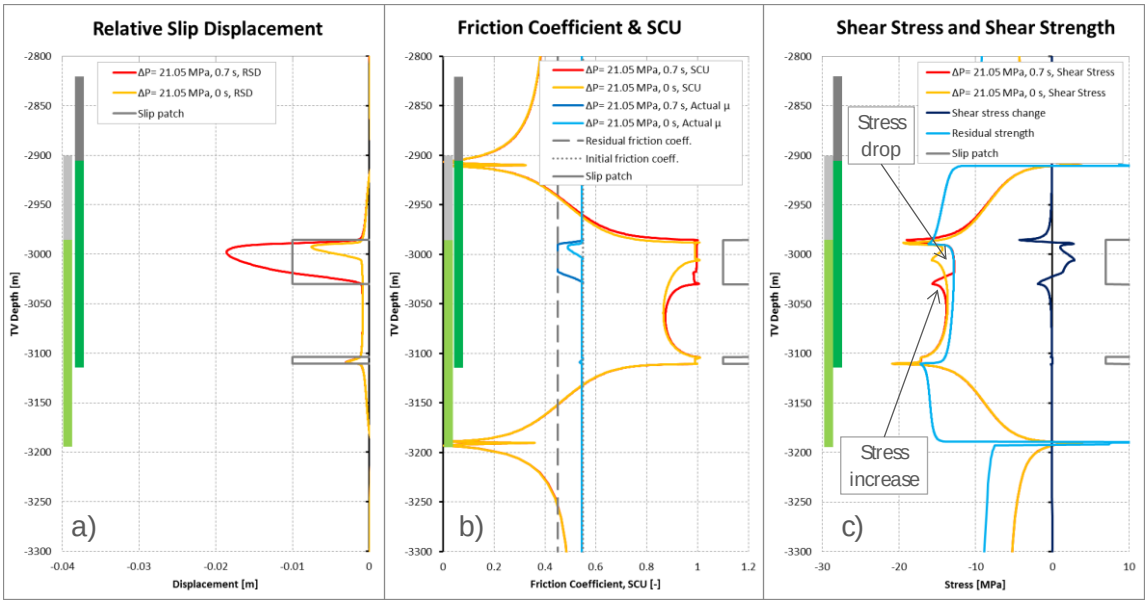

Figure A3.9: *a) Relative Slip Displacement before (t=0 s, orange line) and after seismic rupture (t=0.7 s, red line), b) the friction coefficient (light and dark blue lines) and SCU (orange and red lines), and c) actual shear stress (orange and red lines), residual shear strength (light blue line) and stress drop (dark blue line) as a function of depth along the fault plane before and after the seismic rupture for case mu55-182.*

Finally, in Figure A3.9, the RSD, the friction coefficient, the SCU and the shear stress distribution along the fault plane is shown before (orange lines) and after the seismic rupture (red lines). The grey boxes in Figure A3.9 indicate the size of the two slip patches after the seismic event as well as the critical slip displacement D_c of 0.01 m for this case. It is seen that only the shallow slip patch, at the top of the hanging wall reservoir, increases in size in downward direction and that the critical slip displacement D_c is exceeded over a large part of the slip patch during the seismic rupture. This is also reflected in Figure A3.9b, where the friction coefficient reduces to the residual value over a large part of the slip patch (dark blue line). Figure A3.9c shows transfer of shear stress to the fault just above and below the slip patch (dark blue line, negative values indicate downward shear stress). Negative values for the change of shear stress indicate a reduction of (downward) shear stress. The average stress change (drop) over the shallow slip patch is calculated at -0.98 MPa for the Base Case, while the stress increases marginally by 0.03 MPa over the second, deeper slip patch. The shear stress peak after the rupture (red line in Figure A3.9c) indicates the front of the slip patch after the seismic rupture.

APPENDIX 4. SHEAR LOADING

The occurrence of fault instability at 21.05 MPa reservoir depletion is evaluated in detail by considering the total shear load over five parts of the fault (Figure A4.1). The juxtaposition interval is defined by the depth range over which the fault is exposed to reservoir depletion on both sides. The foot wall and hanging wall intervals are only exposed to reservoir depletion on one side, whereas the fault is not exposed to reservoir depletion over the "Overburden" and "Underburden" intervals. In the Base Case (APPENDIX 3), the foot wall and hanging wall intervals both span a depth range of 80 m, the juxtaposition interval spans 120 m. Note that the length of the fault intervals is larger depending on the dip angle.

For the Base Case, the incremental, linear-elastic *shear force* over the entire depth range of the model between 0 and 6000 m is calculated at $-55.2 \cdot 10^6$ N per MPa reservoir depletion and per meter of fault (2D model). The negative sign indicates a downward direction of the shear load. The shear force is calculated by integration of the incremental shear per unit MPa reservoir depletion over the five intervals as indicated in Figure A4.1a.

The relative distribution of the incremental linear-elastic *shear force* over the five parts of the fault before the *onset of fault slip* is shown in Figure A4.1b. The bar graph shows that the entire shear force increment (106%) is carried by the juxtaposition interval of the fault, while also the foot wall and hanging wall carry another quarter of the incremental shear load (25% and 26% respectively). To maintain equilibrium, the "Overburden" and "Underburden" respond by generating a shear force in opposite (upward) direction. This is also shown by the positive (upward) directed shear stress distribution in Figure A4.1a in the "Overburden" and "Underburden" intervals, just above and below the depleting reservoir. The magnitude of the upward *shear force* over the "Overburden" and "Underburden" each account for 28% of the total shear force induced by reservoir depletion. So, the shear loading induced by reservoir depletion is concentrated over the "Juxtaposition:" interval, while the "Overburden" and "Underburden" intervals are partly unloaded.

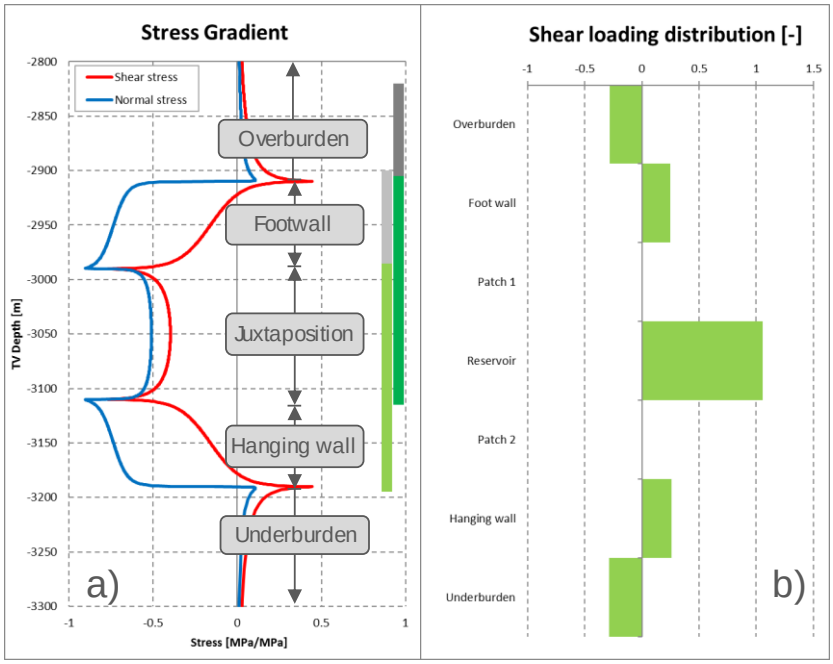

Figure A4.1: *a) Effective normal and shear stress gradient per MPa reservoir depletion as a function of depth along the fault plane under linear-elastic conditions. b) Shear load distribution (fraction) over the fault segments indicated in a)*

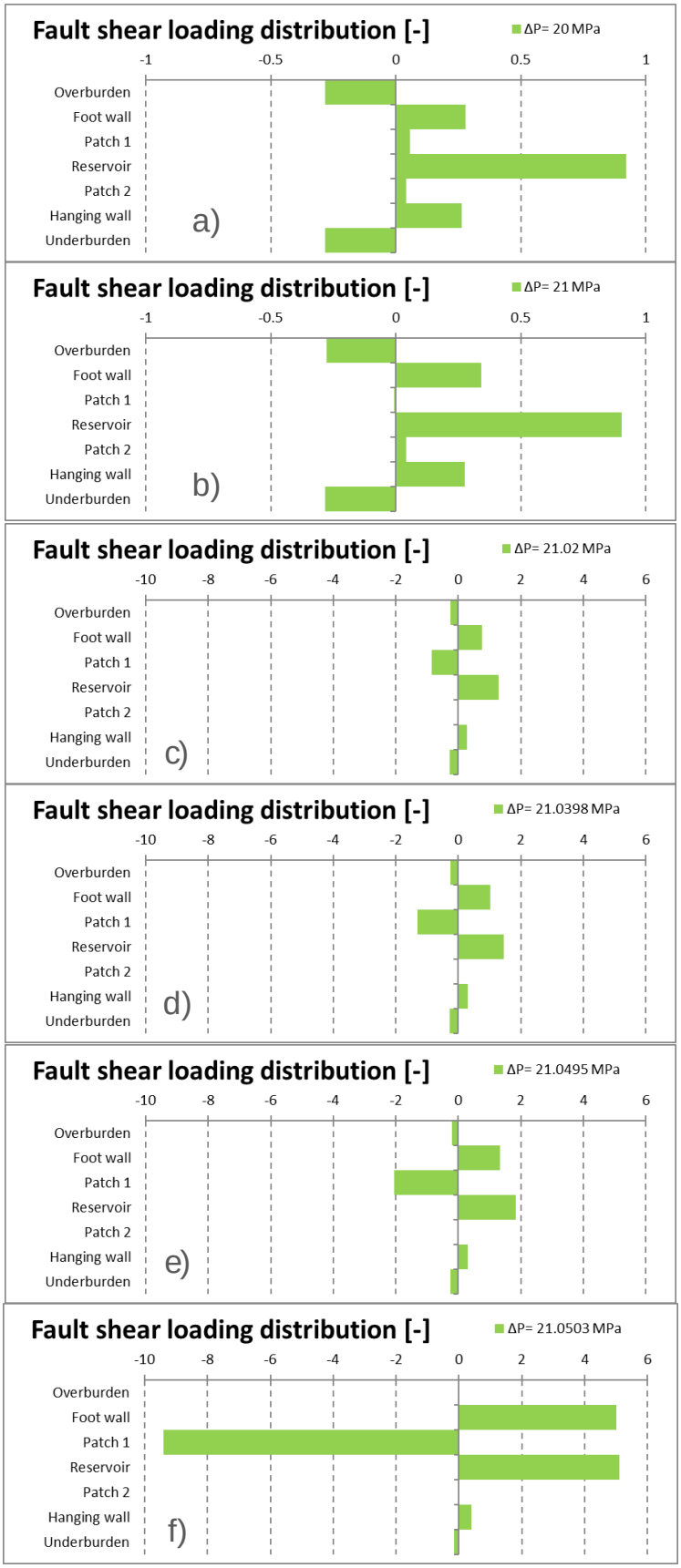

Figure A4.2: The shear load distribution (fraction) at different depletion levels. The distribution at the onset of seismic rupture is given in f). Note the different scale in a) and b) compared to c) through f).

The relative distribution of the *incremental shear force* over the different parts of the fault changes after the onset of fault slip. The contribution of the juxtaposition part reduces to 92% after 20 MPa depletion (Figure A4.2a), while the contribution of the foot wall and hanging wall marginally increase to 28% and 26% respectively. The two fault patches carry a few percent of the incremental shear load, while the "Overburden" and "Underburden" contribution is not significantly different from the linear-elastic contribution in Figure A4.1b. It is noted that both slip patches increase in size with increasing depletion (Figure A3.2), which mainly reduces the size of the juxtaposition interval. The contribution of slip patch 1 carrying incremental shear force is negligible at 21 MPa depletion (Figure A4.2b), while the contribution of the juxtaposition interval has further reduced to 90% and the foot wall increases to 34%. Continued reservoir depletion to 21.02 MPa (Figure A4.2c) shows a negative contribution of slip patch 1, indicating that the incremental shear force is directed upward. In other words: slip patch 1 is unloading. Therefore, the contribution of the foot wall increases to 77% and the juxtaposition to 129% of total shear force gradient of -55.2 MN/(MPa·m). This process of redistribution of shear force and shear stress from slip patch 1 to the foot wall and juxtaposition parts of the fault accelerate very quickly under marginally increasing reservoir depletion (note the different scale in Figure A4.2c through Figure A4.2f). Up to 21.05 MPa, the incremental shear load carried by the foot wall and juxtaposition parts just compensate for the shear load released by slip patch 1, thereby ensuring that fault stability is maintained.

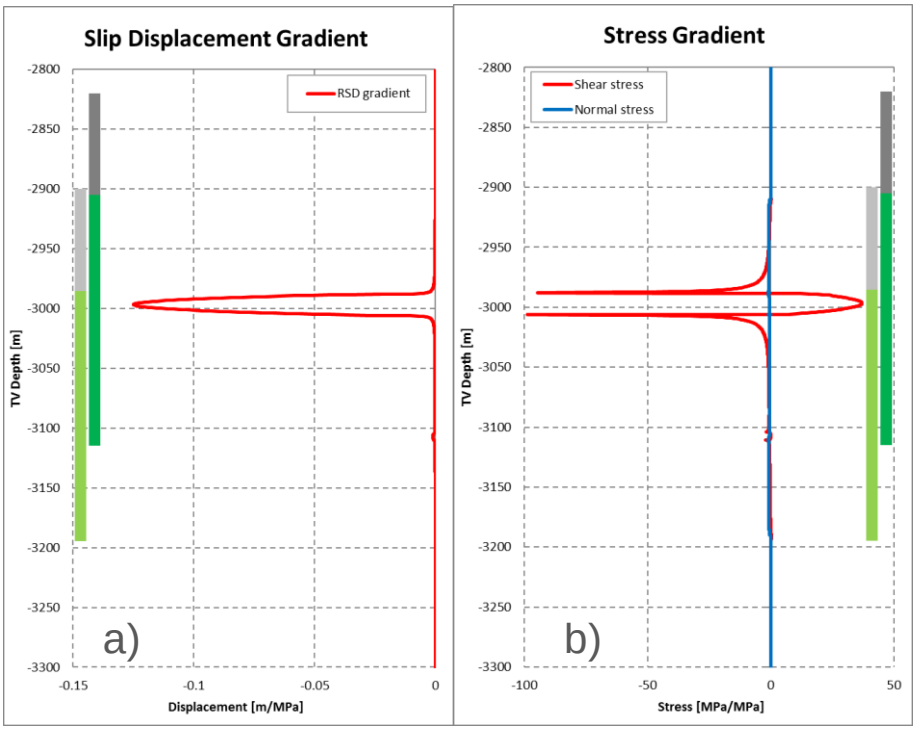

Figure A4.3: a) The change in slip displacement (RSD) in meters per MPa reservoir depletion and b) shear and effective normal stress gradients in MPa per MPa reservoir depletion as a function of depth at 21.05 MPa reservoir depletion, and which is used to calculate Figure A4.2f.

Figure A4.3 shows the change in slip (RSD) and shear stress at the limit point when instable equilibrium is reached. The increase of reservoir depletion by 0.0008 MPa to 21.050 MPa accelerates the incremental RSD to a peak value of about 0.12 m/MPa, and the release of shear stress up to about 37 MPa per MPa reservoir depletion. Is seen that the released shear stress is transferred to the foot wall just above, and the juxtaposition interval just below the shallow slip patch, which is in accordance to Figure A4.2f. Furthermore, it is noticed that slip patch 2 at the bottom of the foot wall has a negligible slip displacement gradient and is not releasing shear stress. So, incremental RSD is localised at the shallow slip patch. The fault is still in equilibrium because the positive (upward) shear stress integrated over slip patch 1 is in balance with the negative (downward) shear stress integrated over the juxtaposition and foot wall intervals. At this depletion level, the fault is in instable equilibrium because an incremental depletion of 0.001 MPa would release more (downward) shear loading from slip patch 1 than the adjacent fault can carry.

APPENDIX 5. POST-BIFURCATION ANALYSIS OF THE BASE CASE

A post-failure analysis as described in section 2.4 is conducted to confirm the onset of seismic rupture at 21.05 MPa reservoir depletion. The results are compared with dynamic rupture simulation given in Appendix A.3.2

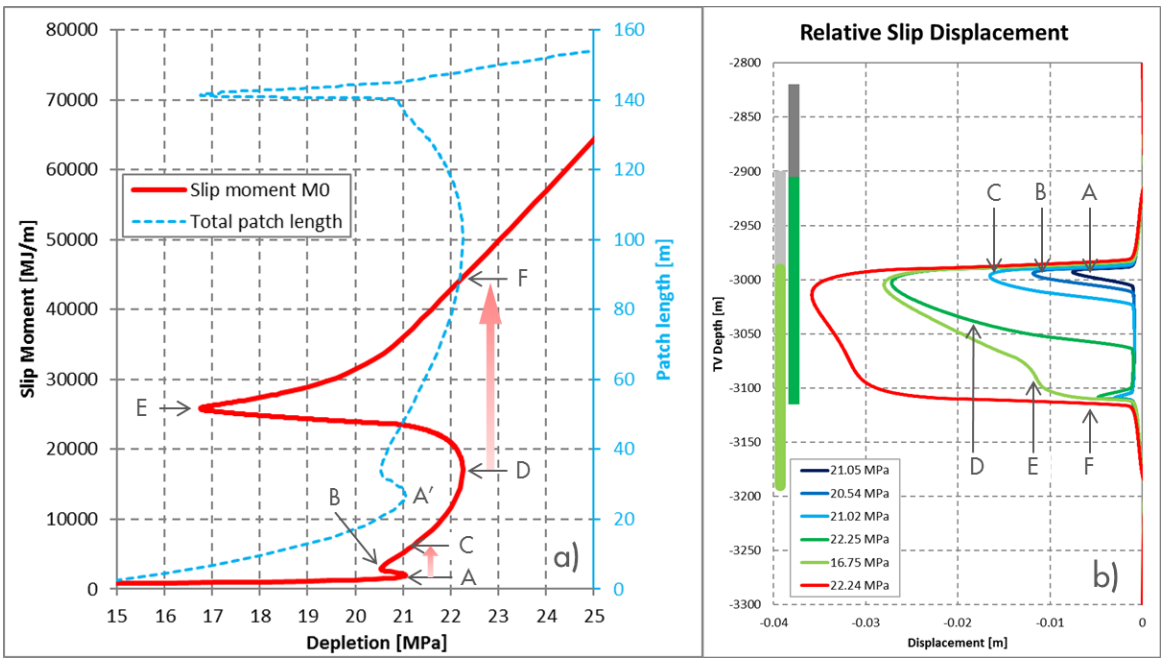

Figure A5.1: *a) Slip moment M_0 and total length of the two slip patches as a function of reservoir depletion from a static, post-bifurcation analysis for case mu55-182. The total patch length is the same as the red line in Figure A3.2 up to 21.05 MPa depletion, and b) the RSD as a function of depth along the fault plane for the various conditions indicated in a).*

Figure A5.1a show the slip moment M_0 (red line) and the total length of the slip patches (light-blue line) as a function of reservoir depletion. The slip moment, which calculated as described in APPENDIX 13, is a-seismic because of the static nature of the post-failure analysis. The slip moment is calculated in exactly the same way in the dynamic rupture analysis discussed in Appendix A.3.2, excepts that the slip moment is truly seismic. The length of the slip patches is defined by the length of the interval where SCU=1 (see sections 2.2). Figure A5.1b shows the Relative Slip Displacement (RSD) corresponding to the different stages A through F in the post-failure analysis. The red line for the total length of the two slip patches in Figure A3.2a is the same as the light-blue line in Figure A5.1a up to point A'. The slip moment M_0 is proportional with the area under the RSD curves in Figure A5.1b (see APPENDIX 13). A limit point is characterised by a local maximum of the reservoir depletion pressure for a monotonically increasing slip moment. The slip moment M_0 is a better metric to determine the limit point than the size of the slip patch, because it also increases if the slip displacement increases over a slip patch that is constant in size. Figure A5.1 shows two limit points: one in point A and one in point D. Limit point A occurs at the lowest reservoir depletion pressure, at 21.05 MPa.

The results in Figure A5.1 have been obtained using an arc-length solution method using the Relative Slip Displacement (RSD) of the interface elements as the controlling

degrees-of-freedom as described in section 2.4. Point A is called a bifurcation point, because (at least) two equilibrium conditions can be identified when increasing the slip moment in Point A: one is Point C, with a significantly larger slip moment and the same depletion pressure, and the second is the path towards Point B. The arc-length method in DIANA facilitates finding the path towards Point B by searching for a converged (static) equilibrium solution with an increasing slip moment M_0 and a decreasing reservoir depletion pressure.

This equilibrium path toward Point B in Figure A5.1a can be compared with that in a uniaxial extension experiment in the laboratory that is conducted under displacement control rather than force control (Rots and de Borst, 1989). In such experiment, the required tensile force is increased until the tensile strength of the sample is reached. The post-failure behaviour after reaching the tensile strength can be measured by allowing the test bench to reduce the tensile force under monotonically increasing extension. The sample would fail instantaneously at the limit point if the experiment would be conducted in a force-controlled manner. Reservoir depletion is also a force-controlled loading mechanism, which can lead to instantaneous failure (seismic rupture). The arc-length method allows a displacement-controlled simulation of the fault beyond the limit point (bifurcation point).

Figure A5.1 shows that the slip moment M_0 and the RSD is increasing from Point A to Point B under a reducing reservoir depletion pressure. Reservoir depletion is increasing again between Points B and C, while slip moment M_0 and RSD continue to increase. This implies that the fault is re-stabilising in Point B at a depletion of 20.54 MPa. This is about 0.48 MPa lower than the limit point in Point A. Fault stabilisation is caused by the RSD exceeding the critical slip displacement D_c of 0.01 m somewhere on the fault plane (Curve B in Figure A5.1b). This implies that the residual friction coefficient of 0.45 is reached over the interval where RSD $\geq D_c$ (Figure A5.2a). The fault strength is reducing in correspondence with the friction coefficient (Figure A5.2b), and the increasing size of the slip patch is clearly recognised from the SCU distribution (Figure A5.2c). So, the residual friction coefficient determines the depletion level at which the fault is re-stabilising. Point C is defined by the same depletion pressure as Point A, but with a larger slip moment M_0. The light-blue lines in Figure A5.2 at 21.02 MPa reservoir depletion is the closest point for which equilibrium results is calculated (the arc-length method employs displacement control, not force control).

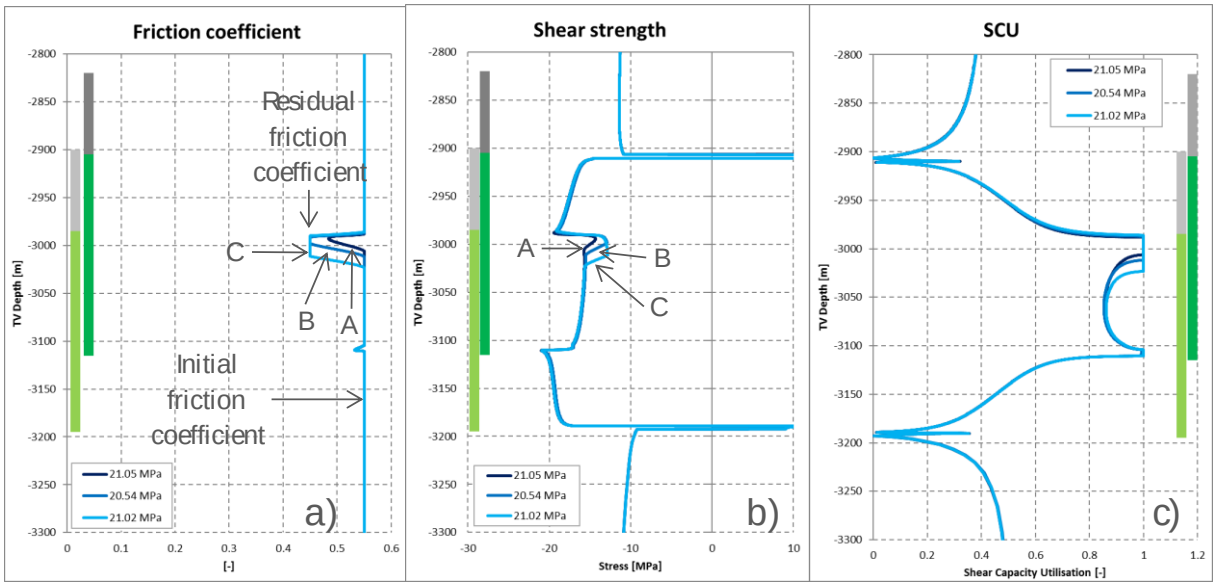

Figure A5.2: *a) The friction coefficient, b) the shear strength distribution, and c) the Shear Capacity Utilisation (SCU) as a function of depth at Points A, B and C (as indicated in Figure A5.1) for case mu55-182.*

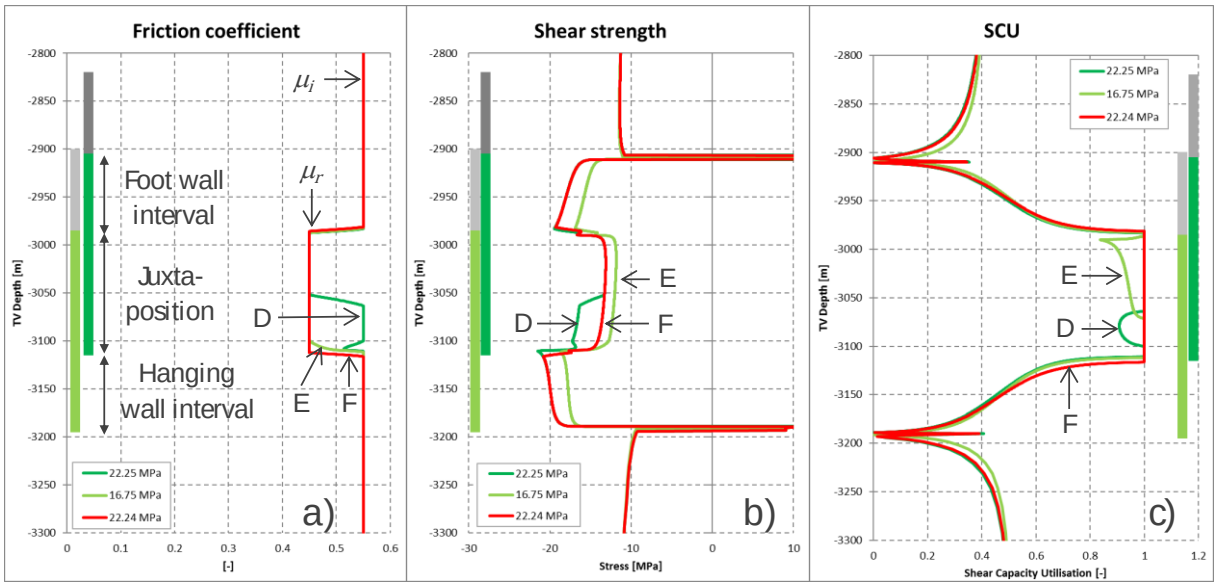

Figure A5.3: *a) The friction coefficient, b) the shear strength distribution, and c) the Shear Capacity Utilisation (SCU) as a function of depth at Points D, E and F (as indicated in Figure A5.1) for case mu55-182.*

A second limit point is found in Point D at 22.25 MPa reservoir depletion and is caused by the merging of the to slip patches. The RSD distribution at the point of instable equilibrium (Point D in Figure A5.1b) shows two slip patches, while the RSD distribution at the point of re-stabilisation (Point E at 16.75 MPa depletion) shows only one large slip patch. The slip displacement increases substantially from Point E to Point F due to the increasing reservoir depletion to 22.25 MPa, while the length of the slip patch hardly increases. The latter suggests that the sharp SCU reduction over the hanging wall interval, indicated by "F" in Figure A5.1c, also contributes to the re-stabilisation after the second fault instability.

The merging of the two slip patches after the second limit point is also recognised from Figure A5.3. The incremental slip displacement between the limit point D and the re-stabilisation point E (Figure A5.1b) causes the friction coefficient to reduce from the initial value 0.55 to the residual value 0.45 (Figure A5.3a) over the deepest part of the juxtaposition interval. The shear stress also reduces over the shallow part of the juxtaposition interval and the foot wall and hanging wall intervals due to the 5.5 MPa lower reservoir depletion at 16.75 MPa (light-green line in Figure A5.3b). The fault stabilises in Point E because sufficient shear stress carrying capacity is available in the Foot wall and Hanging intervals as indicated by the significantly smaller SCU in Figure A5.3c. Further increase of the slip moment is only possible by increasing the reservoir pressure (Figure A5.1a). The increase of slip moment between Point E and Point F is mainly accommodated by an increase of the slip displacement, while the size of the slip patch hardly increases (Figure A5.1b). The incremental reservoir depletion between Point E and Point F is possible because the fault strength increases due to increasing normal stress on the fault plane (Figure A5.3b).

The SCU is equal to 1 at the tips of the slip patch during the bifurcation path from Point D to Point E (Figure A5.3c) and SCU< 1 over the remainder of the existing slip patch. For Point D, the slip patch has not extended yet over the deepest part of the juxtaposition interval, as indicated by the SCU<1 (dark-green line). For Point E, the SCU=1 over this interval, and SCU<1 over the interval just above it (light-green line). This implies that the existing slip patch is unloading because of a reduction of reservoir depletion from point D to E.

The seismic event caused by the merging of the two slip patches is expected to be larger than caused by the instability of the shallow slip patch. This is motivated by the substantial larger increase of slip moment M_0 from Point D to Point F (27.3 GJ/m) compared to the increase from Point A to Point C (3.3 GJ/m) as indicated in Figure A5.1a. Dynamic rupture simulation should confirm this finding from the static analysis.

In Figure A5.4, the post-failure analysis results given Figure A5.2 are compared with the results obtained from the dynamic rupture analysis of the Base Case discussed in APPENDIX 3. The static post-failure analysis and the dynamic rupture analysis have the same starting point at a reservoir depletion of 21.05 MPa. This is represented by the dark-blue lines for the RSD in Figure A5.4a, for the friction coefficient in Figure A5.4b, and for the SCU in Figure A5.4c. The light-blue lines represent the results obtained from the post-failure analysis in Point C (Figure A5.1), whereas the red lines represent the results from the dynamic rupture analysis after 0.7 s. This is well after the seismic rupture is arrested after about 0.4 s.

The slip distribution and size of the shallow slip patch are very similar between the two analyses except that the slip patch is somewhat further developed in the dynamic rupture analysis. The shallow slip patch extends in the same direction and the RSD distribution is similar in shape between the static and dynamic analyses, while the RSD over the second, deep slip patch is the same. The difference is explained by the absence of mass velocity in the static analysis that is increasing after nucleation and is decreasing once the residual friction coefficient is reached. The deceleration of mass in the dynamic rupture analysis requires mobilisation of addition shear stress along the fault plane, leading to a larger slip patch and thus a larger release of formation strain, pressure energy and seismic moment in the dynamic rupture analysis. Therefore, the post-failure analysis provides an under-estimation of the size of the RSD, the slip patch size, and thus the slip moment M_0. On the other hand, the post-failure analysis provides insight into both limit points and their relative order of magnitude.

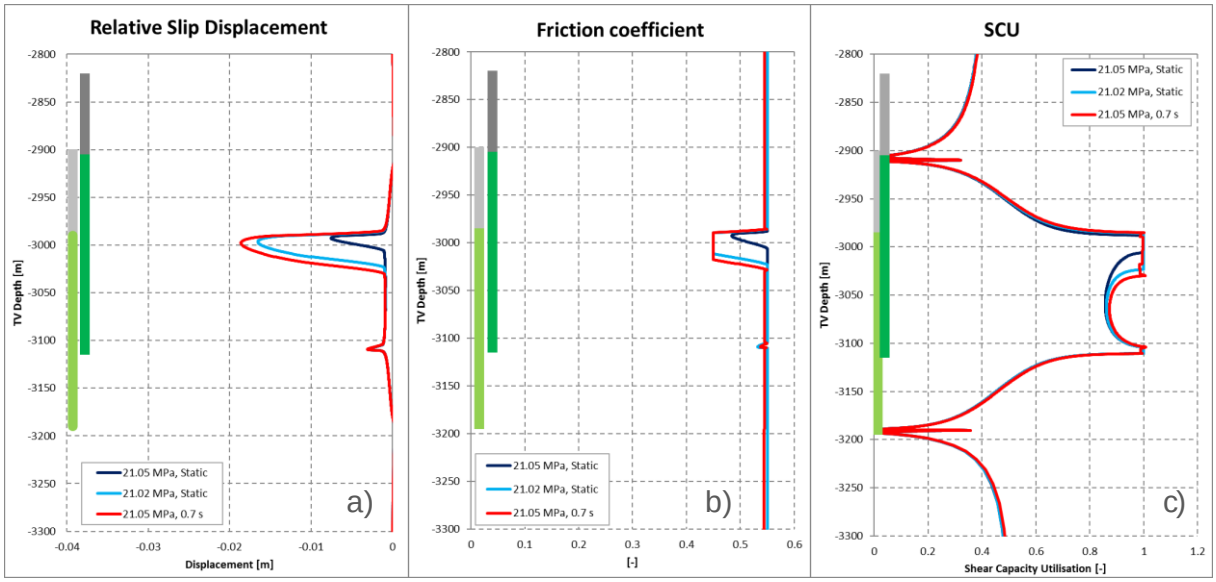

Figure A5.4: *Comparison between a) the Relative Slip Displacement (RSD), b) the friction coefficient, and c) the Shear Capacity Utilisation (SCU) as a function of depth after the seismic event in the Base Case (case mu55-182), obtained from the static (light-blue lines) and dynamic rupture analysis (red lines).*

Conclusions:

The post-failure analysis of the Base Case discussed in this appendix demonstrates that the depletion level at which onset of seismic rupture is found in the dynamic rupture analysis discussed in section 3.2 and Appendix A.3.2 is accurate. Furthermore, the static post-failure analysis in this appendix shows a similar Relative Slip Displacement over the shallow slip patch, with the understanding that the magnitude of the slip displacement and the size of the slip patch is somewhat under-estimated. This is explained by the velocity of the rock mass that needs to be decelerated in the dynamic rupture simulation, and which is ignored in the static post-failure analysis. The second, deep slip patch is stable in both analyses.

The static post-failure analysis, shows that a second limit point and associated seismic event is present at a larger reservoir depletion level. The first seismic event is caused by instability of the shallow slip patch, and is arrested when the residual friction coefficient is reached over a part of the fault. The second seismic rupture is caused by merging of the two slip patches, and is expected to have a larger seismic slip moment than the first seismic rupture at this location.

APPENDIX 6. RESIDUAL FRICTION COEFFICIENT

The influence of the residual friction coefficient μ_r on the simulated seismic rupture is evaluated in this appendix. The slope of the descending branch of the linear slip-weakening relationship W_μ (Figure A6.1) is kept the same as in the Base Case (APPENDIX 3), because it strongly influences the depletion level at which onset of seismic rupture occurs (Uenishi and Rice, 2003, and Buijze et al., 2015) and thereby the moment magnitude of the simulated seismic event. The slope in the Base Case is calculated from the initial and residual friction coefficient of μ_i = 0.55 and μ_r = 0.45 respectively, and the critical slip displacement D_c = 0.01 m according to $W_\mu = (\mu_i - \mu_r)/D_c = 0.01\ mm^{-1}$. The slope W_μ is kept constant by adjusting the critical slip displacement D_c in conjunction with the residual friction coefficient (Table A6.1).

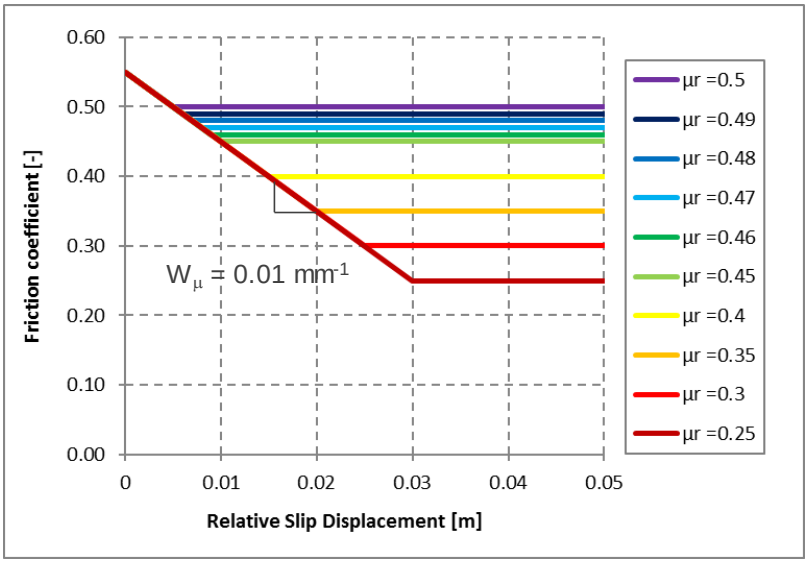

Figure A6.1: Linear slip-weakening relationships with an initial friction coefficient of 0.55 and a residual friction coefficient between 0.25 and 0.50 and a slope Wμ = 0.01 mm-1 of the descending branch.

Table A6.1: Overview of the analysis cases and the fault slip parameters used. The Base Case discussed in APPENDIX 3 is highlighted in bold.

Case	Cohesion [MPa]	Initial friction coefficient [-]	Residual friction coefficient [-]	Critical slip displacement [m]
Mu55-181	0	0.55	0.50	0.005
Mu55-182	**0**	**0.55**	**0.45**	**0.010**
Mu55-183	0	0.55	0.40	0.015
Mu55-184	0	0.55	0.35	0.020
Mu55-185	0	0.55	0.30	0.025
Mu55-186	0	0.55	0.25	0.030
Mu55-187	0	0.55	0.49	0.006
Mu55-188	0	0.55	0.48	0.007
Mu55-189	0	0.55	0.47	0.008

Mu55-190	0	0.55	0.46	0.009

In sections A.6.1, the different development of the a-seismic slip patches with increasing reservoir depletion is discussed for a residual friction coefficient larger than the Base Case ($0.45 \leq \mu_r \leq 0.50$). In section A.6.2, attention is focussed on the case with $\mu_r = 0.50$, followed by a comparison of all cases with $0.48 \leq \mu_r \leq 0.50$ in section A.6.3. In section A.6.4, the seismic rupture is discussed for a residual friction coefficient smaller than the Base Case ($0.25 \leq \mu_r \leq 0.45$).

Smaller values than 0.25 for the residual friction coefficient are not considered, because this would lead to ongoing seismic rupture along the entire fault plane. This implies that the residual friction is too small to carry the assumed initial, pre-production in-situ stress condition (Buijze, 2015). This lower bound also correspond with experimental values obtained by Di Torro et al. (2011). Evidence for a smaller residual friction coefficient would require reconsideration of other modelling assumptions in general, and the in-situ stress condition. A residual friction coefficient larger than 0.50 converges to a fault without slip-weakening, in which no fault instability and associated seismic rupture occurs (van den Bogert, 2015).

A.6.1. Onset of seismic rupture for $0.45 \leq \mu_r \leq 0.50$

In this section, the onset of seismic rupture is evaluated for cases with a residual friction coefficient $0.45 \leq \mu_r \leq 0.50$ in Table A6.1. The slope in the slip-weakening diagram W_μ = 0.01 mm^{-1} is the same for all cases (Figure A6.1). All other parameters are the same as for the Base Case in APPENDIX 3.

Onset of seismic rupture occurs at 21.05 MPa for all cases in Table A6.1 with a residual friction coefficient of 0.47 or smaller, which includes the Base Case discussed in APPENDIX 3. For these cases, the total length of the two slip patches develops identical and is about 27 m at the onset of seismic rupture at 21.05 MPa depletion (Figure A6.2). The maximum RSD is also identical with -0.0075 m. For the cases with $\mu_r \geq$ 0.48, onset of seismic rupture occurs at a significantly larger depletion level and increases with the residual friction coefficient. So, the onset of seismic rupture is not impacted by the residual friction coefficient if the difference with the initial friction coefficient exceeds a certain threshold level.

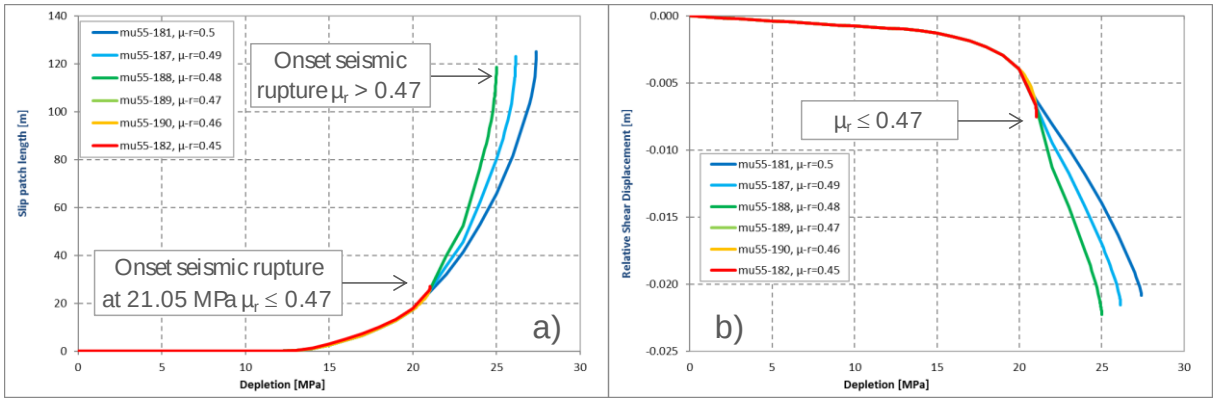

Figure A6.2: a) Total length of the slip patches, and b) the maximum Relative Slip Displacement (RSD) as a function of reservoir depletion for the cases in Table A6.1.

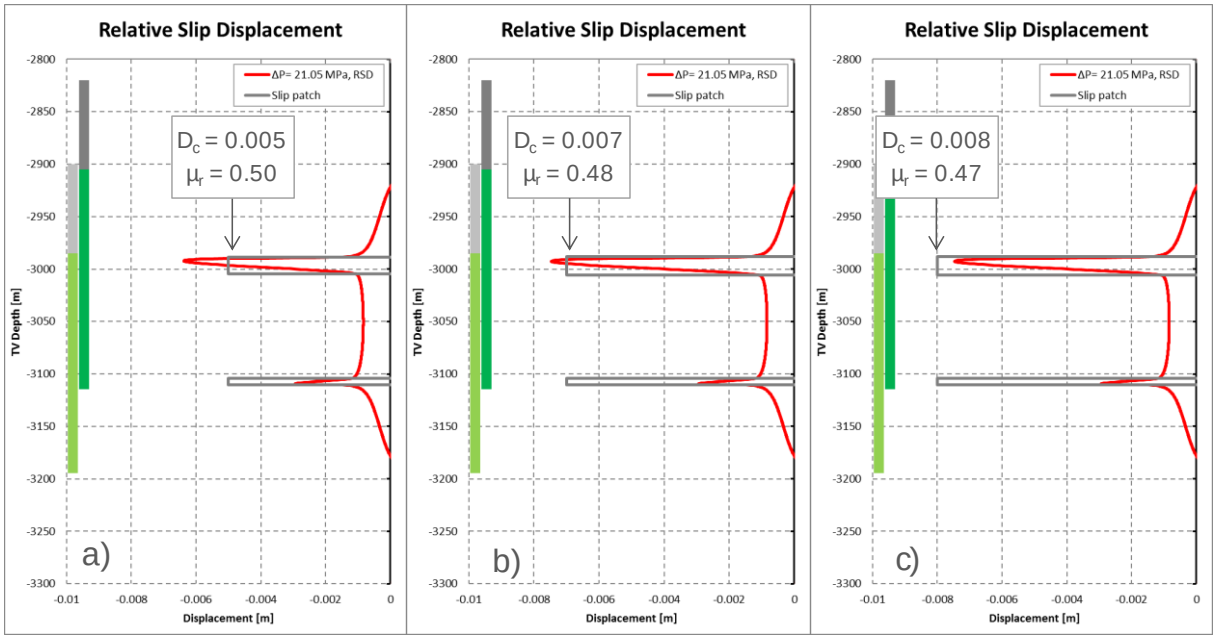

Figure A6.3: The Relative Slip Displacement (RSD) as a function of depth along the fault plane at 21.05 MPa reservoir depletion for μ_r = 0.50 (a), μ_r = 0.48 (b), and μ_r = 0.47 (c). Negative RSD values indicate downward slip of the hanging wall relative to the foot wall.

The existence of a threshold level is explained by the RSD at 21.05 MPa reservoir depletion for the different cases. For the case with μ_r = 0.50 (Figure A6.3a) and μ_r = 0.48 (Figure A6.3b), the calculated maximum RSD is larger than the critical slip displacement D_c of 0.005 and 0.007 respectively. However, for the case with μ_r = 0.47 the maximum RSD of -0.0075 is smaller than the critical slip displacement of 0.008 (Figure A6.3c). In the latter case, onset of seismic rupture is found at 21.05 MPa reservoir depletion, whereas reservoir depletion can be continued for the other two cases. Reaching the critical slip displacement and thus the residual friction coefficient has a stabilising effect on the fault, because the fault strength does not further reduce with increasing slip displacement (APPENDIX 3 and APPENDIX 5). So, reaching the critical slip displacement in cases with $\mu_r \geq 0.48$ suppresses instability of the shallow slip patch. Instability of the shallow slip patch is not suppressed for cases with $\mu_r \leq 0.47$. For these cases, onset of seismic rupture occurs at the same reservoir depletion, because the identical slope in the slip-weakening diagram enforces the same RSD and stress distribution along the fault plane (compare Figure A6.3c and Figure A3.3a). So, onset of seismic rupture is the same for cases with the same slope W_μ in the slip-weakening diagram provided that the critical slip displacement D_c is not reached.

The threshold value for the residual friction coefficient to cause onset of seismic rupture at 21.05 MPa is about 0.475. For the Base Case, the maximum absolute RSD is about 0.0075 m and about 75% of the critical slip displacement of 0.010 m. This means that the friction coefficient is also 75% down the descending branch of the slip-weakening diagram from 0.55 to 0.45. This implies that fault instability is reached at 21.05 MPa reservoir depletion for a residual friction coefficient smaller than about 0.475 provided that the slope of the descending branch in the linear slip-weakening diagram W_μ = 0.01 mm^{-1}. The threshold value of the friction coefficient can be estimated from any of the cases in Table A6.1 that become unstable at 21.05 MPa.

A.6.2. Seismic rupture for μ_r = 0.50

Figure A6.4 shows the fault condition at the onset of seismic rupture at 27.40 MPa depletion for the case with μ_r = 0.50 (case mu55-181, Table A6.1). Figure A6.4a shows that the RSD exceeds the critical slip displacement D_c of 0.005 m over the two almost merging slip patches (grey boxes). Correspondingly, the friction coefficient has dropped to the prescribed residual value over a large part of both slip patches (Figure A6.4b). Hardly any shear stress carrying capacity is left on the fault between the two slip patches indicated by the SCU of almost 1 (red line in Figure A6.4b). This is also seen by the small difference between the shear stress (red line) and shear strength (dark blue line) between the two slip patches in Figure A6.4c. The shear strength τ_{max} is calculated from the actual friction coefficient in Figure A6.4b and the normal effective stress (not shown) and the cohesion according to expression (2.1). This part of the fault is in unstable equilibrium because the shear stress is larger than the residual shear strength over this part of the fault (light blue line). In this case, seismic rupture is caused by merging of the two slip patches.

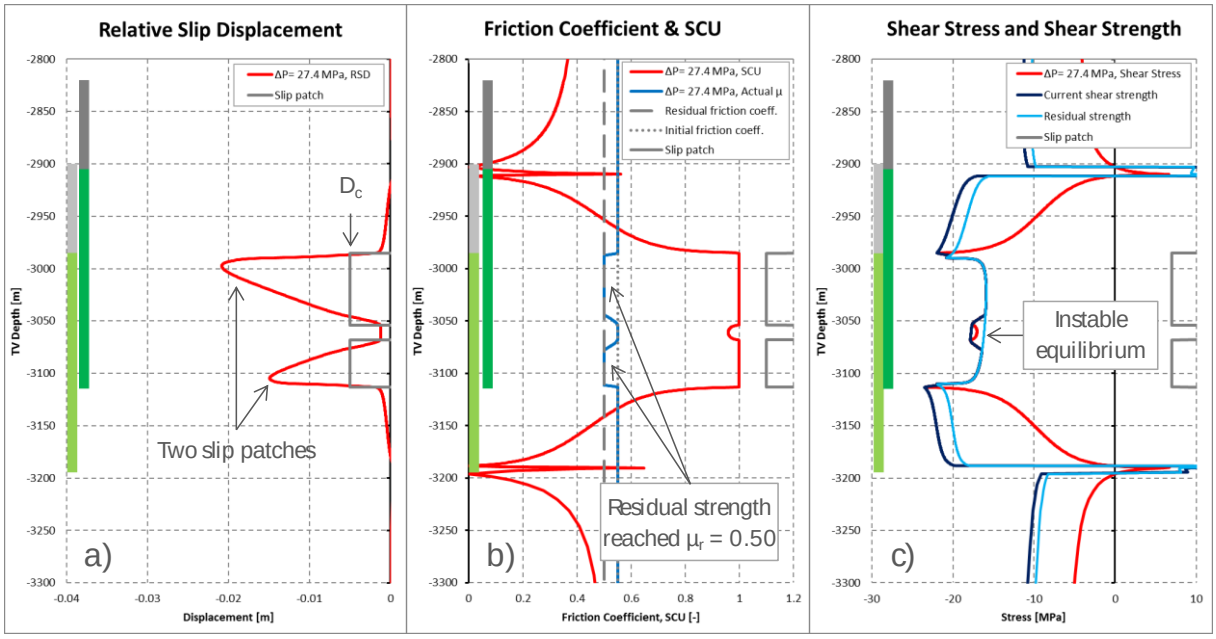

Figure A6.4: a) the Relative Slip Displacement (RSD), b) the Friction coefficient and Shear Capacity Utilisation, and c) the Shear stress and Shear strength as a function of depth along the fault plane at the onset of fault slip at 27.40 MPa depletion for case mu55-181 with μ_r = 0.50 (Table A6.1)

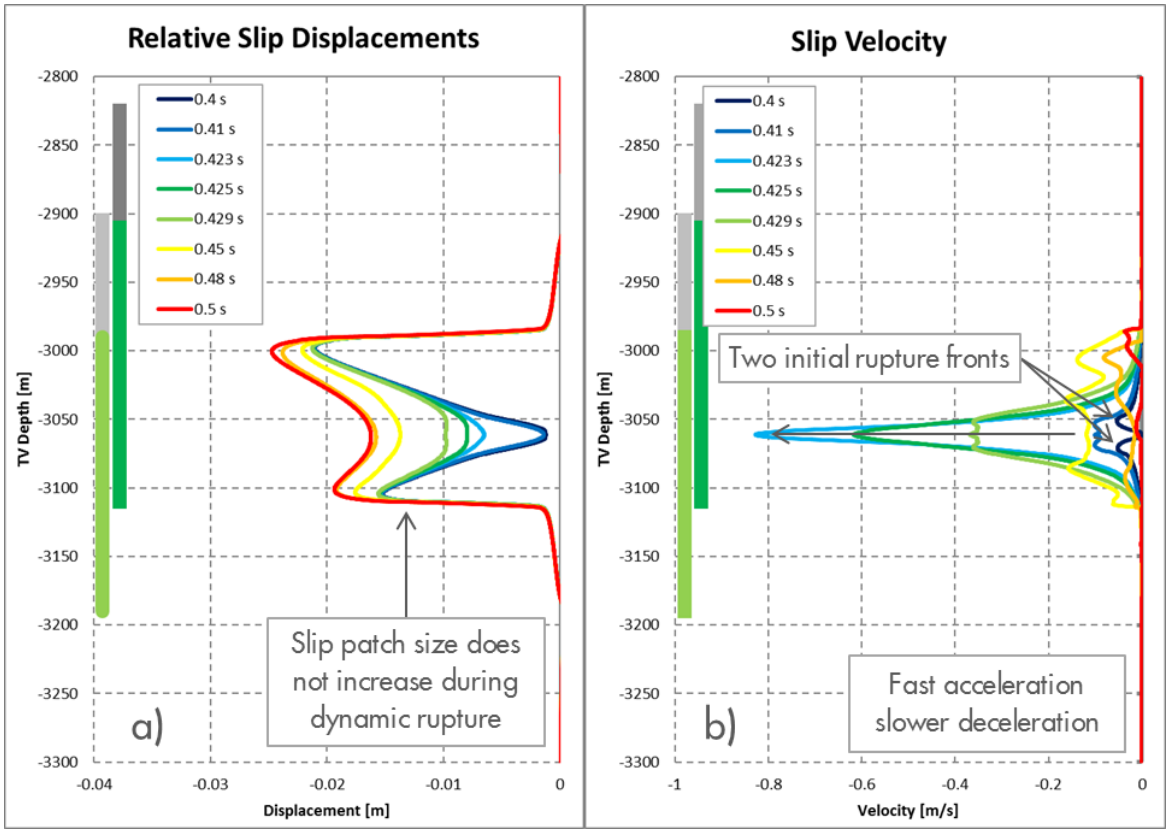

Figure A6.5: *a) Relative Slip Displacement, and b) relative slip velocity as a function of depth along the fault plane at various moments during the rupture process for μ_r = 0.50 (case mu55-181). Slip displacement and slip velocity are oriented tangential to the fault plane and are given for the hanging wall relative to the foot wall.*

The relative slip velocity at the start of the seismic rupture after 0.4 s in Figure A6.5 shows two peak values: one at the bottom of the shallow slip patch and one at the top of the deep slip patch, thereby confirming that seismic rupture is caused by merging of the two slip patches. The maximum (absolute) relative slip velocity of about 0.83 m/s is reached after 0.423 s and is exactly located between the two slip patches. Note that the RSD does not significantly increase over most of the two original slip patches until this point in the simulation. Deceleration of the seismic rupture occurs more gradual and extends the RSD over the entire area of the two merged slip patches. However, the merged slip patch does not extend beyond its original size, and remains contained to the juxtaposition interval of the fault (where the fault is exposed to reservoir depletion on both sides).

A.6.3. Seismic rupture for $0.45 \leq \mu_r \leq 0.50$

Two different root causes of fault instability and seismic rupture are found when increasing the residual friction from 0.45 in the Base Case (APPENDIX 3) to 0.50 (previous section), namely:

- Instability is caused by the shallow slip patch at 21.05 MPa reservoir depletion for cases with $\mu_r \leq 0.47$. This occurs if the limit point is reached before the maximum RSD reaches the critical slip displacement D_c.
- Instability is caused by the merging of the two slip patches for $\mu_r \geq 0.48$. Instability of the shallow slip patch is suppressed if the RSD reaches D_c before depletion

reaches the limit point. Incremental reservoir depletion is required to propagate the two slip patches a-seismically until they merge.

The results of all cases in Table A6.1 are compared in this section

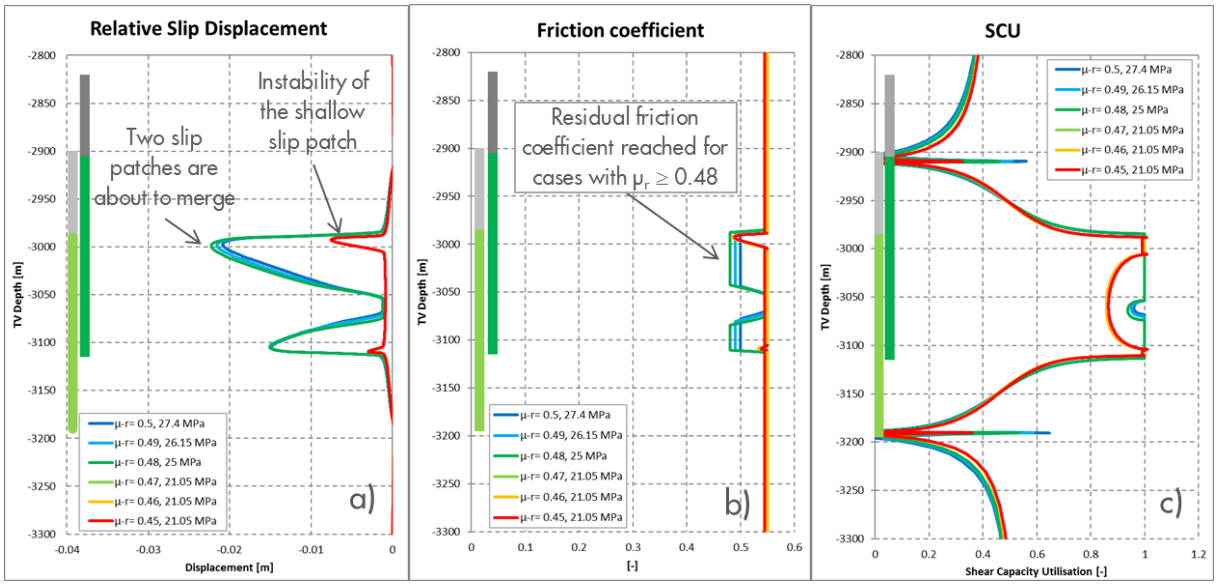

Figure A6.6: *a) The Relative Slip Displacement (RSD), b) the friction coefficient, and c) the Shear Capacity Utilisation (SCU) as a function of depth for all cases in Table A6.1 with 0.45 ≤ μ_r ≤ 0.50.*

Figure A6.6 shows the Relative Slip Displacement, the actual friction coefficient and the Shear Capacity Utilisation at the onset of seismic rupture for all cases in Table A6.1. The red lines valid for all cases with $\mu_r \leq 0.47$, show an instable shallow slip patch at the top of the hanging wall, and – at some distance – a small stable slip patch at the bottom of the foot wall. In cases with $\mu_r \geq 0.48$, reservoir depletion can be increased beyond 21.05 MPa, because the residual friction coefficient is reached over both slip patches (Figure A6.6b). The fault strength τ_{max} as given by (2.1) increases with increasing value of the residual friction coefficient and so does the reservoir depletion at the onset of seismic rupture (Figure A6.2). This allows the RSD and the slip patches to be much larger compared to the cases with $\mu_r \leq 0.47$. Seismic rupture is caused by merging of the two slip patches in cases with $\mu_r \geq 0.48$.

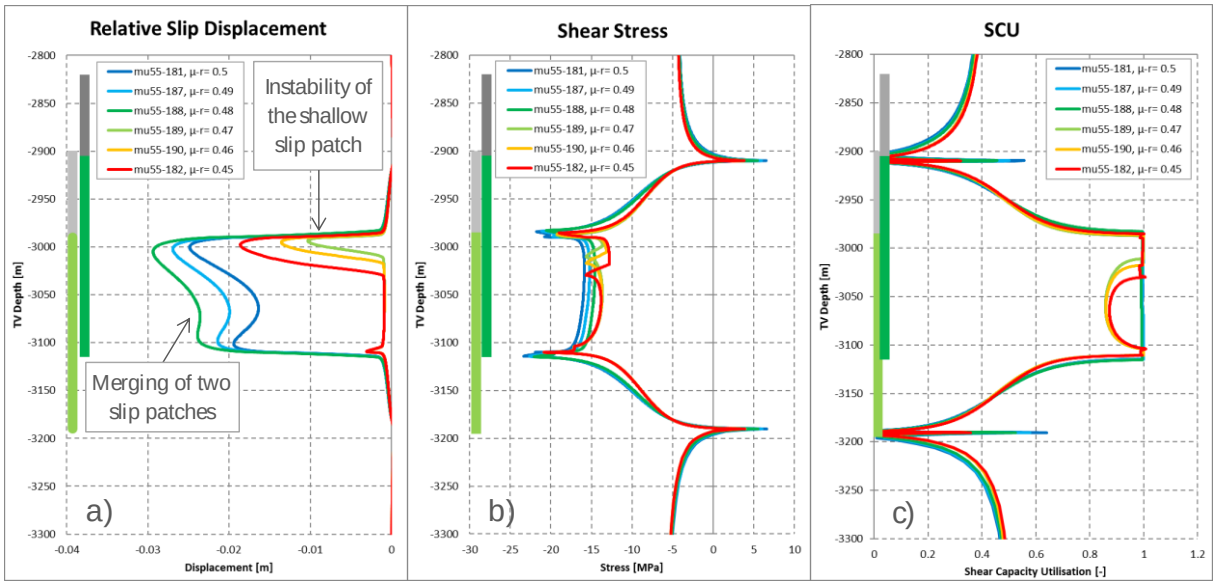

Figure A6.7: a) The RSD, b) the Shear stress, and c) the SCU as a function of depth along the fault plane after 0.7 s when the seismic event has ceased for the cases with 0.45 ≤ μ_r ≤0.50

Figure A6.7 shows the RSD after the seismic rupture for all six cases in the range 0.45 ≤ μ_r ≤ 0.50. The dark blue lines represent the case with μ_r = 0.50 of Figure A6.5. The RSD after the seismic event increases when lowering the residual friction coefficient from 0.50 to 0.48 (dark green line), but the size of the slip patch is not significantly larger. Note that the seismic event occurs at a lower reservoir depletion for μ_r = 0.48 compared to μ_r = 0.50 (Figure A6.2). Lowering of the residual friction coefficient to 0.47 causes the shallow slip patch to become instable at 21.05 MPa, as explained in the previous sections. For this case, the maximum RSD increases from about -0.0075 m to -0.010 m during the seismic rupture (light green line). Further reduction of the residual friction coefficient increases the size of the slip patch as well as the maximum RSD. The red lines represent the Base Case results with μ_r = 0.45 and are also shown in Figure A3.9.

The development of the total length of the two slip patches, the maximum RSD and other rupture parameters are given in Figure A6.8 and Figure A6.9 as a function of time (the same line colours are used for each case as in Figure A6.7). Note that time shifts have been applied to align the results of different cases. Formation strain and pressure energy is released (negative) during the rupture process and is dissipated by fault slip and is radiated as (kinetic) wave energy. Seismic Moment M_0 is dependent on the rupture mechanism and the residual friction coefficient. Seismic efficiency (equation A12.12) is not constant, but also dependent on the rupture mechanism and the residual friction coefficient. The Base Case results (red lines) are the same as in Figure A3.9.

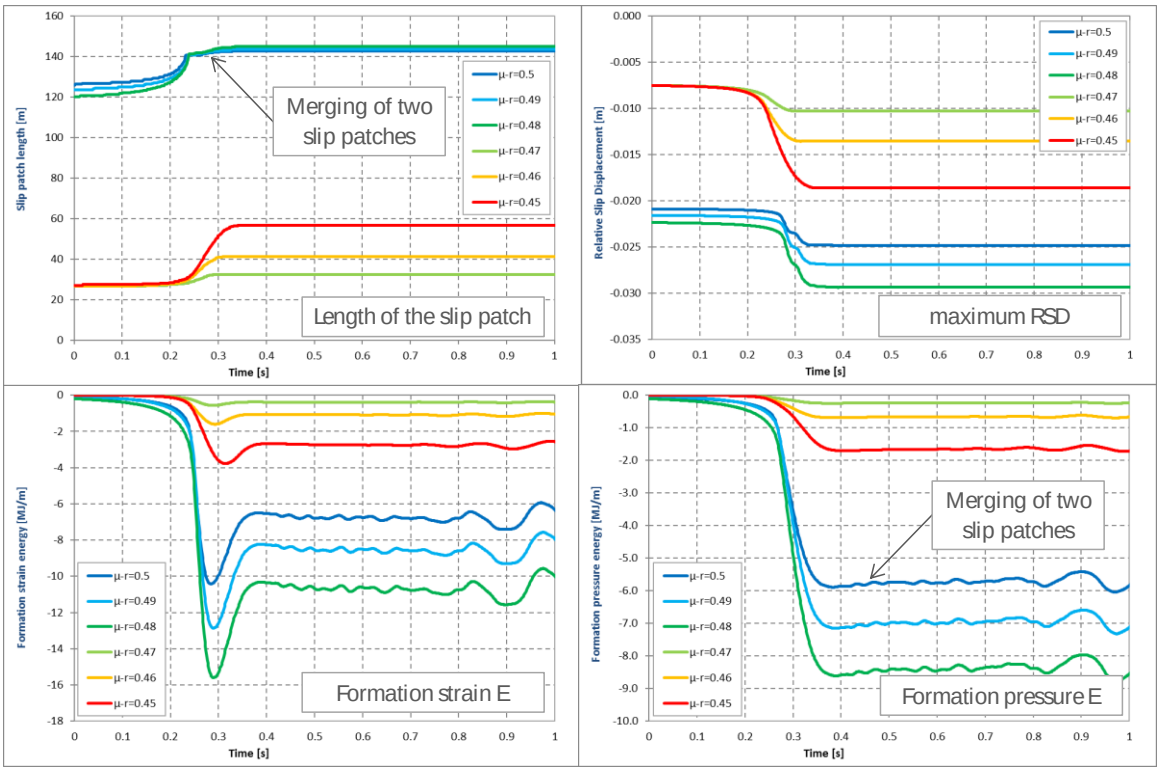

Figure A6.8: The total length of the two slip patches, the maximum RSD, the formation strain energy and the formation pressure energy as a function of time for the cases with 0.45 ≤ μ_r ≤0.50

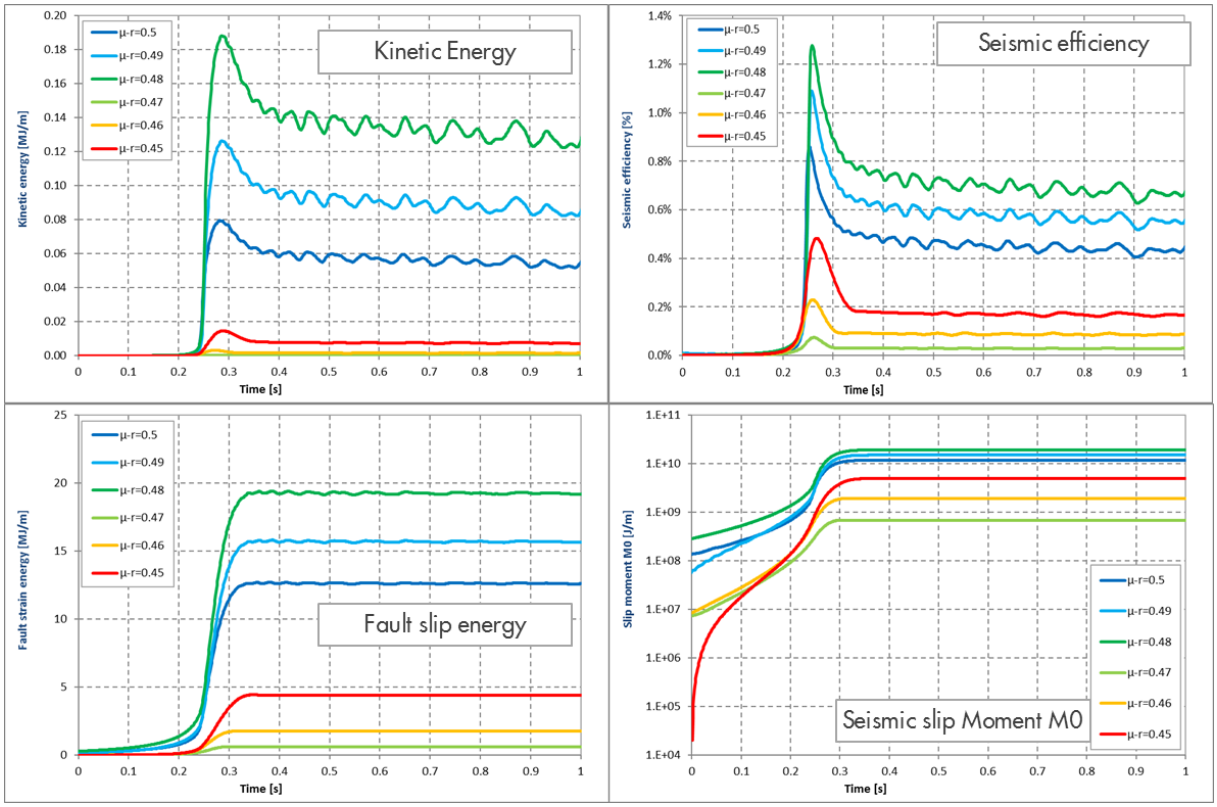

Figure A6.9: The kinetic energy, seismic efficiency, energy dissipated by fault slip and the seismic slip moment M0 as a function of time for the cases with 0.45 ≤ μ_r ≤ 0.50

A.6.4. Seismic rupture for μ_r = 0.35

So far, two different rupture mechanisms are presented in this appendix. One is caused by instability of the shallow slip patch and occurs for cases with 0.45 ≤ μ_r ≤ 0.47, while a second rupture mechanism is caused by merging of the two slip patches and occurs for cases with 0.48 ≤ μ_r ≤ 0.50. In this section, a third rupture mechanism is presented that occurs if μ_r = 0.35 (case mu55-184 in Table A6.1). Onset of seismic rupture occurs at 21.05 MPa reservoir depletion and is caused by instability of the shallow slip patch as for all cases with μ_r ≤ 0.47 in Table A6.1. At this depletion level, the fault condition is the same as discussed for the Base Case in Appendix A.3.1.

The third Rupture Mechanism is presented in Figure A6.10 for the case with μ_r = 0.35 by means of the RSD and the (relative) slip velocity during seven stages of the simulation. The nucleation phase of the rupture (indicated by 0 in Figure A6.10a and b) is characterised by an increasing parabolic relative slip velocity distribution over the shallow slip patch. Velocity front 1 decelerates after entering upwards into the foot wall interval where the SCU is lower (see the Base Case results with μ_r = 0.45 in Figure A6.6c, and APPENDIX 4 for the interval definition). Velocity front 2 accelerates and extends the slip patch in downward direction over the juxtaposition interval. The relative slip velocity at each point on the fault plane reduces once the velocity front has passed and the residual friction coefficient is reached (D_c = 0.02 m for this case). In comparison, the maximum relative slip velocity for the Base Case with D_c = 0.01 m that nucleates under the same stress conditions is only 0.35 m/s (Figure A3.4). The (peak) velocity and patch size keeps increasing relative to the Base Case because of the lower residual friction coefficient.

The two slip patches start to merge after about 0.32 s (Figure A6.10c and d). Velocity front 3 develops very quickly just above the deep slip patch between 0.330 and 0.338 s. In the meantime, main velocity front 2 accelerates, while front 1 continues deceleration. The RSD graph shows that additional slip occurs over the deepest part of the slip patch, which does not extend downwards so far. Note that the time interval between the curves in Figure A6.10c and d is not constant.

Velocity front 3 exists very briefly and merges with velocity front 4 that develops when the slip patch enters the hanging wall interval of the fault (Figure A6.10e and f). Velocity front 3 reduces between 0.338 s and 0.344 s (indicated by arrow 3), when front 4 appears at the interface between the foot wall reservoir and the basement. Velocity front 2 continues to accelerate and front 1 continues to decelerate.

The deceleration phase of the rupture starts after about 0.344 s (Figure A6.10g and h). The peak velocity of main front 2 is reducing, while also front 4 decelerates due to the less favourable stress conditions over the hanging wall interval of the fault. Velocity front 1 is stable and increases the slip patch marginally in upwards direction. Velocity front 4 dies out rather quickly, being hardly unable to extend the slip patch between 0.36 and 0.37 s (Figure A6.10i and j). The main velocity front 2 is reducing steadily, while front 1 remains stable at low velocity. Furthermore, it is noticed that the (downward) relative slip velocity is increasing again in the shallow half of the slip patch.

The brief revival of velocity front 2 between 0.376 and 0.4 s (Figure A6.10k and l) may be explained by the reduced fault strength caused by velocity front 4 previously. Also, velocity front 1 accelerates somewhat, because of the arrival of velocity waves coming from below. Figure A6.10m and n shows the last episode of the rupture process in which the main velocity front 2 has ceased, and some last waves move the shallow boundary of the slip patch a little further.

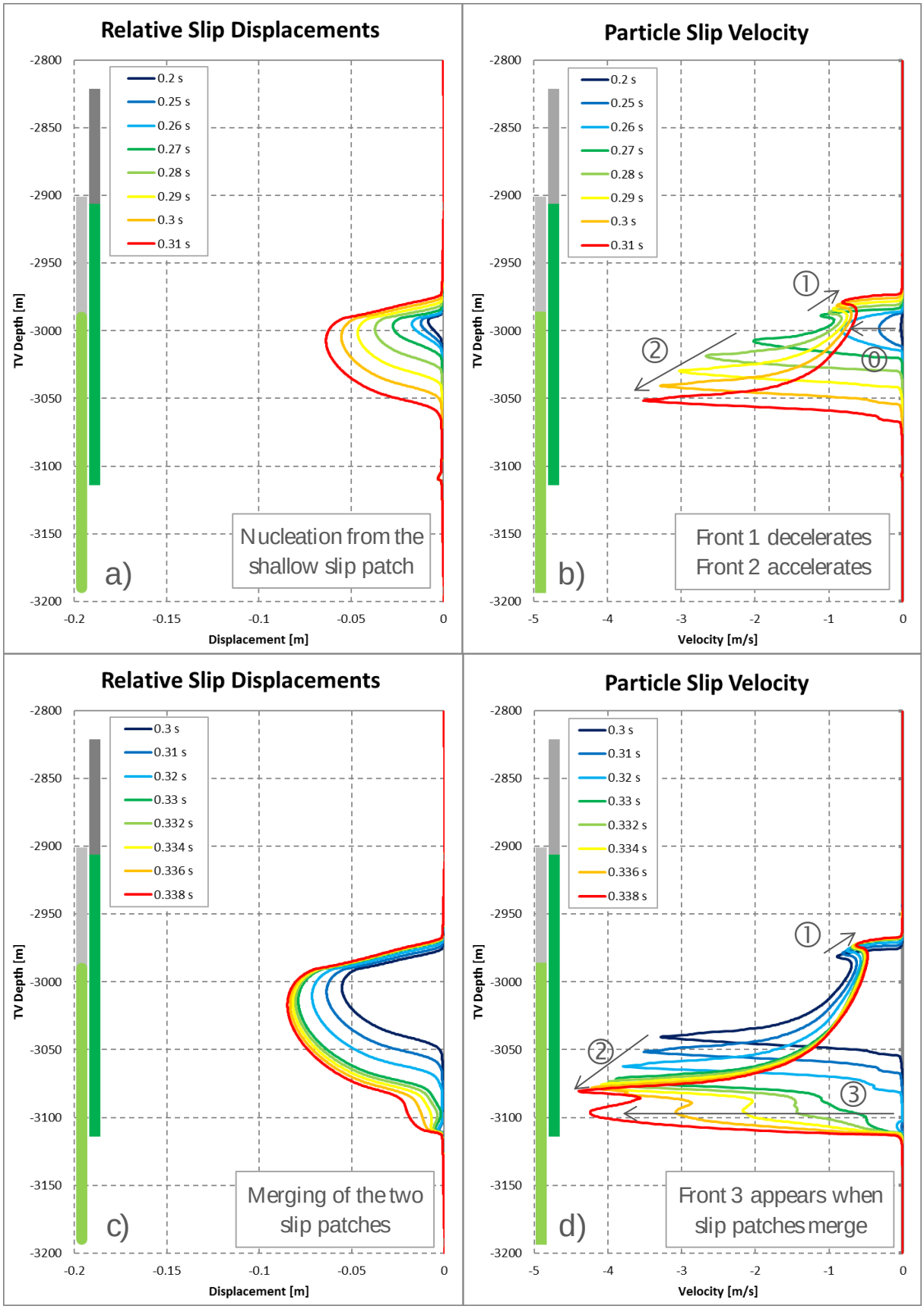

Figure A6.10: The Relative Slip Displacement and relative slip velocity as a function of depth along the fault plane for during the nucleation (top) and merging phase (bottom) for μr = 0.35 (case mu55-184).

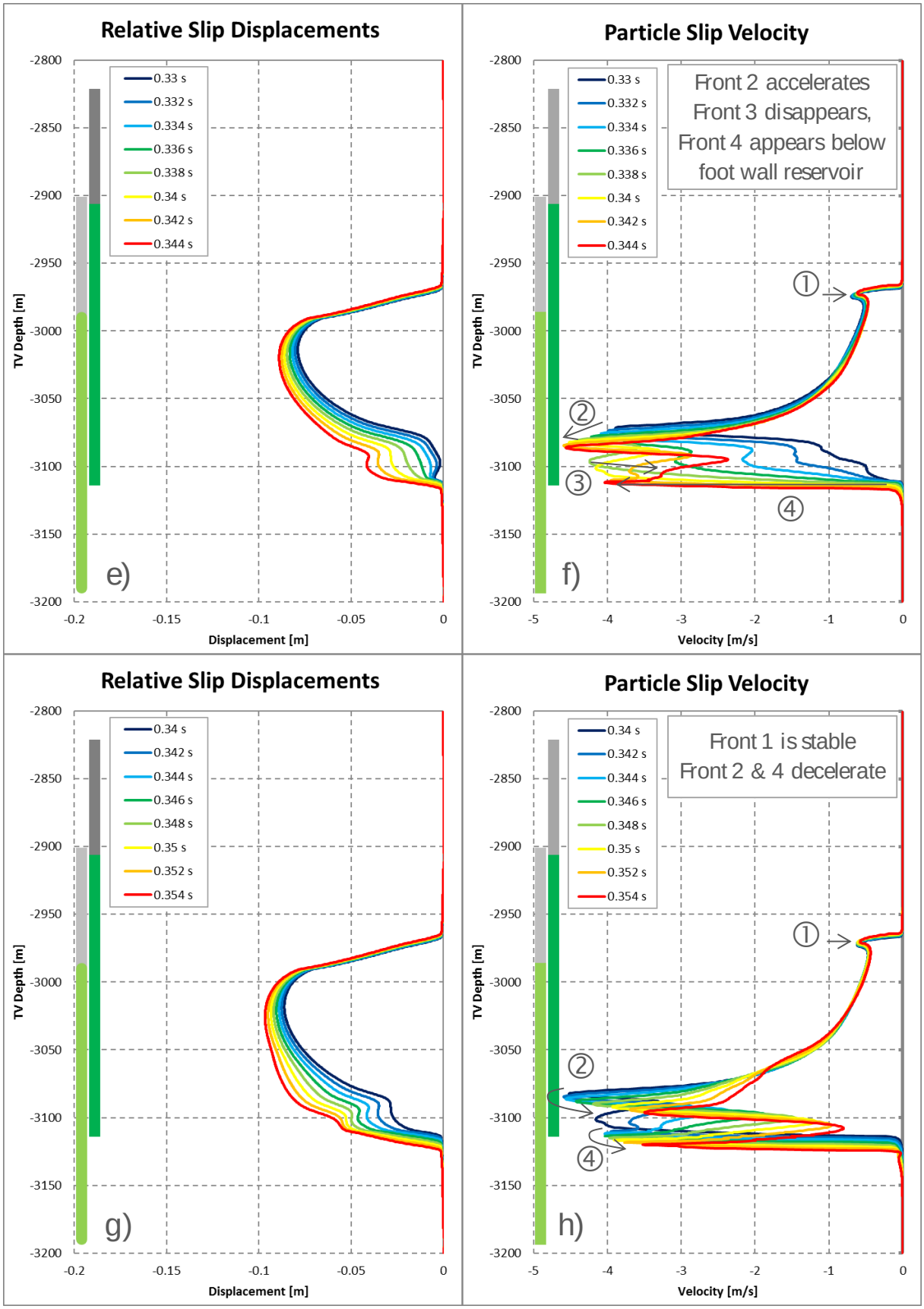

Figure A6.10: The Relative Slip Displacement and relative slip velocity as a function of depth along the fault plane for during the acceleration (top) and deceleration phase (bottom) for μ_r = 0.40 (case mu55-183), continued.

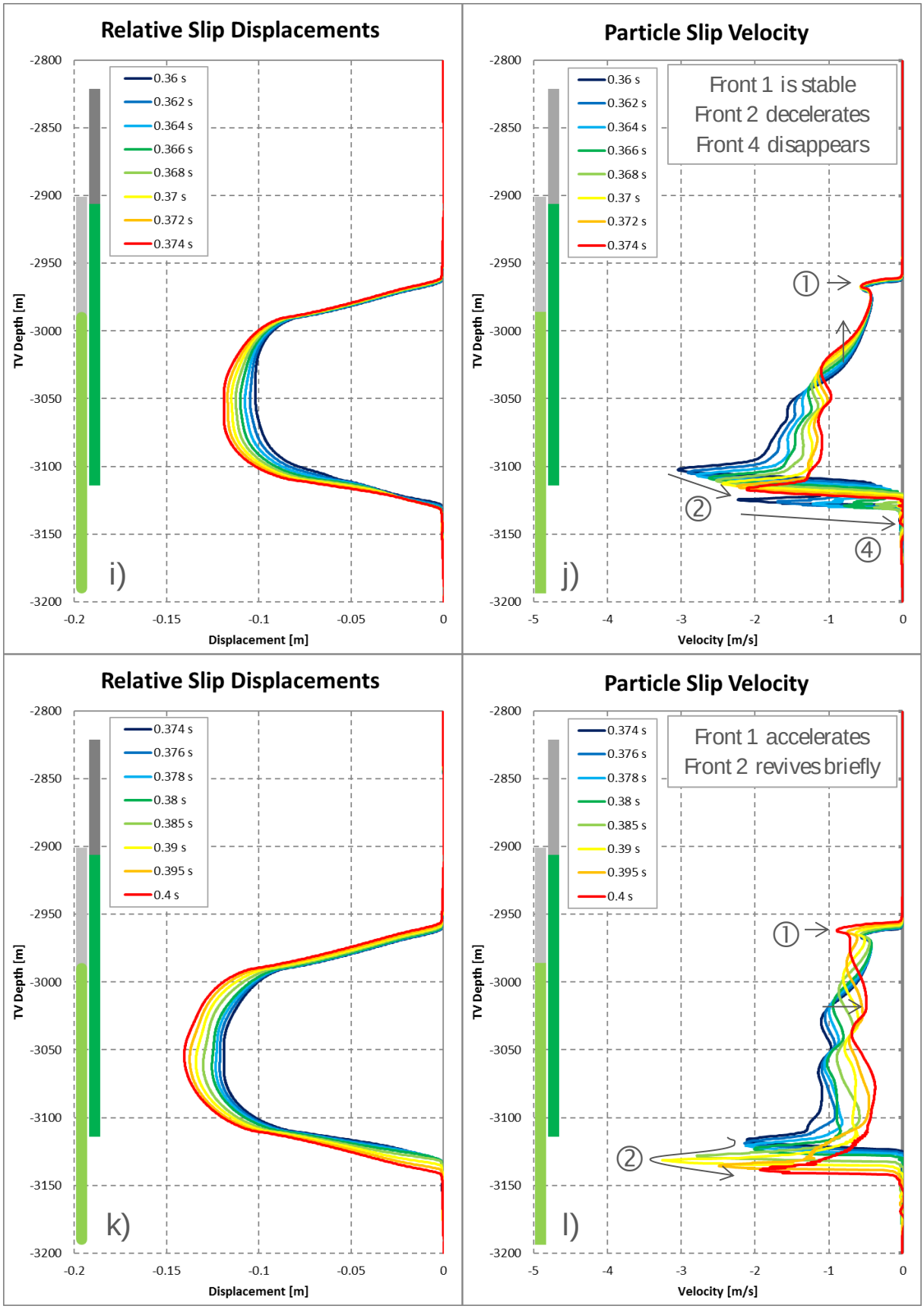

Figure A6.10: The Relative Slip Displacement and relative slip velocity as a function of depth along the fault plane for during the acceleration (top) and deceleration phase (bottom) for μ_r = 0.40 (case mu55-183), continued.

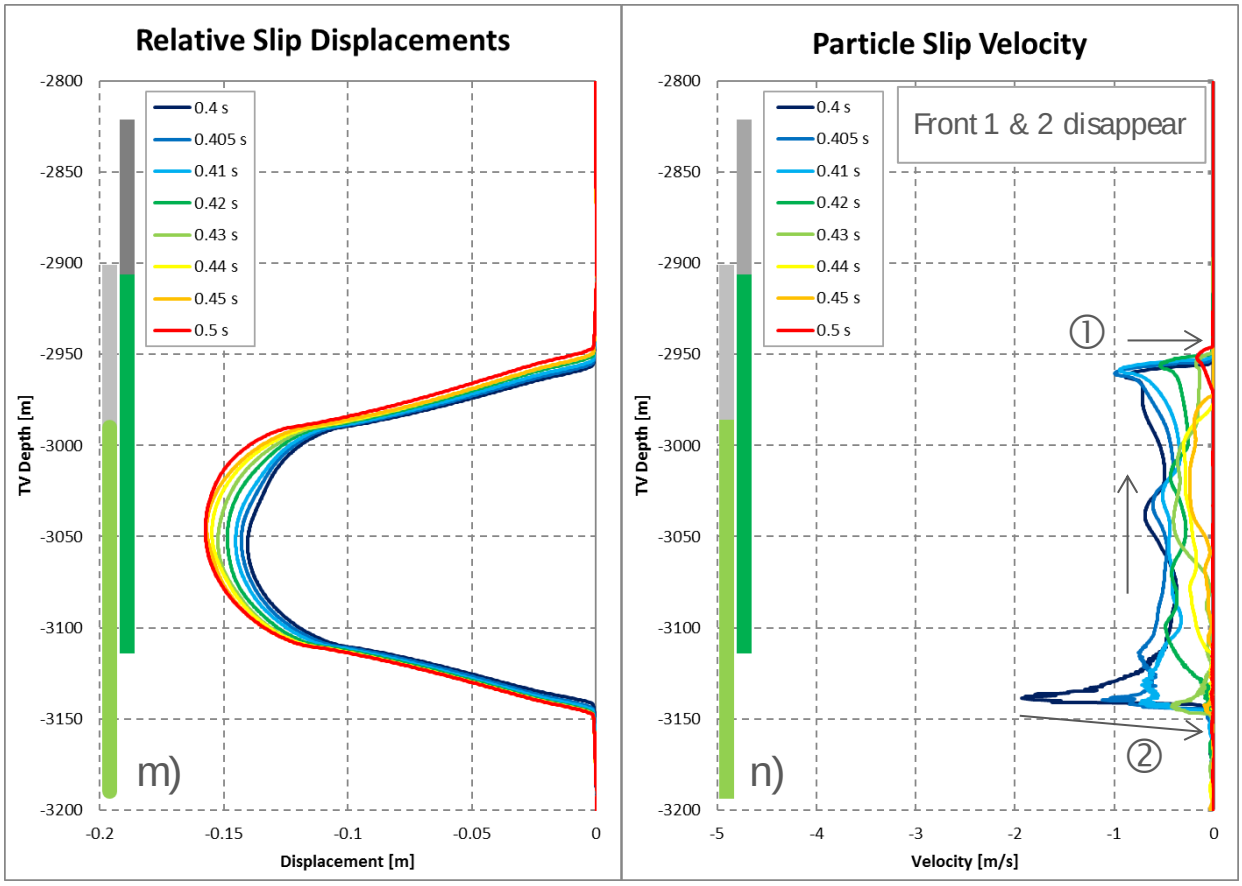

Figure A6.10: The Relative Slip Displacement and relative slip velocity as a function of depth along the fault plane for during the acceleration (top) and deceleration phase (bottom) for μ_r = 0.40 (case mu55-183), continued.

The rupture mechanism for all cases with $0.25 \leq \mu_r \leq 0.40$ can be described by nucleation at the shallow slip patch, downward acceleration, and subsequent merger with the deep slip patch, followed by propagation into the fault hanging wall interval. The slip patch propagates further into the hanging wall interval for a lower value of the residual friction coefficient.

A.6.5. Overview of the rupture mechanisms

Three different rupture mechanisms have been discussed in this appendix, while using the same fault and reservoir geometry, the same initial friction coefficient of 0.55 and the same slope in the slip-weakening diagram at W_μ = 0.01 mm^{-1}. The residual friction coefficient is the only parameter that has been varied. The three rupture mechanisms are

- Rupture Mechanism 1: Merging of the two slip patches for $0.48 \leq \mu_r \leq 0.50$.
- Rupture Mechanism 2: Instability of the shallow slip patch without merging with the deep slip patch for $0.45 \leq \mu_r \leq 0.47$.
- Rupture Mechanism 3: Instability of the shallow slip patch and merging with the deep patch for $0.25 \leq \mu_r \leq 0.40$.

The three rupture mechanisms are recognised in Figure A6.11a that shows the RSD after the seismic rupture for a selection of the cases in Table A6.1. The dark-blue line for the case with μ_r = 0.50 (Rupture Mechanism 1) shows a slip patch over the juxtaposition interval, the light-blue the case for with μ_r = 0.45 (Rupture Mechanism 2)

shows a small slip patch at the top of the hanging wall reservoir formation, and the other cases with $\mu_r \leq 0.40$ (Rupture Mechanism 3) show a slip patch that extends into the hanging wall and foot wall intervals of the fault, while the maximum RSD is increasing with lower value for the residual friction coefficient. The slip patch propagates into the basement, below the hanging wall interval for the case with μ_r = 0.25 (mu55-186 in Table A6.1, red line). The irregular RSD distribution in the basement for this case is caused by the increased size of the interface elements, and reduces simulation accuracy.

The shear stress over the slip patch after the seismic rupture (Figure A6.11b) reflects the lower fault strength with reducing value for the residual friction coefficient. Note that the reservoir depletion at onset of fault rupture is the same for all cases, except for the case with μ_r = 0.50 (dark-blue line). This implies that the fault normal stress distribution is the same, and that the fault strength is proportional with the (residual) friction coefficient. Figure A6.11b shows the residual fault strength over the juxtaposition interval as the critical slip displacement is exceeded is all cases.

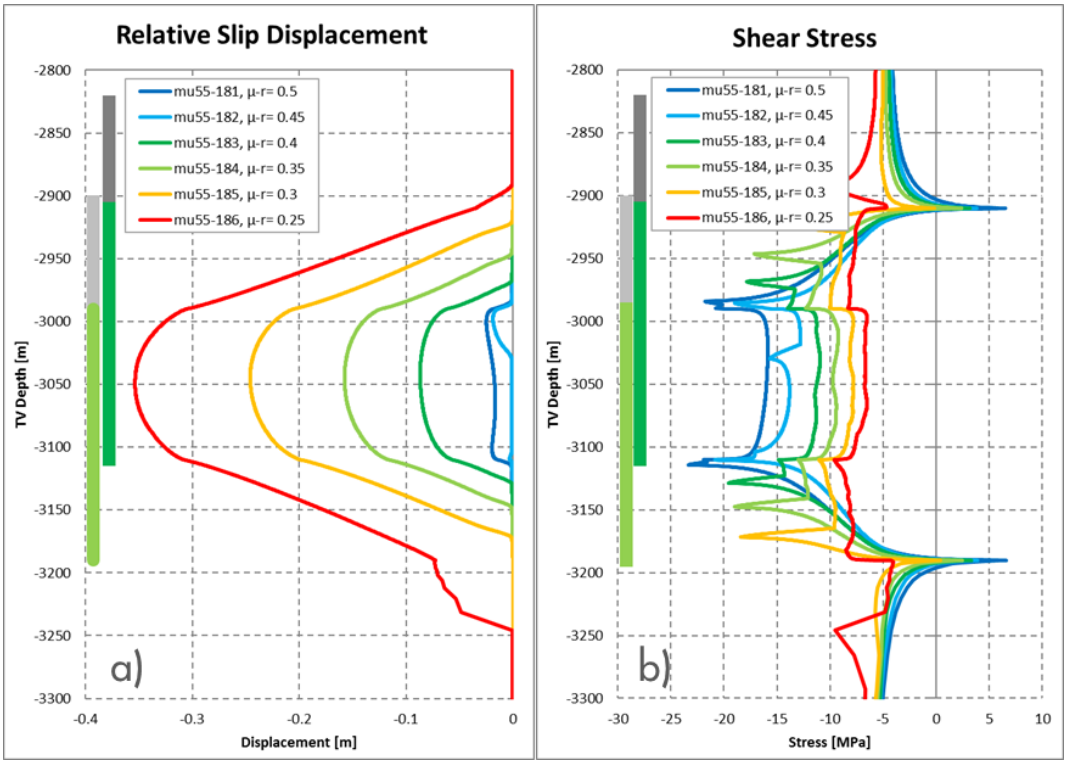

Figure A6.11: The Relative Slip Displacement (a), and the shear stress (b) after the seismic event (0.7 s) for the cases with a residual friction coefficient of 0.50, 0.45, 0.40, 0.35, 0.30 and 0.25.

The three different rupture mechanisms are also recognised in Figure A6.12 and Figure A6.13, which show various rupture parameters as a function of time. The increase of length of the two slip patches for Mechanism 3 starts at the same moment in time as Mechanism 2, because instability occurs under the same conditions. The total length of the slip patches is significantly larger if the patches merge in cases that exhibit Rupture Mechanism 3 ($0.25 \leq \mu_r \leq 0.40$) compared to Rupture Mechanism 2 ($0.45 \leq \mu_r \leq 0.47$) in which they remain separated. A similar step-change is found for the other parameters in Figure A6.12 and Figure A6.13: a lower value of the residual friction coefficient causes a larger release of formation stain and pressure energy, more kinetic energy and energy dissipated by fault slip, and a larger seismic efficiency and seismic slip moment for Mechanism 2 and Mechanism 3. The response for Mechanism

1 falls between those for Mechanism 2 and 3. The seismic efficiency also increases when assuming a smaller residual friction coefficient, which implies that kinetic energy transmitted from the seismic event increases more than proportional with the reduction of the friction coefficient.

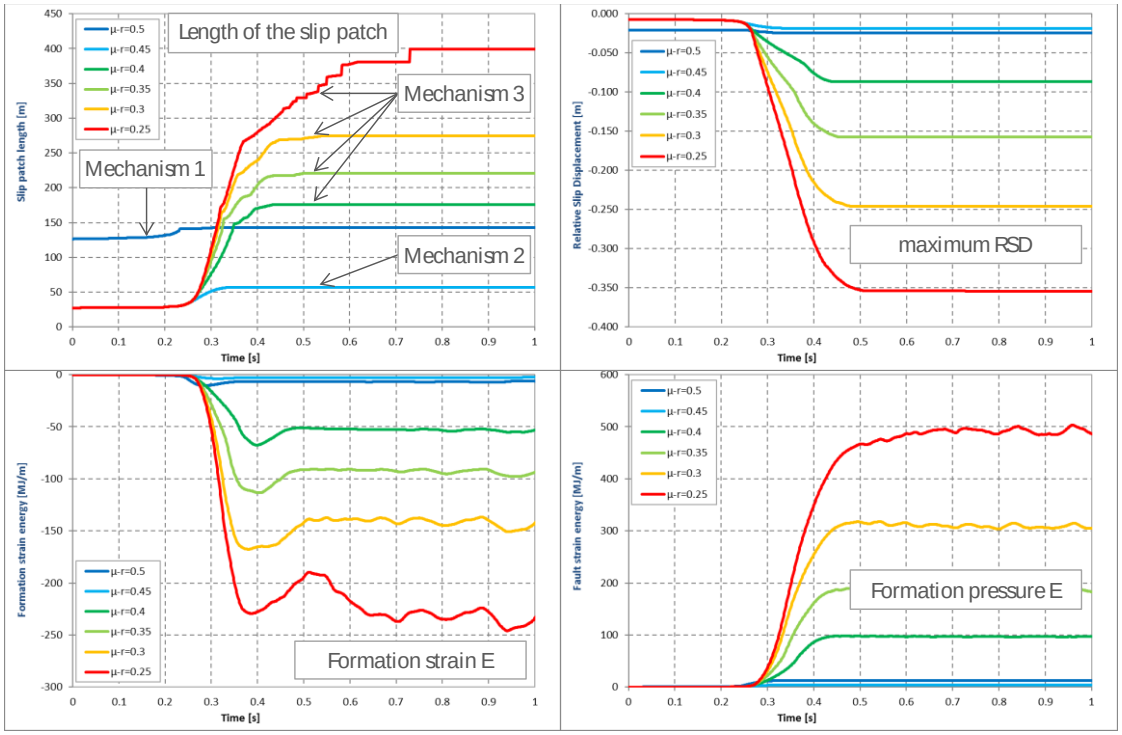

Figure A6.12: The total length of the two slip patches, the maximum RSD, the formation strain energy and the formation pressure energy as a function of time for the cases with 0.25 ≤μ_r ≤0.40

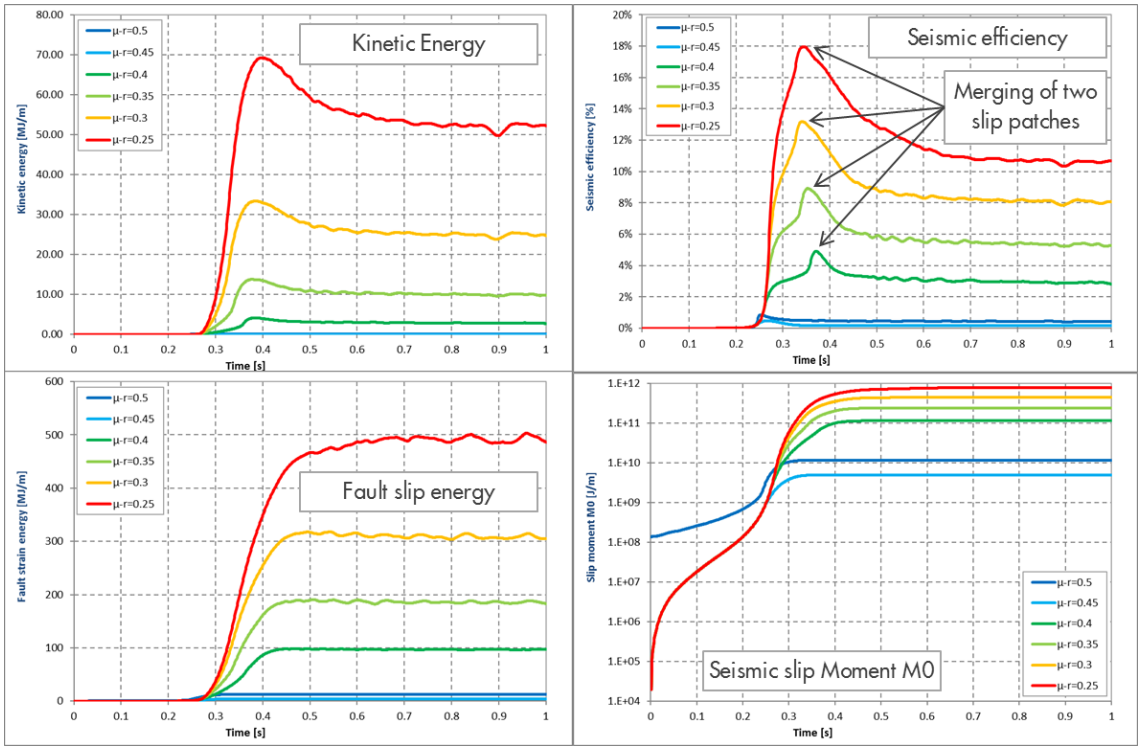

Figure A6.13: The kinetic energy, seismic efficiency, energy dissipated by fault slip and the seismic slip moment M0 as a function of time for the cases with 0.25 ≤ μ_r ≤ 0.40

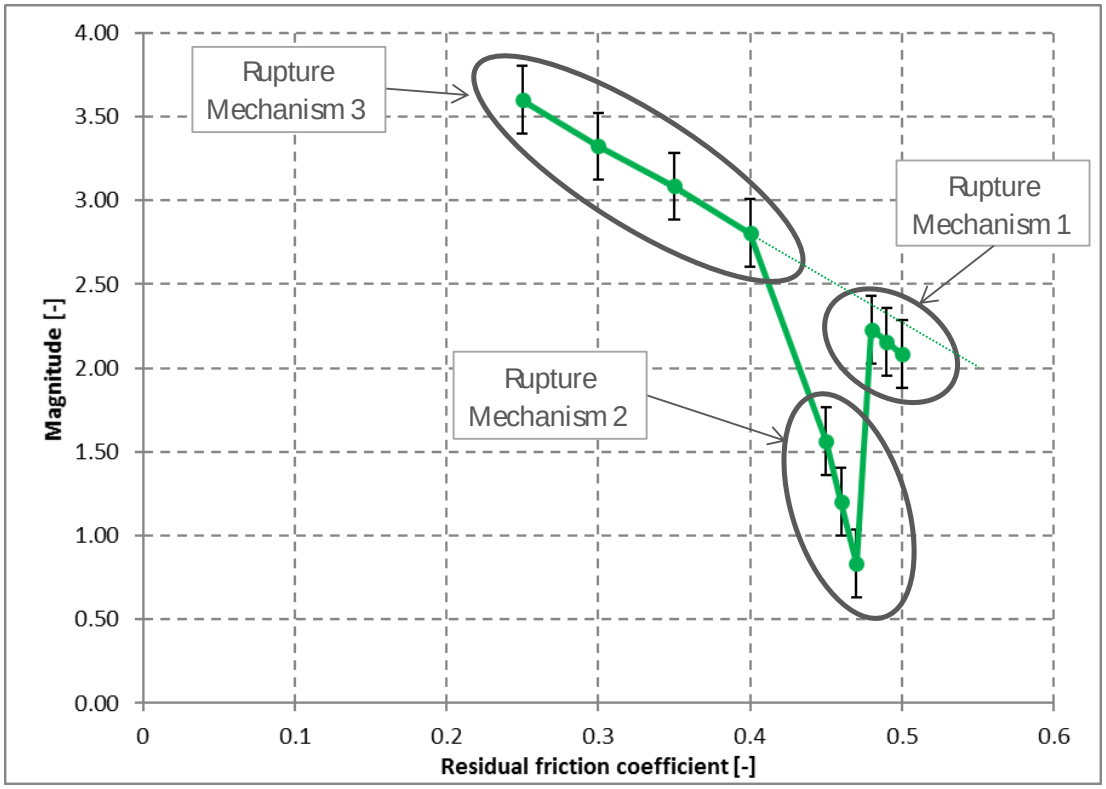

Figure A6.14: Moment magnitude M_w as a function of the residual friction coefficient for the cases in Table A6.1 Slip-weakening relationship is as indicated in Figure A6.1 with μ_i = 0.55 and W_μ = -0.01 mm^{-1}. The fault and reservoir configuration is the same as in the Base Case (APPENDIX 3).

Figure A6.14 shows a proportional increase of the moment magnitude M_w with a reduction of the residual friction coefficient for each rupture mechanism separately. Rupture Mechanism 2 generates significantly smaller seismic events and shows a distinctly different dependency on the residual friction coefficient in comparison with Rupture Mechanisms 1 and 3. This is attributed to the fact that Rupture Mechanism 2 does not include that merging of two slip patches, which releases more energy than seismic rupture of a single slip patch (Appendix A.6.5). The merging of two slip patches that Rupture Mechanism 1 and 3 share may also be the reason that the moment magnitude of these events follow almost the same trendline, albeit that the trendline for Rupture Mechanism 1 is somewhat below that for Rupture Mechanism 3, as indicated by the dotted line.

It is concluded that the moment magnitude is strongly influenced by the rupture mechanism, which is related to the merging of the two slip patches. Rupture Mechanism 2 results is smaller earthquakes than Rupture Mechanism 1 or 3 under the same conditions. The distance between the two slip patches as well as the residual friction coefficient is an influencing factor whether the two slip patches merge or not. The distance between the slip patches is determined by the reservoir thickness and offset.

APPENDIX 7. RESERVOIR OFFSET

The influence of the reservoir offset O on the simulated seismic rupture is evaluated in this appendix. Reservoir offset dominates the stress distribution along a fault plane that intersects a depleting reservoir formations, and therefore also dominates the onset of fault slip (van den Bogert, 2015) as well as the onset of seismic rupture (Buijze, 2016). To this end, the reservoir offset of the Base Case (APPENDIX 3) is varied between 0 and 400 m by adjusting the depth of the hanging wall reservoir formation, while keeping the foot wall at 2910 m depth. All other parameters are identical to the Base Case: the initial friction coefficient μ_i is 0.55, the cohesion C is negligible and the residual friction coefficient μ_r is 0.45, which is reached after a critical slip displacement D_c of 0.01 m. So, the slope in the slip-weakening diagram is W_μ = 0.01 mm^{-1}.

The fault stability condition is discussed for an offset smaller than reservoir thickness in section A.7.1, for an offset about equal to the reservoir thickness in section A.7.2, and for an offset larger than reservoir thickness in section A.7.3. The considered analysis cases are specified in each section, while a complete overview of all cases in this study is provided APPENDIX 2.

A.7.1. Offset smaller than reservoir thickness

In this section, a series of 16 analyses are presented (Table A7.1) with an offset smaller than the reservoir thickness of 200 m. This includes the Base Case is discussed in APPENDIX 3.

Table A7.1: Overview of analysis cases conducted for an offset smaller than the reservoir thickness of 200 m. Normalised offset is offset divided by reservoir thickness. The Base Case (APPENDIX 3) is highlighted in bold.

Case	Offset O [m]	Normalised offset Ō [-]
Mu55-121	0	0.000
Mu55-122	5	0.025
Mu55-123	10	0.050
Mu55-124	15	0.075
Mu55-125	20	0.100
Mu55-126	25	0.125
Mu55-132	30	0.15
Mu55-142	40	0.20
Mu55-152	50	0.25
Mu55-162	60	0.30
Mu55-172	70	0.35
Mu55-182	**80**	**0.40**
Mu55-192	90	0.45
Mu55-202	100	0.5
Mu55-212	120	0.6
Mu55-218	140	0.7

Mu55-222	160	0.8

A.7.1.1. ONSET OF SEISMIC RUPTURE

The impact of the reservoir offset on the linear-elastic stress distribution for different reservoir offset at 10 MPa depletion is shown in Figure A7.1. The green bars at the left-hand side represent the reservoir depth range for the case with an offset of 30 m, and normal stress is negative under compression. The normal effective stress on the fault plane (Figure A7.1a) is lower over the juxtaposition interval, where the fault is exposed to reservoir depletion on both sides, compared to the foot wall and hanging wall intervals where the fault is exposed to reservoir depletion from just one side. A lower normal effective stress implies that the fault strength is also lower in accordance with the assumed Mohr-Coulomb friction law.

The two shear stress peaks associated with the hanging wall reservoir are deeper for cases with a larger offset (Figure A7.1b). The other two shear stress peaks, at 2910 m depth and at 3110 m depth remain in the same location, because these are caused by depletion in the foot wall reservoir. Consequently, the distance between the two peaks in the SCU value (Figure A7.1c) is smaller if the reservoir offset is larger.

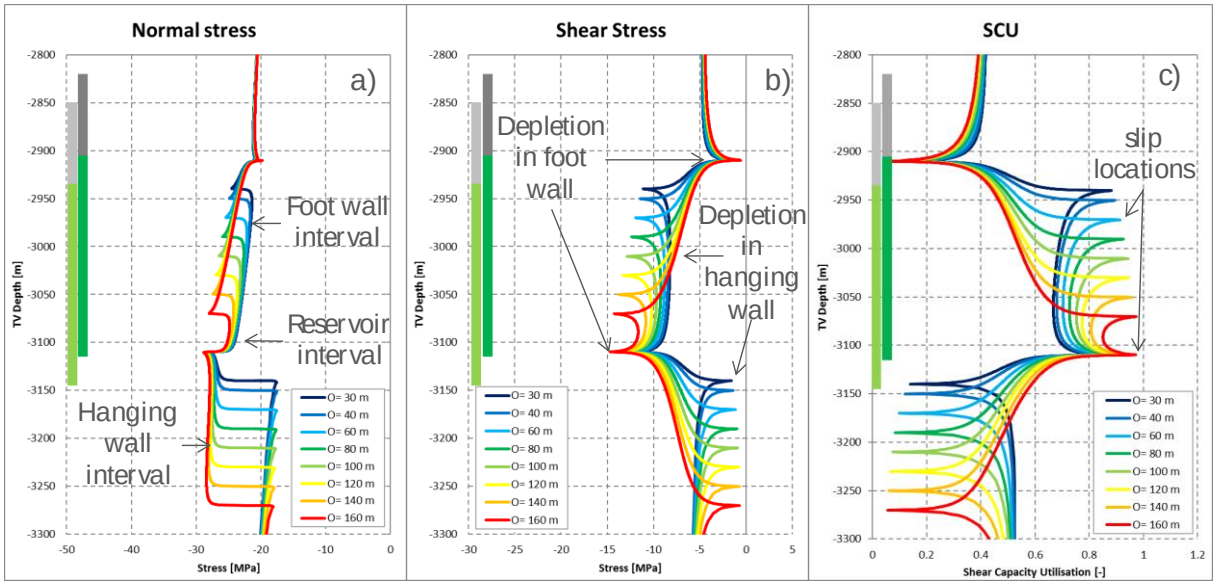

Figure A7.1: a) The effective normal stress distribution, b) the shear stress distribution and c) the Shear Capacity Utilisation (SCU) as a function of depth along the fault plane at 10 MPa reservoir depletion for different reservoir formation offset (O).

Onset of fault slip occurs at a lower depletion level with increasing reservoir formation offset (Figure A7.2). The onset of fault slip is determined when the SCU is equal to 1 in any interface element of 0.3 m on the fault plane, and thus when the length of the slip patch is larger than 0. Figure A7.2 confirms that all cases with an offset between 0 and 160 m are in an elastic stress condition at 10 MPa depletion. Onset of fault slip occurs at 10.5 MPa reservoir depletion in case of 160 m offset (red line), and at 15.6 MPa in case of 30 m offset (dark blue line). Onset of fault slip is determined by the initial friction coefficient and the cohesion, and is not impacted by the slip-weakening behaviour. Therefore, results are similar to those in a previous study (van den Bogert, 2015). The fault is mechanically stable and the slip is a-seismic for all cases in Figure A7.2, because it requires incremental reservoir depletion to extend the size of the slip patch.

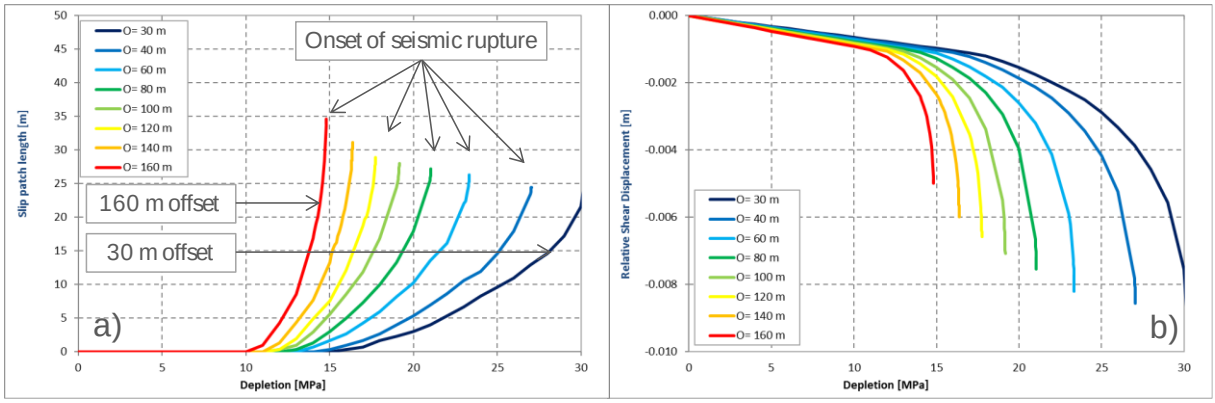

Figure A7.2: *a) Total length of the slip patches, and b) the maximum Relative Slip Displacement (RSD, right) as a function of reservoir depletion for the cases with an offset between 30 and 160 m.*

Onset of seismic rupture – which is characterised by a vertical gradient of the slip-depletion curve in Figure A7.2 – is found at a lower depletion level with increasing reservoir offset. This is valid for all cases except for the case with 30 m offset, which requires a depletion larger than 30 MPa to become unstable. Reservoir depletion has been limited to 30 MPa, because this corresponds to an absolute reservoir pressure close to zero. So, cases with an offset of 30 m or smaller do not become seismogenic up to 30 MPa reservoir depletion and show only a-seismic slip. The fault becomes unstable at a depletion level that decreases with increasing offset for cases with an offset larger than 30 m. The same simulations without slip weakening do not lead to fault instability. So, it is concluded that (slip) weakening of the fault is a required but insufficient condition to explain seismogenic behaviour. Reservoir offset also strongly influences at which reservoir depletion onset of seismic rupture occurs: cases with a small reservoir offset are less vulnerable for seismic slip compared to cases with an offset about equal to the reservoir thickness under the same fault slip properties.

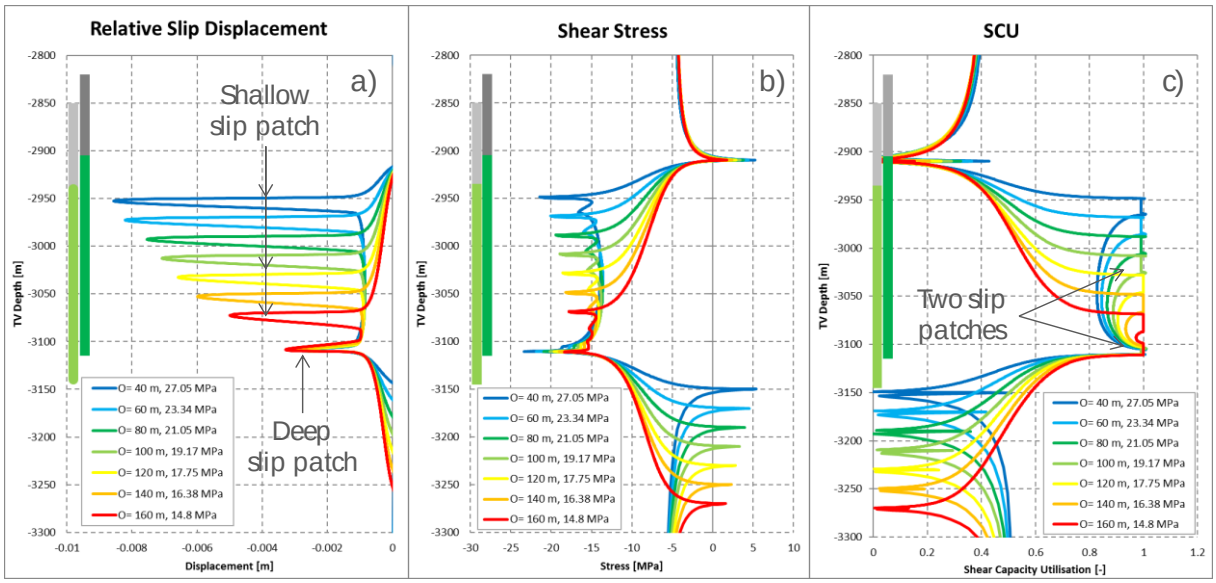

Figure A7.3: *a) The RSD, b) the shear stress distribution and c) the Shear Capacity Utilisation (SCU) as a function of depth along the fault plane at the onset of seismic rupture for the cases with an offset between 40 and 160 m.*

Figure A7.3 shows the fault condition at the onset of seismic rupture for the same cases as in Figure A7.2. This includes the Base Case with 80 m offset discussed in APPENDIX 3 (dark-green line). The green bars at the side of the graph represent the case with the smallest offset (40 m). The shallow slip patch occurs at a deeper location with increasing offset, because it is associated with depletion in the hanging wall, while the deep slip patch remains in the same location because it is associated with depletion of the foot wall reservoir, which is at the same depth in all cases. Fault slip (RSD) localises at the shallow patch after the onset of fault slip similar to the Base Case. The RSD develops further over a somewhat larger slip patch at the onset of seismic rupture for a reducing reservoir offset (Figure A7.2b and Figure A7.3a). The absolute shear stress between the two slip patches (Figure A7.3b) is quite similar at the onset of seismic rupture for all cases, although reservoir depletion reduces with increasing offset. Seismic rupture nucleates at the shallow slip patch for all cases in this section.

Onset of seismic rupture occurs at a lower depletion level because the shear stress loading of the fault occurs over a smaller depth interval with increasing reservoir offset (see Appendix A.3.1 for the Base Case). Figure A7.3c shows that the two slip patches are located closer and the SCU between the patches is larger with increasing offset. In other words: the entire juxtaposition interval – where the fault is exposed to depletion on both sides – is closer to failure at the onset of seismic rupture. A smaller reservoir depletion is required the reach onset of seismic rupture if the offset is larger, because shear stress is concentrating over a smaller juxtaposition interval.

A.7.1.2. FAULT RUPTURE

This section presents the dynamic rupture simulations of the seismic events that follow after the fault has reached instable equilibrium for the cases discussed in the previous section. For each case, the rupture mechanism is determined in accordance with the classification introduced in APPENDIX 6:

- Rupture Mechanism 1: Merging of the two slip patches for $0.48 \leq \mu_r \leq 0.50$.
- Rupture Mechanism 2: Instability of the shallow slip patch without merging with the deep slip patch for $0.45 \leq \mu_r \leq 0.47$.
- Rupture Mechanism 3: Instability of the shallow slip patch and merging with the deep patch for $0.25 \leq \mu_r \leq 0.40$.

Rupture Mechanism 1 does not apply for the cases considered here, because the two slip patches shown in Figure A7.3 are still separated at the onset of seismic rupture.

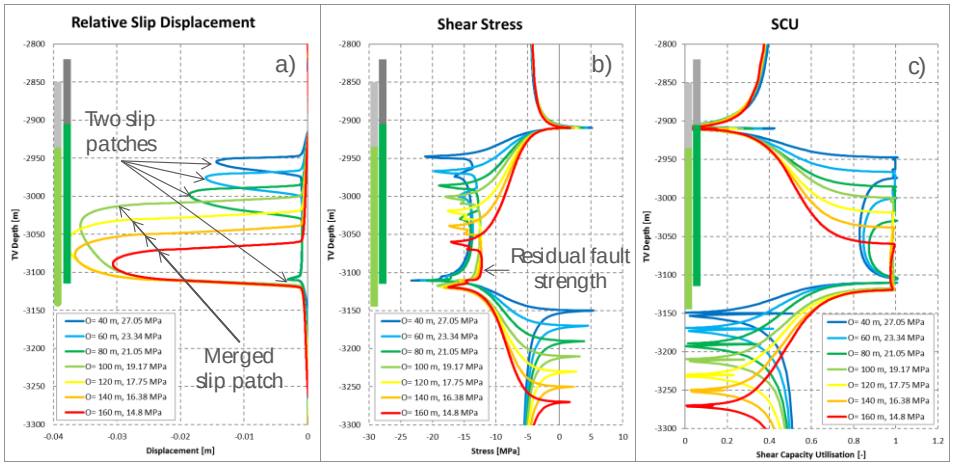

Figure A7.4: a) The Relative Slip Displacement, b) the shear stress, and c) the Shear Capacity Utilisation after the seismic event for a selection of the cases in Table A7.1.

Rupture Mechanism 2 is simulated for cases with an offset up to 90 m (0.45 normalised offset), whereas Rupture Mechanism 3 is found for cases from 100 to 180 m offset. This is seen from the Relative Slip Displacement after the seismic event shown in Figure A7.4a, which shows two slip patches for the cases with 40, 60 and 80 m offset. The same is found for the case with 90 m offset (not shown). The maximum RSD increases with increasing reservoir offset for cases with Rupture Mechanism 2, although the depletion level is lower at the onset of seismic rupture.

Rupture Mechanism 3 applies for the cases with an offset from 100 to 180 m, because a single merged slip patch is simulated after the seismic event. The size of the slip patch and RSD is larger than for Rupture Mechanism 2. However, the maximum RSD after the seismic event is reducing for cases with an offset of 140 m or larger (orange and red lines). Furthermore, it is noted that the critical slip displacement of 0.01 m is exceeded in all cases during the seismic event (Figure A7.4a). This implies that the residual friction coefficient is reached in all cases. The shear stress over the slip patch interval in Figure A7.4b therefore represents the residual fault strength.

The slip patch remains contained within the juxtaposition interval of the fault for all cases, including those with Rupture Mechanism 3. This is explained by the SCU value reducing from 1 to 0 between the bottom of the foot wall reservoir to the bottom of the hanging wall reservoir (the hanging wall interval of the fault) as shown in Figure A7.4c. This implies a large capacity of the fault to carry additional shear stress, which prevents the rupture to propagate far into the hanging wall interval of the fault. This limits the growth of the slip patch and the RSD for a reservoir offset of 140 m and larger (0.7 normalised reservoir offset).

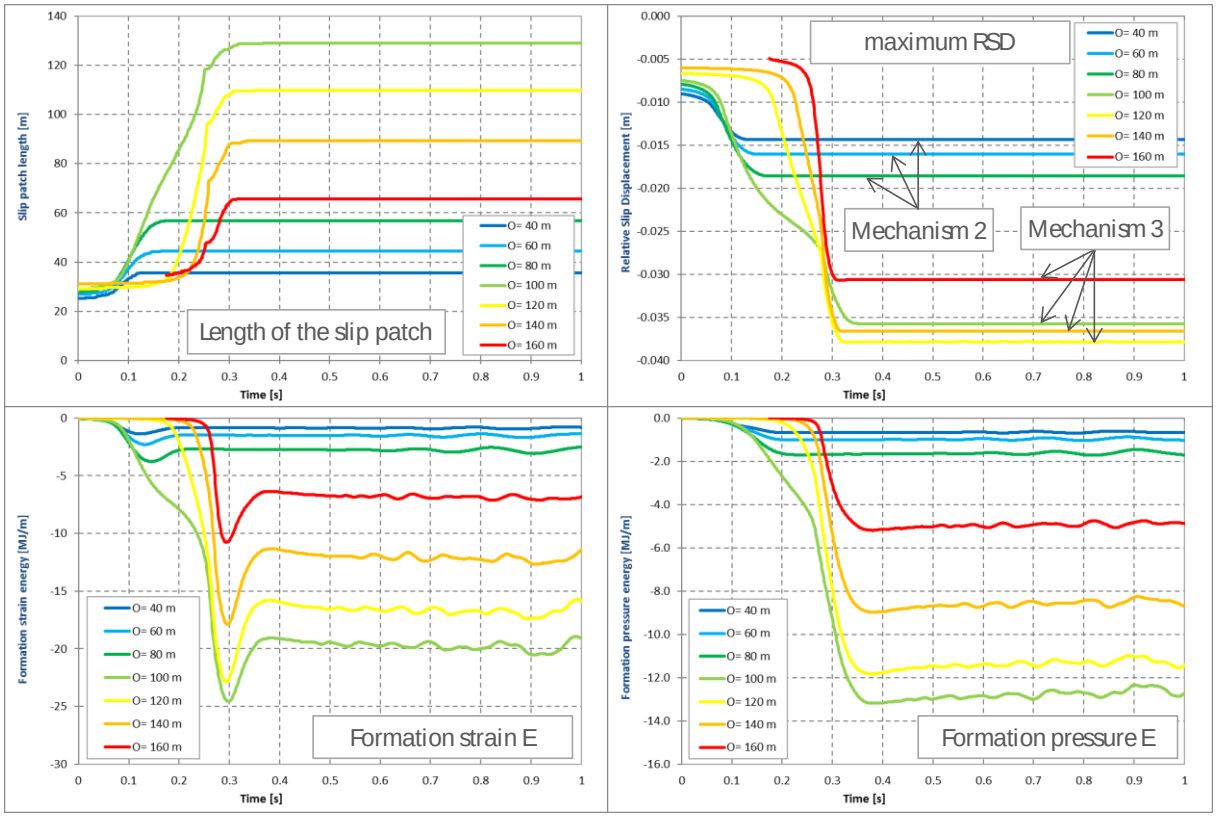

Figure A7.5: *The total length of the two slip patches, the maximum RSD, the formation strain energy and the formation pressure energy as a function of time for a selection of the cases in Table A7.1.*

The occurrence of the two different rupture mechanisms is also recognised in the evolution of the slip patch size, the RSD and the energy components during the rupture process. The top-right graph of Figure A7.5 shows that the RSD is significantly larger after an event with Rupture Mechanism 3 than after Rupture Mechanism 2. Furthermore, it is seen that the largest RSD is reached for an offset of 120 m (yellow line). Note that time shifts have been applied to align results. The evolution of the RSD over time is fastest for the case with 160 m offset (red line), but also shows a sudden arrestment after about 0.3 s. Re-stabilisation of the fault plane occurs more gradually over time for the cases with a smaller reservoir offset, in particular for those that exhibit Rupture Mechanism 2. This is explained by the stress contrasts between the juxtaposition and hanging wall interval of the fault. Note that the case with 100 m offset shows the largest size of the slip patch and release of formation strain and pressure energy, but not the largest RSD after the seismic rupture.

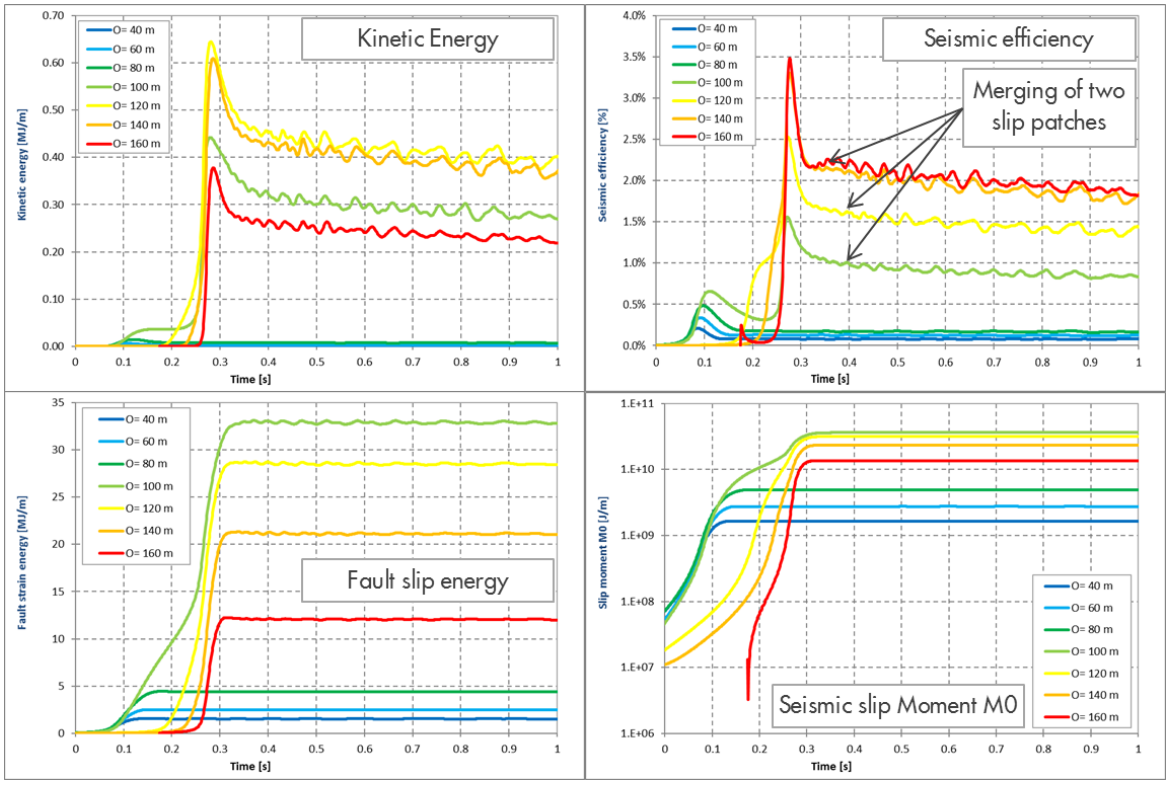

Figure A7.6: The kinetic energy, seismic efficiency, energy dissipated by fault slip and the seismic slip moment M_0 as a function of time for a selection of cases in Table A7.1

The kinetic energy is a good indicator for the start of the seismic rupture process, as well as the transition point from the acceleration to the deceleration phase. The seismic rupture starts when the kinetic energy takes off, while the deceleration phase starts at the point with the largest kinetic energy. The seismic rupture ceases when the seismic slip moment M_0 does not further increase (note the logarithmic scale). This is the case after about 0.4 s for all cases in Figure A7.6 (timelines have been shifted to align results). The remaining kinetic energy in the model represents the radiated wave energy that is transmitted into the subsurface.

The case with 100 m offset (0.5 normalised reservoir offset) generates an event with the largest seismic slip moment M_0 (light-green line in Figure A7.6). The seismic slip moment is calculated from the RSD and the size of the slip patch as described in APPENDIX 13. This case also dissipates the largest amount of energy by fault slip. Therefore, less kinetic energy is available compared to some other cases with Rupture Mechanism 3. Interestingly, the seismic efficiency after 1 s, when the seismic events has ceased in all cases, increases monotonically with reservoir offset. The seismic slip moment and the seismic efficiency for Rupture Mechanism 2 is an order of magnitude smaller compared to Rupture Mechanism 3.

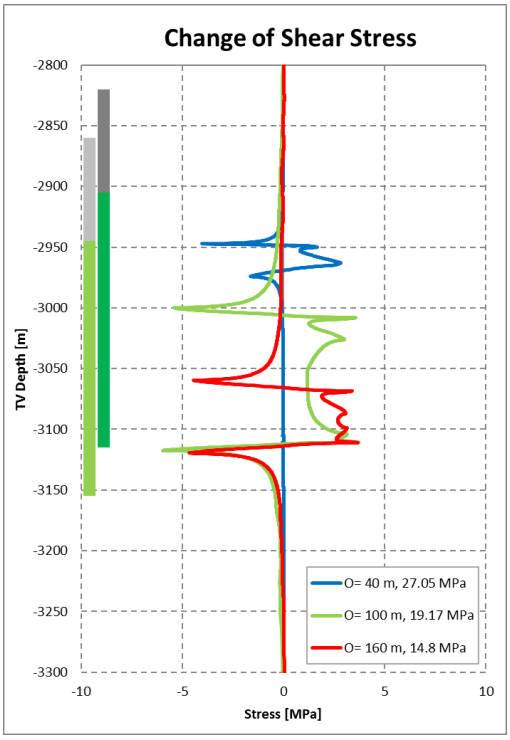

Figure A7.7: Change of shear stress along the fault plane as a function of depth as a result of the seismic rupture for a selection of the cases in Table A7.1. Positive values represent the stress drop over the seismic slip patch.

The stress drop is not uniformly distributed over a seismic slip patch. Figure A7.7 shows the difference between the shear stress distribution before the seismic event (Figure A7.3b) and after the seismic event (Figure A7.4b) Positive values for the stress change mean that the incremental shear stress is directed upwards and constitutes a stress drop over the slip patch. The stress drop over the center of the slip patch is compensated by negative (downward) shear stress just above and below the seismic slip patch. Integration of the change of shear stress along the entire fault plane should be zero, because reservoir depletion is the same before and after the seismic event and so is the total (shear) stress loading along the fault plane. A seismic rupture causes a redistribution of mainly shear stress from the seismic rupture area to locations adjacent to it. This highlights the importance of a low SCU adjacent to juxtaposition interval of the fault plane to arrest a seismic rupture.

A.7.2. Offset of about 1 reservoir thickness

Attention is focussed at three cases (Table A7.2) with a normalised reservoir offset of 0.9, 1.0 and 1.1. The close vicinity of the two slip patches has a distinct impact on the onset of seismic rupture and the rupture mechanism and is therefore discussed separately.

Table A7.2: Overview of analysis cases conducted for an offset of about one reservoir thickness of 200 m. Normalised offset is offset divided by reservoir thickness.

Case	Offset O [m]	Normalised offset Ō [-]
Mu55-232	180	0.9
Mu55-242	200	1.0

Mu55-252	220	1.1

A.7.2.1. ONSET OF SEISMIC RUPTURE

Onset of seismic rupture occurs at 12.22 MPa reservoir depletion for the case with 180 m offset (orange lines in Figure A7.8). This is lower than for the case with 160 m offset (blue line included for reference) and is a continuation of the trend found in the previous section. However, the total length of the two slip patches for 180 m offset is smaller than for 160 m offset, which is a deviation from the trend found in the previous section.

Onset of seismic rupture does not occur if the offset is 200 m, which is equal to the reservoir thickness. The green line in Figure A7.8a shows a diminishing slope if reservoir depletion becomes larger than 15 MPa. This implies that the fault becomes more stable with increasing depletion, because a larger incremental reservoir depletion is required to propagate the slip patch.

Onset of seismic rupture occurs at 11.16 MPa reservoir depletion for the case with 220 m offset (red lines in Figure A7.8). The total length of the slip patch is somewhat larger compared to the case with 180 m offset, although the depletion level is somewhat smaller.

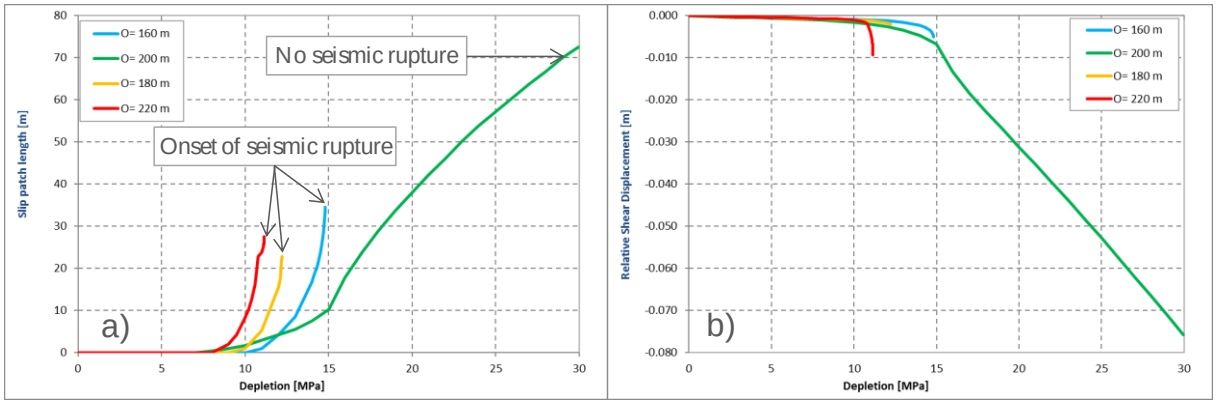

Figure A7.8: a) Total length of the slip patches, and b) the maximum Relative Slip Displacement (RSD, right) as a function of reservoir depletion for the cases with an offset between 160 and 220 m.

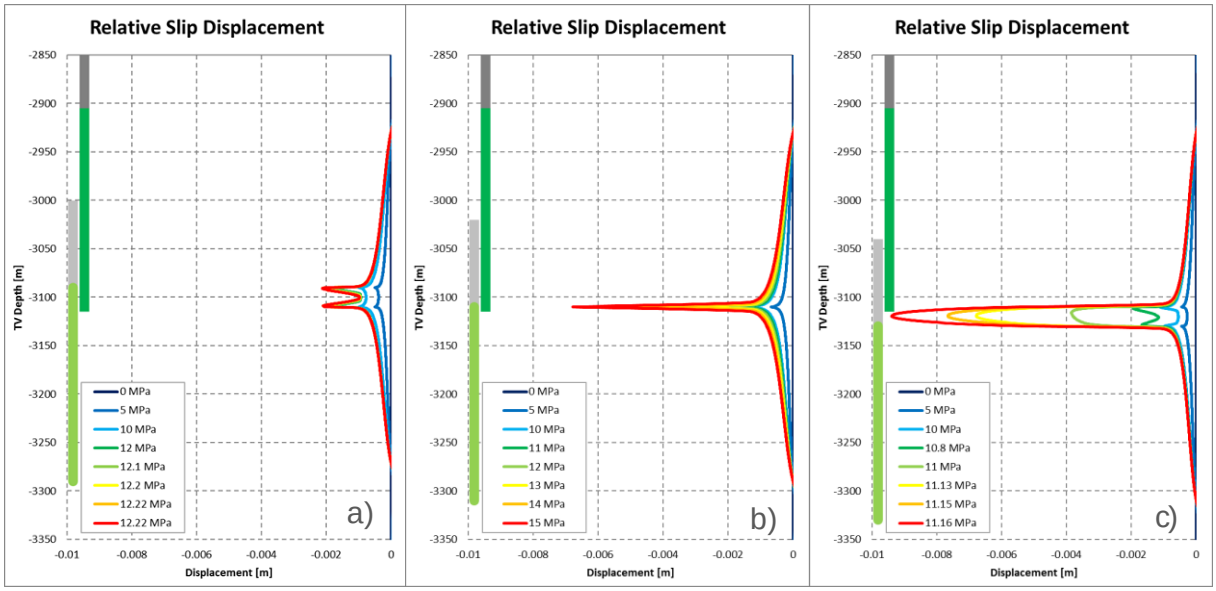

Figure A7.9: Relative Slip Displacement (RSD) as a function of depth at different depletion levels up to the onset of seismic rupture for a reservoir offset of a) 180 m, b) 200 m and c) 220 m.

The different response is explained by the RSD distribution at the onset of seismic rupture. The development of the RSD for 180 m offset in Figure A7.9a shows two a-seismic slip patches that are about equal in size with about the same maximum RSD. The limited distance between the slip patches, which is dictated by the offset and the reservoir thickness (indicated by the green bars at the left-hand side of the graph), prevents the localisation of slip at the shallow patch as found for cases with smaller offset. Instead, fault instability is caused by merging of the two slip patches at 12.22 MPa reservoir depletion (red line). This means that Rupture Mechanism 1 applies for an offset of 180 m.

Only one slip patch develops if the offset is equal to the reservoir thickness (Figure A7.9b). This is explained by the fact that the critical shear stress locations caused by depletion in the foot wall and the hanging wall coincide. This concentration of shear stress in one location is the reason why this configuration is most prone to a-seismic fault slip. Onset of seismic rupture does not occur, because the critical slip displacement of 0.010 m is reached before the single slip patch becomes unstable. This occurs at slightly more than 15 MPa reservoir depletion and causes the sudden change in slope of the green line in Figure A7.8a. A different assumption for the slip-weakening relationship is required to simulate seismic rupture for this fault configuration.

For an offset of 220 m, two slip patches develop after about 8.2 MPa depletion that merge into a single slip patch after about 11 MPa (Figure A7.9c). The fault becomes instable after 11.16 MPa reservoir depletion when the merged slip patch is 27.5 m and the maximum RSD is -0.009 m. So, merging of the two slip patches occurs in a stable fashion and onset of seismic rupture is caused by instability of the merged slip patch (Rupture Mechanism 2). This is remarkable, because merging of two slip patches causes fault instability in all other cases discussed thus far.

So, merging of the two slip patches (Rupture Mechanism 1) causes onset of seismic rupture in case of 180 m offset, but it does not in case of 220 m offset. In the latter case, seismic rupture occurs starting from a single, merged patch (Rupture Mechanism 2). Note that the critical slip displacement of 0.01 m is not reached in

either cases. This is different from the cases that exhibit Rupture Mechanism 1 in APPENDIX 6, which all have reached the critical slip displacement at the onset of seismic rupture. Also, it is found that the case with 200 m offset (normalised offset 1) – which is most prone to a-seismic slip – does not necessarily lead to fault instability and seismic rupture.

A.7.2.2. FAULT RUPTURE

Figure A7.10 shows the RSD, the stress drop and the SCU after seismic rupture for the cases with 180 m (orange) and 220 offset (red). The case with 160 m offset discussed in section A.7.1 is included for reference (blue). The green bars at the left-hand side of the graph represent the case with 220 m offset. Note that the depth of the hanging wall increases with offset, while the foot wall is at the same depth for all cases. It is seen that that the size of the slip patch, which is determined from the SCU distribution, and the maximum RSD are relatively small for 180 m offset compared to the case with 160 m offset, while the stress drop is quite similar, albeit over a smaller slip patch. So, stress drop is not proportional with RSD. This is the consequence of a presumed linear slip-weakening relationship for the fault. The assumption of a residual friction coefficient implies a limitation of the reduction of the fault strength if the critical slip displacement is exceeded.

The SCU distribution as a function of depth in Figure A7.10c explains why the slip patches are confined by the reservoir boundaries. The SCU reduces quickly below the bottom of the foot wall, and above the top of the hanging wall reservoir formation for all cases. The substantially lower SCU values adjacent to the seismic slip patch indicates a substantial capacity to carry additional shear stress and arrest a seismic rupture.

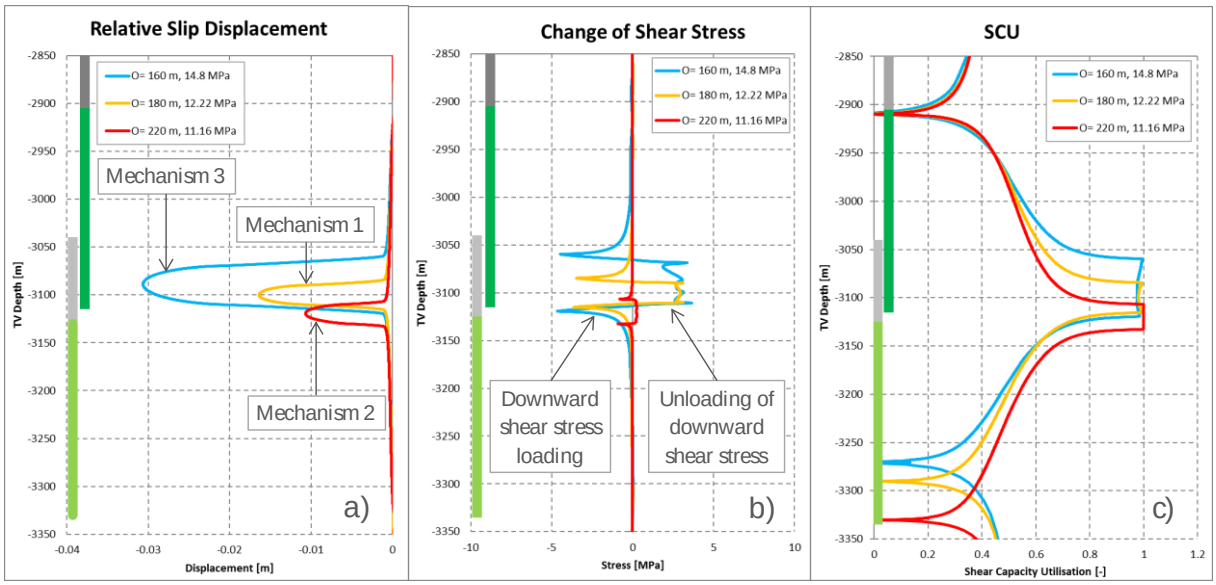

Figure A7.10: a) The Relative Slip Displacement, b) the change of shear stress, and c) the Shear Capacity Utilisation as a function of depth after the seismic event for cases with an offset of 160, 180 and 220 m. A negative value indicates a downward directed change of shear stress (fault loading) and positive values indicate an upward directed change (unloading).

A.7.3. Offset larger than reservoir thickness

In this section, cases with a reservoir offset between 240 m to 400 m (normalised offset between 1 and 2) are discussed (Table A7.3). All other modelling parameters are the same as in the previous sections and identical to the Base Case. The offset is varied by increasing the depth of the hanging wall, while keeping the foot wall at the same depth.

Table A7.3: Overview of analysis cases conducted for an offset of more than the reservoir thickness of 200 m. Normalised offset is offset divided by reservoir thickness.

Case	Offset O [m]	Normalised offset Ō [-]
Mu55-262	240	1.2
Mu55-272	260	1.3
Mu55-282	300	1.5
Mu55-292	400	2.0

A.7.3.1. ONSET OF SEISMIC RUPTURE

The reservoir depletion that causes onset of seismic rupture increases from 13.06 MPa for 240 m offset to 17.69 MPa for 400 m offset (Figure A7.11a). The maximum RSD at the onset of seismic rupture also increases (Figure A7.11b), while the size of the slip patch decreases with increasing offset. The case with 220 m offset discussed in the previous section is included for reference, showing a deviation of this trend caused by the close vicinity of the two slip patches causes.

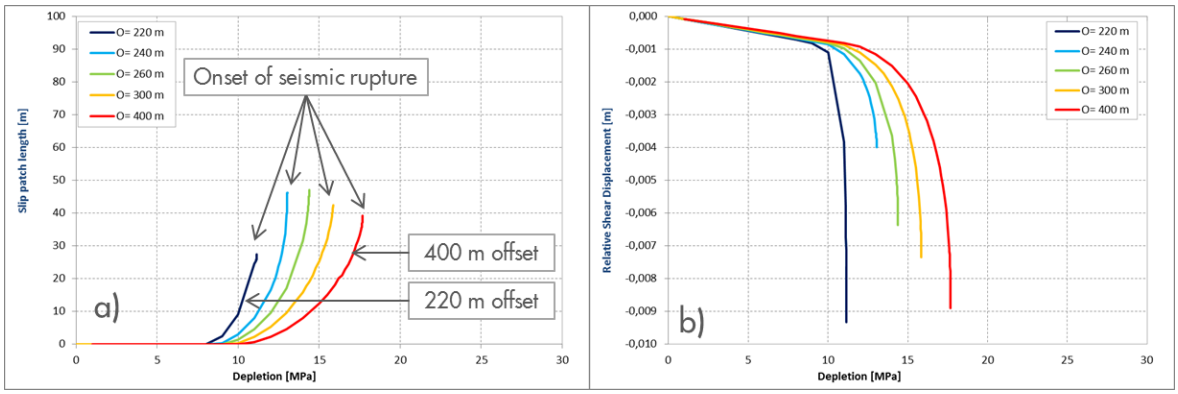

Figure A7.11: a) Total length of the two slip patches, and b) the maximum Relative Slip Displacement (RSD) as a function of reservoir depletion for an offset larger than reservoir thickness

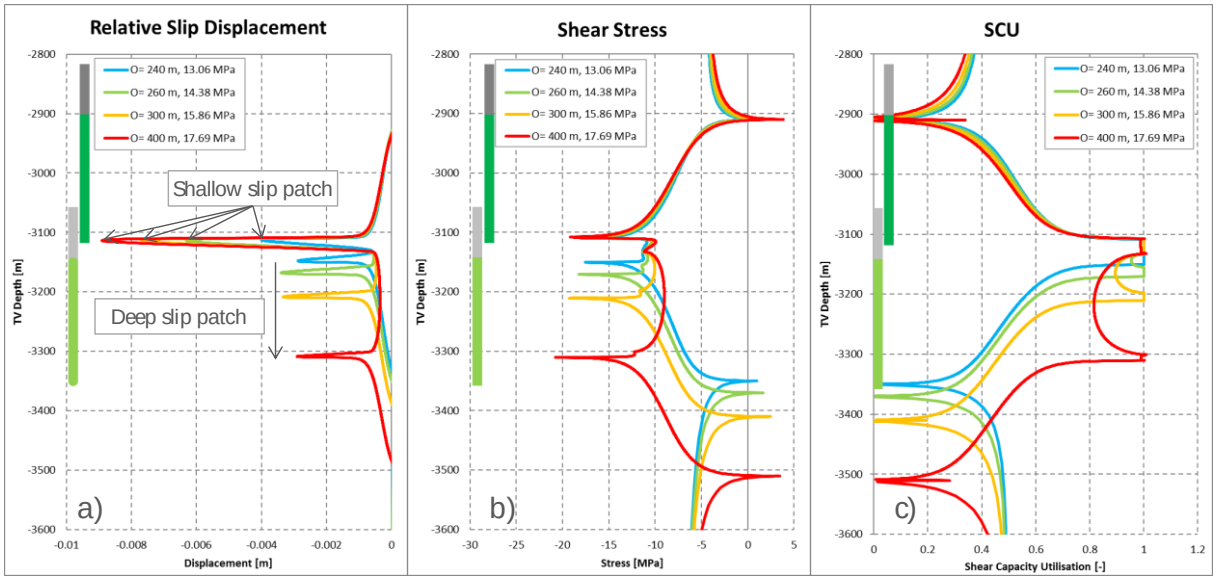

Figure A7.12: *a) The RSD, b) the shear stress distribution and c) the Shear Capacity Utilisation (SCU) as a function of depth along the fault plane at the onset of seismic rupture for the cases with an offset (O) larger than reservoir thickness.*

The fault condition at the onset of seismic rupture are shown in Figure A7.12 for the cases in Table A7.3. The green bars at the side of each graph represent the depth of the foot wall and hanging wall formation for the case with 240 m offset. Two slip patches are present at the onset of seismic rupture for all cases as indicated by the RSD and SCU distribution. Note that the shallow slip patch is located at the bottom of the foot wall, whereas it is located at the top of the hanging for a reservoir offset smaller than the reservoir thickness. Slip displacement localises at the shallow slip patch, similar to the cases with an offset smaller than the reservoir thickness. The maximum RSD at the shallow slip patch is larger for larger offset, which is also attributed to the higher depletion level at which onset of seismic rupture occurs. The deep slip patch is stable and is not significantly influenced by the offset. In all cases the critical slip displacement D_c=0.01 and seismic rupture is caused by instability of the shallow slip patch (Rupture Mechanism 2 or 3), except for the case with 240 m offset, in which merging of the two slip patches is the root cause of fault instability (Rupture Mechanism 1).

A.7.3.2. FAULT RUPTURE

All three rupture mechanisms are found for the cases in Table A7.3. Figure A7.13a shows the RSD distribution over the fault plane after the seismic rupture has ceased. For 240 m offset (light blue line), the rupture mechanism is caused by merging of the two slip patches (Rupture Mechanism 1), whereas onset of seismic rupture is caused by instability of the shallow slip patch for an offset of 260 m and larger. The instable shallow slip patch merges with the deeper slip patch during the seismic rupture for the cases with 260 and 300 m offset (Rupture Mechanism 3), whereas merging this does not occur if the offset is 400m (red line). The deep slip patch remains stable and a-seismic in this case and Rupture Mechanism 2 applies.

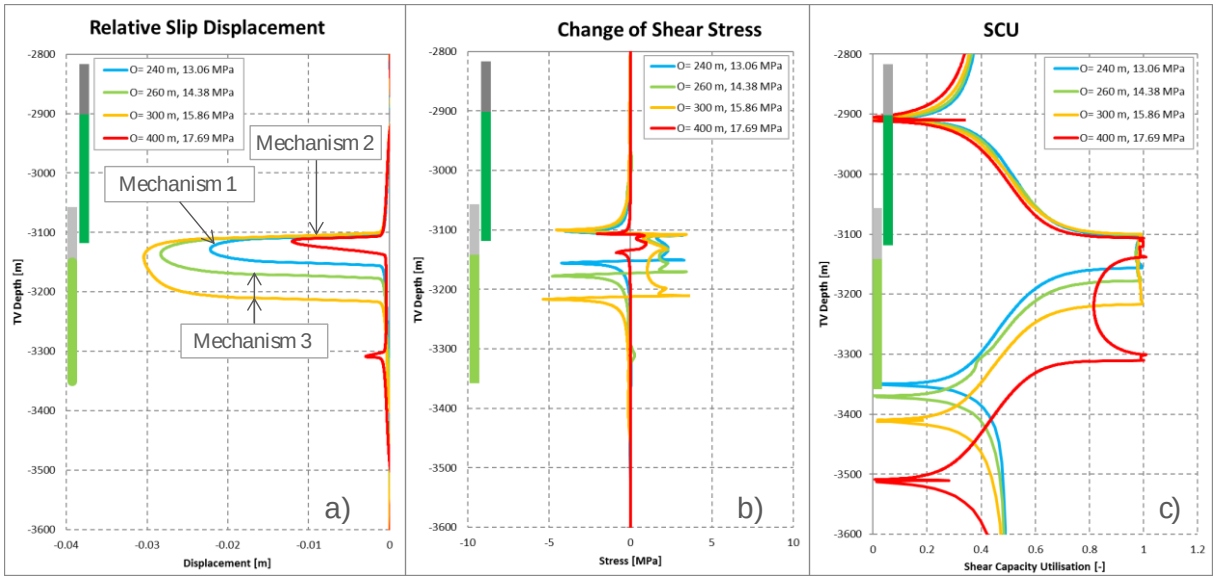

Figure A7.13: *a) The Relative Slip Displacement, b) the change of shear stress, and c) the Shear Capacity Utilisation as a function of depth after the seismic event for cases with an offset larger than reservoir thickness.*

It is seen that the slip patches are located just below the bottom of the foot wall reservoir in all cases. Propagation to shallower depth into the foot wall reservoir is prohibited by the lower SCU (Figure A7.13c). Propagation downward is prohibited by the lower SCU in the hanging wall reservoir. This is the reason why the seismic slip patch remains confined to the interval between the foot wall and hanging wall in all cases considered in this section. The lower SCU value is caused by a lower shear stress as well as a larger fault strength. The latter is caused by reservoir depletion that induces a higher (effective) normal stress on the fault plane over the foot wall and hanging wall intervals compared to the juxtaposition interval (where the fault is exposed to reservoir depletion on both sides).

The stress drop (Figure A7.13b) is limited to about 2 MPa. This is caused by the prescribed reduction of the friction coefficient from 0.55 to 0.45 if the RSD reaches the critical slip displacement D_c of 0.01 m. Figure A7.13a shows that the critical slip displacement is exceeded only over a small part of the slip patch for the case with 400 m offset. This explains why the stress drop is proportional with the RSD until the critical slip displacement is reached, and why the stress drop is smaller for an offset of 400 m compared to the other cases in Figure A7.13.

A.7.3.3. ONSET OF SEISMIC RUPTURE AND MOMENT MAGNITUDE

The *onset of fault slip* and the *onset of seismic rupture* have been discussed by varying the reservoir offset between 0 and 400 m and compared to the Base Case configuration. The length of the slip patches and the Relative Slip Displacement just before and after the seismic rupture event have been determined. For each case, the rupture mechanism is determined in accordance with the classification introduced in APPENDIX 6:

- Rupture Mechanism 1: Merging of the two slip patches for $0.48 \leq \mu_r \leq 0.50$.

- Rupture Mechanism 2: Instability of the shallow slip patch without merging with the deep slip patch for $0.45 \leq \mu_r \leq 0.47$.
- Rupture Mechanism 3: Instability of the shallow slip patch and merging with the deep patch for $0.25 \leq \mu_r \leq 0.40$.

In this section, the results of the previous three sections are combined to evaluate the influence of the normalised reservoir offset $\bar{O}$ on the simulated response.

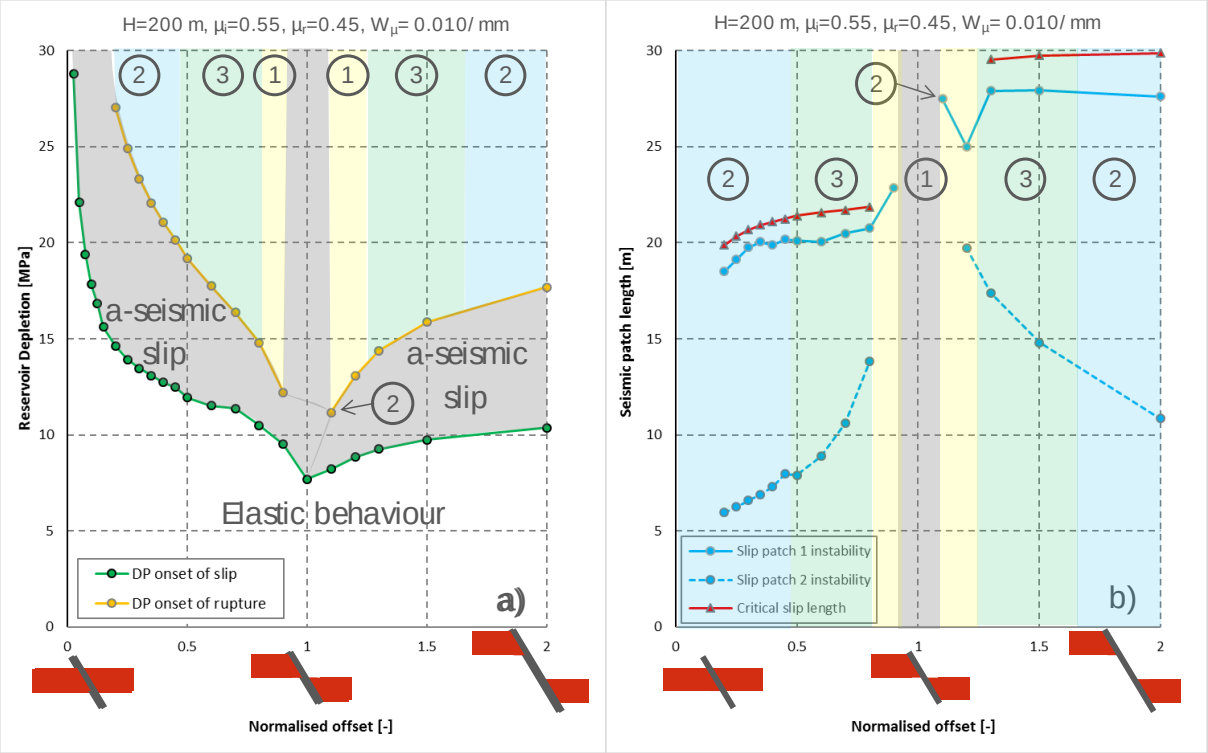

Figure A7.14: a) Reservoir depletion at the onset of fault slip and the onset of seismic rupture, b) the length of slip patch 1 (shallow) and slip patch 2 (deep) at the onset of seismic rupture, both as a function of the normalised reservoir offset. The background colour and number refers to Rupture Mechanism 1, 2 or 3.

Figure A7.14a shows the impact of the normalised reservoir offset on the reservoir depletion that causes onset of fault slip and the onset of seismic rupture. The *onset of fault slip* (green line) is similar to the result found in a previous study (van den Bogert, 2015), and indicates the depletion pressure below which no fault slip occurs and small displacement are considered recoverable (elastic). A reservoir with an offset about equal to the reservoir thickness is most prone to *fault slip*, whereas a reservoir without offset is least prone to fault slip due to reservoir depletion. The relationship in Figure A7.14a also implies that reservoir depletion on one side of the fault does not constitute a worst-case scenario, as this condition is represented by the case with a very large offset.

Fault slip is accommodated in an a-seismic fashion in the depletion range between the onset of fault slip (green line) and the onset of seismic rupture (yellow line). A similar relationship is found for the *onset of seismic rupture* compared to the *onset of fault slip*. It is seen that this depletion range is smallest for an offset of about the reservoir thickness and it is increasing for a smaller and larger offset. In case of a normalised offset of $\bar{O}$ = 0.2, onset of fault slip occurs at 14.6 MPa, while onset of seismic rupture does not occur up to 30 MPa depletion. A normalised offset of 1 is a special case in

which no seismic rupture is simulated for the assumed linear slip-weakening parameters μ_r and W_μ.

A large depletion range with a-seismic fault slip can be regarded as structurally ductile behaviour, whereas a small depletion range with a-seismic fault slip can be considered as a brittle response. In this sense, a small (normalised) reservoir offset demonstrates a more ductile structural response, whereas a normalised offset of about 1 demonstrates a more brittle response under the same fault slip-weakening assumptions.

The rupture mechanism that occurs after the onset of seismic rupture is indicated by the background colour in Figure A7.14. Rupture Mechanism 2 applies (indicated by the blue areas) if the distance between the two slip patches is relatively large and instability of the shallow slip patch does not lead to merger with the deep slip patch. For the assumed slip-weakening behaviour this is found for a normalised offset smaller than 0.5, or larger than about 1.5. Rupture Mechanism 3 applies (green areas) if the distance between the slip patches is sufficiently small to allow an instable shallow slip patch to merge with the deeper slip patch. Merging of the slip patches is the root cause of seismic rupture (Rupture Mechanism 1, yellow area) if the normalised offset if s close to 1 and. An exception is found in the case with 220 m offset, in which merging of the two slip patches occurs in a stable fashion. Rupture Mechanism 2 is assigned to this case, because fault instability occurs from a single merged slip patch. This case shows that merging of two slip patches not necessarily leads to fault instability.

The length of the shallow slip patch (slip patch 1) at the onset of seismic rupture (solid blue line in Figure A7.14b) is consistently smaller than the critical slip length L_c (red line) analytically derived following Uenishi and Rice (2003), which reads

$$L_c = \frac{1.158}{(1-\nu)}\frac{G}{W}.$$

Herein, ν is Poisson's Ratio, G is the shear modulus of the fault and W is the slope of the descending branch of the linear slip-weakening diagram in [MPa/m]. The value for W is the product of W_μ = 0.01 mm^{-1} and the normal effective stress according to equation (3.2) and varies with depth. The value for L_c plotted in Figure A7.14b is based on the average value of W over the juxtaposition interval for $\bar{0}$ <1 and the fault interval between the foot wall and hanging wall reservoirs for $\bar{0}$ >1. The shear modulus G is 4 GPa (Young's modulus of 10 GPa and Poisson's ratio of 0.25). So, the critical slip length is not the same in all cases because the depletion level and the average normal effective stress is dependent on the reservoir offset. The length of the slip patch at the onset of seismic rupture is between 93% and 96% of the analytical value of L_c for the cases in this chapter. The correspondence between the calculated length of the shallow slip patch and the theoretical value would increase by about 2% if the average value of W would be calculated over the shallow slip patch only. Buijze (2015) found that faults become unstable at about 80% of this analytical nucleation length. It is concluded that the theoretically calculated value of L_c corresponds rather good with the dynamic rupture simulations in this chapter, despite the variation of W over the fault plane.

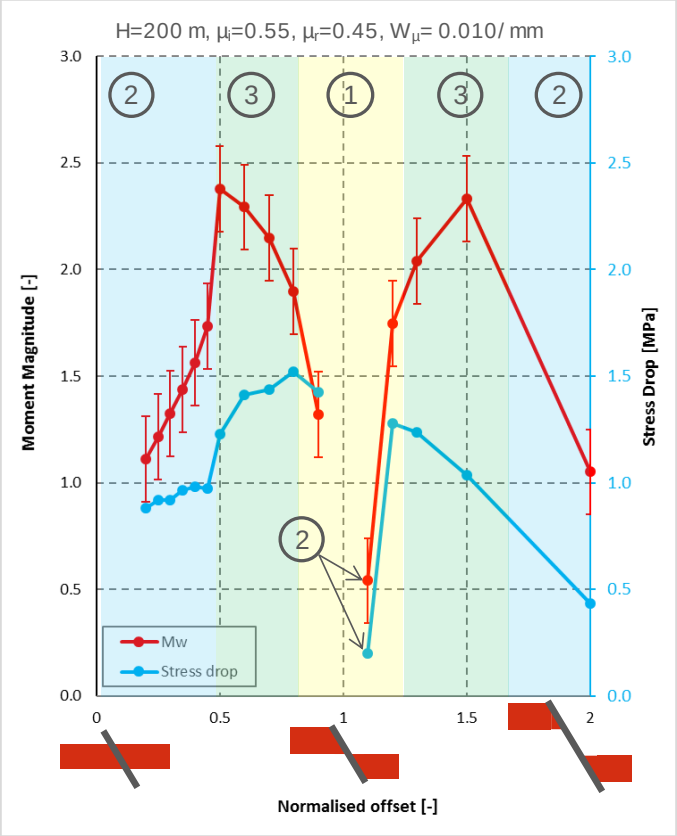

Figure A7.15: Moment magnitude and stress drop (right-hand side) as a function of normalised reservoir offset with $\mu_i = 0.55$, $\mu_r = 0.45$ and $W_\mu = 0.01$ mm^{-1} ($C = 0$ MPa). For the calculation of M_w, it is assumed that the rupture width (in strike direction of the fault) is equal to the rupture length (in dip direction). The length of the bars indicates the moment magnitude if the rupture width would be 0.5 and 2 times the length of the slip patch.

Figure A7.15 shows the complex relationship between the moment magnitude M_w and the average stress drop with the normalised reservoir offset for the fault slip behaviour assumed in this chapter thus far. The moment magnitude is calculated from the (seismic) slip moment M_0 as given in Figure A7.6 (after 0.7 s) for a $\bar{O}$ <1 using the expression in APPENDIX 13, while assuming a rupture width between 0.5 and 2 times the calculated slip patch length (Figure A7.5 after 0.7 s). The moment magnitude shows a step change between the Rupture Mechanisms 2 and 3, but follows a clear trend for each rupture mechanism separately. Some more analyses cases would be required with a normalised offset of about 1 to evaluate the competition between different rupture mechanisms, or the absence thereof. Figure A7.15 does allow the conclusion that Rupture Mechanism 3 causes seismic events with the largest magnitudes, while Rupture Mechanism 1 and 2 generally yield a smaller moment magnitude.

The stress drop in Figure A7.15 is the average over the seismic slip patch as presented in Figure A7.7 and similar results for the other cases. No generally applicable relationship is found between stress drop and moment magnitude. Stress drop increases with moment magnitude for cases with $\bar{O}$ <1 and Rupture Mechanism 2, while stress drop is constant with reducing moment magnitude for cases with $\bar{O}$ <1 and Rupture Mechanism 3. A negative correlation between stress drop and moment magnitude is found for Rupture Mechanism 3 and $\bar{O}$ >1. This mixed relationship is attributed to the imposed residual friction coefficient, which limits the stress drop for

increasing values of the Relative Slip Displacement. Based on Figure A7.15 it is concluded that Rupture Mechanism 2 generates a smaller stress drop than Rupture Mechanism 1 and 3.

A.7.3.4. RESIDUAL FRICTION COEFFICIENT

Three different rupture mechanisms may occur depending on the reservoir offset while assuming the same fault slip behaviour. The same three rupture mechanisms may occur by varying the residual friction coefficient for a given reservoir offset (APPENDIX 6). In this section, the combination of the two influencing factors is investigated by repeating the analyses discussed so far in this chapter for a residual friction coefficient in the range between 0.50 and 0.25. The critical slip displacement D_c is adjusted to maintain the slope in the linear slip-weakening diagram at W_μ = 0.01 mm^{-1} (Figure A6.1). All other parameters are the same as in the Base Case.

A.7.3.5. ONSET OF SEISMIC RUPTURE

For the Base Case with 80 m offset discussed in APPENDIX 3, it is found that merging of the two slip patches (Rupture Mechanism 1) is the root cause of seismic rupture for $\mu_r \geq 0.48$, and instability of the shallow slip patch (Rupture Mechanism 2 or 3) is the root cause for $\mu_r \leq 0.47$. More precisely, the threshold value for the residual friction coefficient that marks the transition between the two root causes is determined at $\mu_r = 0.475$. In this section, the transition between the two root causes is investigated for different offset. To this end, cases are run with a residual friction coefficient of 0.50 and with D_c=0.005 m (Table A7.3).

Table A7.3: Cases with a residual friction coefficient of 0.50, a critical slip displacement of 0.005 m ($W\mu$ = 0.01 mm^{-1}) and a normalised offset $\bar{O}$ between 0 and 2.

Case	Offset O [m]	Normalised offset $\bar{O}$ [-]		Case	Offset O [m]	Normalised offset $\bar{O}$ [-]
Mu55-151	50	0.25		Mu55-221	160	0.80
Mu55-161	60	0.30		Mu55-231	180	0.90
Mu55-171	70	0.35		Mu55-251	220	1.1
Mu55-181	80	0.40		Mu55-261	240	1.2
Mu55-191	90	0.45		Mu55-271	260	1.3
Mu55-201	100	0.50		Mu55-281	300	1.5
Mu55-211	120	0.60		Mu55-291	400	2.0
Mu55-217	140	0.70				

Figure A7.16 shows the total length of the two slip patches as a function of reservoir depletion for an offset between 50 and 400 m and a residual friction coefficient of 0.45 (solid lines) and 0.50 (dashed lines). Instability of the shallow slip patch is the root cause of seismic rupture for $\mu_r \leq 0.45$ and O ≤ 160 m. This is indicated by the vertical slope at the end of the *solid lines* (see previous sections of this chapter). The root cause and depletion level at which seismic rupture occurs is the same for a residual friction coefficient smaller than 0.45, because the slope of the descending branch in the linear slip-weakening relationship remains the same, as discussed in Chapter

APPENDIX 6. Instability of the shallow slip patch is also the root cause of seismic rupture for $\mu_r \leq 0.45$ and a reservoir offset of 240 m and larger (Figure A7.16b).

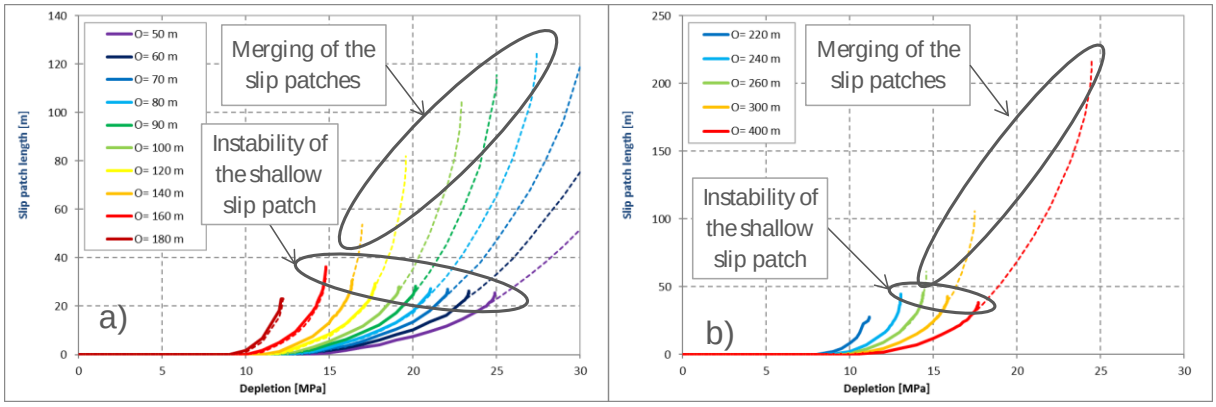

Figure A7.16: Total length of the slip patches as a function of reservoir depletion for a residual friction coefficient of 0.50 (dashed lines) and 0.45 or smaller (solid lines) and for a reservoir offset smaller (a) and larger than the reservoir thickness (b).

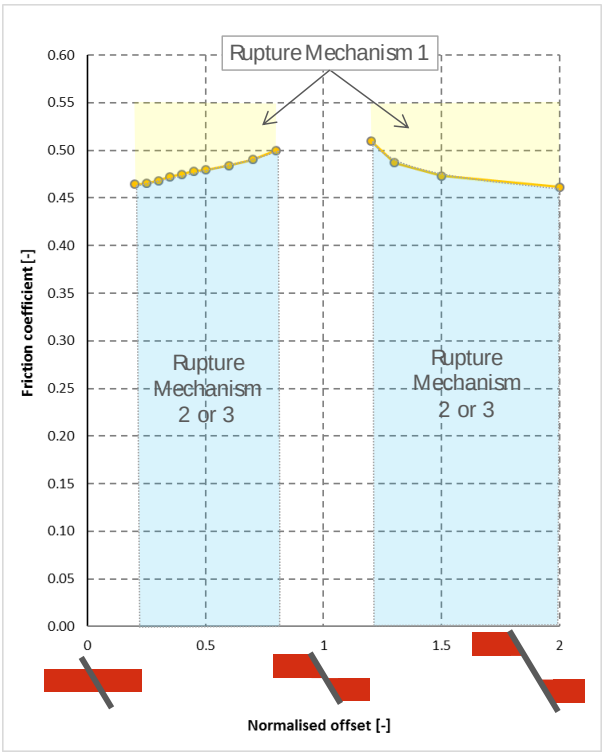

Figure A7.17: The threshold value for the residual friction coefficient that marks the transition between the root causes of seismic rupture: Rupture Mechanism 1 that is caused by merging of the two slip patches and Rupture Mechanisms 2 and 3 that is caused by instability of the shallow slip patch.

The vertical slope at the end of the *dashed lines* in Figure A7.16 indicate onset of seismic rupture for μ_r = 0.50 and is caused by merging of the two slip patches. This implies that the root cause of the seismic rupture changes for a value for the residual friction coefficient between 0.45 and 0.50. The threshold value for the residual friction coefficient at which this transition occurs is calculated at μ_r=0.475 for the Base Case with 80 m offset in Appendix A.6.1. The threshold value for the cases with a different offset are calculated in the same way and are shown in Figure A7.17. It is seen that

the threshold value is largest for a normalised offset close to 1. The merging of the two slip patches is caused by the residual friction coefficient that is reached over some part of the slip patch, thereby suppressing instability of the shallow slip patch.

Merging of the two slip patches is caused by the small distance between the two slip patches, without the residual friction coefficient being reached for a normalised offset of about 1. The absolute maximum RSD is about 0.002 m at the onset of seismic rupture for an offset of 180 m (normalised offset 0.9) and μ_r=0.45 (Figure A7.9a). This implies that instability is postponed to a larger depletion level if D_c is smaller than 0.002 m, which is the case for $0.53 \leq \mu_r \leq 0.55$. So, seismic rupture by merging of the two slip patches can be caused by reaching the residual friction coefficient, which is the case for an offset of 160 or smaller, or by a small distance between the two slip patches, which is the case for an offset of 180 m. Instability of the shallow slip patch is suppressed in a different way, but with the same result.

Furthermore, Figure A7.17 shows that a normalised offset of 0.35 or smaller (offset 70 m) does not lead to fault instability within 30 MPa reservoir depletion if a residual friction coefficient of 0.50 is assumed. It is seen that incremental depletion is still required to propagate the slip patch at 30 MPa for the cases with 50, 60 and 70 m offset. The same trend is visible for $\bar{O}$ >1: more incremental depletion is required to reach an instable fault condition for μ_r=0.50 in comparison with μ_r=0.45 for increasing reservoir offset.

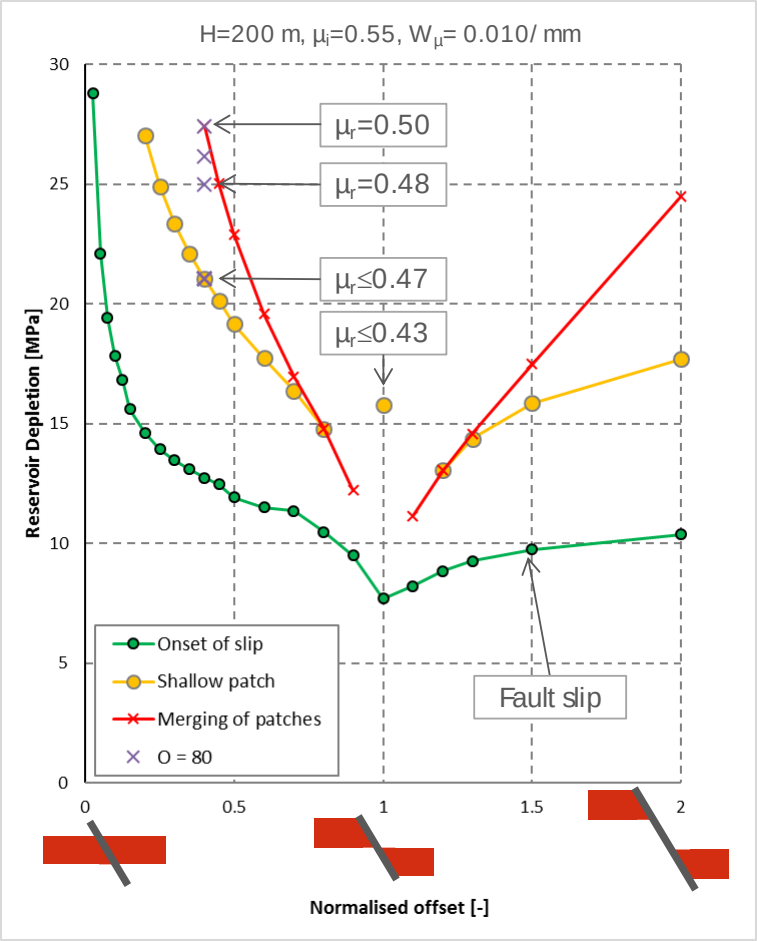

Figure A7.18: Reservoir depletion at the onset of fault slip (green line), and the onset of seismic rupture for μ_r=0.45 (yellow line, Rupture Mechanism 2 or 3) and μ_r=0.50 (red line, Rupture Mechanism 1) as a function of the normalised reservoir offset.

Figure A7.18 shows a comparison of the reservoir depletion pressure that causes seismic rupture by instability of the shallow slip patch (yellow line) and merging of the two slip patches (red line). The yellow line, which is taken from cases with μ_r=0.45, is the lower bound for seismic rupture for a slope in the descending branch of the slip-weakening diagram of W_μ = 0.01 mm^{-1} (Figure A6.1). This minimum depletion pressure is valid for a residual friction coefficient smaller than the threshold value given in Figure A7.17. The depletion level at the onset of seismic rupture increases with a step-change for a residual friction coefficient larger than the threshold value and increases gradually with further increasing value of the friction coefficient (see section A.6.1). This is reflected by results for the Base Case configuration with 80 m offset in Figure A7.18 (purple crosses). The convergence of the red line for μ_r=0.50 and the yellow line for μ_r=0.45 suggest that the step-change in reservoir depletion pressure that causes onset of seismic rupture reduces for a normalised offset of about 1. For a normalised reservoir offset of 1, onset of seismic rupture occurs by instability of the single slip patch (Rupture Mechanism 2) at 15.8 MPa reservoir depletion if $\mu_r \leq 0.43$. The green line represents the onset of fault slip (the same as in Figure A7.14a) and is included for reference.

A.7.3.6. FAULT RUPTURE

The moment magnitude increases with a reduction of the residual friction coefficient for cases that that nucleate at the same depletion pressure, i.e. the cases that are cause by instability of the single slip patch (Rupture Mechanism 2 and 3). Figure A7.19 shows the moment magnitude as a function of the normalised reservoir offset for all values of the residual friction coefficient considered in this chapter. The dark-green line for μ_r=0.45 is the same as in Figure A7.15. The results for different values of the residual friction coefficient in the Base configuration (80 m offset, Figure A6.14) are included at a normalised offset of 0.40. It is assumed that the width of the seismic slip patch in strike direction of the fault is the same as the simulated slip patch size in dip direction for the calculation of the Moment magnitude. The moment magnitude increases with about 0.2 each time the assumption for the aspect ratio of the slip patch size is doubled, or reduced with about 0.2 each time the aspect ratio is halved. Further detail of the calculation method is provided in APPENDIX 13.

It is emphasised that the moment magnitude and the reservoir depletion that causes onset of seismic rupture in dependent on other modelling parameters that are not addressed in this chapter, in particular the initial stress conditions, the fault dip and azimuth angle, the initial friction coefficient μ_i and the slope of the slip-weakening diagram W_μ.

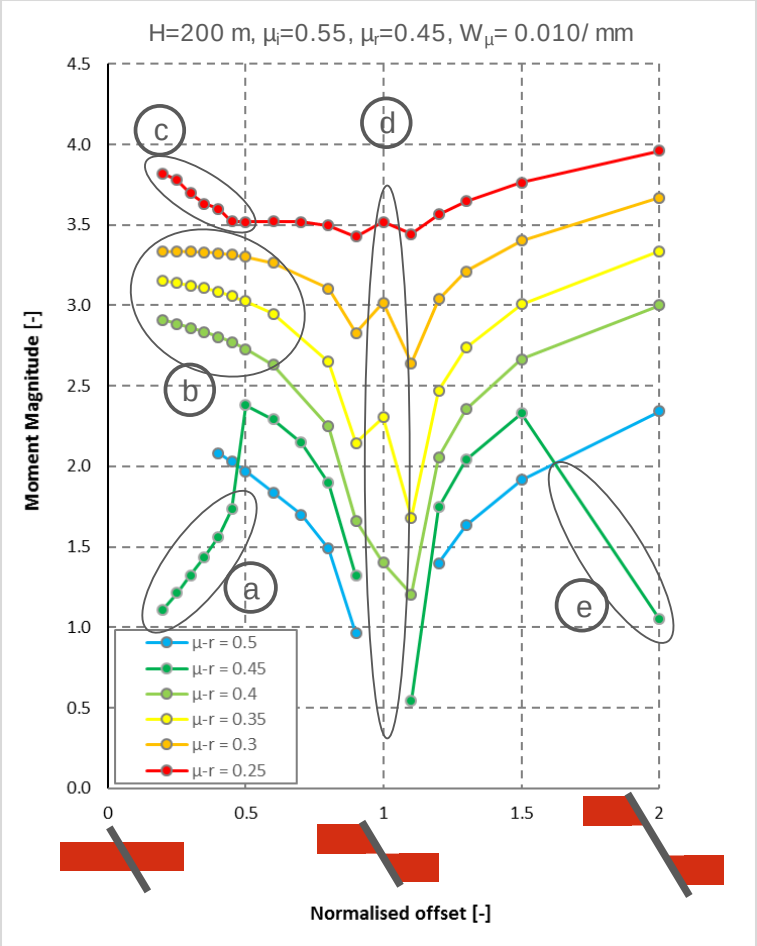

Figure A7.19: moment magnitude as a function of normalised reservoir offset for different values of the residual friction coefficient.

The following notes are made associated with Figure A7.19:

a. A relatively small moment magnitude is calculated for cases with μ_r=0.45 and $\bar{O}$ <0.5, because the slip patches do not merge (Rupture Mechanism 2).
b. Merging of the slip patches occurs for $\mu_r \leq 0.40$ and $0.20 \leq \bar{O} \leq 0.45$ (Rupture Mechanism 3), resulting into a significantly larger moment magnitude.
c. The rupture extends into the overburden and basement for μ_r=0.25 and $\bar{O} \leq 0.45$. The low SCU value in overburden and basement (Figure A7.4) is a barrier for rupture propagation, and the depth interval of the fault exposed to reservoir depletion is increasing with offset, which implies that the rupture needs to grow larger before propagating into the overburden and basement. This explains that only cases with relatively small offset and small residual friction coefficient cause the rupture to extend outside the reservoir depth range.
d. The single slip patch generated for $\bar{O}$ =1 becomes unstable at 15.8 MPa depletion if $\mu_r \leq 0.43$ (Figure A7.18). A larger residual friction coefficient does not lead to fault instability. The moment magnitude increases for smaller values of the residual friction coefficient.
e. Additional cases are required to establish the transition between rupture Mechanism 2 and 3 and associated moment magnitude for μ_r=0.45 and $\bar{O}$ >1.5. A mirrored trend is expected as highlighted under note a.

APPENDIX 8. RESERVOIR THICKNESS

The rupture analyses in Chapter APPENDIX 7 have been partly repeated for a reservoir thickness of 140, 170 230, 260 and 300 m. The top of the foot wall reservoir is kept at the same depth of 2910 m as in the Base Case (APPENDIX 3), while the reservoir thickness is adjusted. The offset is achieved by adjusting the depth of the hanging wall, while keeping the foot wall at the same depth. This implies that the absolute depth of the hanging wall is not the same for different reservoir thickness with the same normalised offset, and that the normal and shear stress condition is slightly different.

A.8.1. Onset of seismic rupture

The influence of reservoir thickness on the onset of seismic rupture is evaluated for cases with a normalised offset between 0 and 0.6. Attention is focussed on cases with μ_r=0.45 (Table A8.1), because onset of seismic rupture occurs at the same reservoir depletion for smaller values of the residual friction coefficient (APPENDIX 6).

Table A8.1: Overview of analysis cases conducted for a reservoir thickness of 170 m and 230 m and μr=0.45. Normalised offset is offset divided by reservoir thickness.

Reservoir thickness H=170 m		
Case	**Offset O [m]**	**Normalised offset Ō [-]**
Mu55-2	0	0
Mu55-12	10	0.059
Mu55-22	20	0.118
Mu55-32	30	0.176
Mu55-42	40	0.235
Mu55-52	50	0.294
Mu55-62	60	0.353
Mu55-72	70	0.412
Mu55-82	80	0.471
Mu55-92	90	0.529
Mu55-102	100	0.588

Reservoir thickness H=230 m		
Case	**Offset O [m]**	**Normalised offset Ō [-]**
Mu55-302	0	0
Mu55-312	15	0.065
Mu55-322	30	0.130
Mu55-332	45	0.196
Mu55-342	60	0.261
Mu55-352	75	0.326
Mu55-362	90	0.391
Mu55-372	105	0.457
Mu55-382	120	0.522
Mu55-392	135	0.587

The *onset of fault slip* for the cases in Table A8.1 for 170 and 230 m reservoir thickness is found at the same depletion level as for 200 m thickness and the same normalised reservoir offset $\bar{0}$ (Figure A8.1). This is the same result as found in previous work (Van den Bogert, 2015). Onset of fault slip is determined by SCU=1 at the top of the hanging wall, which is at slightly larger depth for larger reservoir thickness, and causes the slight difference in depletion pressure at the onset of fault slip (green lines) in Table A8.1. The result implies that the shear stress distribution along the fault plane, which is imposed by the reservoir offset, can be scaled with the reservoir thickness.

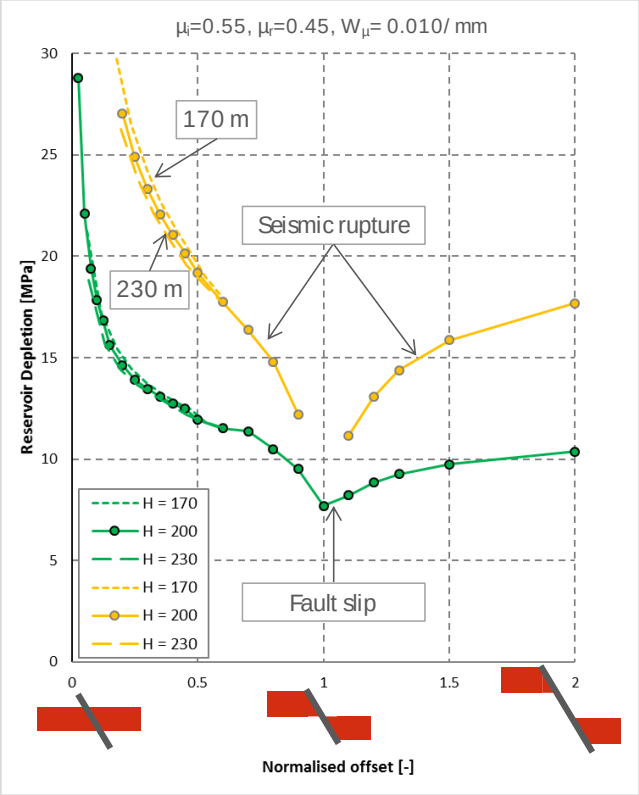

Figure A8.1: *Onset of fault slip (green) and onset of seismic rupture (yellow) for a reservoir thickness of 170, 200 and 230 m. The results for 200 m thickness are identical to those in Figure A7.14.*

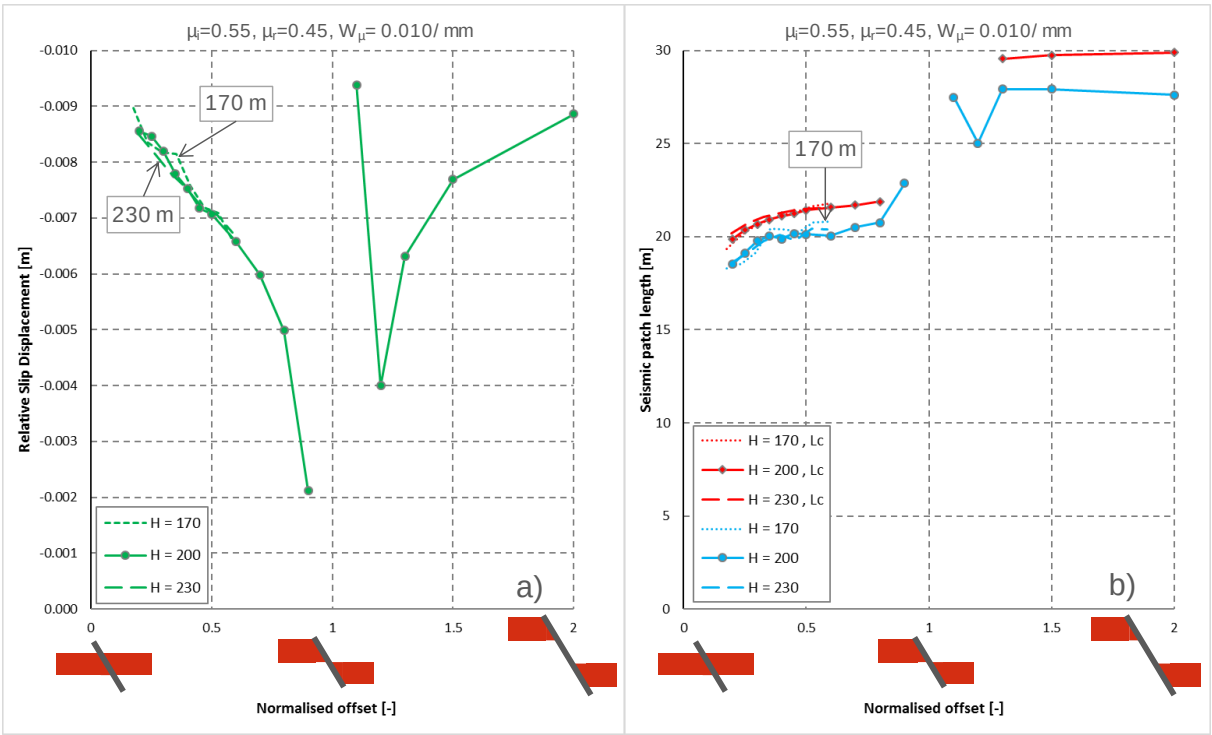

Figure A8.2: *a) Maximum Relative Slip Displacement, and b) the analytical critical slip patch length Lc and the simulated length of the slip patch length at the onset of seismic rupture as a function of normalised reservoir offset for different values for the reservoir thickness.*

The *onset of seismic rupture* for a reservoir thickness of 170 and 230 m follows the same trend as a function of normalised reservoir offset compared to a thickness H=200 m. However, the onset of seismic rupture for 170 m reservoir thickness (yellow short-dashed line in Figure A8.1) occurs at slightly larger reservoir depletion pressure, and for 230 m thickness (yellow long-dashed line) at a slightly lower reservoir depletion pressure compared to 200 m reservoir thickness (yellow solid line).

The maximum Relative Slip Displacement (RSD) and the length of the slip patch are virtually the same at the onset of seismic rupture for the same normalised offset (Figure A8.2), despite the different reservoir thickness. The critical slip length L_c – derived from the numerical results using expression (3.1) – is also the same for different reservoir thickness (red lines in Figure A8.2b). This implies that the same slip patch develops in terms of absolute size and slip displacement until the fault reaches instable equilibrium, and confirms that the size of the a-seismic slip determines the onset of seismic rupture when using a linear slip-weakening relationship as derived by Uenishi and Rice (2003). The simulated length of the slip patch at the onset of seismic rupture for the cases in Figure A8.2is between 92% and 98% of the analytical value L_c, with an average of 95%.

Table A8.2: Overview of analysis cases conducted with different reservoir thickness and a normalised offset of 0.4, μ_r=0.45 and D_c=0.01 m.

Case	Reservoir thickness H [m]	Offset O [m]	Normalised offset Ō [-]
Mu55-112	140	56	0.4
Mu55-111	170	68	0.4
Mu55-182	200	80	0.4
Mu55-113	230	92	0.4
Mu55-114	260	104	0.4
Mu55-115	300	120	0.4

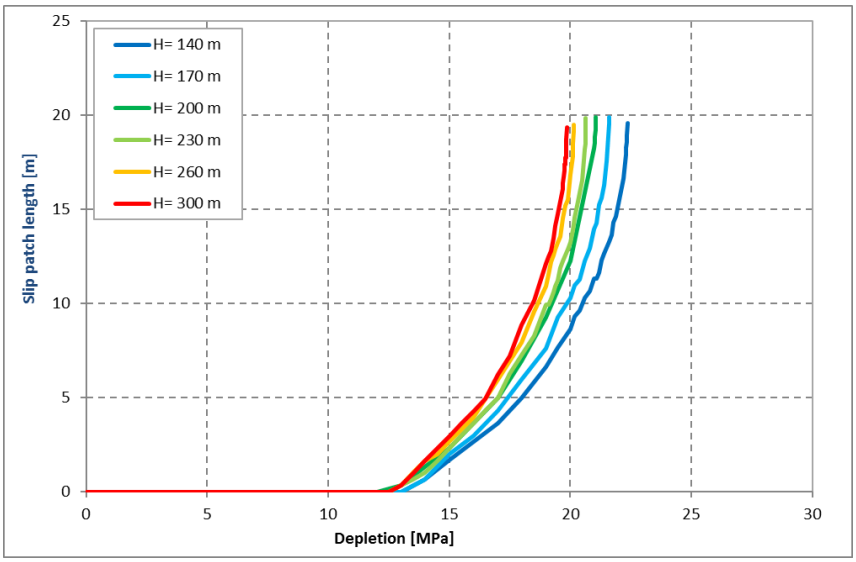

Figure A8.3: Absolute (dashed lines) and normalised length of the shallow slip patch (solid lines) as a function of reservoir depletion for different reservoir thickness H and a normalised reservoir offset of 0.4. The Base Case (APPENDIX 3) is represented by the dark-green line (H=200 m).

Additional cases with 140, 260 and 300 m reservoir thickness and a normalised offset of 0.4 have been conducted to better describe the influence of reservoir thickness on the depletion level at onset of seismic rupture (Table A8.2). Figure A8.3 shows the length of the shallow slip patch as a function of reservoir depletion. All curves end at the onset of seismic rupture, which is characterised by a vertical slope, implying that no additional reservoir depletion is required to propagate the slip patch. It is seen that onset of seismic rupture is reached at the same size of the slip patch, but at a reducing depletion level for increasing reservoir thickness.

This is explained by the fact that the stress distribution scales with reservoir thickness, but that onset of seismic rupture is reached at a critical, absolute length of the slip patch. The scaling of the stress distribution implies that the critical stress area and the slip patch length increases with reservoir thickness for the same reservoir depletion. The depletion level at which a certain critical slip length L_c is reached is therefore reducing with reservoir thickness.

A.8.1.1. FAULT RUPTURE

In this section, the influence of the reservoir thickness on the moment magnitude is presented for a normalised offset between 0 and 0.6 and a residual friction coefficient between 0.25 and 0.50. The initial friction coefficient is 0.55 and the slope in the slip-weakening diagram W_μ = 0.01 mm^{-1} and is the same as in APPENDIX 7.

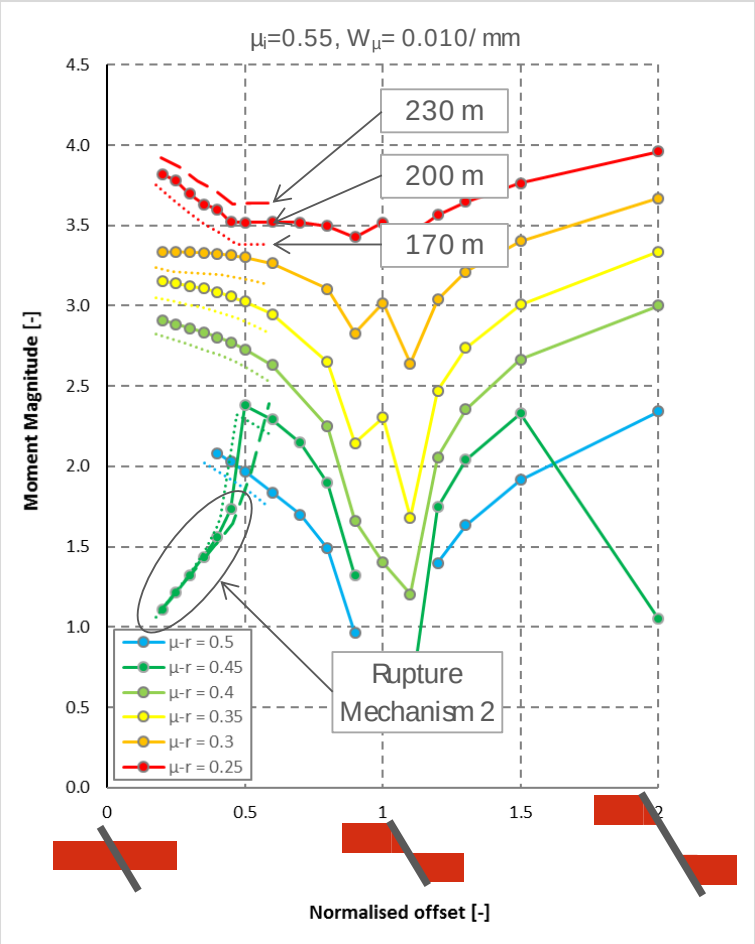

Figure A8.4: Moment magnitude as a function of normalised reservoir offset Ō for a reservoir thickness of 170 m (short-dashed lines), 200 m (solid lines) and 230 m (long-dashed lines).

Moment magnitude increases with reservoir thickness for the same normalised offset and fault slip properties. Figure A8.4 is the same as Figure A7.19, but includes the results for the cases with a reservoir thickness of 170 and 230 m, as well as cases with smaller value for the residual friction coefficient and a reservoir thickness of 170 m (see APPENDIX 2). The moment magnitude for 170 m reservoir thickness and $\mu_r = 0.25$ (red short-dashed line) is smaller, and for 230 m reservoir thickness and $\mu_r = 0.25$ (red long-dashed red line) is larger than for 200 m reservoir thickness (red solid line). The same is found for a residual friction coefficient of 0.30, 0.35 and 0.40, which all exhibit Rupture Mechanism 3 (see section A.7.3.4). Moment magnitude also reduces with reservoir thickness for cases with $\mu_r = 0.50$ (light-blue dashed and solid lines in Figure A8.4), which exhibit Rupture Mechanism 1.

However, the moment magnitude is converging to the same value for different reservoir thickness if Rupture Mechanism 2 is simulated (slip of the shallow slip patch only). This occurs if $\mu_r = 0.45$ and the normalised offset is smaller than 0.45 (dark-green lines in Figure A8.4). The shallow slip patch merges with the deep slip patch during the seismic event (Rupture Mechanism 3) if the normalised offset is 0.5 or larger and $\mu_r = 0.45$. The transition from Rupture Mechanism 2 to Rupture Mechanism 3 occurs at a lower normalised for a smaller reservoir thickness, because the absolute distance between the slip patches is smaller for smaller reservoir thickness.

The independence of the moment magnitude on reservoir thickness for Rupture Mechanism 2 is evaluated in detail for a reservoir thickness between 140 and 300 m and a normalised offset of 0.2. This small offset is chosen to ensure that the influence of the second deeper slip patch is minimal even for the smallest reservoir thickness. Figure A8.5a shows that the moment magnitude is 1.11±0.01 for all cases in Table A8.3 (red line). The length of the shallow slip patch differs 0.9 m (3 elements) between 140 m and 300 m reservoir thickness at the onset of seismic rupture (light-blue line), while the difference is 1.8 m (6 elements) after the seismic (dark-blue line). The difference in terms of the (absolute) RSD between 140 m and 300 m reservoir thickness is 0.4 mm before and after the seismic rupture (Figure A8.5b). The reservoir depletion at the onset of seismic rupture increases from 24.5 MPa at 300 m reservoir thickness to almost 30 MPa for 140 m reservoir thickness (yellow line in Figure A8.5a) and confirms the finding of the previous section that a larger reservoir thickness is more susceptible for seismic rupture under the same assumptions for the linear fault slip-weakening behaviour and normalised reservoir offset.

Table A8.3: Overview of analysis cases conducted with different reservoir thickness and a normalised offset of 0.2, μ_r=0.45 and D_c=0.01 m.

Case	Reservoir thickness H [m]	Offset O [m]	Normalised offset Ō [-]
Mu55-116	140	28	0.2
Mu55-117	170	34	0.2
Mu55-142	200	40	0.2
Mu55-118	230	46	0.2
Mu55-119	260	52	0.2

Mu55-120	300	60	0.2

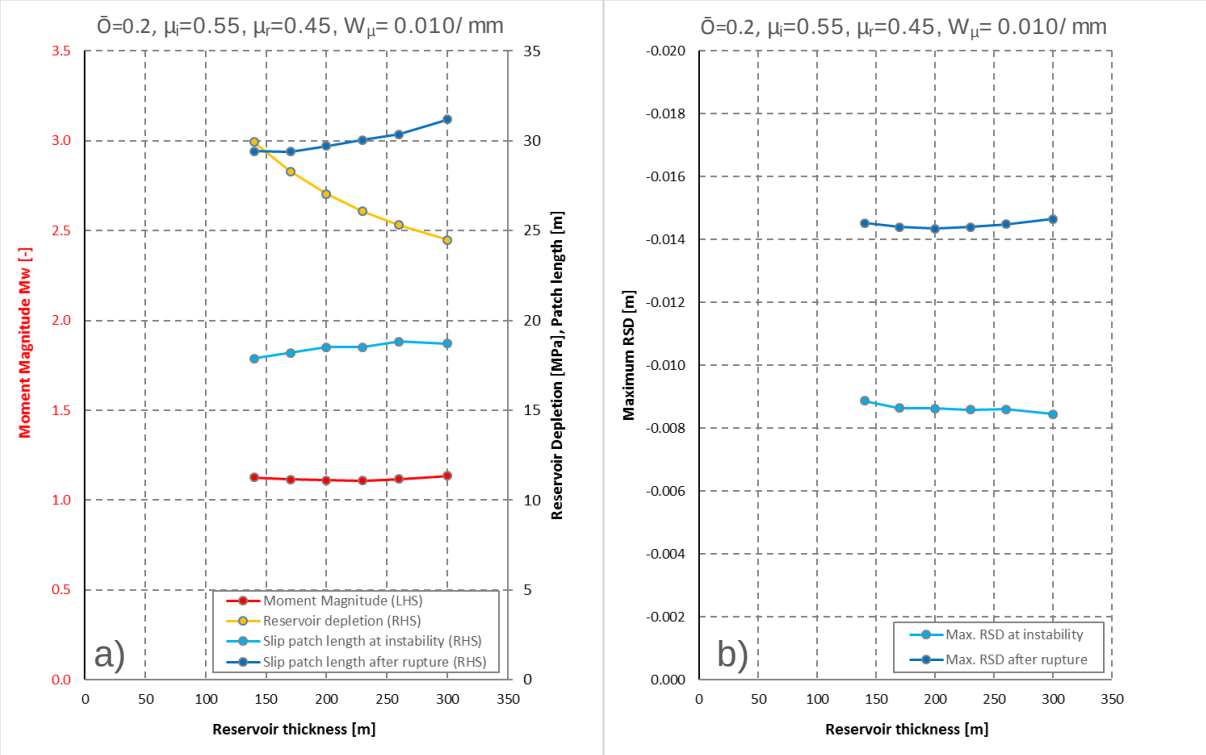

Figure A8.5: *a) moment magnitude (left-hand side, LHS), reservoir depletion (right-hand side, RHS) and length of the slip patch before and after the seismic event (right-hand side), and b) Relative Slip Displacement before and after the seismic event as a function of reservoir thickness for $\bar{O}$ =0.2, μ_i=0.55, μ_r =0.45 and W_μ = 0.01 mm^{-1}.*

A.8.1.2. CONCLUSIONS

The main findings in this chapter are:

- Onset of seismic rupture occurs for a linear fault slip-weakening behaviour if the critical slip length L_c is exceeded, independent of the reservoir thickness. The numerically simulated size of the slip patch is somewhat smaller, but at least 90% of critical slip patch size analytically derived by Uenishi and Rice.
- Onset of seismic rupture occurs at a lower reservoir depletion level for larger reservoir thickness. This is explained by the fact that fault instability occurs if the slip patch reaches a critical absolute length, whereas the stress distribution and length of the slip patch for a given depletion level scales with reservoir thickness.
- moment magnitude increases with reservoir thickness for a given normalised reservoir offset, except for Rupture Mechanism 2. For small normalised offset, moment magnitude is independent of the reservoir thickness when considering the same linear slip-weakening behaviour.

APPENDIX 9. SLOPE OF THE SLIP-WEAKENING DIAGRAM

The slope of the descending branch in the linear slip-weakening diagram (Figure A6.1) is the same for all cases discussed so far, because it facilitates evaluation of the residual friction coefficient, the reservoir offset and reservoir thickness as independent parameters. The slope W_μ in the slip-weakening diagram determines the critical slip length L_c (equation 3.1) at which the fault becomes unstable. In this chapter, the slope W_μ is varied between 0.001 and 0.1 mm^{-1} for a normalised reservoir offset $\bar{O}$ of 0.2, 0.4, 0.6, and 0.8 (Table A9.1). All other modelling parameters are in accordance with the Bases Case (APPENDIX 3). This means that the reservoir thickness is 200 m, and the initial and residual friction coefficient are 0.55 and 0.45 respectively. The results for the cases with W_μ = 0.01 mm^{-1} are taken from Chapter APPENDIX 7.

Table A9.1: Overview of additional analysis cases conducted with different values for Dc and a reservoir thickness of 200 m. Cases with D_c=0.010 (mu55-142, mu55-182 and mu55-222 with and offset of 40, 80 and 160 m respectively) are presented in Chapter APPENDIX 7.

Offset 40 m $\bar{O}$ =0.2	
Case	**W_μ [mm^{-1}]**
Mu55-531	0.001
Mu55-532	0.002
Mu55-533	0.005
Mu55-142	0.010
Mu55-537	0.015
Mu55-534	0.020
Mu55-538	0.030
Mu55-539	0.040
Mu55-535	0.050
Mu55-540	0.070
Mu55-536	0.100

Offset 80 m $\bar{O}$ =0.4	
Case	**W_μ [mm^{-1}]**
Mu55-551	0.001
Mu55-552	0.002
Mu55-553	0.005
Mu55-182	0.010
Mu55-554	0.020
Mu55-555	0.050
Mu55-556	0.100

Offset 80 m $\bar{O}$ =0.6		
Case	**W_μ [mm^{-1}]**	
Mu55-571	0.001	
Mu55-572	0.002	
Mu55-573	0.005	
Mu55-212	0.010	
Mu55-574	0.020	
Mu55-575	0.050	
Mu55-576	0.100	

Offset 160 m $\bar{O}$ =0.8	
Case	**W_μ [mm^{-1}]**
Mu55-591	0.001
Mu55-592	0.002
Mu55-593	0.005
Mu55-222	0.010
Mu55-594	0.020
Mu55-595	0.050
Mu55-596	0.100

A.9.1. Results

Figure A9.1 shows the development of the slip patch and the maximum Relative Slip Displacement as a function of reservoir depletion for cases with a normalised offset $\bar{O}$ = 0.4 (80 m) and different values of W_μ. Seismic rupture does not occur up to 30 MPa reservoir depletion for relatively ductile fault slip behaviour with a gently dipping branch in the slip-weakening diagram ($W_\mu \leq 0.002$/mm). Onset of seismic rupture occurs at decreasing reservoir depletion pressure and smaller size of the slip patch in case of more brittle fault slip behaviour with larger values of W_μ. This is consistent with analytical expression (3.1), which indicates a smaller critical size of the slip patch with increasing slope W. Note that the Base Case (APPENDIX 3) is represented by the dark-green line with W_μ= 0.01/mm.

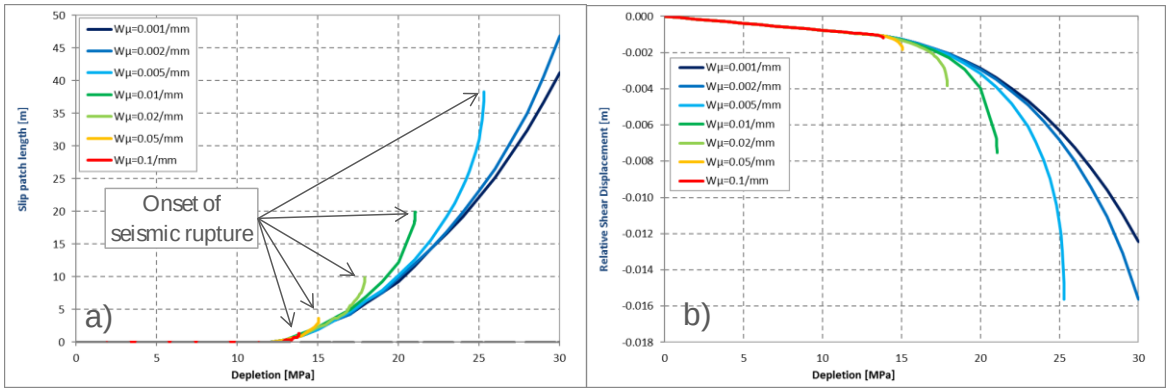

Figure A9.1: *a) Length of the shallow slip patch, and b) the maximum RSD as a function of reservoir depletion for the cases with an offset of 80 m ($\bar{0}$ = 0.4) in Table A9.1. The Base Case discussed in APPENDIX 3 is represented by the dark-green lines.*

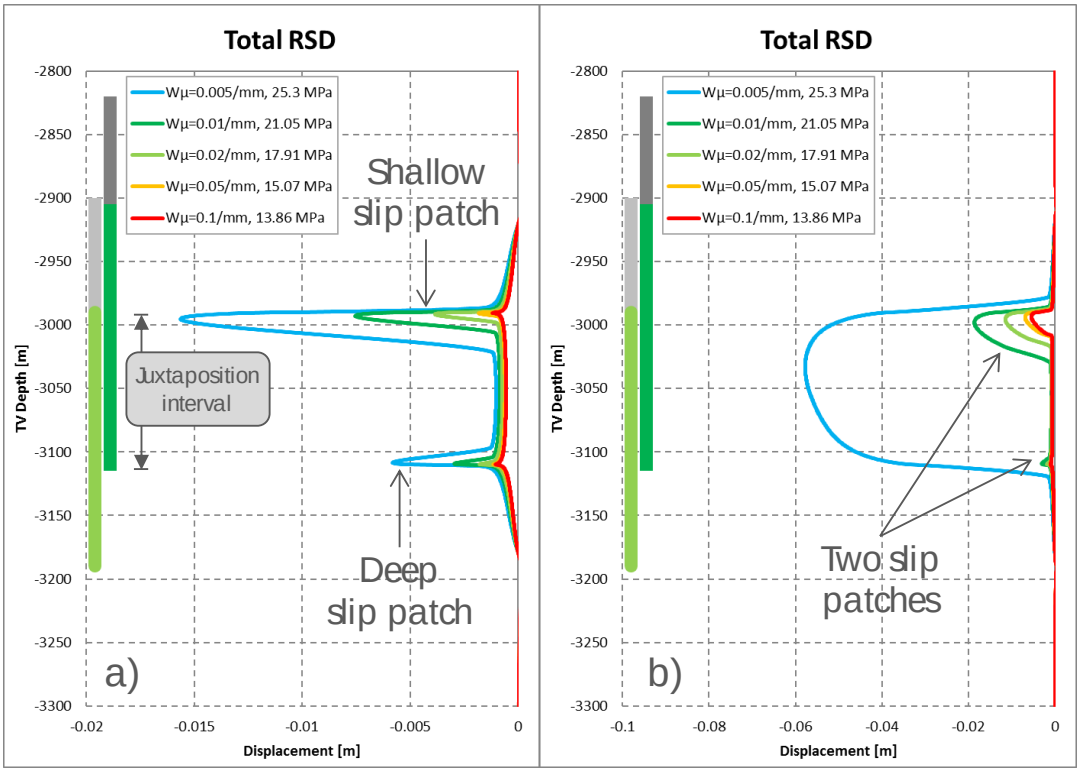

Figure A9.2: *The Relative Slip Displacement as a function of depth along the fault plane before (a) and after (b) the seismic event for the cases with $\bar{0}$ = 0.4 in Table A9.1. Note that the displacement scale is different in (a) and (b).*

All cases with a normalised offset $\bar{0}$ = 0.4 in Table A9.1 exhibit Rupture Mechanism 2, except for the case with W_μ = 0.005/mm (case mu55-553), which is characterised by Rupture Mechanism 3. Figure A9.2a shows that the RSD and the size of the two slip patches is smaller for larger values of W_μ. Slip displacement localises at the shallow slip patch with increasing reservoir depletion, until it reaches the critical length L_c, becomes instable and generates a seismic event. Figure A9.2b shows two slip patches after the seismic event for all cases except for W_μ = 0.005 mm^{-1}, which shows a single merged slip patch covering the entire reservoir juxtaposition interval. So, a transition occurs from Rupture Mechanism 2 if $W_\mu \geq 0.010$ mm^{-1} to Rupture Mechanism 3 if W_μ =

0.005 mm^{-1}, while no seismic rupture occurs for $W_\mu \leq 0.002$ mm^{-1} up to 30 MPa reservoir depletion.

Rupture Mechanism 2 is found for all cases with a normalised offset $\bar{o} = 0.2$. The slip displacement before and after the seismic event looks very similar to the results in Figure A9.2 for $\bar{o} = 0.4$, except that the distance between the slip patches is larger due to the smaller offset. For this reason, the two slip patches do not merge for the cases considered. Also, seismic rupture does not occur up to 30 MPa reservoir depletion if the slope in the slip-weakening diagram is too gentle. This is found for $W_\mu \leq 0.005$ mm^{-1} (cases mu55-531 through mu55-533 in Table A9.1) if the normalised offset of 0.2.

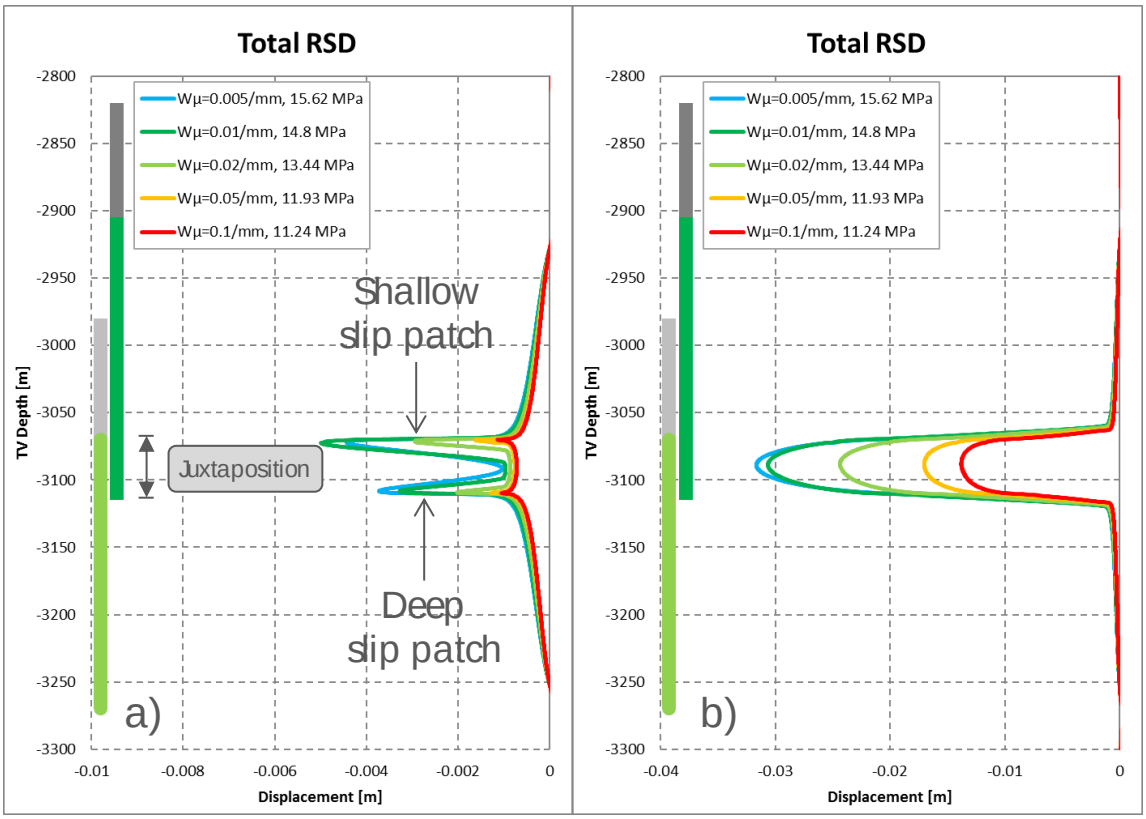

Figure A9.3: The Relative Slip Displacement as a function of depth along the fault plane before (a) and after (b) the seismic event for the cases with $\bar{o} = 0.8$ in Table A9.1. Note that the displacement scale is different in (a) and (b).

The slope of the slip-weakening diagram determines if Rupture Mechanism 3 or Rupture Mechanism 1 occurs in case of a normalised offset $\bar{o} = 0.8$. The large reservoir offset implies a small juxtaposition interval and a small distance between the slip patches (Figure A9.3a). Instability of the shallow slip patch is the root cause of the seismic event if the critical slip length L_c is sufficiently small and W_μ is sufficiently large. This is found for $W_\mu \geq 0.010$ mm^{-1}. The two slip patches merge during the seismic rupture (Figure A9.3b) because of the small distance (Rupture Mechanism 3). Seismic rupture is caused by merging of the slip patches (Rupture Mechanism 1) if W_μ=0.005 mm^{-1} (light-blue lines in Figure A9.3). No seismic event is simulated for smaller values of W_μ because the merging of the two slip patches occurs in a stable and a-seismic fashion.

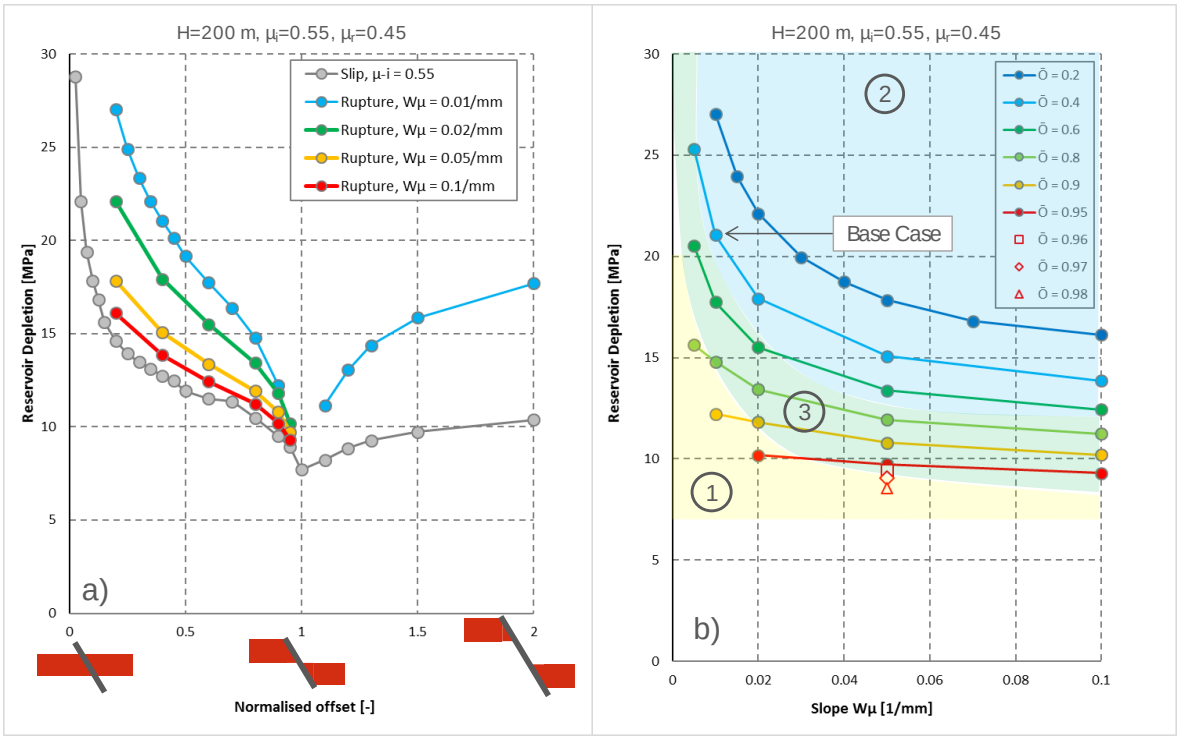

Figure A9.4: *Reservoir depletion at the onset of seismic rupture as a function of normalised reservoir offset (a) and as function of the slope W_μ (b). Background colour refers to the simulated rupture mechanism*

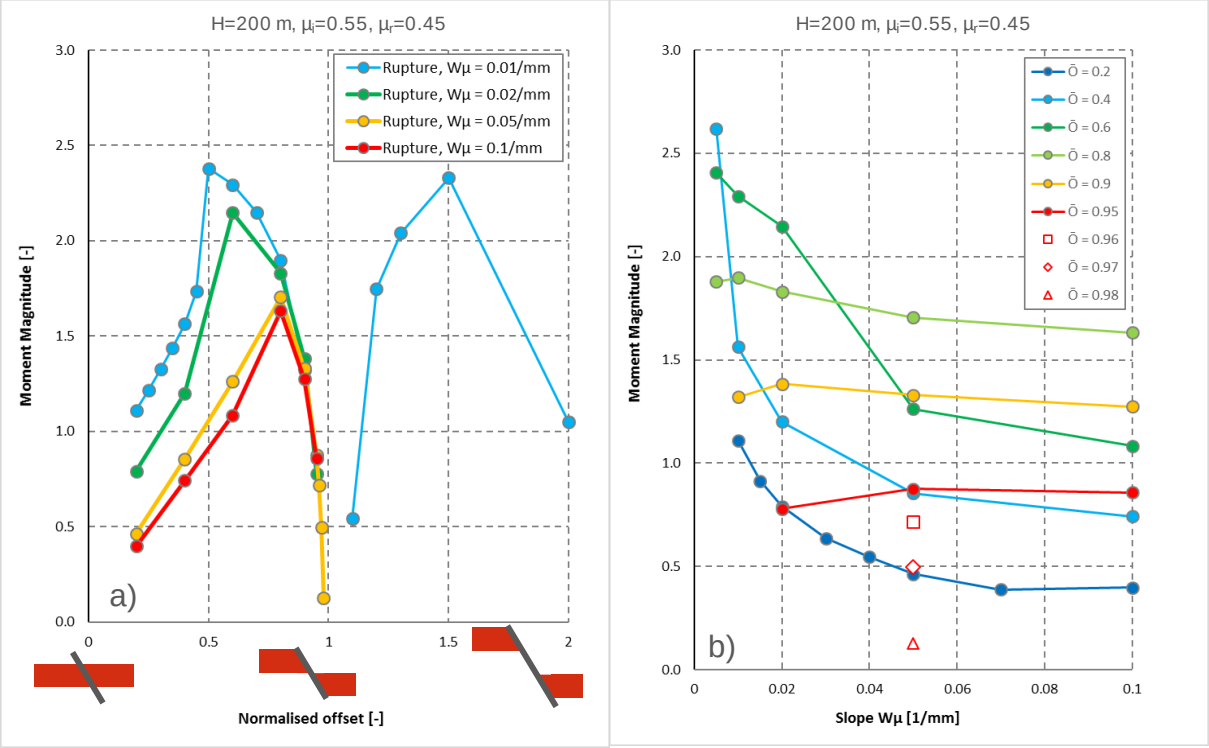

Figure A9.5: *Influence of the slope W_μ of the linear slip-weakening diagram on a) the depletion level at the onset of seismic rupture, and b) the moment magnitude M_w. The Base Case (APPENDIX 3) and the applicable rupture mechanism are indicated.*

The reservoir depletion at the *onset of seismic rupture* approaches the depletion at the *onset of fault slip* for an increasing slope W_μ of the linear slip-weakening diagram. Figure A9.4a shows the same data as Figure A7.14a including the results of this chapter. The grey line indicating the reservoir depletion at the onset of fault slip for μ_i =0.55, and the coloured lines indicating the depletion at the onset of seismic rupture for μ_r =0.45 and different values of W_μ. It is seen that the depletion level for the *onset of seismic rupture* approach the line for fault slip for an increasing value of W_μ. Figure A9.4b shows that the dependency on W_μ reduces with increasing value for W_μ. Furthermore, it is seen that the depletion range between onset of fault slip and onset of seismic rupture is smaller if the normalised offset approaches 1.

The different rupture mechanisms are indicated by the background colour in Figure A9.4b. Rupture Mechanism 2 (blue back ground) is found for $\bar{O}$ = 0.2 (dark-blue line) and all considered values for W_μ (in combination with μ_i =0.55 and μ_r =0.45). Rupture Mechanism 2 is also found for a larger normalised offset provided that the slope in the slip-weakening diagram is sufficiently steep (W_μ sufficiently large). This corresponds with more brittle fault slip behaviour. If not, Rupture Mechanism 3 (green back ground) occurs in which the shallow slip patch merges with the deep slip patch.

Rupture Mechanism 3 is prevailing for a normalised offset approaching 1, although Rupture Mechanism 1 is found for small values of W_μ. In these cases, the critical slip length L_c is too large and the distance between the two slip patches too small to cause instability of the shallow slip patch. Inversely, only very brittle fault slip behaviour can cause Rupture Mechanism 2 if for $\bar{o} \approx 1$, as discussed above.

The range for the normalised offset in which Rupture Mechanism 1 occurs for $\bar{o} \approx 1$ (see also Figure A7.14a) is smaller for increasing value for W_μ. The transition between Rupture Mechanism 1 and Rupture Mechanism 3 occurs in the range $0.90 < \bar{O} < 0.95$ for W_μ = 0.020/mm (green line in Figure A9.4a), while it is in the range $0.96 < \bar{O} < 0.97$ for W_μ = 0.050/mm (yellow line). This is explained from the reducing critical slip length L_c for increasing slope W_μ (expression 3.1), which allows slip patches to be closer together and a normalised offset closer to 1 before merging takes place and Rupture Mechanism 1 occurs.

The rupture mechanism is also reflected in the moment magnitude of the simulated seismic event. Figure A9.5 shows the moment magnitude as function of the normalised offset, as well as the slope W_μ. Note that Figure A9.5a does not include the moment magnitude for cases with W_μ=0.005/mm which are included in Figure A9.5b. The (light-blue) line for is the same as in Figure A7.15. In general, moment magnitude reduces with increasing slope of the slip-weakening diagram. The impact is largest for a small normalised reservoir offset, whereas the impact of the slope on moment magnitude is almost negligible for a normalised reservoir offset close to 1. Rupture Mechanism 3 tends to generate the largest seismic events, which are roughly found for $0.5 < \bar{o} < 0.8$ and $1.2 < \bar{o} < 1.5$. Note that a smaller residual friction coefficient can also cause a Rupture Mechanism 3 and a correspondingly larger moment magnitude for a normalised offset smaller than 0.5 (section A.7.3.3).

A.9.2. Conclusion

In this chapter it is found that

- an increase of the slope of the descending branch of the linear slip-weakening diagram causes the depletion level at which *onset of seismic rupture* occurs to approach the depletion level for *onset of fault slip*. A steeper slope corresponds

with more brittle fault slip behaviour, whereas a gentler slope corresponds with ductile fault slip response.

- a steeper slope in the slip-weakening diagram generally leads to a smaller moment magnitude for a given normalised reservoir offset. This influence is most prominent for small offsets, and vanishes for a normalised offset that approaches 1.
- the slope of the slip-weakening diagram, the reservoir offset and the residual friction coefficient determine the rupture mechanism that occurs if the onset of seismic rupture has been reached. The critical slip length L_c – which derived from the slope W_μ – and the available distance between the slip patches – which is fixed by the reservoir offset – determines whether a seismic event occurs due to merging of two slip patches (Rupture Mechanism 1) or instability of a single slip patch (Rupture Mechanism 2 or 3). The residual friction coefficient determines whether the rupture is arrested before or after merging with the deep slip patch, and thereby determines the occurrence of Rupture Mechanism 2 or 3 respectively.

APPENDIX 10. THE SOURCE-TIME FUNCTION

A source-time function gives the average relative slip velocity over the slip patch as a function of time. So, it is the average velocity over the slip patch as given in Figure A3.4 for the Base Case (APPENDIX 3). The method for calculating the average velocity in normal and slip direction to the fault plane is discussed in section A.10.1. Only the source-time function in slip direction along the fault plane is discussed, because the velocity in normal direction is negligible.

The source-time function is presented for selected cases discussed in the previous chapters, covering the characteristics of Rupture Mechanisms 1, 2 and 3, the influence of reservoir offset and thickness, the residual friction coefficient and the slope of the slip-weakening diagram. The Base Case with a reservoir thickness of 200 m and an offset of 80 m is the point of departure for this evaluation. The fault is dipping under an angle of 66 degrees and has an initial friction coefficient of 0.55 and a negligible cohesion. Initial stress conditions and elastic properties are presented in Chapter 2.

In the section A.10.2, the influence of the residual friction is evaluated for the cases discussed in APPENDIX 6, which includes the Base Case discussed in APPENDIX 3. The value for the critical slip displacement D_c is adjusted in conjunction with the value of the residual friction coefficient μ_r such that the slope of the descending branch of the slip-weakening diagram W_μ remains the same for all cases. The influence of reservoir offset is discussed in section A.10.3, and the slope in the slip-weakening diagram W_μ on the source-time function is evaluated in section A.10.4.

A.10.1. Computing the source-time function of a seismic rupture

The source-time function of a seismic rupture $\boldsymbol{v}_\Delta(t)$ is defined as the average relative slip velocity vector over the slip patch at time t. The relative slip velocity $v_{\Delta\alpha i}$ in direction α=(x, y) of node *i* is computed as (Figure A10.1)

$$v_{\Delta\alpha i} = v_{lxi} - v_{rxi},$$

in which $v_{\mathrm{lx}i}$ is the velocity at the left-hand side of the fault and $v_{\mathrm{rx}i}$ is the velocity at the right-hand side. The source function is calculated as

$$v_{\Delta\alpha}(\mathrm{t}) = \frac{1}{l_r}\sum_{i=1}^{n} v_{\Delta\alpha i}(t)\cdot l_i,$$

in which l_i is the length of the slip patch for which the velocity is given in node *i*, and l_r the length of the entire rupture area. An area is assumed to belong to the rupture area if a certain threshold velocity v_t is exceeded. In this report a threshold velocity of v_t=0.001 m/s is used. This expression can be evaluated for a global XY-coordinate system or a local coordinate system normal and tangential to the fault plane (interface element).

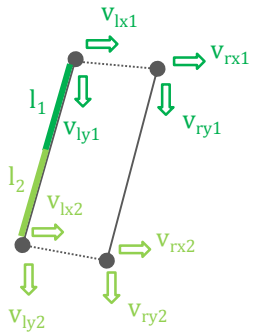

Figure A10.1: DIANA interface element and velocity degrees of freedom. The length l1 and l2 are half the distance between node 1 and node 2 for linear elements.

A.10.2. Residual friction coefficient

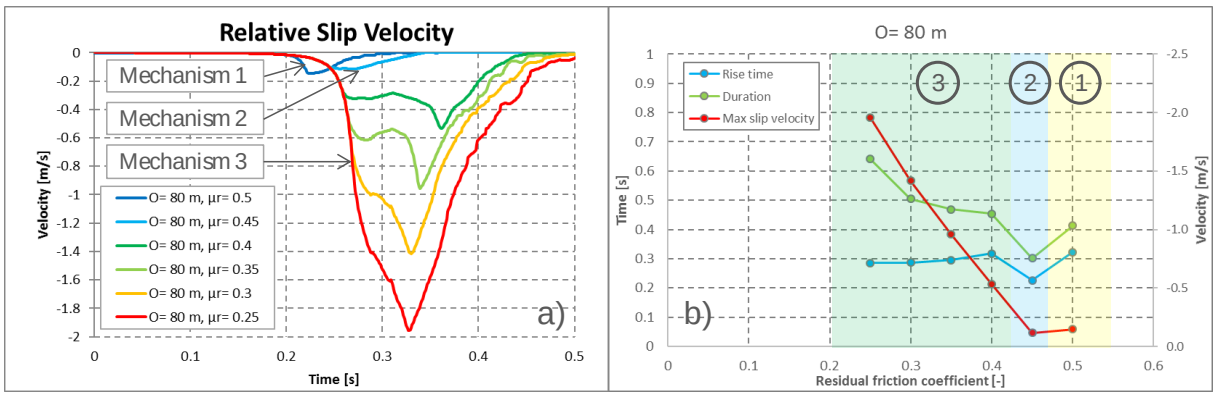

Figure A10.2: a) Average relative slip velocity as a function of time (source-time function) for different values of the residual friction coefficient and an offset of 80 m ($\bar{O}$ = 0.4). The Base Case (APPENDIX 3) is represented by light-blue line (μr=0.45), b) the rise time, duration and Peak Slip Velocity (PSV, right-hand scale) of the source-time function as a function of the residual friction coefficient. The coloured areas indicate the simulated Rupture Mechanism.

Figure A10.2a shows the source-time function for a selection of the cases in Table A6.1 in APPENDIX 6. The identical slope in the slip-weakening diagram not only causes seismic rupture to nucleate at the same depletion level by instability of the shallow slip patch for cases with $\mu_r \leq 0.45$, but also results in an identical source-time function until the critical slip displacement D_c is reached at some point along the fault plane. For the Base Case with $\mu_r=0.45$ (light-blue line, Rupture Mechanism 2), the seismic rupture at the shallow slip patch stops before merging with the second, deeper patch. For the cases with a smaller residual friction coefficient, particularly for $\mu_r=0.40$ and 0.35, the average velocity reduces somewhat before a second, larger peak velocity is reached that is caused by merging of the two slip patches (Rupture Mechanism 3). The average slip velocity increases monotonically for $\mu_r \leq 0.45$. The peak velocity in the source-time function increases proportional with a reduction of the residual friction coefficient, as shown in Figure A10.2b (red line, right-hand scale). Furthermore, it is seen that Rupture Mechanism 1 – generated if $\mu_r=0.50$ – accelerates much faster compared to Rupture Mechanism 2 or 3.

Figure A10.2b also shows the rise time and duration of the seismic rupture (left-hand scale). The rise time is defined by the time it takes to reach the peak velocity in the

source-time function, while the start of the rupture is defined by the moment when the average velocity exceeds 0.001 m/s. The end of the rupture is taken when the average velocity drops below the threshold value of 0.001 m/s. It is seen that the rise time is virtually independent of the residual friction coefficient for Rupture Mechanism 3. The duration of the seismic rupture increases with lower value of the residual friction coefficient, which means that the deceleration phase of the rupture is longer. Apparently, it takes longer to slow-down the rock mass from a higher Peak Slip Velocity. The deceleration phase is represented by the distance (time) between the green and blue lines in Figure A10.2b. The rise time for Rupture Mechanism 1 (μ_r=0.50) is about the same (0.32 s) compared to Rupture Mechanism 3 according to the current definition, although the graphical interpretation suggests a smaller rise time. A larger value of the threshold slip velocity of 0.002 or 0.005 m/s does not resolve this issue.

A.10.3. Reservoir offset

The influence of reservoir offset on the source-time function is evaluated using the cases discussed in APPENDIX 7 with a slope W_μ = 0.010/mm. The source-time function for the cases with a residual friction coefficient of 0.5 and 0.45 have been plotted in Figure A10.3. The source-time functions associated with Rupture Mechanism 1 are very similar in shape for different values of the reservoir offset. Figure A10.3a shows a similar rise time for different values of the reservoir offset, while the peak slip velocity increases and the duration and moment magnitude decrease.

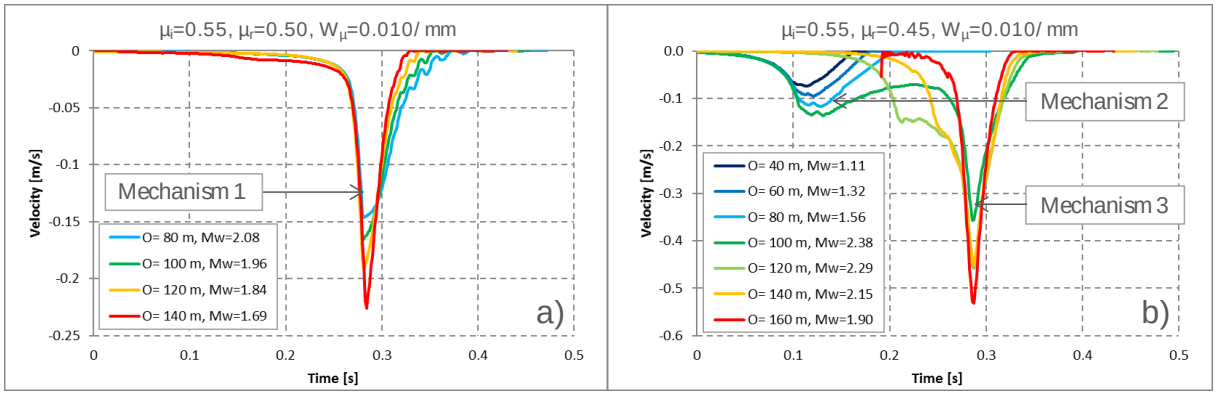

Figure A10.3: Average relative slip velocity as a function of time (or source-time functions) for a selection of cases with an offset smaller than reservoir thickness that display a) Rupture Mechanism 1, and b) Rupture Mechanism 2 or 3.

A more gradual acceleration is seen in Figure A10.3b that shows the source-time function of seismic events caused by instability of the shallow slip patch (Rupture Mechanism 2 and 3). The acceleration after the onset of seismic rupture is the same because the slope W_μ of the slip-weakening diagram is the same (see previous section). Rupture Mechanism 2 is found for cases with a sufficiently small offset, such as the Base Case (80 m offset, light-blue line). A smaller peak slip velocity, duration and moment magnitude is found for cases with a smaller reservoir offset. Rupture Mechanism 3 is found for cases with an offset of 100 m and larger. Similar to the previous section a period of lower average slip velocity is simulated before merging of the two slip patches gives rise to the second, larger peak velocity. This period disappears if the reservoir offset approaches 200 m and the normalised offset approaches 1. It is noted that the peak velocity monotonically increases with offset,

while the largest moment magnitude is calculated for the case with 100 m offset and gradually decreases with increasing offset (see also Figure A9.5).

The source-time function is derived in the same fashion for other cases discussed in Chapter APPENDIX 7, where the residual friction coefficient is varied in the range between 0.5 and 0.25 and the normalised reservoir offset between 0 and 2. The peak slip velocity in Figure A10.4 shows some different dependencies on the normalised offset and residual friction coefficient than the Moment magnitude shown in Figure A7.19 for the same cases. The peak slip velocity is largest between a normalised offset of 0.5 and 1 for a given value of the residual friction coefficient, whereas moment magnitude is largest for a small offset or a very large (normalised) reservoir offset. Furthermore, the peak slip velocity shows a more profound reduction for a normalised offset of about 1 than the moment magnitude.

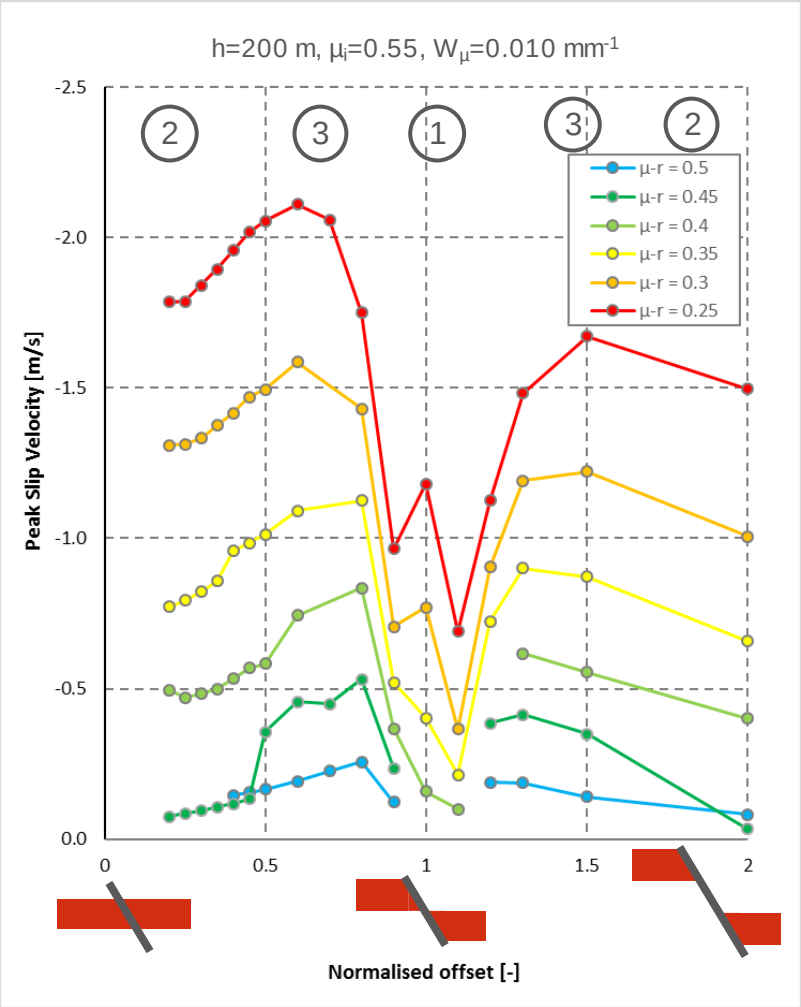

Figure A10.4: The peak slip velocity of the source-time function as a function of normalised reservoir offset for different values for the residual friction coefficient, but with the same slope in the slip-weakening diagram.

A.10.4. Slope of the slip-weakening diagram

A selection of cases from the previous chapter are considered to evaluate the impact of the slope in the slip-weakening diagram. Attention is focused at the cases with an offset of 80 m ($\bar{o}$ = 0.4, cases mu55-551 through 556 and Base Case mu55-182, Table A9.1). The source-time functions in Figure A10.5a show a faster acceleration of the

average relative slip velocity for an increasing slope W_μ in comparison to the Base Case (dark-green line with W_μ = 0.010/mm). However, the peak slip velocity hardly increases with W_μ Figure A10.5b). The shorter rise time with increasing slope W_μ also implies a larger acceleration. The deceleration phase is almost equally long in all cases as the total duration follows the curve for the rise-time. The rise time is longest for the case with W_μ = 0.005/mm, which exhibits Rupture Mechanism 3. The peak slip velocity is more than three times as large as in the Base Case, while initial and residual friction coefficients are the same. The moment magnitude for this case is also significantly larger (see Figure A9.5b).

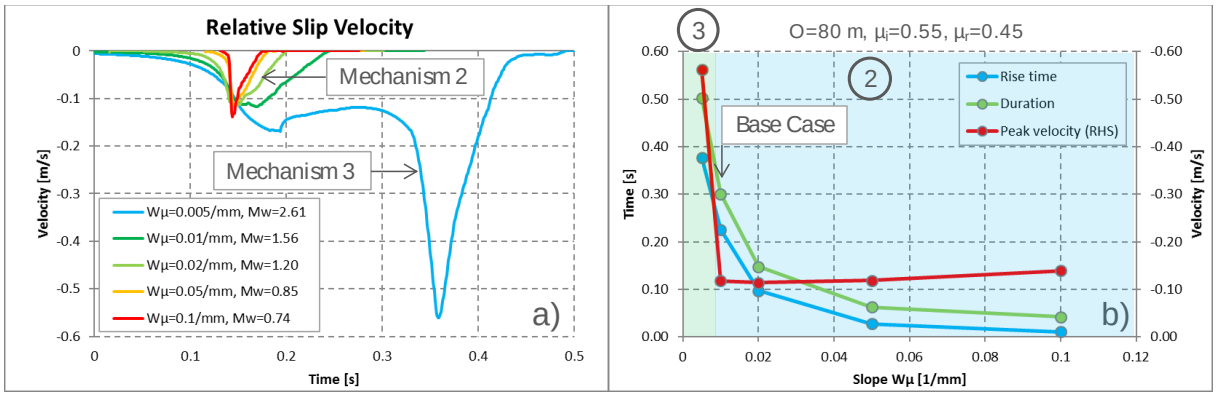

Figure A10.5: a) Average relative slip velocity as a function of time (source-time function) for an offset of 80 m ($\bar{O}$ = 0.4) and different values of the slope W_μ. The Base Case, discussed in APPENDIX 3 with W_μ = 0.010/mm is represented by dark-green line. b) the rise time, duration and peak slip velocity (right-hand scale) of the source-time function as a function of the slope W_μ.

A.10.5. Summary of findings

It is demonstrated that each source-time function is associated with a particular rupture mechanism.

Main findings for the source-time function of Rupture Mechanism 1:

- The shape of the source-time function shows a fast acceleration with a sharp peak.
- The rise-time is shorter compared to Rupture Mechanism 2 or 3 for the same fault configuration and slope in the slip-weakening diagram.
- The duration of the rupture is shorter for a normalised offset close to 1, which is mainly attributed to a shorter deceleration phase.

Main findings for the source-time function of Rupture Mechanism 2:

- The rise time is strongly influenced by the slope in the slip-weakening diagram
- The peak slip velocity is not significantly influence by the slope of the slip-weakening diagram
- The peak slip velocity is lower in caparison to Rupture Mechanism 1 for a similar reduction of the friction coefficient (μ_i - μ_r).

Main findings for the source-time function of Rupture Mechanism 2 and 3:

- The shape of the source-time function has a more gradual acceleration and deceleration phase compared to Rupture Mechanism 1, and is not significantly influenced by the offset

- The rise time is strongly influenced by the slope in the slip-weakening diagram, but not by the reduction in friction coefficient (μ_i - μ_r)
- The peak slip velocity increases proportional with the reduction of the friction coefficient
  (μ_i - μ_r).
- The deceleration phase – and thereby the duration of the rupture – increases with increasing peak slip velocity, which linked to the reduction of the friction coefficient (μ_i - μ_r).

APPENDIX 11. SCALING RELATIONSHIPS

Scaling relationships are useful to relate the (field measured) moment magnitude M_w with various 2D simulation results in this report. To this end, the simulation results of all analyses (APPENDIX 2) have been collected and various correlation relationships with moment magnitude have been attempted. The results are presented in this chapter. For the moment magnitude, it is assumed that the size of the seismic slip patch in strike direction of the fault is equal to the size in dip direction, which is obtained from the 2D dynamic rupture analysis in this report.

A.11.1. Slip patch size and slip displacement

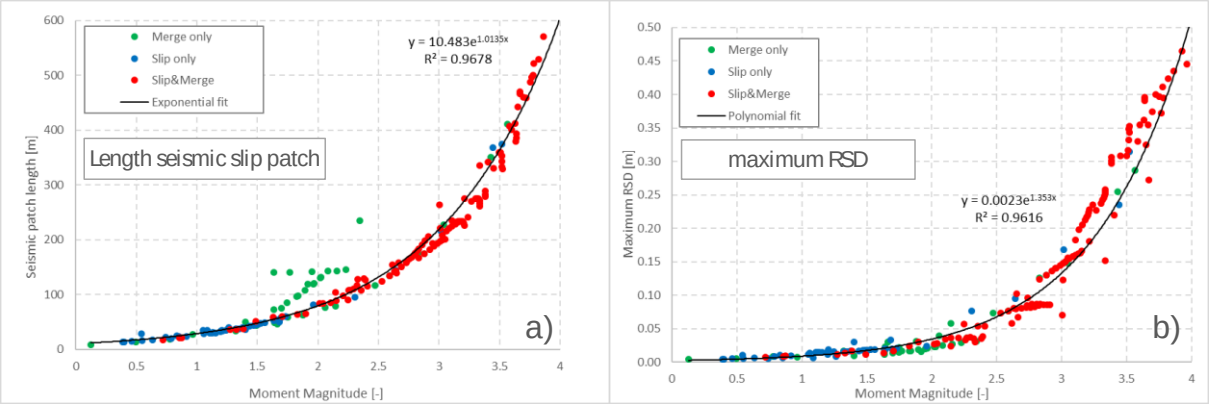

Figure A11.1: a) The size of the seismic slip patch and b) the Relative Slip Displacement (RSD) as a function of moment magnitude M_w and rupture mechanism for all cases in this report (APPENDIX 2).

The size of the slip patch (L_s) and the maximum Relative Slip Displacement (RSD_{max}) correlate rather well with the moment magnitude according to a power law function (Figure A11.1):

$$L_s = 10.483 \cdot e^{1.0135\, M_w},$$

$$RSD_{max} = 2.3 \cdot 10^{-3} \cdot e^{1.353\, M_w}.$$

A correlation between the moment magnitude and the log value of the size of the seismic slip patch and the RSD is less good.

The good fit between moment magnitude on one hand, and the size of the seismic slip patch and the Relative Slip Displacement on the other hand is not unexpected because of the definition for the moment magnitude (APPENDIX 13). The result in Figure A11.1 suggest that a preferred slip distribution over the slip patch might exists. A linear relationship between the seismic slip patch and the RSD can be established (Figure A11.2a) for large seismic events with $M_w > 3$ and a seismic slip patch larger than about 200 m, but accuracy is rather limited for smaller events, as shown in Figure A11.2b. A separate and quite different correlation can be established for Rupture Mechanism 2 (blue dots) and $M_w \leq 2$. Furthermore, alignment of a limited number of points is found for Rupture Mechanism 1 (green dots in Figure A11.2a and Figure A11.2b) that is attributed to impact of a single modelling parameter. Reservoir offset is found to have a significant impact on the seismic slip patch in terms of size and relative slip displacement, which is not reflected in a simple correlation with moment magnitude. Similar alignment of points is found for Rupture Mechanism 3 (red dots).

Hence, it is concluded that the above correlations for the size of the seismic slip patch and the maximum RSD should be used carefully with in mind that large deviations may exist between the estimated size and maximum RSD and the actual event, in particular for events with small magnitude.

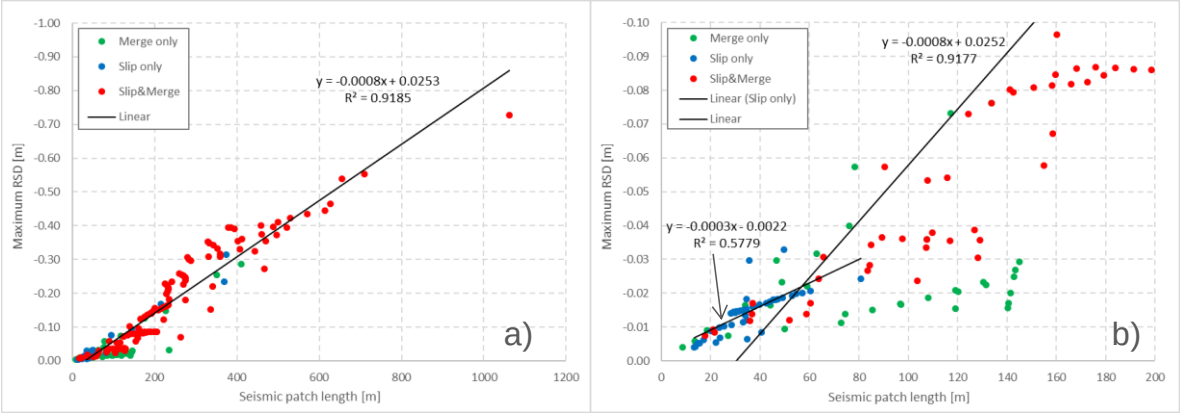

Figure A11.2: Relationship between the length of the slip patch and the maximum Relative Slip Displacement (RSD) for each of the rupture mechanisms, with b) zoom-in of graph a) for small seismic events.

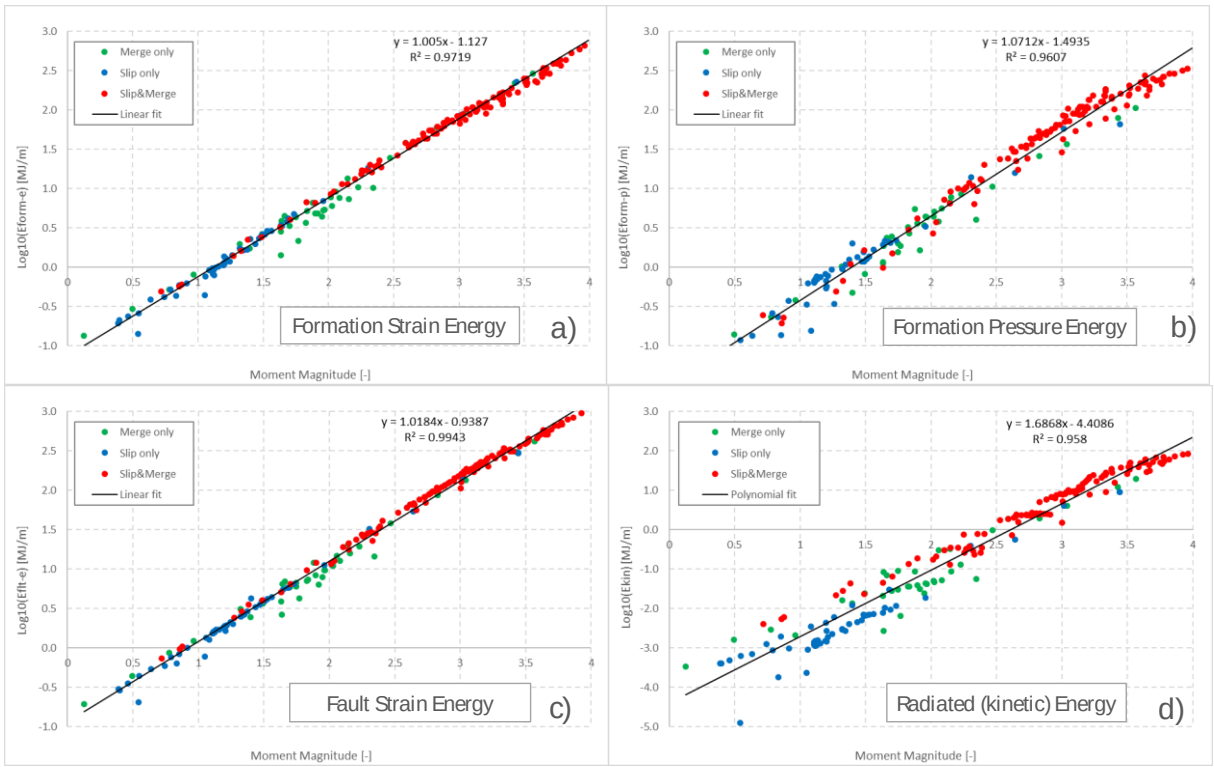

Figure A11.3: The log10 value of the formation strain (a) and formation pressure energy (b), the (radiated) kinetic energy (c) and the energy dissipated by fault slip (d) in MJ/m as a function of moment magnitude Mw and rupture mechanism, for all cases in this report (APPENDIX 2).

A.11.2. Energy components

The four main components of the energy balance equation – as defined in APPENDIX 8 – correlate well with the moment magnitude. Figure A11.3 shows the logarithmic

value of the formation strain and pressure energy, the kinetic energy and the fault strain energy as a function of the moment magnitude and the rupture mechanism. The energy unit is MJ/m due to the 2-dimensional character of the model. As discussed in section A.3.2, gravity performs labour during the depletion stage of the simulation, which is mainly stored in the form of formation strain and pore pressure energy (compaction), while a small part is dissipated by fault slip, if any. Formation strain and pore pressure energy (Figure A11.3a and b) is released during the simulated seismic event. Most of the released energy is dissipated by fault slip (Figure A11.3c), while the remaining energy is converted into kinetic energy (mass velocity, Figure A11.3d). The release of formation strain and pore pressure energy stops when no incremental fault slip occurs over the slip patch. This implies that the moment magnitude does not further increase and that no more energy is dissipated by fault slip (fault strain energy). The remaining kinetic energy W_k in the model after the seismic rupture is radiated to the surface. This energy (in MJ/m) is plotted in Figure A11.3d and correlates linearly with the calculated moment magnitude according to

$$log_{10}(W_k) = 1.6868 \cdot M_w - 4.4086.$$

For the formation strain energy W_ε, the formation pressure energy W_p and the fault shear strain energy W_s the following linear relationships are found:

$$log_{10}(W_\varepsilon) = 1.005 \cdot M_w - 1.127,$$

$$log_{10}(W_p) = 1.0712 \cdot M_w - 1.4935,$$

$$log_{10}(W_s) = 1.0184 \cdot M_w - 0.9387.$$

A second order polynomial fit does not improve the correlation for any of the energy components. The seismic efficiency *R* is the radiated (kinetic) energy W_k as fraction of the total energy released by formation strain and pore pressure W_ε+W_p (see section A.3.2). The following correlation is found

$$R = 2 \cdot 10^{-4} \cdot e^{1.6299\, M_w}.$$

The correlation for the seismic efficiency with moment magnitude is not as good as for the individual energy components. The deviation from the trendline is more profound for Rupture Mechanism 3 compared to the deviation shown for Rupture Mechanism 1 and 2, in particular for a moment magnitude larger than about 2.5. Some clustering of the points is seen, similar to the correlation between maximum RSD and patch length in Figure A11.2, which is attributed to the selection of parameters for the different sensitivities evaluated in this study.

A.11.3. Stress drop and residual friction coefficient

The assumption of a residual friction coefficient in a linear-slip weakening diagram is one of the causes of the poor correlation with moment magnitude for some modelling parameters. The residual friction coefficient is reached if the slip displacement reaches the prescribed critical value D_c (Figure 2.2). This implies that the fault strength, and thus the fault stress, cannot reduce further if the slip displacement becomes larger than D_c. So, slip displacement and thus moment magnitude can increase unlimited without further reducing the friction coefficient and associated stress drop. This has been demonstrated for a few cases in chapter APPENDIX 7, and is reflected in Figure A11.4a, which shows the stress drop as a function of moment magnitude and rupture

mechanism for all cases in this study. It is seen that the average stress drop over the slip patch may vary considerably for any given moment magnitude. For this reason, stress drop is not an effective parameter when using a linear fault slip-weakening relationship. Other constitutive relationships for seismic slip may show a better correlation between stress drop and moment magnitude, but are not evaluated in this study.

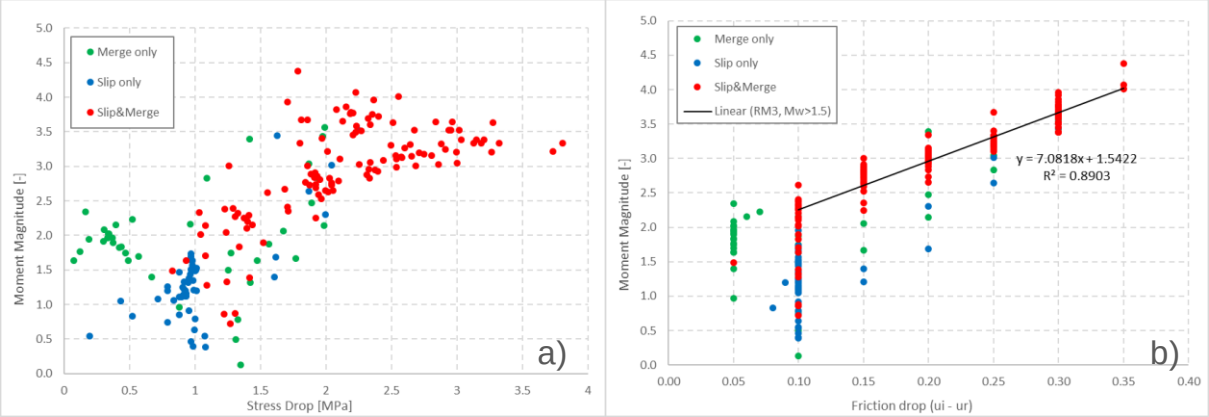

Figure A11.4: The moment magnitude and rupture mechanism as a function of a) the average stress drop over the slip patch, and b) the reduction of the friction coefficient. The linear trendline represents cases that exhibit Rupture Mechanism 3 with M_w > 1.5.

The reduction of friction coefficient (μ_i-μ_r) provides a better correlation with moment magnitude. Figure A11.4b shows a linearly increasing magnitude for seismic events with M_w > 1.5 that exhibit Rupture Mechanism 3. The six cases with Rupture Mechanism 3 and M_w < 1.5 have a normalised offset close to 1 and a slip-weakening diagram with a slope W_μ > 0.010/mm. So, a large range for the moment magnitude is possible despite the linear relationship with the residual friction coefficient found in APPENDIX 6. This is caused by dependencies on other modelling parameters, such as (normalised) reservoir offset and the slope W_μ in the slip-weakening diagram. Also, the initial friction coefficient, the in-situ stress and fault dip angle – which are not considered in this study – are likely to impact moment magnitude.

A.11.4. Concluding remarks

The scaling relationships between moment magnitude and the size of slip patch and the maximum RSD as well as with the different energy components seem relatively good, but do not included the influence of parameters, such as the initial friction coefficient, the initial stress condition, fault dip and azimuth angle, and formation compressibility. The linear relationship between moment magnitude and the reduction of the friction coefficient (μ_i-μ_r) shown in Figure A11.4 is obscured by the influence of other parameters, such the slope of descending branch in the slip-weakening diagram and reservoir offset. These aspects have a large impact on the rupture mechanism and the moment magnitude, as demonstrated in this study. It is therefore not very useful to develop a single relationship between moment magnitude and a particular fault property. Instead, the different relationships presented in this report can be used to constrain the residual friction coefficient and the slope W_μ of the slip-weakening diagram in combination with other data sources such as a geological fault model and the actual seismic event location that could constrain the reservoir thickness, reservoir offset, and fault dip and azimuth angle. The

correlation functions in this chapter should be used with care and understanding of the underlying modelling assumptions that have been used to generated them.

APPENDIX 12. THE ENERGY BALANCE EQUATION

The energy balance equation for the entire finite-element model is evaluated in analysis stage 1, in which a-seismic slip is simulated under incremental reservoir depletion, as well as in analysis stage 2, simulating seismic rupture under constant reservoir depletion pressure. The objective is to understand the change in different energy components during both analysis stages.

The energy balance equation for a seismic rupture process can be written as (Kanamori, 2001):

$$\Delta E_e + \Delta E_g + \Delta E_k + \Delta E_F + \Delta E_G = 0. \quad \text{(A12.1)}$$

In which ΔE_e is the change in strain energy, ΔE_g the gravitational energy, ΔE_k the radiated or kinetic energy, ΔE_F the energy dissipated by fault friction, and ΔE_G the fracture energy. The DIANA finite-element model described in Chapter 2 comprise of two constituent parts, namely the 2D continuum elements representing the formations and the 1D interface elements representing the fault. The change in strain energy is calculated from the continuum elements representing a porous solid with pore fluid. Therefore, the change in strain energy is written as:

$$\Delta E_e = \Delta E_\varepsilon + \Delta E_p. \quad \text{(A12.2)}$$

Herein is

$$E_\varepsilon = \frac{1}{2}\int_V (\sigma + \sigma_0)\varepsilon \, dV \quad \text{(A12.3)}$$

the strain energy of the porous solid, σ is the effective stress tensor and σ_0 is the effective stress tensor in the reference situation and ε is the strain tensor relative to the references situation. The formation pore pressure energy is calculated as

$$E_p = \frac{1}{2}\int_V (p + p_0)\varepsilon_{vol} \, dV, \quad \text{(A12.4)}$$

where p is the pore pressure and p_0 is the pore pressure in the reference situation and ε_{vol} is the volumetric strain relative to the reference situation. Both, the strain energy of the porous solid and the pore pressure energy are integrated over the model domain V.

The gravity energy is calculated only from the continuum elements, as no mass is assigned to the interface elements in the finite-element model. A force field, such as gravity, performs labour if mass is moving through it. The gravitational energy is defined as:

$$E_g = -\int_V \rho \, g du \, dV, \quad \text{(A12.6)}$$

where ρ is the density of the formations and g is the gravity acceleration vector and du is the displacement vector relative to the reference situation. The product of density, gravity acceleration and displacement is integrated over the model domain V.

Interface elements also do not contribute to the kinetic energy, which is defined as:

$$E_k = -\frac{1}{2}\int_V \rho \, g v^2 \, dV, \quad \text{(A12.7)}$$

where v is the length of the velocity vector. The product of density, gravity acceleration and velocity is integrated over the model domain *V*.

The energy dissipated by fault slip and the fracture energy are calculated from the interface elements jointly, while recognising a porous solid and a pore pressure contribution:

$$\Delta E_F + \Delta E_G = \Delta E_{fs} + \Delta E_{fp}, \tag{A12.8}$$

with the fault strain energy for interface elements is defined as:

$$E_{fs} = \frac{1}{2}\int_A (\sigma + \sigma_0) du \, dA, \tag{A12.9}$$

where σ and σ_0 is the effective traction stress in the interface elements in the actual and reference situation respectively, and *du* is the relative displacement vector in the interface elements relative to the reference situation. The fault pore pressure energy for interface elements is defined as:

$$E_{fp} = \frac{1}{2}\int_A (p + p_0) du^n \, dA, \tag{A12.10}$$

where p is the pore pressure and p_0 is the pore pressure in the reference situation and du^n is the interface opening relative to the reference situation. Both contributions are integrated over the interface surface A.

The reference situation is the stress- and strain-free model before stress initialisation and reservoir depletion. DIANA calculates the energy components (A12.3) through (A12.10) after every incremental reservoir depletion during analysis stage 1 and after every time step in analysis stage 2. The energy balance equation (A12.1) during analysis stage 1 is evaluated by calculating the incremental values after stress initialisation, which is at a reservoir depletion of 0 MPa, whereas the energy balance equation during seismic rupture is evaluated by calculating the incremental values relative to t=0, which is at the onset of seismic rupture.

The seismic efficiency represents the fraction of the released energy that is transmitted as seismic waves. Kanamori (2001) defines the seismic efficiency as

$$\eta = \Delta E_k / \left(\Delta E_e + \Delta E_g\right), \tag{A12.11}$$

where the strain energy ΔE_e also includes the kinetic energy (Aki and Richards, 2002, eq. (5.5) on page 122). Therefore, in the kinetic energy is subtracted from the strain energy ΔE_e in the calculation of the seismic efficiency. In this study the seismic efficiency is calculated after every depletion step in analysis stage 1 and after every time step in analysis stage 2 using the following expression

$$\eta = \Delta E_k / \left(\Delta E_e + \Delta E_g - \Delta E_k\right) = \Delta E_k / \left(\Delta E_\varepsilon + \Delta E_p + \Delta E_g - \Delta E_k\right). \tag{A12.12}$$

APPENDIX 13. COMPUTING MOMENT MAGNITUDE

The moment magnitude M_w of a seismic event is determined from the Relative Slip Displacement (RSD) along the fault plane at the end of the seismic rupture according to

$$\mathrm{M}_w = \frac{2}{3}(\log M_0 - 9.1), \tag{A13.1}$$

with

$$M_0 = \int_{A_{slip}} \mu \mathrm{d}\, \mathrm{dA} = \mathrm{w} \cdot \{\sum_e \mu_e \cdot \mathrm{RSD}_e \cdot l_e\}.$$

Herein, d is the average slip displacement over the slip patch with area A_{slip} and μ the shear modulus. The seismic moment M_0 is calculated from the finite-element analysis results by summation of the Relative Slip Displacement RSD_e over all slipping interface elements with length l_e and shear modulus μ_e. That is, RSD_e is the incremental slip displacement calculated during the dynamic rupture simulation (analysis stage 2), and excludes the slip displacement calculated as a result of reservoir depletion (analysis stage 1).

Bibliographic information

Security Classification	UNRESTRICTED
Report Number	SR.18.01927
Title	Depletion-induced fault slip and seismic rupture
Subject	2D geomechanical models for the Groningen field, The Netherlands
Keywords	Geomechanics; fault reactivation; earthquake; moment magnitude; source-time function; friction coefficient; slip-weakening; FEM; bifurcation
Author(s)	P.A.J. van den Bogert (GSNL-PTD/E/Q)
Publish Date	December 2018
Export Control	Non-US Content – Non Controlled
Approved by	D. Doornhof (NAM-PTD/E/E)
Issuing Company	Shell Global Solutions International B.V., Rijswijk